The University of Queensland

Bachelor of Engineering Thesis

Explicit Finite Element Analysis of
High Speed Piston Impacts

Student Name:	IMRAN YUSUF
Course Code:	MECH4500
Supervisor:	Dr David Gildfind
Submission Date:	28 October 2016

A thesis submitted in partial fulfilment of the requirements of the
Bachelor of Engineering degree in Mechanical Engineering.

UQ Engineering

Faculty of Engineering, Architecture and Information Technology

Abstract

The University of Queensland operates three large scale free-piston drivers which consists of the T4, X2 and X3 facilities. These facilities are designed for the worst case scenarios based on conservative analytical impact mechanics, in terms of avoiding catastrophic piston impacts. However, these do not accurately predict the mechanical response for complex real geometry in the event of a piston impact.

In 2009, there was a high speed impact of a heavy piston that rendered the facility inoperable for two months. Repeated attempts were made to relieve enough stress in the plastically deformed piston to dislodge it from the compression tube. This impact reiterated the potential damage that can be caused by incorrect operation of the free-piston drivers and revealed that there was no structured methodology to estimate the condition of the facility to inform the repair procedure.

In this study, the AUTODYN solver was used to investigate three main explicit structural analysis problems including recreating the 2009 T4 high speed piston impact, perfoming a transient stress analysis of the peak pressure loadings acting on X2's lightweight piston using high strain rate material data and analysing the buffer for the X3 facility.

The approach to this study involved testing the solver's ability to capture the physical mechanisms involved during a high speed piston impact. An axisymmetric analysis of T4 shot 10509 was later developed where the numerical results were compared to observational comments of the facility made by the technician following the repair job. This approach to using an axisymmetric model was also used to analyse the peak pressure loadings acting on the X2 piston and the results from this were validated against a static structural analysis. An axisymmetric model of the X3 buffer was developed and this was validated against a 3D model.

This study has shown that the AUTODYN solver can be used to model high speed piston impacts with relative confidence. Furthermore, there was enough evidence to show that the numerical recreation of T4 shot 10509 did agree with the technician's observations following T4 shot 10509. This allowed for the response of the facility at higher impact speeds and with varying material properties to be investigated. The transient analysis conducted for the X2 lightweight piston agreed closely with the static structural analysis conducted prior. Since the X3 lightweight piston was made out of similar materials to the X2 piston, this validated the material data used for the X3 piston. It was also discovered that the nylon studs in the X3 facility would not likely fracture from an impact speed of 30 m/s by the X3 lightweight piston. This quantification of safe impact speeds for the X3 buffer was deemed important following the development of new driver operating conditons for the X3 facility.

Acknowledgements

Foremost, I would like to thank my supervisor Dr Gildfind for his continued support throughout the year, and faith in my ability to overcome all obstacles that got in my way.

My thanks also goes to Mr Grieve and Mr Hitchcock who since day one were always forthcoming with information about the impulse facilities at UQ.

I would also like to thank Prof. Morgan for his valuable comments on the work I have been conducting this year.

To my friends who allowed me to vent my frustrations with this thesis when things weren't going to plan, I thank you. In no particular order these are Daniel, David, Ambrose, Amedeo, Alex and Tom.

I would also like to thank both my parents for their love and support, especially my mum who took the time to read through my thesis draft even though the subject matter did not appeal to her (strange, I know).

Similiarly, I would like to thank my girlfriend, Angelene, and her family for their continued love and support during this year (and others, but especially this one). I suspect my girlfriend will be more thankful I am done with this thesis than I am.

Table of Contents

List of Figures

List of Tables

1. Introduction

1.1 Chapter Overview

This thesis is concerned with the modelling of high speed piston impacts to investigate how the large scale free-piston drivers at UQ will respond in such a scenario and to assess the survivability of these facilities. The chapter begins with an introduction to the impulse facilities being investigated. The discussion then focuses on the operations and operational challenges faced by these impulse facilities and details the 2009 T4 high speed piston impact and the implications of this incident. The objective of this thesis is then introduced – i.e. to reconstruct the 2009 T4 high speed piston impact using state-of-the-art numerical analysis tools, to validate prior static structural analyses and finally to analyse the buffers of the impulse facilities designed to catch the piston at the end of its stroke. Finally, an overview of the thesis structure is presented.

1.2 Impulse Facilities

Impulse facilities, such as shock tunnels and expansion tubes, are used to study the atmospheric re-entry of space vehicles. This is achieved by passing processed test gas over a scaled model of the space vehicle placed inside the test section of the facility (refer to Figure 1) (Igra, 2015). The specified flow conditions that pass over this model typically last for a few milliseconds, which is a sufficient amount of time to study the flow field surrounding the spacecraft model in these extreme test conditions (RWTH Aechen University, 2007).

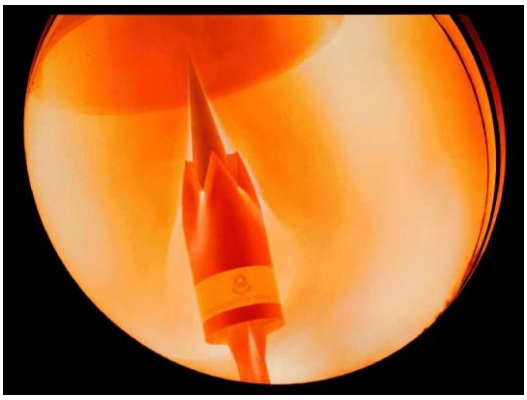

Figure 1 - Scramjet in a Shock Tunnel (Andrew Ridings, 2012)

There exists a variety of different impulse facilities but the highest performing facilities employ a technique first pioneered by Stalker (1972). In this technique, a sliding piston is utilised to compress a light driver gas in the compression tube which ruptures a diaphragm and expands into the tube with the test gas, thus creating a strong shock wave (Igra, 2015). The test gas is then processed by this shock wave, and then processed by a reflected shock and expanded through a nozzle (in the case of a shock tunnel) or processed by an unsteady expansion into a low pressure acceleration tube (in the case of an expansion tube) (Toniato et al., 2015). Refer to Section 1.4 for a detailed description of shock tunnel operations and 1.7 for a detailed description of expansion tube operations.

Two types of ground test facilities at the University of Queensland (UQ) which utilise the technique proposed by Stalker (1972) include the T4 reflected shock tunnel (RST) and the X2 and X3 expansion tubes.

1.3 The T4 Reflected Shock Tunnel

The T4 RST began routine operation at UQ in September 1987, following a five-month commissioning period (Morgan et al., 1988). Its intended use was to study the performance of scramjets and their components (Morgan et al., 1988). This shock tunnel was the latest in a series of free-piston shock tunnels at the time and its design was influenced by a disappointing feature of the T3 facility, at the Australian National University, which was the losses in pressure experienced in the shock tube (Morgan et al., 1988). While the reason for this loss in pressure was unclear Page & Stalker (1983) showed that this could be avoided by increasing the length of the compression tube for the same diameter.

The length of the compression tube for the T4 was set to 26 m in comparison to the 6 m length for the T3 (Morgan et al., 1988). Meanwhile, the compression tube inner diameters for these two facilities were equivalent at 229 mm. The length of T4's shock tube is 10 m and the inner diameter of the shock tube is 76 mm (Stalker, 1990). A diagram of the T4 facility is shown in Figure 2. The reservoir volume for the T4 is 1.2 m^3, which is capable of achieving a maximum working pressure of 14 MPa. A stainless steel piston is utilised to compress the driver gas prior to primary diaphragm rupture (Robinson et al., 2015).

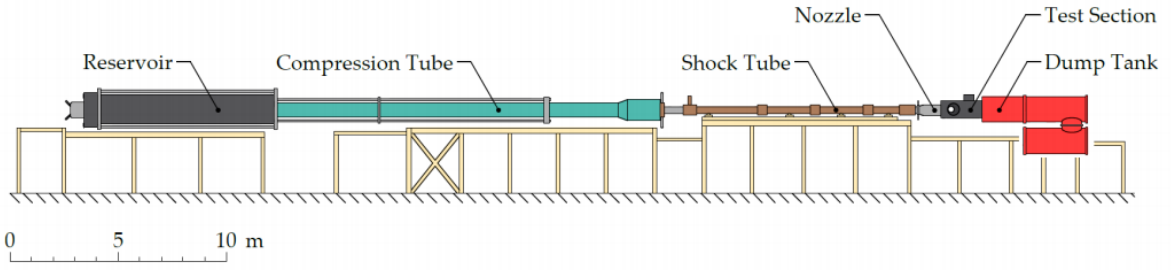

Figure 2 - T4-Free-Piston Driven Shock Tunnel (Robinson et al., 2015)

Scramjet flight up to Mach 10 can be simulated by the T4 and a relatively long test time of one to five milliseconds is achievable (Robinson et al., 2015).

1.4 Reflected Shock Tunnel Operations

An illustration of a free-piston driven reflected shock tunnel is shown in Figure 3. The main sections of the shock tunnel as shown in Figure 2 (which include the reservoir, compression tube, shock tube, nozzle and test section) can also be found in Figure 3. While the layout of the reservoir is different to Figure 2 however, the purpose of each section remains the same.

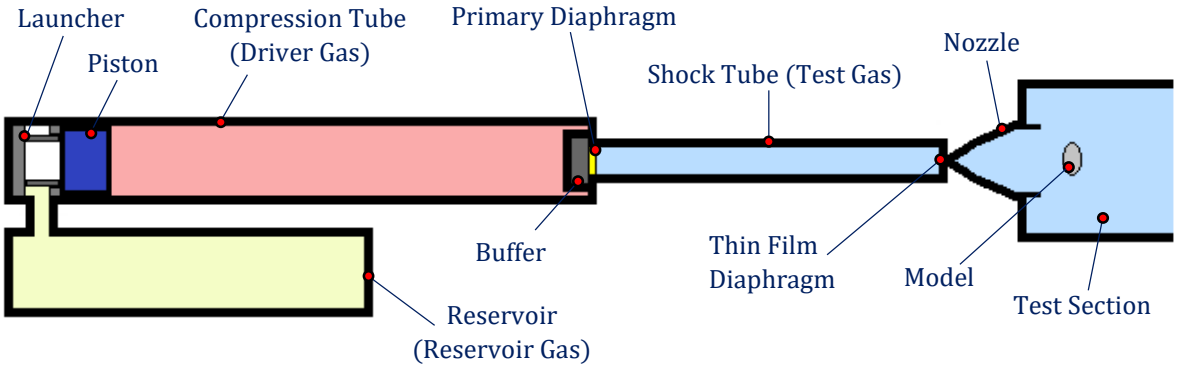

Figure 3 - Illustration of a Free-Piston Driven Reflected Shock Tunnel (Adapted from Gildfind, 2016)

As shown in Figure 3, the piston is initially held at the launcher at the upstream end of the compression tube. The reservoir contains high pressure compressed air and the cylindrical compression tube, which contains a relatively low pressure driver gas, is closed at the other end by the primary diaphragm (Robinson et al., 2015).

The launcher is slotted and allows for the air to expand through it. When the piston is released from the launcher, it accelerates by acquiring kinetic energy from the expanding

reservoir gas until the pressure in front of the piston is equivalent to the pressure behind it. At this point, the piston has high kinetic energy (Stalker, 1967). This is shown in Figure 4.

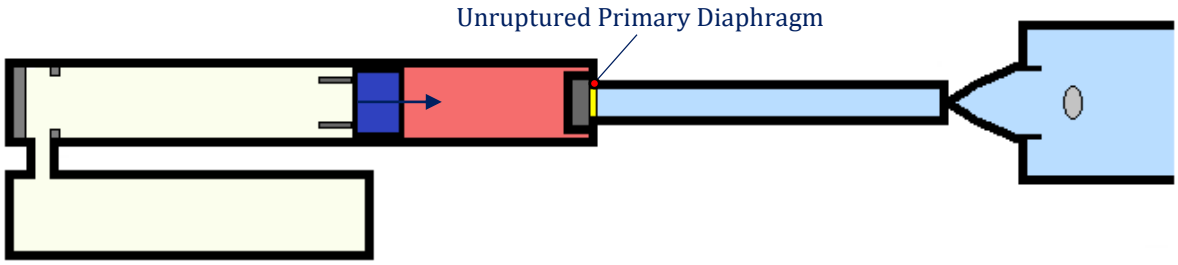

Figure 4 - Piston Released from Launcher in Shock Tunnel (Adapted from Gildfind, 2016)

As the piston travels further downstream of the compression tube, the kinetic energy from the piston is transferred to the driver gas that is being compressed and heated and so the piston loses velocity (Stalker, 1967). The primary diaphragm ruptures when the driver gas pressure reaches the threshold limit, which is dictated by the thickness of the diaphragm and its mechanical properties that reflect the conditions desired in the test section (Lacey, 1992). The rupturing of the primary diaphragm is shown in Figure 5.

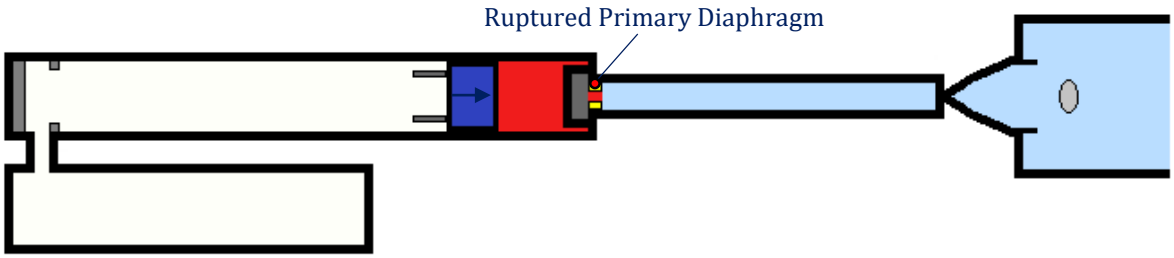

Figure 5 - Rupturing of Primary Diaphragm in Shock Tunnel (Adapted from Gildfind, 2016)

At the end of its stroke the system is designed so that the piston has negligible kinetic energy, having transferred it to the driver gas (Gildfind et al., 2015). The piston can therefore be caught at the end of the compression tube by a buffer. This is shown in Figure 6. Brakes may be incorporated into the piston to prevent the piston from travelling back up the compression tube if there remains residual high pressure driver gas after the piston has come to rest (Gildfind et al., 2015).

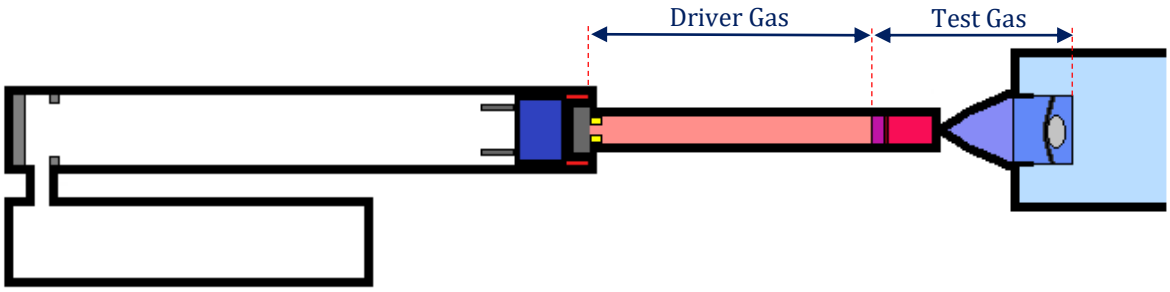

Figure 6 - Expanding Driver Gas into the Shock Tube (Adapted from Gildfind, 2016)

When the primary diaphragm bursts, the expanding driver gas behaves like a piston which compresses the test gas and accelerates it towards the test section (Igra, 2015). A shock wave is developed in the process which processes the test gas and this test gas is then processed again by a reflected shock. The hot test gas ruptures the thin film diaphragm and expands through the nozzle as shown in Figure 7 (Toniato et al., 2015).

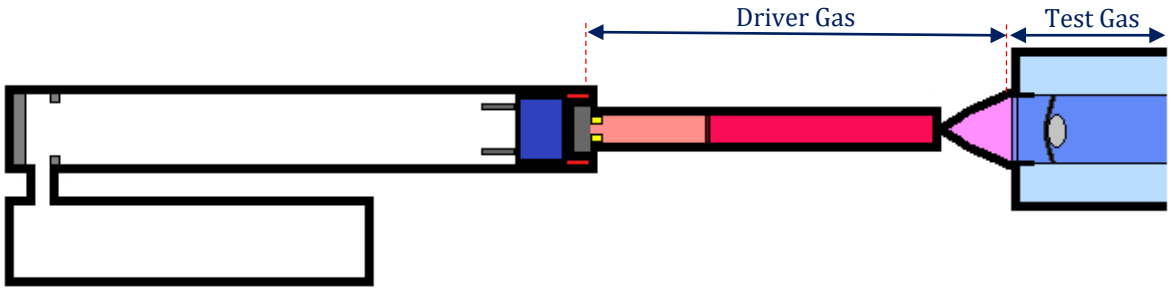

Figure 7 - Start of Test Time in Shock Tunnel (Adapted from Gildfind, 2016)

The expanded test gas flows over the model. The supplied test time, which is up to a few milliseconds, ends when the test gas properties depart too far from the nominal test conditions. When the driver gas reaches the model, the supplied test time is definitely over (Gildfind, 2016). This means that the useful test flow is over before the time shown in Figure 8.

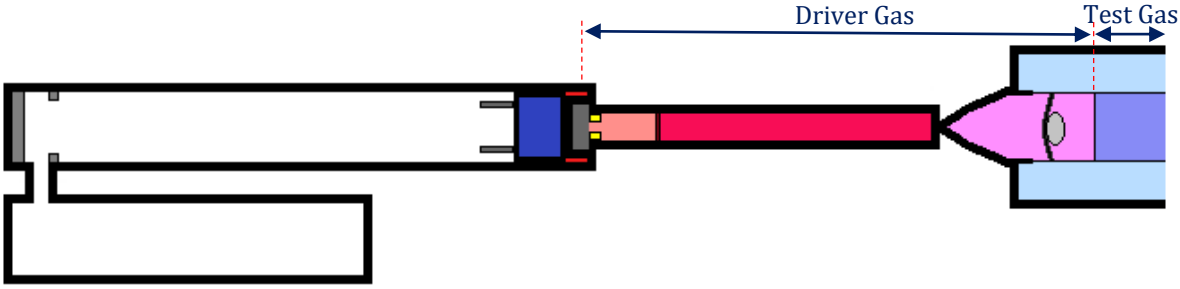

Figure 8 - End of Useful Test Flow in Shock Tunnel (Adapted from Gildfind, 2016)

1.5 The X2 Super-Orbital Expansion Tube

The X2 expansion tube was commissioned at UQ in 1995 (Jacobs et al., 2013). It differs from the T4 reflected shock tunnel in that the test gas is processed by an unsteady expansion into a lower pressure acceleration tube rather than it being processed by a reflected shock and expanded through a nozzle. A diagram of the X2 can be seen in Figure 9.

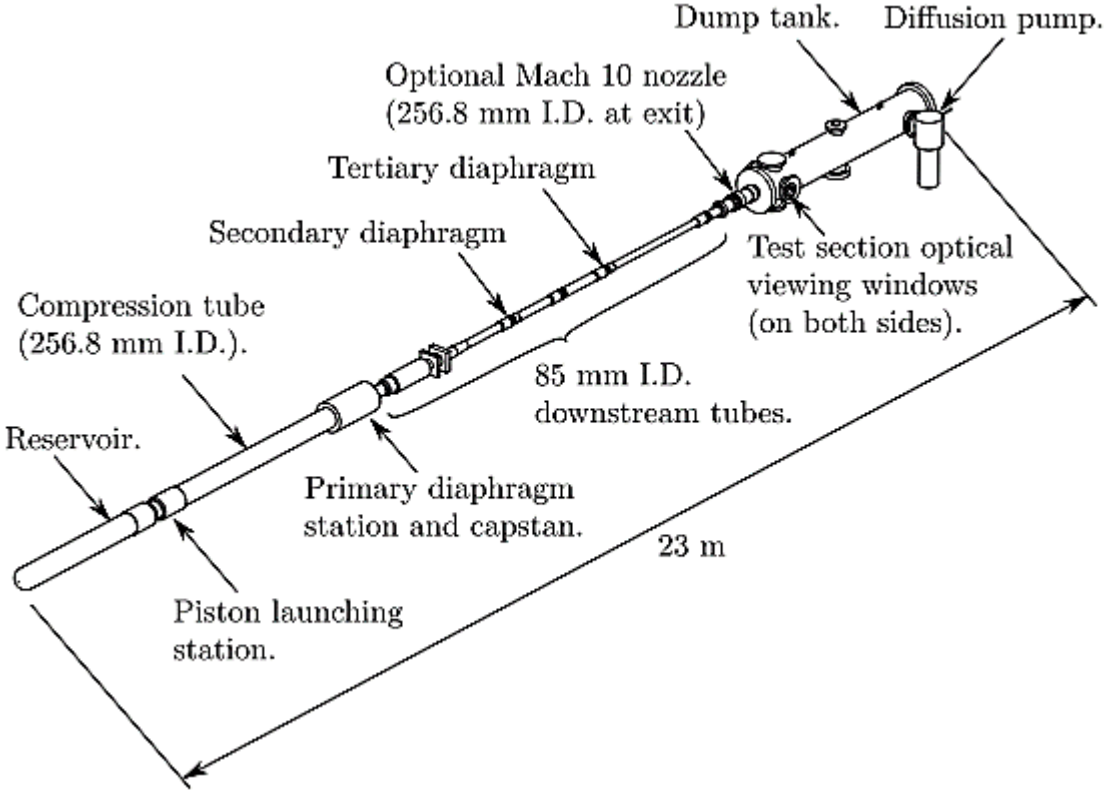

Figure 9 - Illustration of X2 Expansion Tube Facility with Mach 10 Nozzle (Jacobs et al., 2013)

This facility was designed to study super-orbital test flows, such as planetary entry and can simulate scramjet flight up to Mach 15 and planetary entry flows up to 15 km/s (Gildfind, 2016). The test time for the X2 is shorter at 0.05 milliseconds compared to the five millisecond test time that can be achieved by the T4 (Gildfind, 2016).

1.6 The X3 Expansion Tube

The X3 Expansion Tube at UQ was commissioned in 2001 (Gildfind et al., 2012). Like the X2, this facility was designed primarily for superorbital flow conditions (Morgan et al., 2001). While X3 can achieve the same flow conditions as X2, the X3 can accommodate significantly larger models and achieve longer test times (Gildfind et al., 2012). The test time

for the X3 facility is nominally 0.1 to 1 milliseconds (Gildfind, 2016). A diagram of the X3 can be seen in Figure 10.

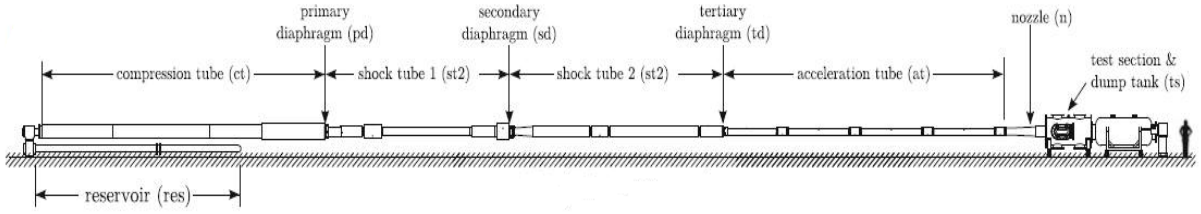

Figure 10 - Illustration of X3 Expansion Tube (Gildfind et al., 2016)

1.7 Expansion Tube Operations

An illustration of a typical expansion tube can be seen in Figure 11. The driver for the expansion tube operates in the same way as the shock tunnel as stated in Section 1.4.

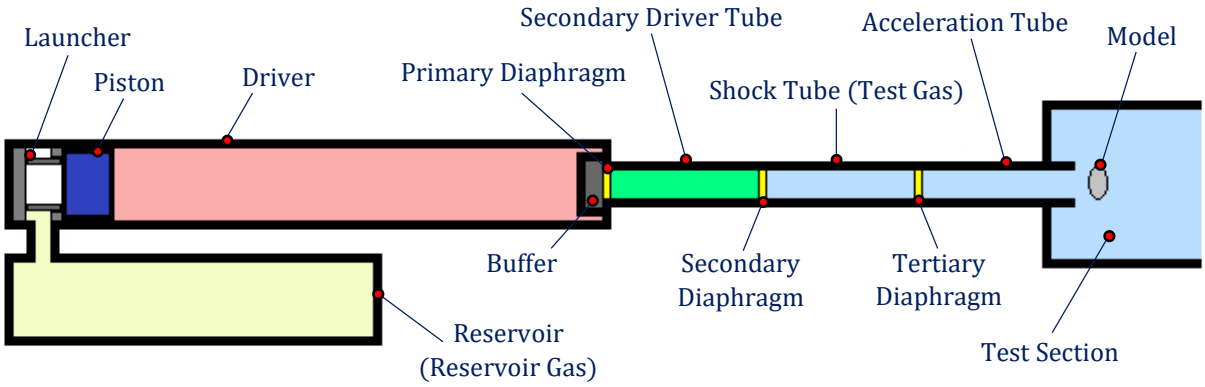

Figure 11 - Illustration of Expansion Tube (Adapted from Gildfind, 2016)

As with the operations of the reflected shock tunnel described in Section 1.4, the piston compresses and heats the driver gas. Close towards the primary diaphragm, the build-up of driver gas pressure is eventually enough to rupture the primary diaphragm and slow down the piston before it reaches the buffer.

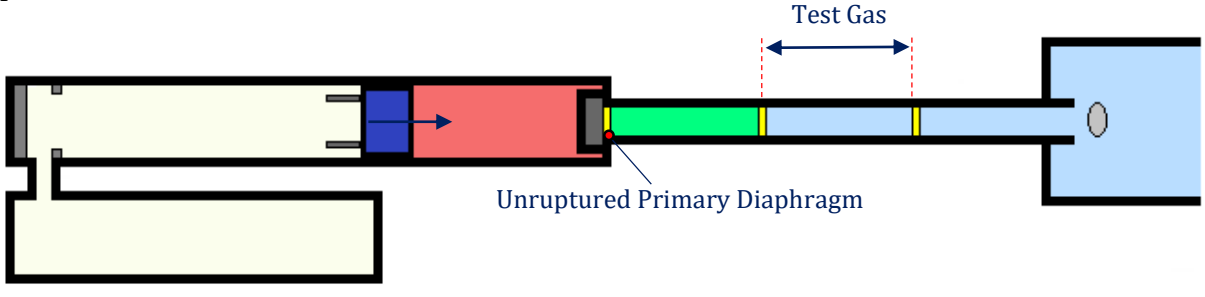

Figure 12 - Piston Released from Launcher in Expansion Tube (Adapted from Gildfind, 2016)

As shown in Figure 13, shock tube flow is initiated in the driver tube once the primary diaphragm is ruptured (Gildfind, 2016).

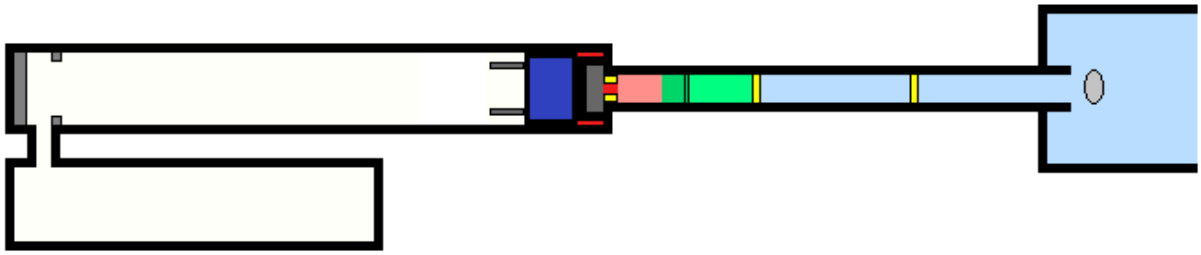

Figure 13 - Rupturing of Primary Diaphragm in Expansion Tube (Adapted from Gildfind, 2016)

The secondary diaphragm separates the secondary driver gas and the test gas. Once the secondary diaphragm is ruptured, the test gas is compressed and accelerated towards the test section (Gildfind, 2016). This is shown in Figure 14.

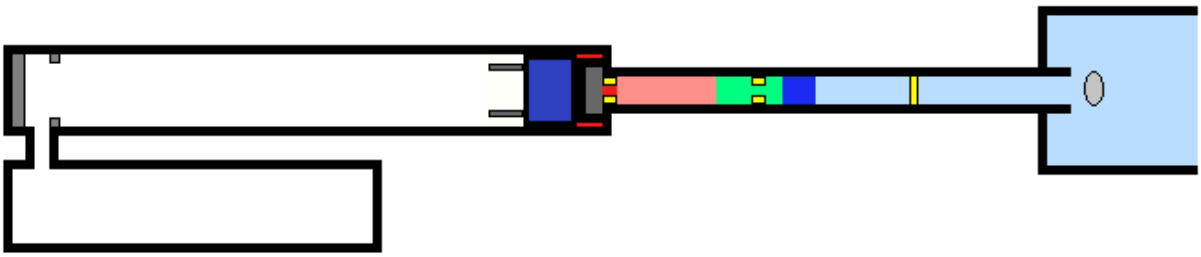

Figure 14 - Rupturing of Secondary Diaphragm in Expansion Tube (Adapted from Gildfind, 2016)

High temperature and pressure test gas then expands into the low pressure acceleration tube as shown in Figure 15.

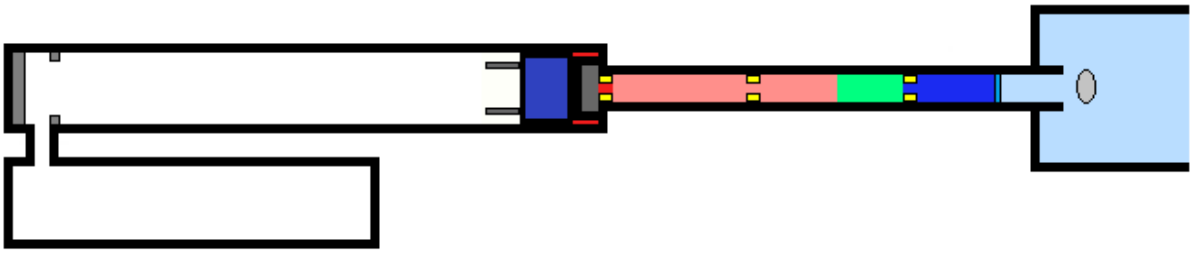

Figure 15 - Rupturing of Tertiary Diaphragm in Expansion Tube (Adapted from Gildfind, 2016)

The expanded test gas reaching the model marks the start of the test time as shown in Figure 16. The test time is then terminated by the arrival of unsteady expansion (Gildfind, 2016).

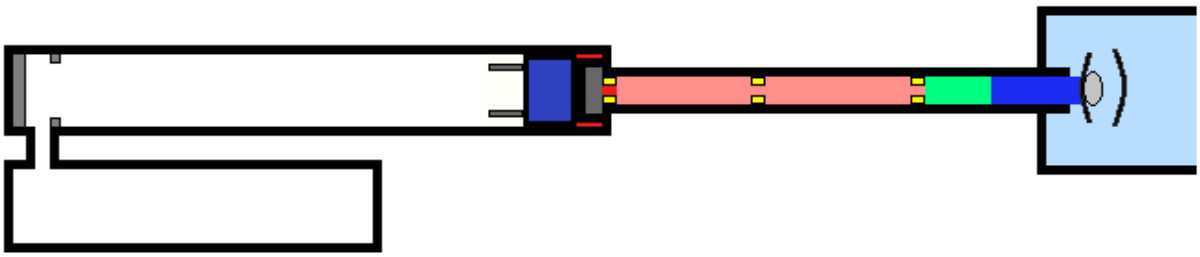

Figure 16 - Start of Useful Test Flow in Expansion Tube (Adapted from Gildfind, 2016)

1.8 Operational Challenges

A prolonged duration of pressure pulse from the driver is necessary so that the drive shock tube processes the full length of the facility (Gildfind et al., 2010).

To achieve this, Stalker (1967) proposed a tailored piston operation. This involved allowing the piston to travel with a sufficient velocity upon the rupturing of the primary diaphragm such that the venting driver gas mass flow could be matched by the piston volumetric rate of displacement (Itoh et al., 1998). Consequently, the non-dimensional piston speed at diaphram rupture, β, would be equal to 1 (Itoh et al., 1998). Refer to Figure 17 for the illustration of this concept.

Stalker (1967) also proposed an over-tailored operation. This involved allowing the piston to momentarily continue to increase the driver gas pressure before the pressure would begin to fall again after the primary diaphragm is ruptured (Itoh et al., 1998). This significantly extended the useful supply time of driver gas pressure where the acceptable limits of varying driver gas pressure would be within 10% (Itoh et al., 1998). Refer to Figure 17 for the illustration of this concept where $\beta > 1$ represents the over-tailored operation (Itoh et al., 1998).

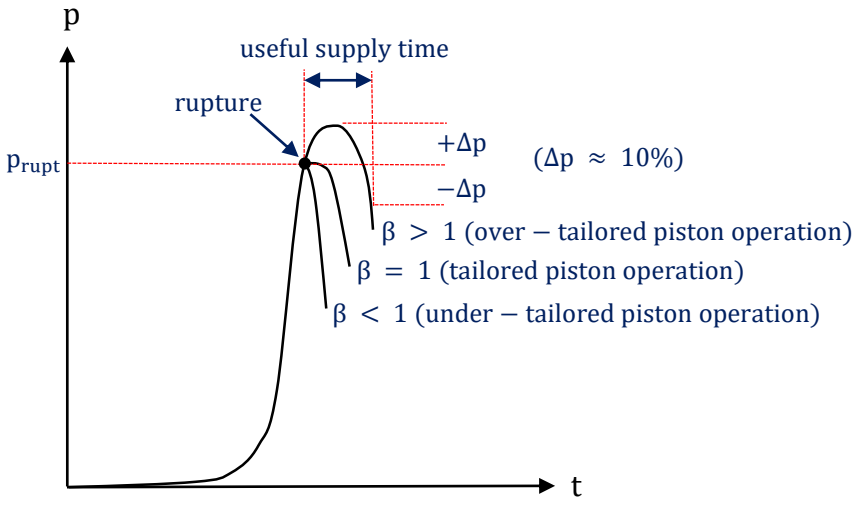

Figure 17 - Effect of Piston Ove-Driving on Driver Pressure (Adapted from Gildfind, 2010)

Making sure the piston dynamics are correct as to satisfy over-driven piston operation but also avoid structural damage to the facility is challenging. This is because high piston speeds in the range of 100 m/s to 300 m/s are necessary to compensate for the driver gas loss into the shock tube but at the same time the piston has to be brought to rest within an extremely short distance before reaching the buffer (Gildfind, 2016). Figure 18 introduces three impact scenarios that exist in the shock tunnels and expansion tubes.

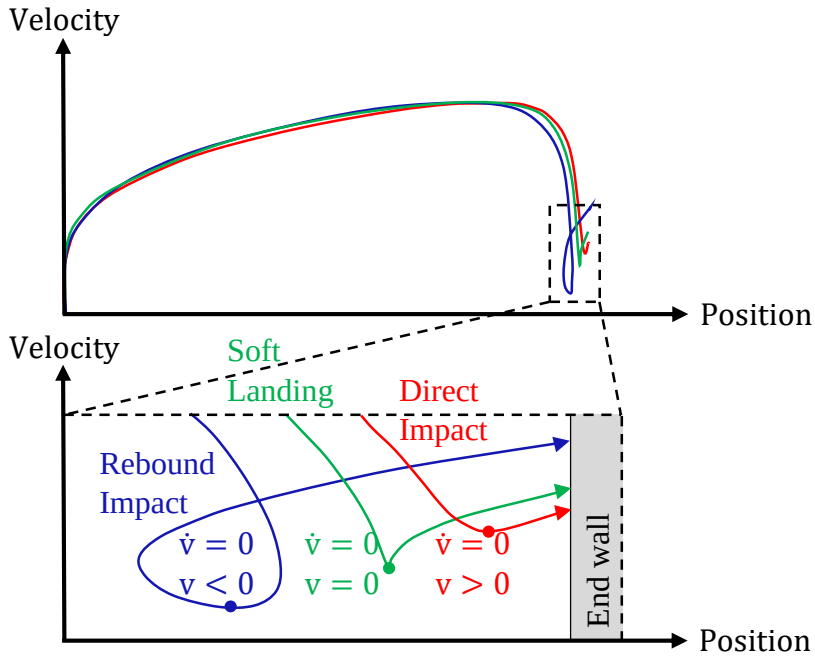

Figure 18 - Three Impact Scenarios in Impulse Facility (Adapted from Gildfind et al., 2015)

A soft landing will occur if a fine balance between intertial and pressure forces acting on the piston is achieved such that the piston can be caught by the buffer when the piston's velocity and acceleration are simulatenously zero (Gildfind et al., 2015). See Figure 18 for illsutration of this concept.

However, if the build-up of driver gas pressure ahead of the piston does not bring the velocity of the piston below zero when the acceleration of the piston is zero at the inflection point then a direct landing into the buffer will occur. Depending on the impact speed, this could lead to irreparable damage (Gildfind et al., 2015).

If the velocity of the piston is above zero when the acceleration of the piston is zero at the inflection point, then a rebound impact will occur. The rebound occurs because the high driver pressure is momentary, but then it vents through the ruptured diaphram resulting in a drop of pressure so that the residual reservoiur pressure accelerates the piston forward again. This could also lead to irreparable damges however, brakes can be installed onto pistons which are designed to prevent the piston from moving backwards (Gildfind et al., 2015).

According to Gildfind et al. (2011), there has been development of new lightweight pistons for the X2 and X3 facilities to achieve the tuned operation conditions mentioned earlier. Minimising the mass of the piston is advantageous because it allows for the piston to be able to accelerate to the high speeds that are required to extend the useful supply time of driver gas pressure and also because it means that the piston can decellerate to rest over shorter distances.

1.9 The 2009 T4 High Speed Piston Impact

On December 18 2009, the T4 shock tunnel facility fired its 10,509th shot. An unexpected, loud noise following this shot prompted an immediate examination of the facility. It was discovered that the buffer had been completely obliterated and the piston had plastically plugged itself into the end of the compression tube thus rendering the facility inoperable.

Upon the reviewal of the shot summaries for the T4 shock tunnel facility, it was evident that this incident was the result of an incorrect selection of fill pressures (i.e. operator error). displays the shot summary for shot 10509 as well shot 10508, which was conducted the day before. The reservoir gas pressure for shot 10509 was supposed to be set at 650 kPa for a driver pressure of 13.7 kPa. However, a reservoir pressure of 1650 kPa was accidently used (which was the same reservoir pressure used in shot 10508). The driver pressure for shot 10509 was still lowered to 13.7 kPa. As a result, the higher than intended reservoir pressure imparted too much kinetic energy to the piston for the driver pressure to slow it down in time before reaching the rubber buffer.

Table 1 - Shot Summaries for Shot 10508 and Shot 10509

Parameter	**Shot 10508**	**Shot 10509**	
		Intended	**Actual**
Reservoir Gas	100% Air	100% Air	100% Air
Reservoir Pressure [kPa]	**1650**	**650**	**1650**
Driver Gas	100% Ar, 0% He	100% Ar, 0% He	100% Ar, 0% He
Driver Pressure [kPa]	**27.4**	**13.7**	**13.7**
Diaphragm [mm]	1	1	1
Shock Tunnel Fill Pressure [kPa]	50.0	50.0	50.0
Air Test-Section Fill Pressure [kPa]	0.4	0.4	0.4

It was unclear at the time whether the piston deformed the tube walls such that pushing on the piston would scrape out the tube's inner surface, thereby seriously damaging the most expensive component in the facility (the compression tube). Repeated attempts were made to relieve the interference loading between the plastically deformed piston and the compression tube.

Figure 19 - Drill-Holes on Front Face of T4 Piston

The first of these included attempting to shrink the piston through the use of liquid nitrogen and then pushing on the piston. When this failed, thirty-nine holes (with a 13 mm cobalt drill) were drilled around the periphery of the front face of the piston in an attempt to stress relieve the piston. By combining cooling from liquid nitrogen, compressed air and further drilling to the piston's accessories, the piston was removed successfully, two months after T4 shot 10509. The piston is still in its partially swollen state. It was found that the compression tube did not suffer any evident permanent yielding.

Figure 20 - T4 Piston in Partially Swollen State

Due to its relatively low cost, the damage to the rubber buffer was of least concern compared to the damage to the piston and the compression tube. However, the damaged mounting buffer plates used in shot 10509 can be seen in Figure 22 and Figure 23.

Figure 21 - T4 Rubber Buffer

Figure 22 – T4 Buffer Plate A

Figure 23 – T4 Buffer Plate B

1.10 Implications of the 2009 T4 High Speed Piston Impact

The 2009 T4 high speed piston impact showed that the incorrect operation of impulse facilities could result in potentially damaging operation at any time (including during commissioning of new conditions), with any number of permutations of error and consequences. Furthermore, it revealed what damage a high speed piston impact can cause.

The impact served as a reminder of the fact that the T4, X2 and X3 facilities were designed according to conservative analytical principles but there is not yet an established methodology to predict the detailed structural response of the system. This is especially important when considering the development of new lightweight pistons for the X2 and X3 facilities for higher speeds at new conditions where there is uncertainty about the conditions being designed. These lighter pistons would be subjected to high loading rates and there is no

established methodology for stress analyses that takes these high loading rates into account or a structured methodology to estimate the condition of the facility to inform the repair procedure.

Prior stress analyses of these facilities has been limited to the driver pressure loading and reservoir pressure loading acting on the X2 and X3 pistons (Gildfind et al., 2010). These analyses were static structural analyses and therefore triansient effects were not modelled directly. To date, there has been no detailed impact analysis that has been performed for any of the impulse facilities at UQ (Gildfind et al., 2010).

The 2009 T4 high speed piston impact also raises a wider issue in relation to what impact speeds can be tolerated by the compression tube and what impact speeds the nylon stud buffer can withstand before damage to the metal components of the facility will occur.

The X2 and X3 facilities use a nylon stud buffer and there does exist an analytical method for determining the maximum permissible impact speed that the nylon stud buffer can withstand (Gildfind, 2010). However, this method makes the assumption that the nylon stud plastically deforms immediately during impact at constant volume at a constant presssure of 10 MPa and so does not account for the changes in strain rates that the studs would experience or provide a detailed transient view of the stresses in the stud during a high speed piston impact (Gildfind, 2010). Furthermore, it makes the assumption that the maximum permissible impact speed occurs when the nylon studs fully occupy the cross-sectional area of the compression tube and does not take into account whether the nylon studs will fracture before this occurs (Gildfind, 2010).

These issues highlight the need for a tool to be developed that will allow for the prediction of a detailed and accurate structural response of the system during a high speed piston impact.

1.11 Problem Statement

The aim of this thesis is to apply explicit FEA techniques to three main structural analysis problems including receating the 2009 T4 high speed piston impact, perfoming a transient analysis of the peak pressure loadings acting on the X2 piston (using high strain rate material data) and analysing the buffer for the T4, X2 and X3 facilities.

Recreating the 2009 T4 high speed piston impact will provide the opportunity to see how well numerical tools can predict the structural response after the impact. Furthermore, this will provide verification of facility survivability for the worst case scenario at higher speeds. The transient analysis of the driver pressure loading and reservoir pressure loading acting on the X2

piston will provide validation of the X2 static structural analysis done previously as well as bring confidence to the high strain rate material data used in the transient analysis.

Analysing the nylon stud buffer will provide the opportunity to see what impact speeds can be tolerated by the buffer during commissioning when there is uncertainty about the conditions being designed.

These three main structural anlaysis problems has signifiance in providing the potential to establish better defined predictions of impact consequences and better inform repair jobs in the occurrence of a high speed piston impact into the end of the compression tube. Additionally, the high strain rate material data which will be acquired for the impact analysis of the T4, X2 and X3 also sets up the capability for future FEA work in the design of new impulse facilities.

1.12 Proposed Approach

The type of impact problem involved in replicating shot 10509 is complex and introduces processes such as high strain rates, material yielding, contact and friction, and a variety of potential deformation modes for the piston and its accessories, as well as the compression tube and buffer.

In practise, existing analytical models lack the ability to model this type of impact problem for complex geometry (see Section 2.2 for discussion on the Taylor model) and so focus has been placed on using numerical tools instead. The X2 static structural analysis mentioned in Section 1.10 used an implict numerical method which was suited to static problems where the time mangitude involved was relatively large. However, in the case of a high speed piston impact where transient effects should be considered and the time magnitude involved is relatively small, the explicit method is better suited (see Section 2.5 for further detail on the implict and explicit method). Therefore, numerical tools which make use of the explicit method promises the best understanding of the structural response of the impulse facility after a high speed piston impact has occurred.

It is of significant interest to this project to be able to produce meaningful results which can be verified in terms of the reliability, robustness and accuracy. Table 2 illustrates the risks that need to be considered to better understand the numerical solver and correctly model the high speed piston impact problem.

Table 2 - Key Sources of Error in Finite Element Analysis (Pointer, 2014)

Hazards	Description
User Error	Not approaching the problem correctly due to operator error or inexperience.
Modelling Error	Not accounting for all important physical processes, such as using the inappropriate material model, using a 2D behaviour that does not allow for potential 3D deformation modes to be visible, etc.
Discretisation Error	Mesh used is not correct to capture the response properly.

The three main structural analysis problems discussed in Section 1.11 will be accomplished by:

1) Selecting an appropriate numerical solver;
2) Devising a series of finite element benchmarks to check that the explicit solver is able to model high speed piston impacts correctly and also to check that the code is being used correctly;
3) Reconstructing the 2009 T4 high speed piston impact, as there exists experimental data it can be compared against, and see if the numerical tool can predict a similar outcome;
4) Examining the response of the T4 facility at higher piston impact speeds to determine limits in terms of permanent damage to the compression tube and piston;
5) Determining the sensitivty of these results to changes in material properties of the compression tube and the piston and changes in piston impact speeds;
6) Reproduce the static structural analysis of the peak loading conditions on the X2 lightweight piston using explicit finite element techniques. This should be done to validate the transient material data used for the X2 and to establish whether the piston can be treated as axisymmetric;
7) Analysing the buffers, which can fail after large displacements and which behave quite differently to metals, so that a better estimate can be made as to what sort of impacts they can resist before damaging the metal components of the facility.

See Section 1.13 for the detailed work scope of the T4, X2 and X3 numerical modelling.

1.13 Work Scope

This work focuses on three main aspects of piston impacts inside these impulse facilities. The first is the ability to accurately reconstruct T4 shot 10509 and validate the model using observations made by the technician after the incident. Following this, a look towards the response of the facility at higher impact speeds will be investigated as well as the influence that changes to material properties have on the structural response. The second is the ability to translate the explicit finite element techniques applied to the T4 facility to an analysis of the peak pressure loadings acting on the X2 piston to see if close agreement can be made with two static structural analyses done prior. In light of the commissining of X3's new lightweight piston, an assessment on the survivability of the nylon stud buffer at impact speeds up to 30 m/s will be carried out also.

It is out of scope to conduct a detailed analysis of the the X2 and X3 lightweight pistons impacting the end of the compression tube at high speeds (> 30 m/s). Furthermore, it is out of scope to acquire the high strain rate material data necessary for these analyses using an experimental approach. Instead, this material data will be obtained from existing literature. Moreover, it is out of scope to validate the quantification of safe impact speeds for the X3 buffer using experimental methods.

1.14 Chapter Outlines

Chapter 2 details a review of relevant literature in the area of explicit finite element modelling and its validity in addressing the high speed piston impact problem.

Chapter 3 discusses the selection of an appropriate numerical solver, a qualitative assessment to identify relevant physical mechanisms leading to the selection of an appropriate numerical solver, followed by benchmarking of the solver for these relevant physical mechanisms.

Chapter 4 details the axisymmetric explicit finite element analysis replicating T4 shot 10509 and also includes an assessment of the T4 facility survivability for the worst case scenario (at higher speeds). The sensivity of the results to changes in friction coefficiencts, changes in piston impact speeds and changes in the material property for the piston body and compression tube is addressed.

Chapter 5 details the transient stress analysis of the X2 lightweight piston, which was analysed as a static problem previously and how the X2 lightweight piston can be treated as axisymmetric. It also provides a discussion on the implication of these results to the X3 lightweight piston.

Chapter 6 details the modelling of the nylon stud buffer of the X3 facility at high impact speeds in light of the comissioning of X3's new lightweight piston and thus new driver conditions. The survivability of these studs at the maximum design impact speed is assessed. Furthermore, the effect that the length of the stud and strain rates that the studs undergo after a piston impact with the X3 piston is assessed in terms of velocity loss of the X3 piston, the effective stress of the studs and maximum compressive deformation of the studs.

Chapter 7 summarises key findings and their relevance. It also provides recommendations for future work to enhance the validity of these findings and progress them further.

2 Literature Review

2.1 Chapter Overview

This chapter presents a detailed discussion on the area of finite element modelling and its validity in addressing the high speed piston impact problem. The chapter begins with a discussion on why existing analytical models lack the capbility to accurately model the high speed piston impacts being investigated and thus why state-of-the-art numerical analysis tools is necessary. The discussion then focuses on the relevant impact simulations that currently exist and the modelling techniques used to make these simulations viable. The question of how to best model metal and polymer materials for components involved in a high speed piston impact is addressed in this discussion.

2.2 The Taylor Model

In 1948, Taylor proposed a method to analyse the behaviour of steel at high-strain rates, which is today referred to as the 'Taylor bar impact test' (Taylor, 1948). It involved firing a flat-nosed cylindrical projectile, of uniform cross-sectional area and constant density into a flat rigid target at a specified impact velocity. While overly simplified, this experiment can be considered to bare a resemblance to a piston impacting the end of a compression tube.

Taylor observed that the cylindrical specimen suffered elastic and plastic stress inside its body, in the form of waves, and observed that the projectile had mushroomed after impact (Buchely et al., 2012). For the deformation mode where mushrooming had occurred, Taylor devised a one-dimensional theoretical model to predict the state of the cylindrical specimen after impact. In short, the ratio between the length of the projectile that suffered no plastic strain, x, and the original length of the projectile, L, was determined using:

$$\log_e\left(\frac{x}{L}\right)^2 = \frac{1}{1-e} - \log_e(1-e) - \frac{1}{1-e_1} + \log_e(1-e_1) \text{ where } \frac{\rho V^2}{S} = \frac{e_1^2}{1-e_1} \quad (1)$$

Where e is the longitudinal strain, e_1 is the longitudinal strain at the moment of impact, ρ is the density, V is the impact velocity and S is the yield stress of the projectile.

Also, the final position of the plastic boundary along the projectile, h, was used to determine the final shape of the projectile after impact:

$$h = -\int_{L}^{x} (1 - e)dx \tag{2}$$

Figure 24 graphically displays the significance of h, x and L dimensions from equations (1) and (2) as well as the mushroomiung deformation mode that the Taylor analytical model predicts.

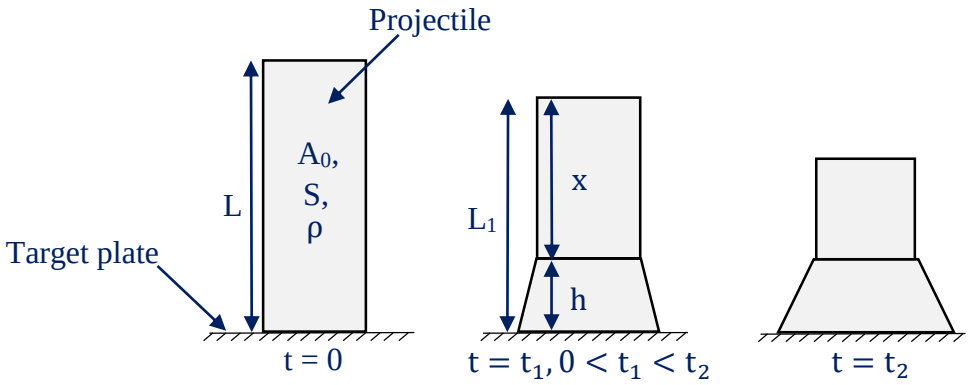

Figure 24 - Illustration of Taylor Model (Adapted from Taylor, 2014)

Close agreement was made between this analytical model and tests where the impact velocity did not exceed 250 m/s. However, even Taylor recognised that this analytical model proved inadequate for predicting the shape of the cylindrical steel projectiles for sufficiently high impact speeds where radial effects could not be ignored. This was primarily because the Taylor analytical model neglected radial effects and consequently did not account for the high radial velocity imparted to the projectile material close to the target plate (Taylor, 2014). Figure 25 shows the steel projectiles which the Taylor analytical model could not adequatly predict.

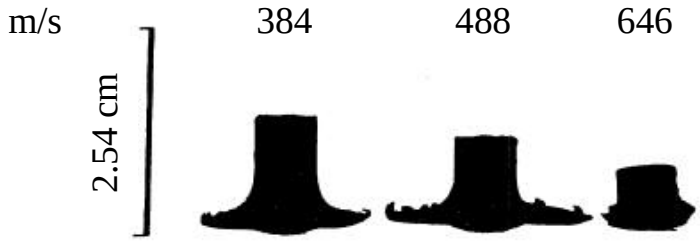

Figure 25 - Steel Cylinders after Taylor Bar Impact Test (Adapted from Whiffin, 1948)

Since the development of the Taylor model, research conducted by Blackman and Goldsmith (1978), Woodward et al. (1992) and Chen et al. (1998) have identified five separate failure and fragmentation modes in the cylindrical projectile through the Taylor bar impact test (refer to Figure 26). In order of increasing severity, these included (a) mushrooming where no visible cracking occurred, (b) tensile splitting where cracking was visible on the mushroomed end due to the tensile hoop strains exceeding the material ductility limit, (c) shear cracking where there existed principal shear fracture or spiral shear fracture and tensile splitting, (d) fragmentation which occurred due to shear cracks and (e) petalling which occurred due to tensile splitting in conjunction with some fragmentation (Rakvåg et al., 2013).

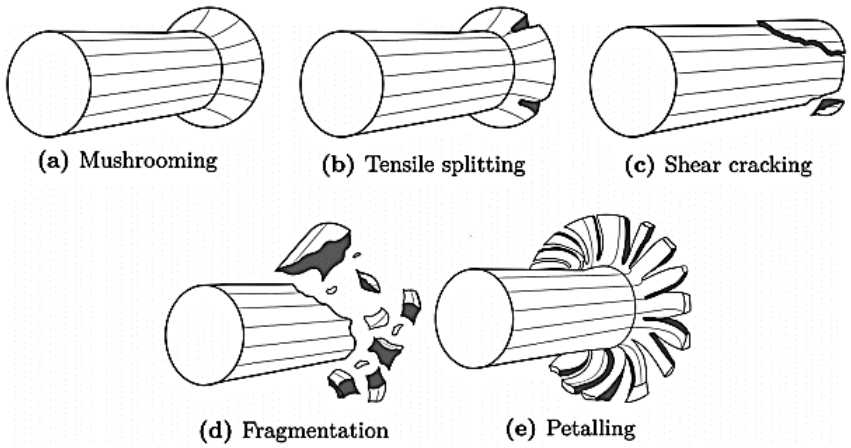

Figure 26 - Five Distinct Deformation Modes of Cylindrical Projectile during Taylor Bar Impact Test (Rakvåg et al., 2013)

Analytical modelling is not the correct approach for modelling high speed piston impact problems because existing analytical models over simplify the problem. First, the Taylor model assumes a perfectly cylindrical projectile whereas the T4, X2 and X3 pistons are more complex in shape (see Appendix A for technical drawings of the T4). Secondly, the projectiles studied by Taylor are not confined radially whereas the piston is confined by the compression tube walls. Furthermore, there will be friction interactions between the piston, piston accessories and the compression tube which is not considered in the analytical model. Moreover, it only addresses the mushrooming deformation mode whereas several other deformation modes have been found through conducting the Taylor bar impact test.

2.3 The Use of Numerical Tools for Impact Problems

The growth and availability of digital computers from the 1940's has increased the use of numerical analysis tools to solve the more complex mathematical models of the world (Atkinson, 2007). In addressing the Taylor model described in Section 2.2, numerical analysis tools have been used to simulate the Taylor bar impact test.

However, the use of numerical tools is not limited to just the Taylor bar impact test. Numerical tools have also been used to simulate bird strikes and bird ingestion, vehicle collisions, ballistic impacts and sheet metal forming. Section 2.4 details important modelling techniques used to make these impact simulations viable.

2.4 Modelling Techniques for Impact Simulations

According to Russ (2012), analysing impact problems require supressing the detail that would otherwise be involved in complex 3D features. The consequences of omitting these details would do little to reduce the accuracy of the results (if done correctly), but would drastically improve the computational performance in terms of mesh size and quality.

Research conducted by Liu et al. (2014), Katukam (2014), Mithun et al. (2012) and Yancey (2011) on the simulation of bird strikes using numerical methods support this statement by Russ (2012). In their papers, a homogenous bird model with a simplified geometrical shape, as shown in Figure 27, is used to study aircraft bird strikes. This bird model is then validated by having it impact a rigid surface and comparing the numerical solution to an experiment.

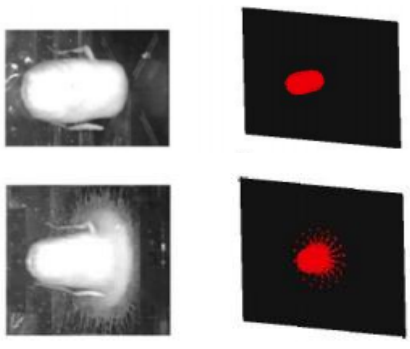

Figure 27 - Comparison of Experimental Test (Left) and Numerical Simulation (Right) of Bird (Mithun et al., 2012)

Once satisfied with the model of the bird, the bird is made to impact the aircraft structure and as shown in Figure 28, good qualitative agreement between experimental data of an aircraft-bird strike can be achieved using this numerical method.

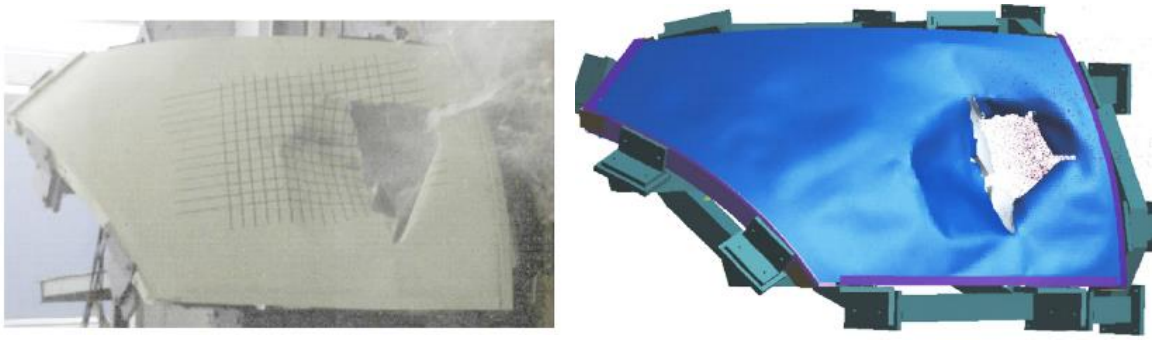

Figure 28 - Comparison of Experimental Test (Left) and Numerical Simulation (Right) of Aircraft Bird Strike (Liu et al., 2014)

This approach of simplifying the model to reduce the simulation run time of the analysis was also used by Younes (2009) in his investigation into crashworthiness of motor vehicles. Instead of numerically modelling the entire vehicle, focus was given towards modelling simple crush tubes and its displacement response to a given load in ABAQUS. Experimental results conducted by Paik et al. (1996) and Zhang et al. (2007) closely matched the numerical simulations conducted by Younes (2009). This is shown in Figure 29 where the numerical load-axial displacements curve and the compressive deformation of the crush tube over time accurately predicted the experimental results obtained by Paik et al. (1996) and Zhang et al. (2007).

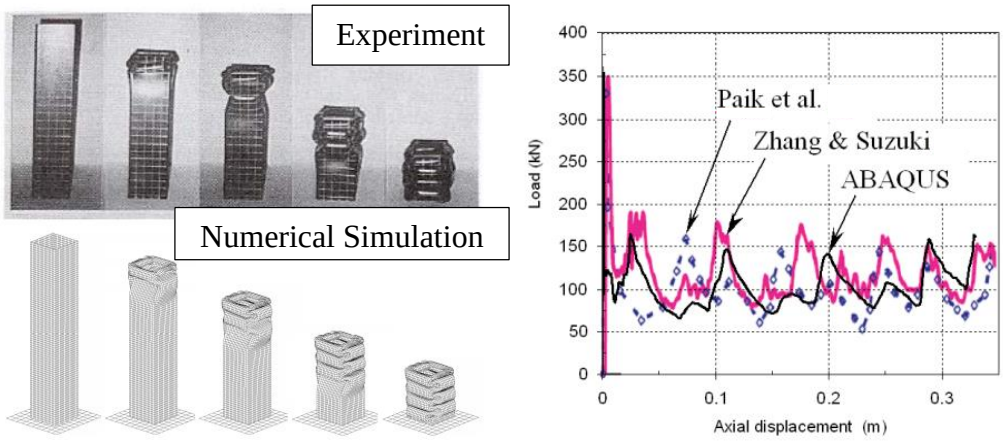

Figure 29 - Comparison of Experimental and Numerical Simulation of Crushing of the Square Tube (Younes, 2009)

According to Adams (2003), numerical simulations of the Taylor bar impact test (discussed in Section 2.2) is an important validation test in ballistics. This validation is achieved by implementing high strain rate material data (discussed further in Section 2.6) into the numerical model and then comparing the final shape and length of the bar between the numerical and experimental results. Close agreement between the numerical and experimental results validates the implemented high strain rate material data.

Following this analysis, Ames (2014) demonstrates that a 2D axisymmetric model of the Taylor bar impact test can be used instead of a 3D model for the mushrooming deformation mode where no fracturing in the projectile occurs (see Figure 30). According to Ames (2014), this significanly reduces the computational time and this has signifiance in that the T4 facility should be able to be modelled as axisymmetric to lower the simulation run times.

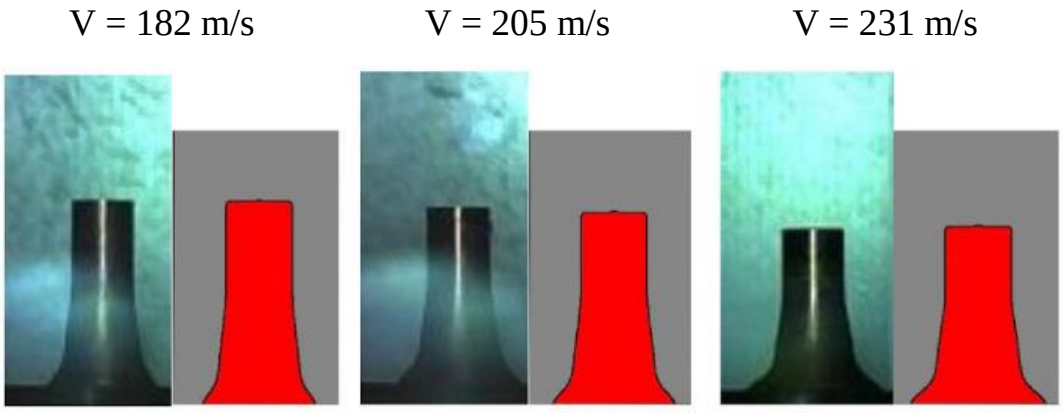

Figure 30 - Comparison between Experimental Solution (Left) and Numerical Solution (Right) of Taylor Bar Impact Test of Copper at Varying Impact Velocities (Ames, 2014)

Modelling techniques also apply to the numerical solution scheme selected in additon to the geometry, materials and dimensions of the model. See Section 2.5 for numerical solution scheme modelling techniques which apply to automative crashes and sheet metal forming as well as a detailed analysis of the implict and explicit numerical solution schemes.

2.5 The Implicit Method and the Explicit Method

It is important, before starting the finite element analysis of piston impacts, to identify what finite element methods are available. Two commonly used methods include the implicit method and the explicit method (Lee, 2015). The implicit method involves solving for equation (3).

$$[M]\{\ddot{x}\} + [C]\{\dot{x}\} + [K]\{x\} = \{F\} \tag{3}$$

Where x, $\dot{x}$ and $\ddot{x}$ represent the nodal displacement, velocity and acceleration, respectively.

The nodal displacements, velocities and accelerations are solved with the help of the Taylor series. The Taylor series expansion for a given integration time step, Δt, (assuming acceleration is linear over the time step) is:

$$\dot{x}_{n+1} = \dot{x}_n + \frac{\Delta t}{2}(\ddot{x}_{n+1} + \ddot{x}_n) \tag{4}$$

$$x_{n+1} = x_n + \Delta t\dot{x}_n + \Delta t^2\left(\frac{1}{6}\ddot{x}_{n+1} + \frac{1}{3}\ddot{x}_n\right) \tag{5}$$

At $n = 0$, the nodal displacement, velocity and acceleration are known. The value for the nodal acceleration at n is then used as an initial guess for the nodal acceleration at $n + 1$. The nodal displacement and velocity at n together with the nodal acceleration at $n + 1$ are used to find the nodal displacement and velocity at $n + 1$ using equations (4) and (5). If equation (3) is not fulfilled using the guess for the nodal acceleration, the guess is updated and another iteration is conducted until convergence is achieved (Lee, 2015). It is important to note that the computational time for the analysis is proportional to the size of the model being studied. As the size of the model increases, the computational time also increases. However, for the implicit method this rise occurs more steeply than for the explicit method (Mashayekhi, 2016).

According to Lee (2015), the explicit method relies on half-step central differences to calculate the nodal displacements in the proceeding time step:

$$\ddot{x}_n = \frac{\dot{x}_{n+\frac{1}{2}} - \dot{x}_{n-\frac{1}{2}}}{\Delta t},$$
$$\text{or } \dot{x}_{n+\frac{1}{2}} = \dot{x}_{n-\frac{1}{2}} + \ddot{x}_n\Delta t \tag{6}$$

$$\dot{x}_{n+\frac{1}{2}} = \frac{x_{n+1} - x_n}{\Delta t},$$
$$\text{or } x_{n+1} = x_n + \dot{x}_{n+\frac{1}{2}}\Delta t \tag{7}$$

Unlike the implicit method, no iterations are needed with the explicit method since the solutions to equations (6) and (7) require knowledge of only known or previously calculated

values. Thus, convergence in the iterations in the explicit method is not needed and so it is able to handle large stresses and large deflection solutions easier (Lee, 2015). However, in order to arrive at a stable result using the explicit method, the integration time step must adhere to the CFL criteria (Barba et al., 2016). This is given by:

$$\text{CFL criteria} = \frac{c\Delta t}{\Delta x} \leq 1 \tag{8}$$

Where c represents the wave speed in the element, Δt represents the timestep and Δx is the distance between two mesh points.

Stability with the CFL condition is achieved by ensuring that the time step used by the solver is sufficiently small such that the information has enough time to propagate through the mesh (Weisstein, 2016). This concept is illustrated further in Figure 31 whereby the distance travelled by the solution within one timestep cΔt must not be greater than the distance between two mesh points Δx for a stable CFL condition to be reached (Barba et al., 2016).

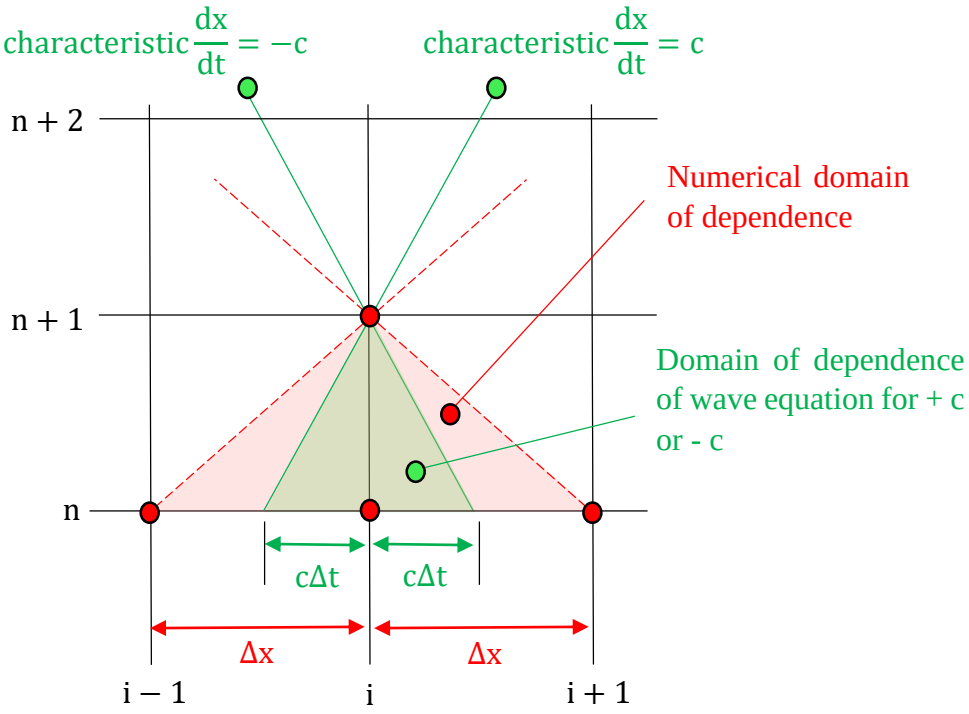

Figure 31 – Graphical Illustration of CFL Condition (Adapted from Barba et al., 2016)

With the nodal displacements known from equation (7), these nodal displacements are then interpolated using the interpolating functions, called shape functions, to calculate the displacement field. The displacement field describes the deformation of a body. It does this

with a vector in (X, Y, Z) for each element which connects the element from the undeformed body to the new position of the same element in the deformed body (Lee, 2015). The displacement field can then be calculated by:

$$\{U\} = [N]\{X\} \tag{9}$$

Where {U} is the displacement field, [N] is the matrix of shape functions and {X} is the nodal displacements.

In the case where deformations are small, the strains can then be calculated by the following equations:

$$\varepsilon_x = \frac{\partial u_x}{\partial X}, \varepsilon_y = \frac{\partial u_y}{\partial Y}, \varepsilon_z = \frac{\partial u_z}{\partial Z} \tag{10}$$

Where ε_x, ε_y and ε_z are the x, y and z strain components, respectively and u_x, u_y and u_z are the x, y and z are the displacement field vector components, respectively.

$$\gamma_{xy} = \frac{\partial u_x}{\partial Y} + \frac{\partial u_y}{\partial X}, \gamma_{yz} = \frac{\partial u_x}{\partial Y} + \frac{\partial u_y}{\partial X}, \gamma_{zx} = \frac{\partial u_z}{\partial X} + \frac{\partial u_x}{\partial Z} \tag{11}$$

Whereγ_{xy}, γ_{yz} and γ_{zx} are the x, y and z shear strain components, respectively.

When the deformations cannot be regarded as small, the displacement-strain relations stated in equations (10) and (11) still remain but also high-order differential terms are added to the equations. The change in the strain with respect to time is also calculated to determine the strain rate.

From here, the volume changes for each of the elements are calculated, according to the equation of state, and the mass density is updated. These changes are required together with a constitutive model for calculating the stresses. Once the stresses are known, it is integrated over the element to determine the external loads which are then added to the internal forces to form the nodal forces.

The acceleration in the current time step, which is needed to find the solution to equation (6), can then be calculated as:

$$\ddot{x}_n = \frac{F_n}{m} + \frac{b}{\rho} \tag{12}$$

Where F_n is the nodal forces, m is the nodal mass, b is the forces distributed in the body and ρ is the mass density.

This process outlined repeats itself until the end time of the analysis is reached (Lee, 2015).

Solution accuracy for the explicit method is based on the principle of conservation of energy rather than the reliance on convergence with the implicit method. When the energy error reaches the maximum energy error specified, the solver stops because the solution is considered to be unstable (Lee, 2015).

$$\text{Energy Error} = \frac{|(\text{Current Energy}) - (\text{Reference Energy}) - (\text{Work Done})_{\text{Reference}\rightarrow\text{Current}}}{\max(|\text{Current Energy}|, |\text{Reference Energy}|, |\text{Kinetic Energy}|)} \quad (13)$$

Where the current energy is calculated, including its kinetic and strain energy. The reference energy is the total energy of a reference time, default to the initial time.

Sources of energy error for explicit finite element codes include using element dimensions which makes the mesh unable to properly capture the solution that is meant to be generated (Lee, 2015). The energy error can be managed by increasing the kinetic energy in the system (by increasing the initial velocity of the object or applying higher loads) or increasing the density of the mesh. However, this would change the nature of the problem and thus is not recommended. Instead, if the simulation stops but there is a need to continue either the maximum energy error can be increased as an input to the code or the reference energy cycle can be changed from 0 to an arbitarily high number such as 999999 (Eureka.im, 2012).

Liu (2010) illustrates the importance of both the implicit and explicit method in determining the crashworthiness and crash responses of thin-walled sections, used as impact absorbers during vehicle crashes. The vehicle crash analysis has relevance to the T4 piston impact analysis in that both of these problems would be expected to involve high strain rate, large deformation and non-linear contacts which occur over a short time interval. Liu (2010) states that the implicit solver can be used to create a pre-stress environment for the static loadings applied to beams being analysed before a car crash analysis is carried out using the explicit solver. This is of interest to any high speed impact problems being analysed where an implicit solver can be used to reduce the computational time compared to if an explicit solver was used alone.

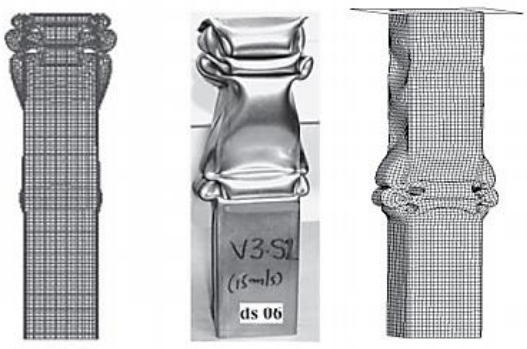

Figure 32 - Explicit Solution (Left), Experimental Solution (Centre) and Implicit Solution (Right) (Kazanci et al. 2011)

In contrast, Kazanci et al. (2011) demonstrates that the implicit method is not only relevant in creating a pre-stress environment but is also relevant in determining the response of the crush tube after impact. In this paper, it is stated that the implicit method can be useful when the maximum response is reached in a long time interval (see Figure 32). He went onto conclude that the deformation along the centre of the thin-walled tube section, shown in Figure 32, for the experimental test case was able to be replicated using the implicit solver within a reasonable time frame, unlike the explicit solver. The explicit solver was best suited to replicating the deformation at the top of the thin-walled tube section for the experimental case, which would have transpired over a shorter time interval. When deciding whether to use the implicit or explicit method, it is not only important to think about the end time but also the ability of the numerical solution scheme to handle the non-linearties involved in the problem.

Simulations of sheet metal forming require a relatively large end time since the velocity of the punch can be as low as 20 mm/s (Mamalis et al., 1997). The implict numerical method has difficulty converging at a solution when non-linear materials, large deformation and non-smooth contacts are involved whereas the explicit numerical method does not have difficulty with these. However, the run time necessary to reach the final response of the sheet metal forming simulation at a punch velocity of 20 mm/s would take a relatively long time using the explicit method comapred to using the implicit method. Refer to Figure 33 for a schematic of the sheet metal forming problem being discussed.

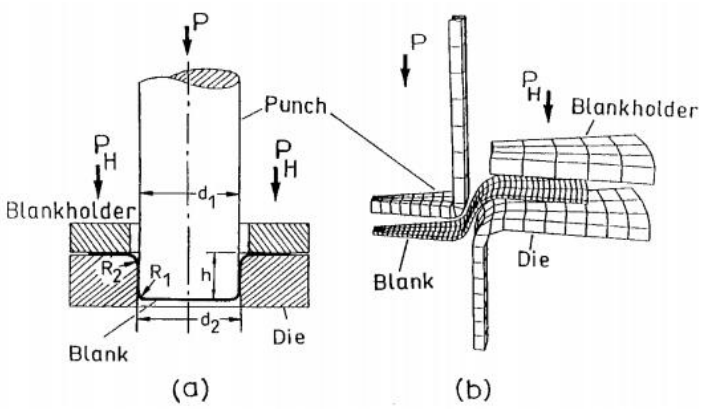

Figure 33 - Deep-Drawing of a Cylindrical Cup: (a) Experimental Set-Up and (b) FE Modelling (Mamalis et al., 1997)

To reduce the end time of the simulation, Mamalis et al. (1997) increased the punch velocity at an order of magnitude 10^4 higher than the actual experimental punch velocity of 20 mm s^{-1}. In addition to this, the density of the blank was decreased by 10^3 in order to minimise the high dynamic effects introduced by simulating a punch velocity 10^4 higher than the actual experimental punch velocity. Figure 34 displays that the finite element method (FEM) solution for the radial, hoop and thickness strains in the blank closely matched the experimental solution thereby validating the method Mamalis et al. (1997) used. Nonetheless, Chung et al. (1998) urges strict control over scaling parameters such as punch velocity and material properties as it does not work if the parameters are scaled too far.

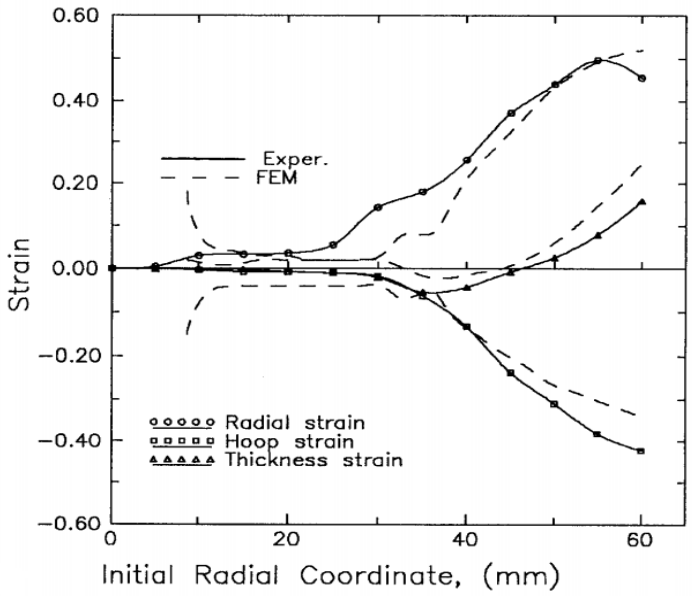

Figure 34 - Comparison between FEM Strain and Experimental Strain in the Blank during Forming using a Blank Density of 7.8×10^{-3} g/cm^3, Punch Velocity of 20×10^4 mm/s and Friction Coefficient of 0.3 (Mamalis et al., 1997)

2.6 Defining Materials in Finite Element Modelling

The behaviour of different materials is defined in finite element modelling through the definition of four different material equations (ANSYS, 2009):

1) Equation of State (EOS): Used to calculate the hydrostatic pressure which is a function of the internal energy density (temperature) and also the mass density (Soares et al., 2014). The EOS would be responsible for capturing the volumetric response (changes in volume) of each element during deformation (Sabadin et al. 2014);

2) Strength Model: Used to describe the non-linear elastic plastic response of the material and its temperature dependence. The strength model would be responsible for capturing the deviatoric response (changes in shape) of each element during deformation (Soares et al., 2014);

3) Failure Model: Used to simulate the different ways in which a material would fracture i.e. the loss of the material's ability to support normal stresses and shear stress and thus result in failure under these stress conditons (Soares et al., 2014);

4) Erosion Algorithm: Used to automatically delete elements during a simulation that become highly distorted. This makes sure that the stability time step continues to stay at a reasonable level up to the specified end time of the simulation. It can also be used to simulate material penetration, cutting and fracture (Sharcnet, 2016).

Note that the word 'failure' used in subsequent chapters will be defined as the onset of plastic yielding and not fracture. Investigating failure models for the purposes of modelling fracture during the piston impact problems is out of scope and will not be explored further. Instead, focus on high strain rate material data will be drawn towards EOS and strength models.

2.6.1 Equation of State

Two commonly used equations of state that are used in impact problems include the isotropic elasticity model and the Mie-Grüneisen EOS (ANSYS, 2009).

In modelling the high speed collision event between the piston and the end of the compression tube, an isotropic elasticity model would not be suitable as it is primarily used to model materials subject to low compression and which exhibit linear elastic material behaviour (ANSYS, 2009). For this reason, an isotropic elasticity model would not accurately describe the shockwave propagation after impact.

The key advantage of using the Mie-Grüneisen EOS in modelling this piston impact problem is that it uses the shock Hugoniot curve as a reference and also takes into account temperature effects so that the shock wave propagation can be described more accurately (Rao, 2016). According to Zocher et al. (2000) The hydrostatic pressure, p, is calculated using the Mie-Grüneisen EOS as follows:

$$p = \frac{\rho_0 C_0^2 \zeta \left[1 + \left(1 - \frac{\Gamma_0}{2}\right)\zeta\right]}{[1 - (S_\alpha - 1)\zeta]^2} + \Gamma_0 E \tag{14}$$

Where C_0 is the bulk speed of sound and Γ_0 is the Grünsien coefficient.

And,

$$\zeta = \frac{\rho}{\rho_0} - 1 \tag{15}$$

Where ζ is a measure of compression, ρ is the current material mass-density and ρ_0 is the initial material density.

Also,

$$S_\alpha = \frac{dU_s}{du_p} \tag{16}$$

Where S_α is a linear Hugoniot slope coefficient, U_s is the shock velocity and u_p is the particle velocity.

And,

$$E = \frac{1}{V_0}\int C_v \, dT \approx \frac{C_v(T - T_0)}{V_0} \tag{17}$$

Where E is the internal energy, C_V is the specific heat at constant volume and V_0 is the reference specific volume at the initial temperature.

Two Mie-Grüneisen forms of equation of state that are available include the Shock EOS and the Polynomial EOS (Jha, 2014). Between these two, the Shock EOS is more commonly used due to its relative accuracy, simpler form and ease in determining parameter values (Rao, 2016).

To define the pressure and energy on the Hugoniot this EOS requires the material shock velocity-particle velocity relationship as a material input. In the numerical solver, this is specified, according to Heider (2003), through:

$$U_s = C_0 + S_\alpha u_p \tag{18}$$

Where Us is the shock velocity, up is the particle velocity, S is the slope of the U_s-u_p relationship and C_0 is the bulk acoustic sound speed.

2.6.2 Strength Model

According to Becker (2001), several relationships must be properly formulated in order to model the elastic-plastic behaviour of a material in a finite element program.

Firstly, a yield criterion must be defined to correctly model the elastic-plastic behaviour of a material. This allows for the multi-axial behaviour of the material to be related to the uniaxial behaviour (Becker, 2001). Several yield criterions exist, including von Mises, Drucker-Prager, Tresca, modified Tresca, Coulomb-Mohr and the modified Cam-clay (Bigoni et al., 2004).

Choosing the yield criterion has the consequence of defining the yield surface for the material. This means that yield is defined in the material in a multiaxial stress state. Rakvåg et al. (2014) used the von Mises yield criterion to model the material of the projectile during the numerical study of the Taylor bar impact test. Unless anisotropic Hill yield criterion is defined, the hardening model will assume a von Mises yield criterion. According to Crocombe (2001), the yield surface for the von Mises yield criterion is given by:

$$F = \frac{1}{\sqrt{2}}[(\sigma_{11} - \sigma_{22})^2 + (\sigma_{22} - \sigma_{33})^2 + (\sigma_{33} - \sigma_{11})^2]^{\frac{1}{2}} - \sigma_{yld} = 0 \tag{19}$$

Where F is the yield function, σ_{yld} is the current yield stress, σ_{11} is the principle stress in direction 1, σ_{22} is the principle stress in direction 2 and σ_{33} is the principle stress in direction 3.

See Figure 35 for a graphical view of the principle stress directions.

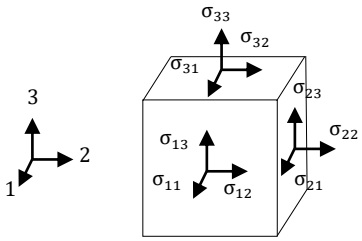

Figure 35 - Principle Stress Directions (Becker, 2001)

The von Mises criterion states that there cannot be stress states outside the yield surface. When $F < 0$, the material exhibits elastic behaviour because the state is within the region enclosed by the yield surface. When $F = 0$, the material exhibits plastic yielding (Becker, 2001).

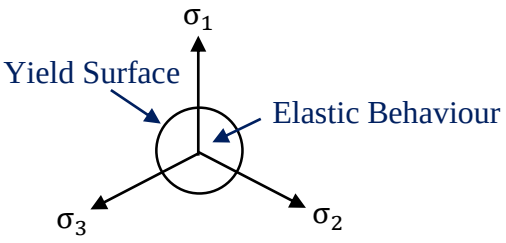

Figure 36 - Yield Surface (Adapted from Becker, 2001)

An elastic perfectly plastic material, where there is never any strain hardening in the material, has the yield stress constant regardless of the true strain it suffers. This is shown in the left side of Figure 37. In reality, metals experience an increase in the sustainable stress after initial yielding as shown in the right side of Figure 37 (Becker, 2001). Consequently, a hardening model is necessary to describe how the shape of the yield surface changes after initial yielding has occurred to reflect this increase in the sustainable stress.

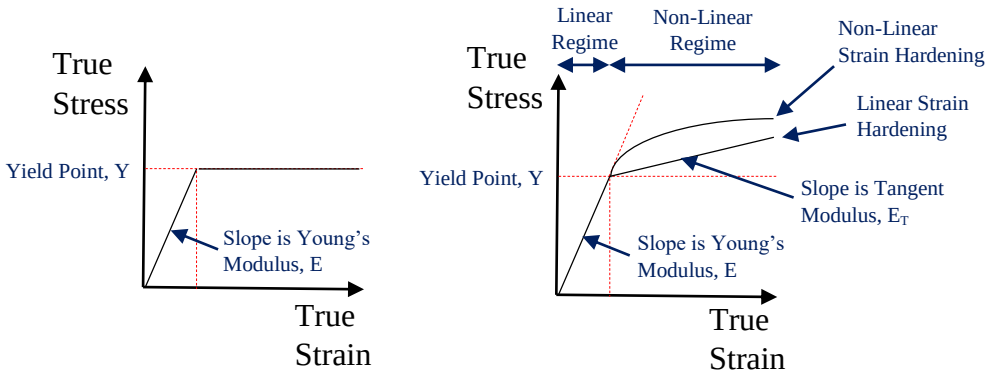

Figure 37 - Comparison between Perfect Plasticity (Left) and Hardening Model (Right) (Adapted from Becker, 2001)

According to Becker (2001), two commonly used hardening models include isotropic hardening and kinematic hardening (refer to Figure 38 and Figure 39). The isotropic hardening model was chosen by Rakvåg et al. (2014) because proportional loading, with no reversal in direction, was assumed in the numerical study of the Taylor bar impact test. According to Crocombe (2001), if the load was reversed, kinematic hardening should have been used. Crocombe goes onto add that these hardening models consist of a hardening curve and a means of including this into the yield surface. In the high speed piston impact problem proportional loading, with no reversal in direction, will be assumed so kinematic hardening will be ignored.

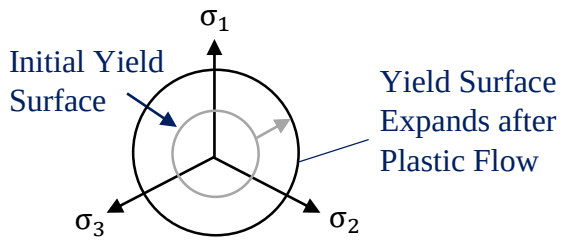

Figure 38 - Isotropic Hardening (Adapted from Becker, 2001)

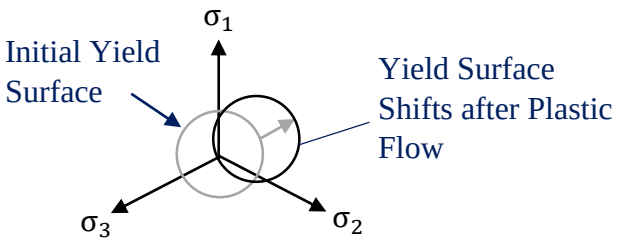

Figure 39 - Kinematic Hardening (Adapted from Becker, 2001)

It is common to describe the hardening curve as a series of straight-line segments so that the non-linear behaviour of the material can be approximated linearly. A bilinear stress-strain relationship is defined by representing the linear regime of the stress-strain relationship using (Becker, 2001):

$$\varepsilon E = \sigma \tag{20}$$

where ε is the strain, E is the Youngs Modulus and σ is the stress.

And, the non-linear regime of the stress-strain relationship using:

$$\varepsilon E_T = \sigma \tag{21}$$

$$\text{where } E_T = \frac{d\sigma}{d\varepsilon^e + d\varepsilon^p} \tag{22}$$

and ε^e is the elastic and ε^p is the plastic strain, respectively

As plastic deformation occurs the plastic strain is then defined by the plastic flow rule. For an isotropic hardening material in the von Mises case, the yield surface expands uniformly in all directions.

However, it is important to note that as the impact velocity of the piston increases, the strain rate that the impacting body endures and the stress in the impacting body increases as well (refer to Figure 40). This is observed for metals and is especially the case at high temperatures (Crocombe, 2001). Consequently, this strength model would not be suitable for modelling high strain rates that would be prevalent in a high speed piston impact problem.

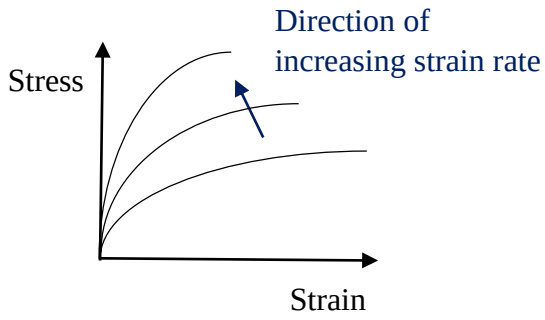

Figure 40 - Rate Dependent Yielding of Metals (Adapted from Crocombe, 2001)

The Zerilli-Armstrong Strength model has application in modelling materials subjected to large strains, high strain rates and high temperatures (He et al., 2014). The formulation of this model is based on dislocation dynamics.

According to He et al., (2014), the yield stress for FCC metals is given by:

$$Y = Y_0 + C_2\sqrt{\varepsilon_p}\exp\left[-C_3T + C_4T\log\dot{\varepsilon}_p\right] \tag{23}$$

According to He et al., (2014), the yield stress for BCC metals is given by:

$$Y = Y_0 + C_1\sqrt{\varepsilon_p}\exp\left[-C_3T + C_4T\log\dot{\varepsilon}_p\right] + C_5\varepsilon_p^n \tag{24}$$

Where C_1 is the hardening constant #1, C_2 is the hardening constant #2, C_3 is the hardening constant #3, C_4 is the hardening constant #4 and C_5 is the hardening constant #5.

According to He et al., (2014) the Zerilli-Armstrong model predicts flow stresses accurately. However, the computational time of the Zerilli-Armstrong model increases by many folds compared to other material models such as the Steinberg-Guinan model and is more difficult to develop. Since conducting experiments to acquire material data is out of scope, the Zerilli-Armstrong model would not be suitable.

The Steinberg-Guinan strength model does not take into account strain rate effects. Instead, the model is more suited when the rate-dependent effects play a minor role (high $\dot{\varepsilon}$) but the pressure effects are of importance (Steinberg et al., 1980). According to Steinberg et al. (1980), this occurs when the stresses approach 10 GPa (or $\dot{\varepsilon} \geq 10^5$/s). The Steinberg-Guinan Strength model, according to Steinberg et al. (1980), calculates stress according to the following equation:

$$G = G_0 \left\{ 1 + \left(\frac{G'_p}{G_0} \right) \frac{P}{\eta^{\frac{1}{3}}} + \left(\frac{G'_T}{G_0} \right) (T - 300) \right\} \tag{25}$$

Where G_0 is the shear modulus at the reference state, G_P' is the derivative dG/dP, η is the compression (v_0/v), G_T' is the derivative dG/dT, T is the temperature.

$$Y = Y_0 \left\{ 1 + \left(\frac{Y'_p}{Y_0} \right) \frac{P}{\eta^{\frac{1}{3}}} + \left(\frac{G'_T}{G_0} \right) (T - 300) \right\} \left(1 + B\varepsilon_p\right)^n \tag{26}$$

Subject to the limitation that:

$$Y_0 \left(1 + B\varepsilon_p\right)^n \leq Y_{max}$$

Where Y_P' is the derivative dY/dP, B is the hardening constant, n is the hardening exponent and Y_{max} is the maximum yield stress.

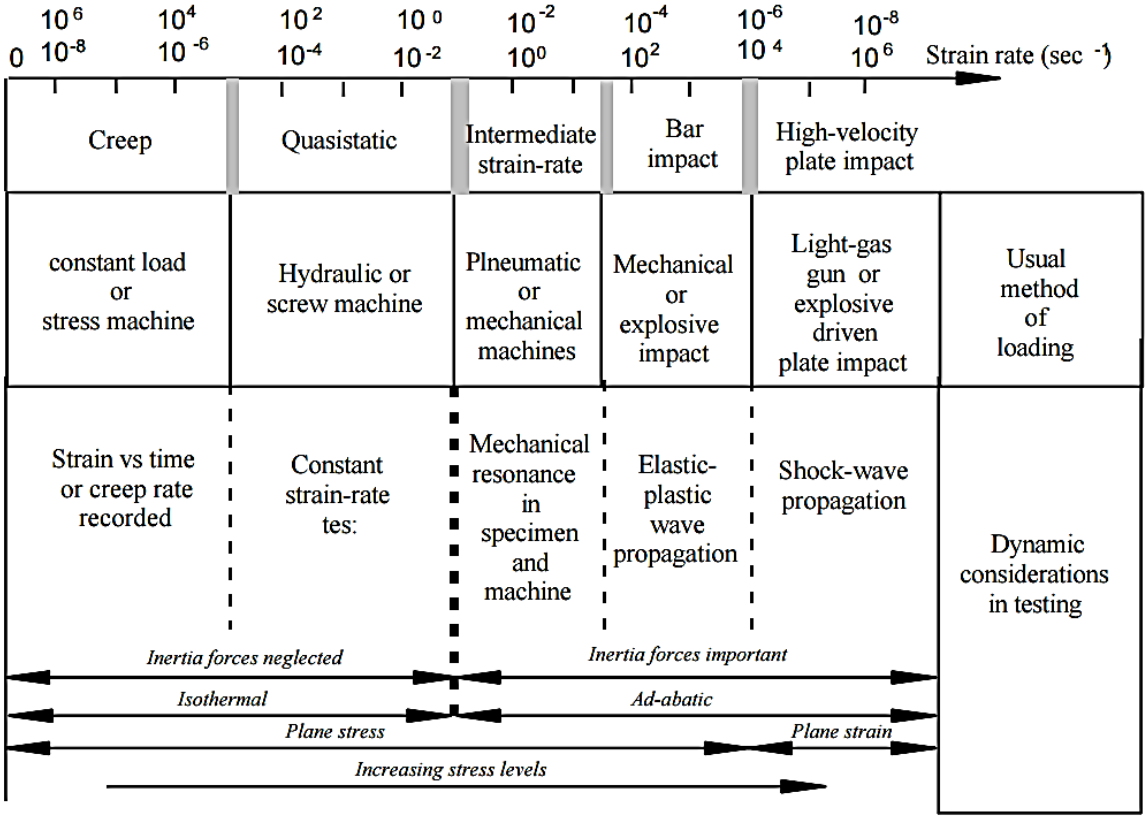

Figure 41 - Dynamic Aspects of Mechanical Testing (Sierakowski, 2008)

Figure 41 reveals how the applicability of the Steinberg-Guinan strength model is limited to high-velocity plate impacts whereas the focus will be on bar impacts which is addressed using the Johnson-Cook strength model. Thus, the Steinberg-Guinan strength model will not be suitable to model the piston impact problem.

The Johnson-Cook strength model is commonly used in simulations of impact and penetration problems (Banerjee et al., 2015). It takes into account strain rate dependence of the stress where the strain rate is between $\varepsilon_0 = 10^{-2}$/s and $\varepsilon_0 = 10^{6}$/s (Shrot, 2012). It is popular because of the simple form of the equation and the ease in which the model constants of the equation can be derived. This makes it most suitable to model the piston impact problem being investigated (compared to the Zerilli-Armstrong and Steinberg-Guinan strength models). According to Dorogoy et al. (2009), the Johnson-Cook strength model calculates stress according to equation (27).

$$Y = \underbrace{\left[A + B\varepsilon_p^n\right]}_{\text{Strain hardening effect}} \underbrace{\left[1 + \left[C \times \ln\left(\frac{\dot{\varepsilon}_p}{\dot{\varepsilon}_{p0}}\right)\right]\right]}_{\text{Strain-rate (viscosity) effect}} \underbrace{\left[1 - T_H^m\right]}_{\text{Thermal softening effect}} \quad (27)$$

Where A is the initial yield stress, B is the hardening constant, n is the hardening exponent, C is the strain rate constant, m is the thermal softening exponent, ε_p is the equivalent plastic strain, $\dot{\varepsilon}_p$ is the strain rate and $\dot{\varepsilon}_{p0}$ is the user defined reference accumulative plastic strain rate and T_H is the nondimensional temperature.

Also,

$$T_H = \begin{cases} 0 & \text{for} \quad T < T_{room} \\ \dfrac{T - T_{room}}{T_{melt} - T_{room}} & \text{for} \quad T_{room} \leq T \leq T_{melt} \\ 1 & \text{for} \quad T > T_{melt} \end{cases} \quad (28)$$

Where T is the temperature of the object, T_{room} is the room temperature and T_{melt} is the melting temperature of the object's material.

Table 3 - Influence of the Johnson-Cook Parameters (Li et al., 2015)

Quantity	Symbol	Description
Yield strength	A	Relates to the strength of the bonds, the hardness and the energy required in high-velocity deformation of the material. These increase with an increase in the yield strength, A. Furthermore, as the yield strength increases, the earlier the occurrence of the thermal softening phenomenon.
Hardening modulus	B	As the hardening modulus, B, increases so too does the flow stress (the instantaneous value of stress needed to maintain the plastic deformation of the material and thus keep the metal flowing) (Sharma, 2016). The thermal softening phenomena is more pronounced with a higher hardening modulus.
Strain rate sensitivity coefficient	C	A higher strain rate sensitivity coefficient, C, means that the stress-strain relationship is more sensitive to changes in the strain rate.
Thermal softening effect	m	An increase in the thermal softening effect, m, means that for a given strain post yield, the sustainable stress is lower.
Strain-hardening effect	n	An increase in the strain-hardening effect, n, means that the hardening effect will be more pronounced.

The Taylor bar impact test, described in Section 2.2, is a commonly used method in determining the Johnson-Cook model parameters (Adams, 2003). This involves varying the parameters until an agreeable match is achieved between the experimental solution of the deformed projectile and the numerical results.

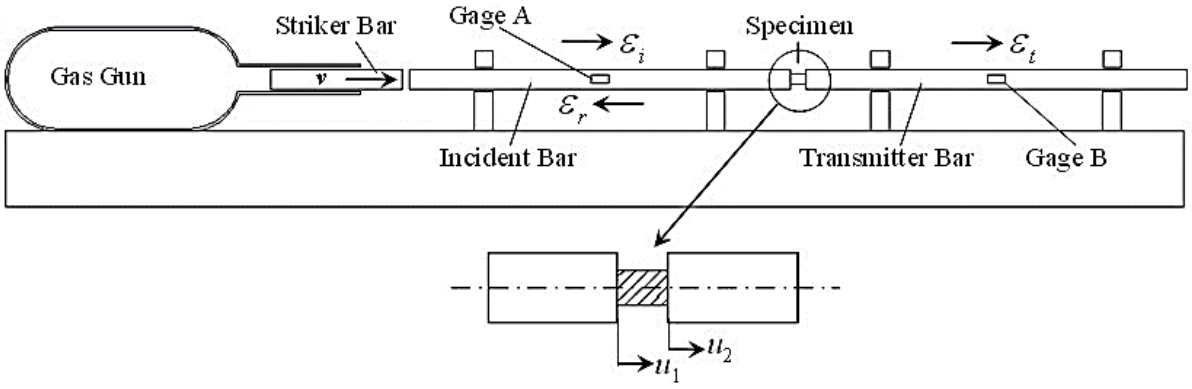

Figure 42 - Split Hopkinson Pressure Bar Test Apparatus (The Ohio State University, 2016)

Alternatively, the Split-Hopkinson pressure bar test, created by Bertram Hopkinson in 1914, can be used determine the Johnson-Cook model parameters at strain rates in the range of 10^3 to 10^4 s^{-1} (refer to Figure 42) (Yang, 2014). The test involves positioning the material sample between two bars (the incident bar and the transmitted bar) and accelerating a striker bar into the incident bar causing an elastic wave pulse to be produced. Part of this wave pulse is then reflected at the end of the incident bar but the other part of the wave pulse travels through the material sample and into the transmitted bar. The strain gauge installed on the incident bar and the transmitted bar are used to measure the strains in the material sample and this data is then used to study the dynamic behaviour of the material (HBM, 2016).

As mentioned earlier in this section, the yield condition states that there cannot be any stress state outside the surface defined by the criterion, in this case the von Mises criterion. However, this surface does not have fixed dimensions (except for the case of perfect plasticity). By taking the square of both sides of the von Mises criterion, the equation for an infinite cylinder in 3D is produced where the axes are the principle stresses (refer to Figure 43). This radius can change due to strain hardening which is accounted for in simple hardening models such as bilinear isotropic hardening. However, by selecting the Johnson-Cook model, this provides a new method of calculating the radius of this cylinder that also takes into account strain rate and temperature effects (see Figure 43) (Banerjee, 2012).

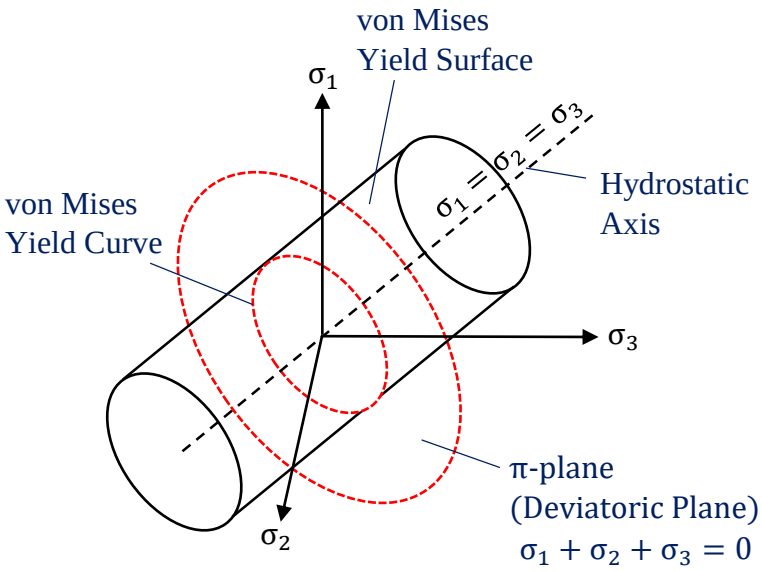

Figure 43 - The von Mises Yield Surfaces in Principal Stress Coordinates (Adapted from Bob McGinty, 2012)

2.6.3 Polymers and Metals

According to Fiene (2016), the stress-strain curve for polymers (such as nylon) is sufficiently different from that of of metals in both shape and magnitude. That is, polymers typically reach much higher strains than metals prior to yield and polymers exhibit non-linear elasticity whereas metals exhibit linear elasticity (Fiene, 2016). At increasing strain rate, polymers do display brittle behaviour like metals however and the stresses that can be sustained at a given strain does often increase like metals do (Crocombe, 2001). See both Figure 40 and Figure 44 for illustration of this concept.

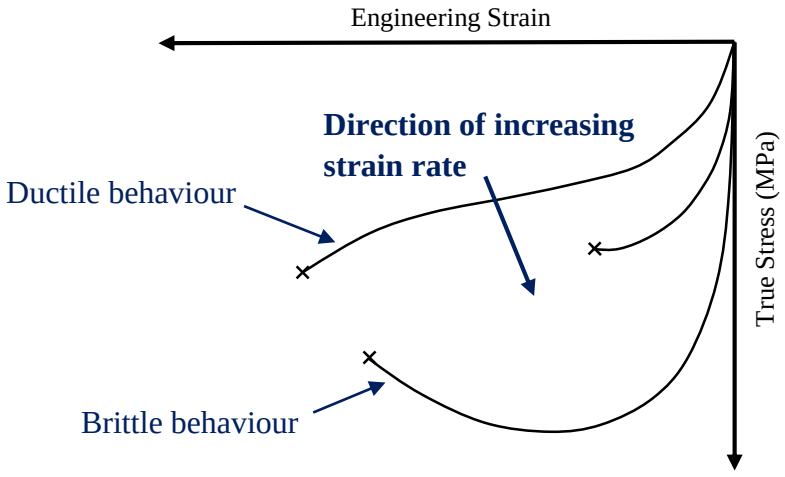

Figure 44 –Response of Nylon under Dynamic Compression at Increasing Strain Rate (Adapted from Pouriayevali, 2013)

According to Lobo (2006), while the Johnson-Cook material model can describe metals, there are significant drawbacks to using a material model such as the Johnson-Cook for polymers even at high strain rates where polymers behave somewhat brittley. This is because polymers exhibit non-linear elasticity and the strain that is reached prior to yield can vary significantly (Lobo, 2006). Additionally, the strain at which fracture occurs changes significantly with the strain rate as shown in Figure 44. This also makes it difficult to properly capture fracturing of the polymer at changing strain rates. Al-Maliky (1994) shows that nylon does fracture at approximately 18% true strain at a constant strain rate of 1700 s^{-1}.

In the numerical modelling of nylon at high strain rates, Al-Maliky (1997) selects a representative strain rate for the problem being analysed and uses a bilinear material model to represent the stress-strain experimental data instead of a strain-dependent material model. This is due to the simplicity of a bilinear material model and because a strain-dependent material model would not necssarily capture the behaviour of the polymer more accurately.

This has implications for the numerical modelling of the nylon buffer in that it justifies the use of a bilinear material model. At a given strain rate selected, the strain at which fracture occurs can also be found and used to determine the impact tolerance of the nylon stud buffer.

Note that the x-axis in Figure 44 is in engineering strain rather than true strain. When adding material data into numerical solvers, it is important to use true stress-strain values instead of the engineering stress-strain values as they are more representative measures of the state of the material during deformation (ANSYS, 2010).

2.7 Methods of Connecting Parts in the Model

There exists three different ways in connecting parts together, which could have different material assignments, in a finite element analysis. This includes connecting them through using bonded contacts, a continuous mesh between connected parts or through constraint equations (Sean Harvey, August 2000).

Bonded contacts have an advantage in that large deflections are permitted and connecting bodies with differing mesh densities can be joined. However, when a very fine mesh is required for the connecting bodies this advantage can be dismissed (Sean Harvey, August 2000). The stresses between the connecting bodies, using bonded contacts, is discontinuous and low contact stiffness can negatively affect the accuracy of the results. Furthermore, in a 2D axisymmetric explicit analysis, bonded contacts are typically not supported by some numerical solvers (such as LS-DYNA and AUTODYN) (Sharcnet, 2016).

Constraint equations are supported in a 2D axisymmetric explicit analysis but lead to slower run times and increased memory requirements (Sean Harvey, August 2000). Furthermore, equations need to be generated for each interface which becomes tedious (Sean Harvey, August 2000).

A continuous mesh would be the preferred choice in connecting parts together in a 2D axisymmetric explicit dynamics analysis problem, such as the 2009 T4 piston impact problem, since large deflections are allowed; there is continuous stress between the parts and there are no limitations on the types of analysis it can be used in (Sean Harvey, August 2000). While the mesh must be close to the same size between parts, this does not adversely affect the results since a fine mesh between all parts is favourable in terms of the quality of the results.

2.8 Lagrangian and Euler Meshes

Two commonly used finite element formulations include the Lagrangian and Euler meshes (Jaiswal, 2011). Each mesh type comes with its own set of advantages and disadvantages and an understanding of each of these will best inform which type to use in the piston impact problem.

In the Lagrangian scheme, the meshes are imbedded in the material and therefore travel and deform with the material. This mesh type is most suitable for modelling solid materials as it has been found to compute the response of structures most efficiently and accurately compared to an Euler mesh in the absence of large material deformation (Lodygowski et al., 2013). The limitations of the Lagrangian scheme is that if there is high material deformation, the mesh may become extremely distorted which would lead to inaccurate solutions and may also cause the solution to terminate due to mesh tangling (Jaiswal, 2011). This problem can usually be avoided by the application of an erosion algorithm which deletes extremely distorted cells if the element strain exceeds a user defined limit typically in the range of 150% to 200% (Jaiswal, 2011).

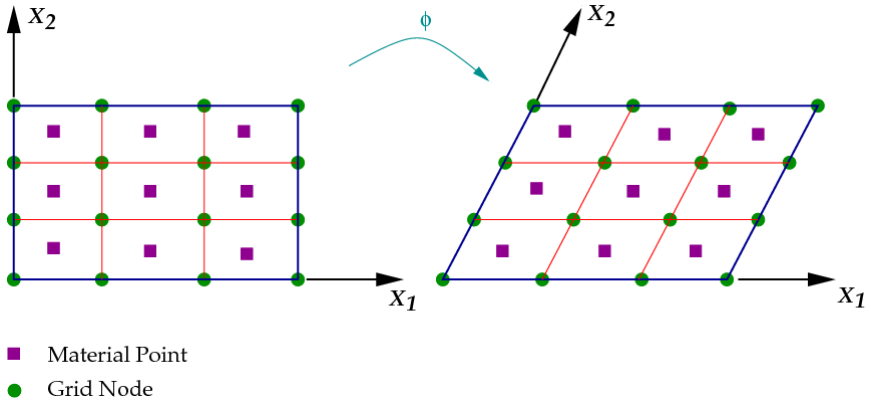

Figure 45 - Lagrangian Mesh: Before Distortion (Left) and After Distortion (Right) (Banerjee, 2007)

In contrast, the Euler scheme uses meshes that are fixed in space and the materials are allowed to flow through the mesh as the material deforms (Jaiswal, 2011). This scheme provides a better solution for fluid flow but also provides an alternative to modelling solids undergoing extreme distortion as it avoids the problem of mesh distortion and tangling. Extreme element distortion can result in very small time steps however which increase the computational power required (Jaiswal, 2011).

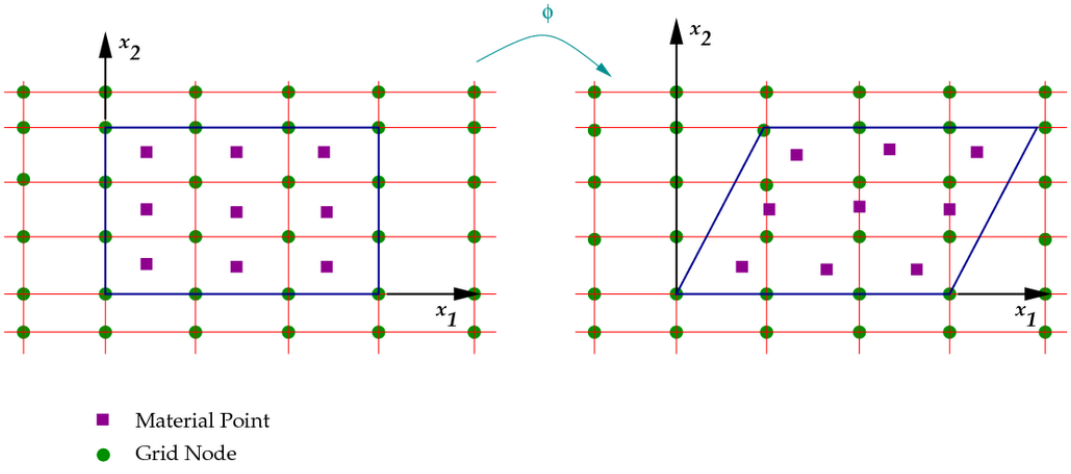

Figure 46 - Eulerian Mesh: Before Distortion (Left) and After Distortion (Right) (Banerjee, 2007)

Rakvåg et al. (2014) emphasises the importance of using a Lagrangian approach to model the Taylor bar impact test since it is best at following the history dependant behaviour of a material point in plasticity. This provides justification for using the Lagrangian approach during the finite element analysis of the piston impact problem. However, it is important when conducting the piston impact simulations to check for large distortions of the mesh which could be an indicator of an inaccurate solution.

2.9 Frictional Contact

According to Reid et al. (2004), the instantaneous coefficient of friction, μ, is computed in the numerical solver by the following relation:

$$\mu = \mu_d + (\mu_s - \mu_d)e^{-c|v|} \tag{29}$$

Where μ_s is the static friction coefficient, μ_d is the dynamic friction coeffiicent, c is the decay coefficient and v is the relative velocity between the slave node and the master segment.

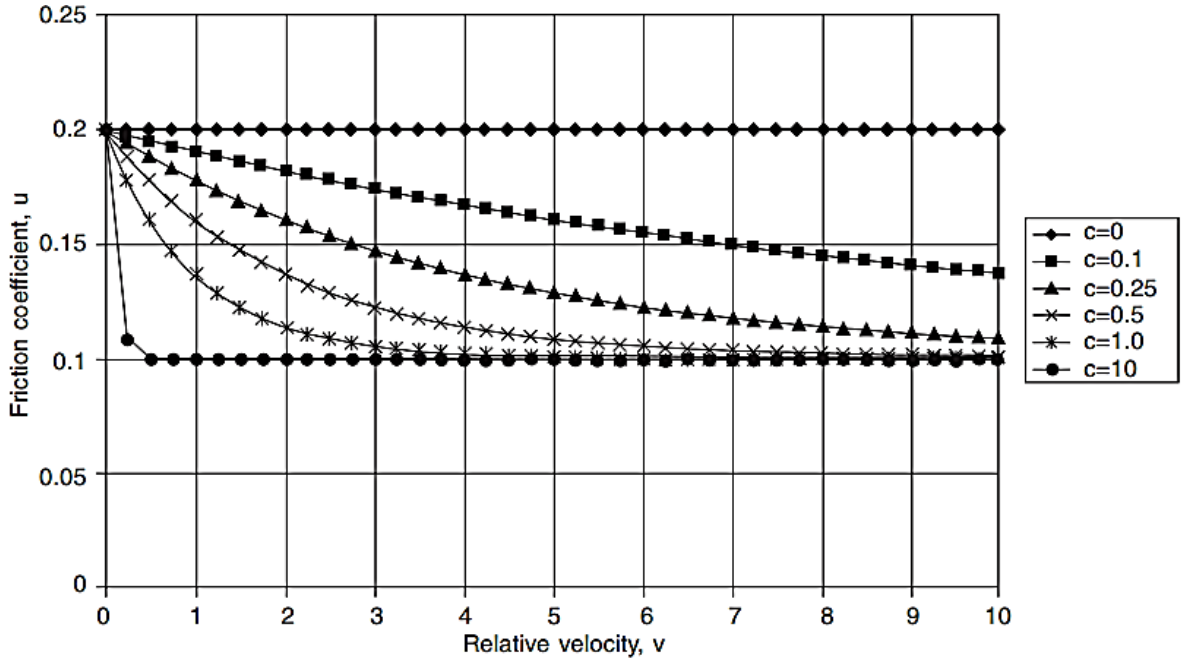

Figure 47 - Friction vs. Relative Velocity with Static Friction Coefficient of 0.2 and Kinematic Friction Coefficient of 0.1 (Reid et al., 2004)

As illustrated in Figure 47, the static friction coefficient is larger than the dynamic friction coefficient and the transition between these two requires a decay coefficient which is assumed to be constant. The decay constant is found through trial and error procedure where a larger decay constant will mean a quicker transition between the static friction coefficient and the dynamic friction coefficient.

According to LS-DYNA Support (2016), the static and dynamic coefficents are typically set to be the same in order to avoid the creation of additional noise in an already noisy problem that arises from conducting an impact simulation. An upper limit bound (the static friction coefficient) and a lower limit bound (the dynamic friction coefficient) can then be set one at a time to evaluate the sensitivity of friction coefficients during the numerical analysis.

3 Numerical Solver

3.1 Chapter Overview

This chapter details the qualtiative assesment of T4 shot 10509 as well as the selection of a suitable numerical solver to model the high speed piston impacts being investigated. A discussion on the solver's ability to capture the physical mechanisms involved during a high speed piston impact is then presented through a series of numerical benchmarks which have been conducted – i.e. hertzian contact stress between two surfaces, free vibration in a bar, stress wave propagation through a bar, the perfect plasticity and isotropic hardening model, friction between two surfaces, sheet metal forming and the Taylor bar impact test.

3.2 Qualitative Assessment of T4 Shot 10509

Finite element modelling of shot 10509 is complex. This is because it introduces time dependent non-linear material models (which makes the material properties harder to obtain), plastic yielding, large strains, friction and contact non-linearity and also the computation time will become high as many solution steps are required for load incrementation and iterations. Sections 2.4 and 2.5 details the selection of a solver and modelling techniques capable of handling these features.

3.3 Selection of Numerical Solver

The Mechanical APDL solver in ANSYS is an example of an implicit finite element program which utilises the implicit method, described in Section 2.5. Non-linear loading problems can be solved with the Mechanical APDL solver using the Newton-Raphson method in which the applied load is partitioned into increments and these increments of the load are then applied over many load steps (Broenink, 2000). Also, non-linear contacts can be solved using the Mechanical APDL solver using either a 'Pure Penalty' method, where a target face is pushed back by a normal force proportional to the penetration of the contacting point, or the 'Augmented Lagrange' method, where a target face is pushed back by a normal force proportional to the penetration of the contact point plus the contact pressure (Lee, 2015). However, the ability for the Mechanical APDL solver to model non-linear problems does not immediately make it suitable for modelling piston impact problems.

This is because it is important to select a finite element solver that keeps the error associated with the solution at a minimum and also one that requires the least amount of computational power to solve a problem. If the time scale of interest is equal to or below the time step used for the analysis, then a solver using the explicit method will achieve this result. However, if the time scale of interest is larger than this time step, then an implicit method would be better because it would reach the solution quicker by taking larger time steps (at the expense of the smaller scale dynamics of the system) (Straalen B, 2014). Given that the time scale of interest for the case of a high speed piston impact is short (less than 0.001s), this would suggest that an explicit method would be best suited to approach the problem. Furthermore, the explicit method can also solve non-linear problems with large stresses and deformation often easier than the implicit method since it does not have to rely on convergence in its iterations to reach a solution. However, as realised in Section 2.4, the implicit method would still serve as beneficial if a pre-stress environment was required before undertaking an explicit method analysis.

Finite element codes such as ABAQUS, AUTODYN, LS-DYNA and even the IMPETUS Afea solver share a similarity in that they can all use the explicit method to solve a problem (Bhat, 2009). The two solvers which are available to this project for conducting the finite element analysis of the piston impacts are AUTODYN and LS-DYNA. These two codes have differing values for analysis settings which are commonly set to '*Program Controlled*' such as the damping controls and the maximum energy error value, which can be adjusted by the user if needed.

AUTODYN was selected as the explicit solver as it has access to the ANSYS material library which contains a large database of various materials and also includes the Johnson-Cook material model. LS-DYNA can also make use of the ANSYS material library but the LS-DYNA Export system does not support 2D axisymmetric analyses which can be used for modelling the T4 facility. Furthermore, AUTODYN was compatible with the Mechanical APDL solver which prove useful for creating pre-stress environments that are better suited for an implicit method.

While the high speed piston impact problem can be compared to existing experimental results, these results are not well resolved since the piston is now in its partially swollen state and the piston's accessories were damaged in the attempt to remove the piston from the compression tube. This meant that confidence in the solver needed to be high in order to achieve a reasonable level of certainty in the numerical results. To ensure that the solver selected had the capability to capture the physical proceses involved in a high speed piston impact before producing the numerical models of the T4, X2 and X3 facilities. Consequently, a series of benchmarks were devised in order to test the APDL and AUTODYN solvers.

3.4 Benchmarks

3.4.1 Hertzian Contact Stress

The first benchmark involved validating the implicit APDL solver (separate to the AUTODYN solver) so that it could potentially be used to create a pre-stress environment for the AUTODYN solver, if found necessary. The problem investigated for this validation test case was the Hertzian contact stresses between two mating teeth and was conducted using a 2D plane stress model. See Figure 48 for a picture of the problem being solved.

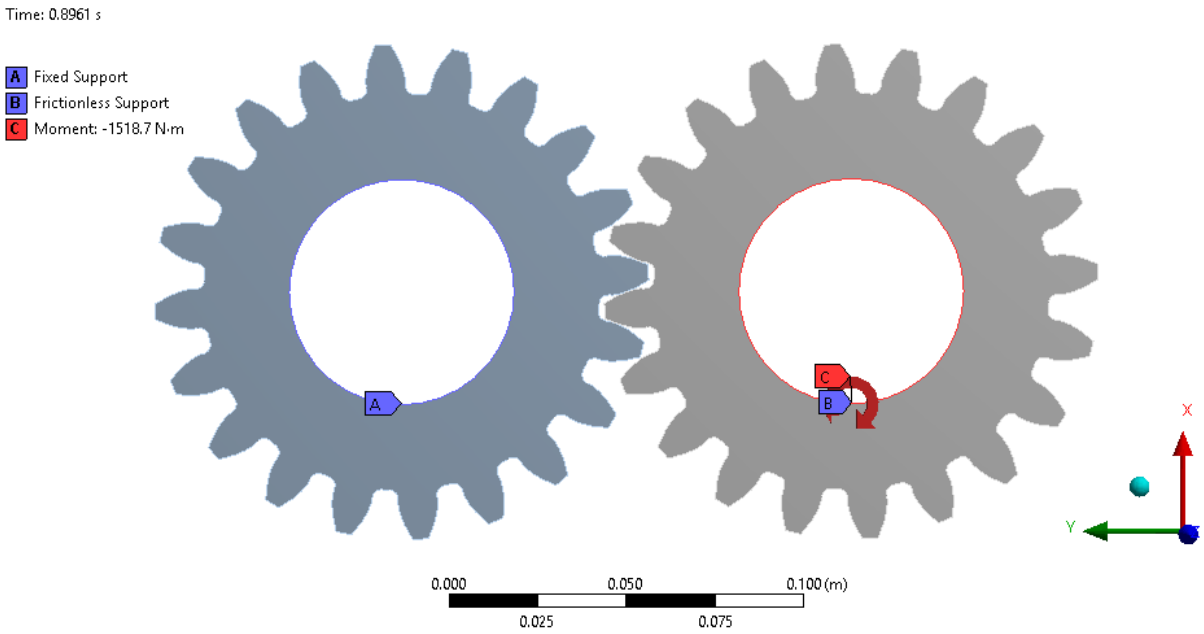

Figure 48 – 2D Model of Hertzian Contact Stress in Spur Gears

It was found that the numerical solution had a percentage error of 39.9% to the analytical solution. The equation for the analytical solution was calculated by Hassan (2009) and Karaveer et al. (2013). This error seemed high. However, good agreement with a separate numerical solution produced by Lee (2015) was achieved which meant that the numerical model was being conducted correctly. See Figure 49 and Figure 50 for this. The detailed description of this benchmark as well as calculation of the reference solution can be found in Appendix B.1.

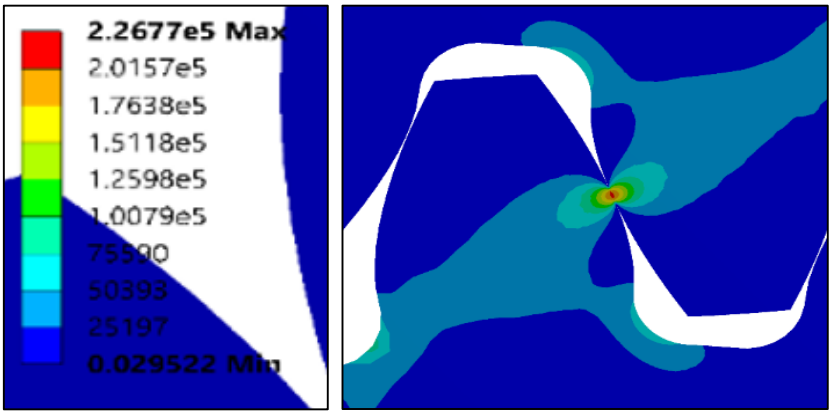

Figure 49 - Equivalent Stress in Two Mating Teeth

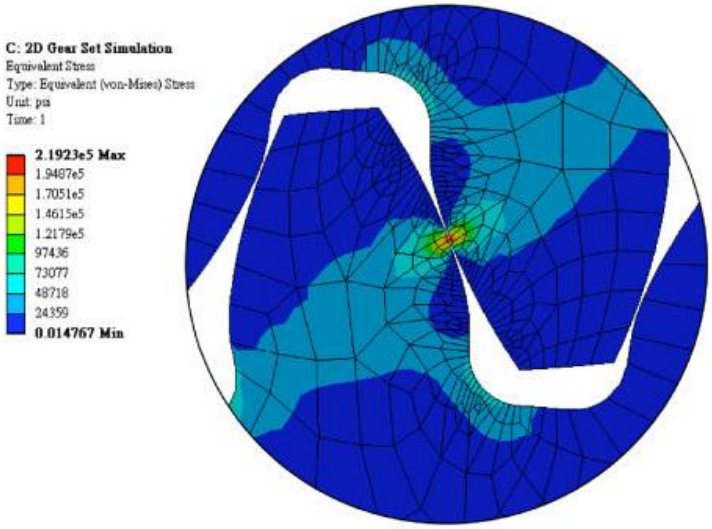

Figure 50 - Reference Solution of Equivalent Stress in Two Mating Teeth (Lee, 2015)

3.4.2 Free Vibration

The second benchmark involved testing for the time accuracy of the AUTODYN solver. This was considered by looking at the free vibration of a bar in AUTODYN due to an impulse loading. In this benchmark, the APDL solver was used to apply a pressure which ramped to 0.1 MPa after one second. The vibration of the bar was then analysed using the AUTODYN solver. See Figure 51 for a picture of the problem being solved.

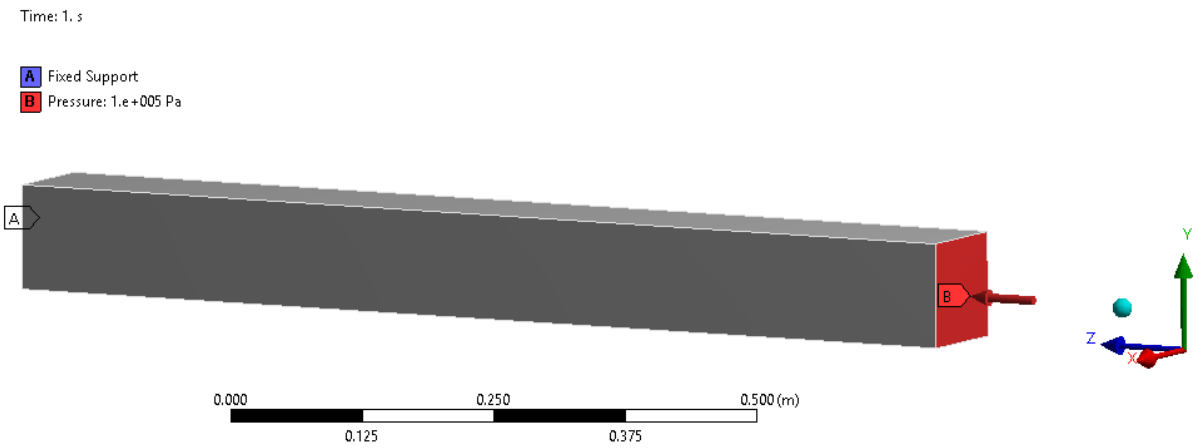

Figure 51 - Model of Free Vibration in a Bar

As can be seen in Figure 52, the analytical solution for the directional deformation at the free end of the bar revealed a near-identical match to the numerical solution. From this analysis, AUTODYN was validated for its capacity to be time accurate. The equation for the analytical solution was calculated by Rao (2010). The detailed description of this benchmark, as well as the calculations for obtaining the reference solution, can be found in Appendix B.2.

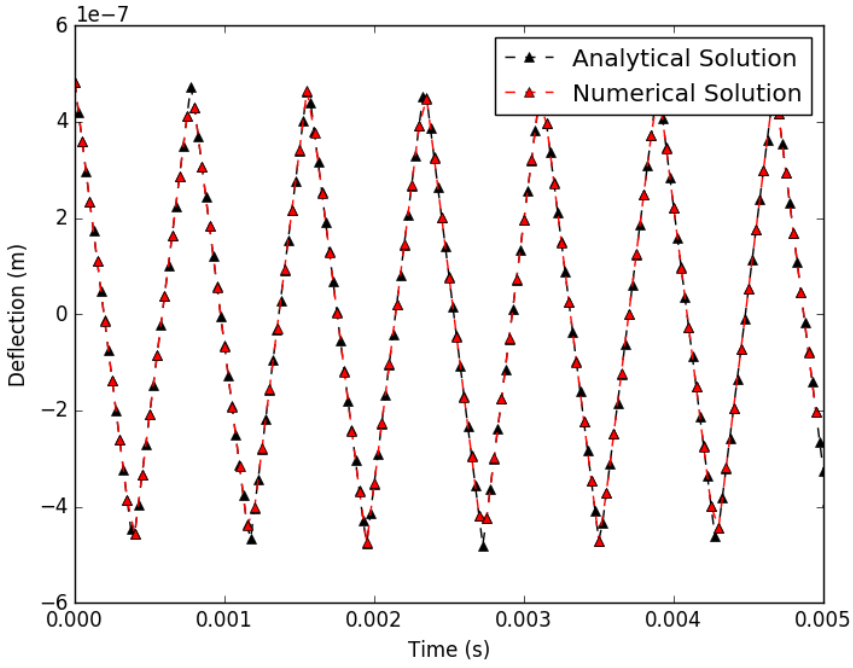

Figure 52 - Directional Deformation at Free End of Bar

3.4.3 Stress Wave Propagation

The third benchmark involved looking at the stress wave propagation through a bar due to an impulse loading. A pressure of 0.1 MPa was applied to one end of the bar over a period of 3.88×10^{-5} seconds. See Figure 53 for a picture of the problem being solved.

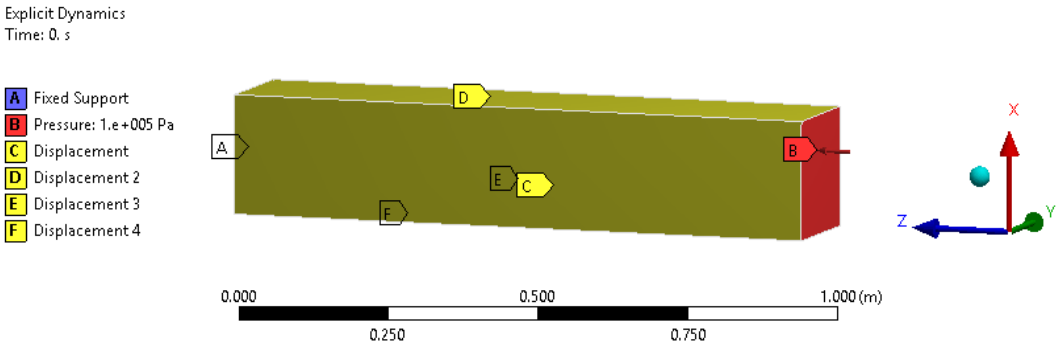

Figure 53 - Model of Stress Wave Propagation through a Bar

It was found that the numerical solution for the speed of the wave had a percent error of 0.47% from the analytical solution. Furthermore, the numerical solution of the width of the wave had a percent error of 2.25%.

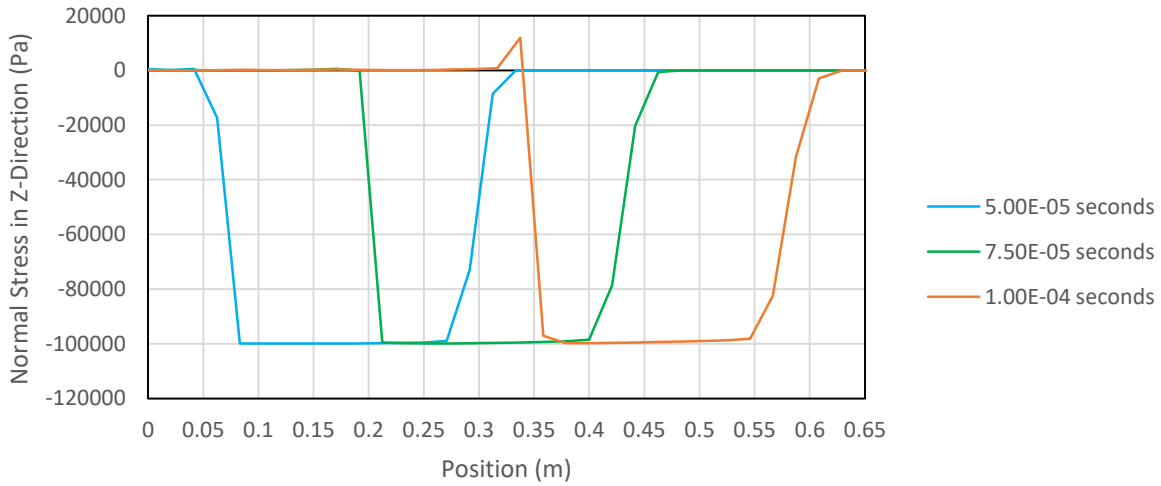

Figure 54 - Numerical Solution for Stress Wave Propagation through a Bar

These errors were deemed to be at acceptable levels but nonetheless, this study was also replicated using the LS-DYNA solver and it was found that the same maximum normal z-stress value of 100,000 Pa and the same wave speed and width was calculated as was in the case for the AUTODYN solver. Thus, AUTODYN had been validated for modelling elastic stress wave propagation through a bar. The equations for the analytical solution was calculated following

the procedure outlined by Institut national des sciences appliquées de Toulouse, (2014). The detailed description of this benchmark, as well as calculations for the reference solution, can be found in Appendix B.3.

3.4.4 The Perfect Plasticity Model and Isotropic Hardening Model

The fourth benchmark involved analysing a pressurised cylinder in a 2D axisymmetric setting. It looked into yielding using the von Mises criteria with a perfect plasticity model and an isotropic hardening model and it looked at the increase in the plastic zone size with an increase in the load applied. See Figure 55 for a picture of the problem being solved.

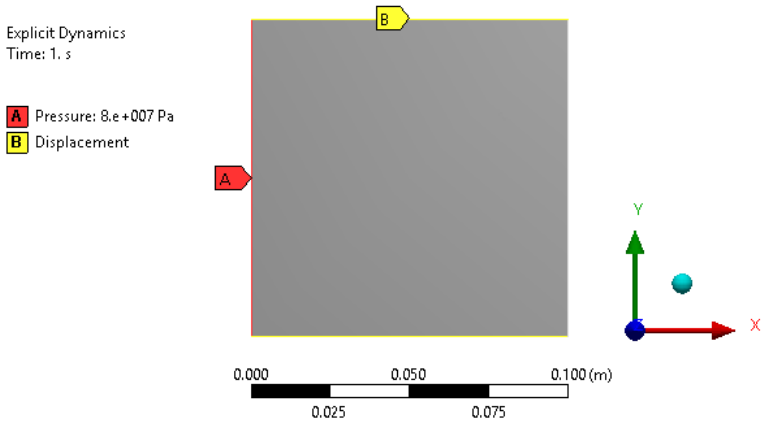

Figure 55 - Axisymmetric Model of Pressure Applied to Inner Surface of Thick Walled Cylindrical Pressure Vessel

It was found that when the applied load increased for the perfect plasticity model, the von Mises stress (effective stress) experienced in the through-thickness section of the cylinder increased but did not grow past the yield stress of the material of 207 GPa. This was expected with the utilisation of a perfect plasticity model. The results for the radial, hoop and effective stresses came within good agreement with the reference solution as shown in Figure 56, Figure 57 and Figure 58, respectively.

However, it is important to note that only 64 elements were used for the analysis and it was found that this was not sufficient in order to achieve mesh independence. Only 64 elements were used in the simulation since the reference solution only used 64 elements and to match the reference solutions the mesh densities between these two studies needed to be matched. Therefore, the solution could be assumed to be accurate in the real-world case. It is only accurate for comparing with the reference solution provided by Becker (2001) from *NAFEMS*.

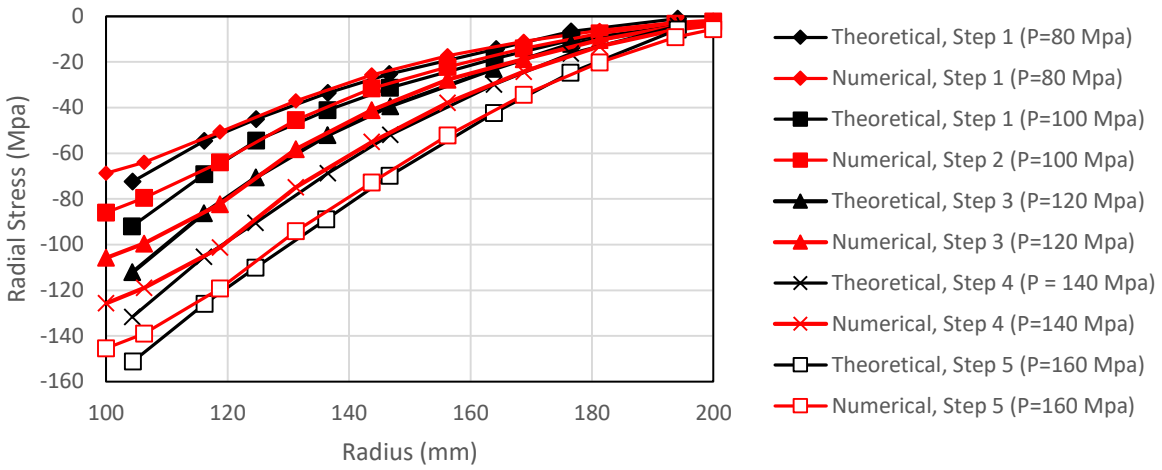

Figure 56 – Radial Through-Thickness Stresses in Cylindrical Pressure Vessel

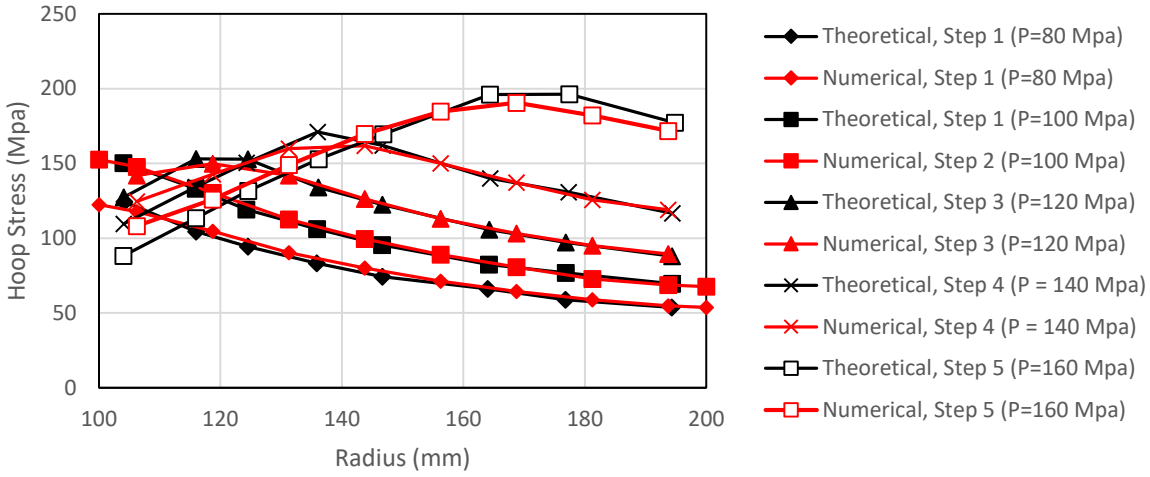

Figure 57 - Hoop Through-Thickness Stresses in Cylindrical Pressure Vessel

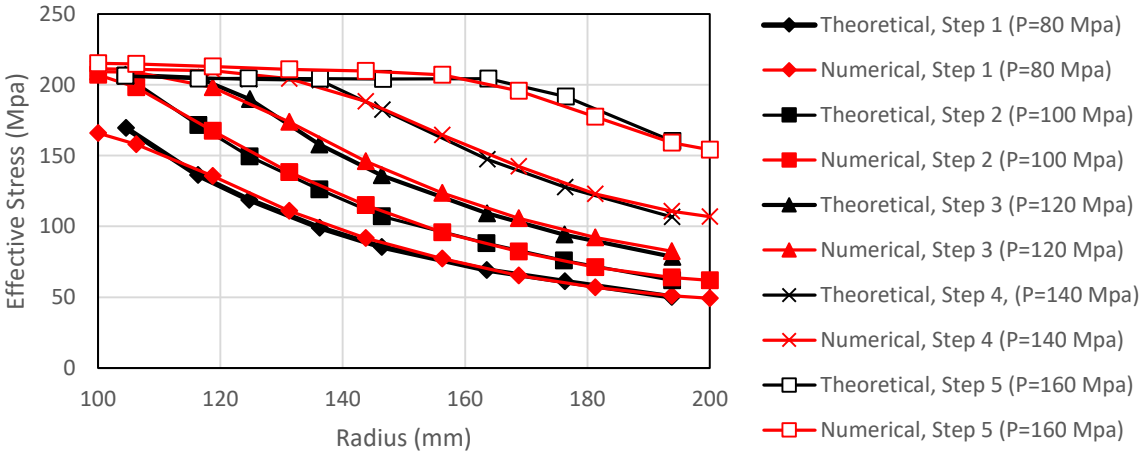

Figure 58 - Effective Through-Thickness Stresses

Furthermore, it was found that when an isotropic hardening model was used, the stress was able to extend beyond the yield stress. Good agreement was made with the reference solution, as shown in Figure 59. The detailed description of this benchmark can be found in Appendix B.4.

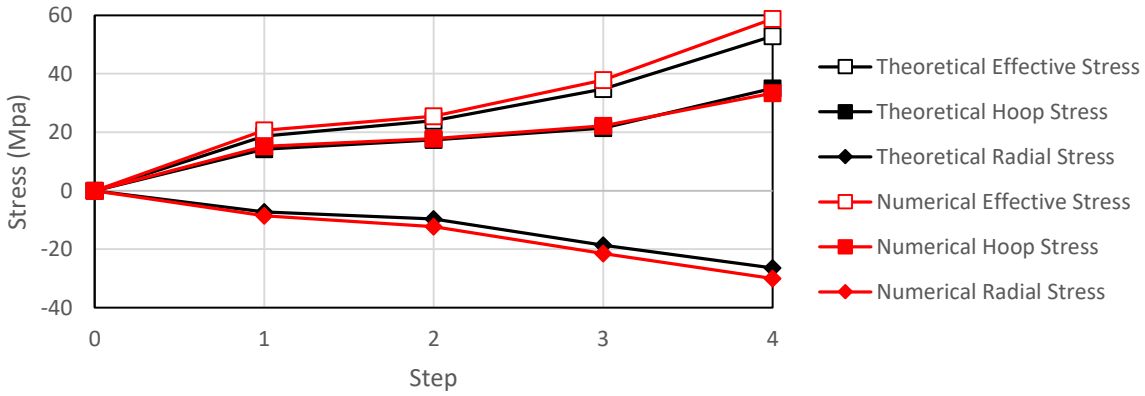

Figure 59 - Stresses for Pressurised Cylinder (Isotropic Hardening Model)

3.4.5 Friction between Two Surfaces

For this benchmark, the friction between the bottom surface of a cube and floor was analysed. The sideward force applied to the cuve was varied between 3500 N to 14000 N, a 7000 N downward force was applied to the cube and the friction coefficient between the contacting surface was 0.5. See Figure 60 for a picture of the problem being solved.

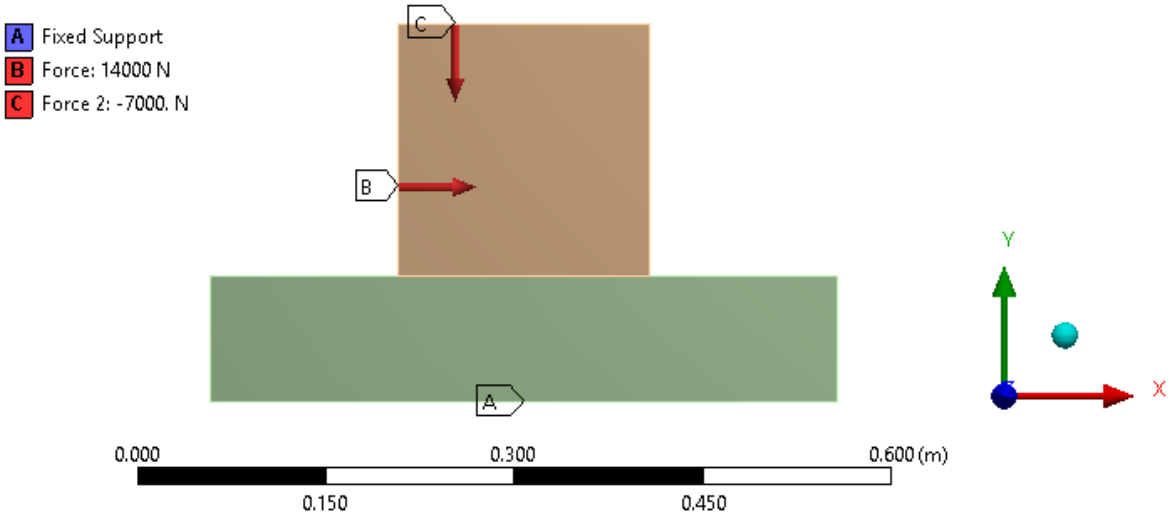

Figure 60 - Model of Friction between Two Surfaces

It was found that for an applied sideward force of 10,000 N and above, the numerical and analytical solution for the displacement of the cube had good agreement (see Figure 61). However, as the force applied dropped below 10,000 N, it was apparent that the error between the numerical and analytical solution grew. Furthermore, it was noticed that for the analytical solution where the cube should have been stationary due to the sufficiently high frictional force applied, the cube still moved. This indicated a limitation of the AUTODYN solver in modelling scenarios where the kinetic energy throughout the simulation was sufficiently low.

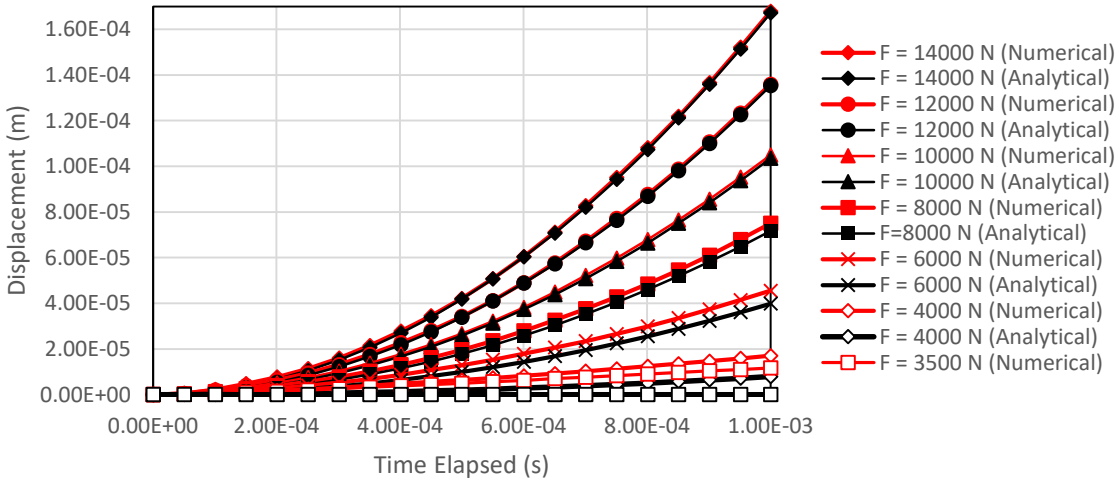

Figure 61 - Displacement-Time Curves

It was observed that as the error between the analytical and numerical solution increased the energy error recorded by the solver also increased. From this it was concluded that as long as the energy error remained below the recommended value of 10% for future simulations that involve friction then this limitation of the AUTODYN solver would not lead to significant error in the results obtained. The detailed description of this benchmark, as well as the calculations for the analytical solution, can be found in Appendix B.5.

3.4.6 Sheet Metal Forming

This benchmark involved replicating an experimental study conducted by Mamalis et al. (1997) which was to simulate sheet metal forming at punch velocities 10^4 higher than the experimental punch speeds and decreasing the density by 10^3 in order to decrease the dynamic effects caused by using such high punch velocities. The punch velocity was increased to reduce the end time of the simulation and the density was decreased in order to minimise the high dynamic effects introduced by simulating a punch velocity 10^4 higher than the actual experimental punch velocity. See Figure 62 for a picture of the problem being solved.

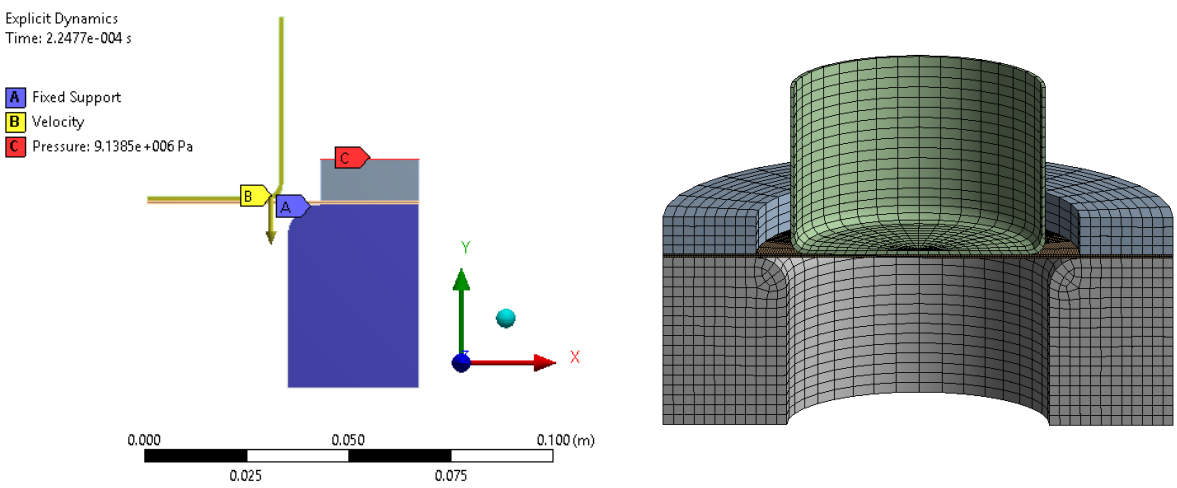

Figure 62 – Axisymmetric Model of Sheet Metal Forming (Left) with Half Model Shown for Visual Aid (Right)

It was found that the symmetry tool could be used in the AUTODYN solver to visualise 2D axisymmetric models in 3D (see right hand side of Figure 62). Furthermore, it was shown that the force reaction probe could be reliably used to measure the forces involved in an impact problem as the simulated punch load-punch travel curve matched the experimental punch load-punch travel curve closely, as shown in Figure 63.

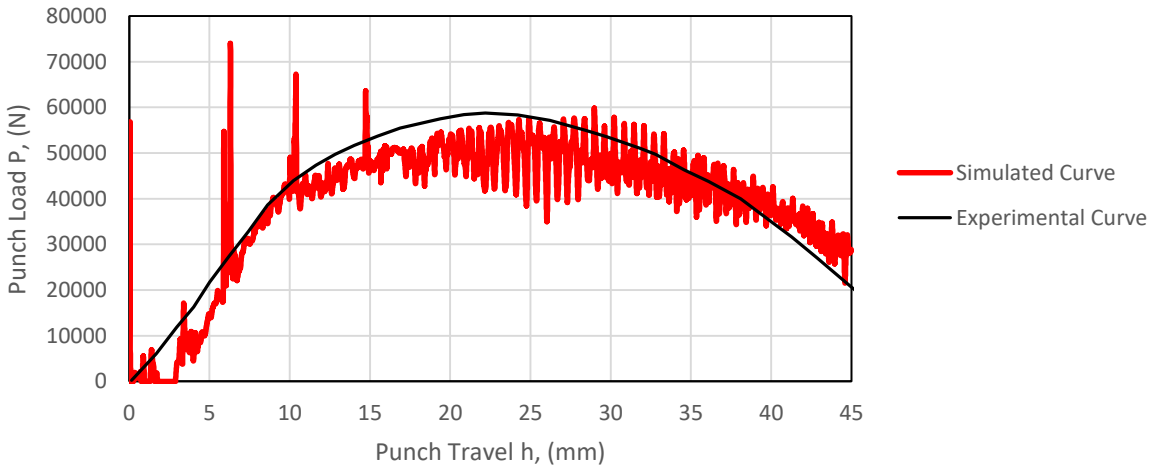

Figure 63 - Punch Load plotted against Punch Travel

This tool would be useful for the T4 piston impact problem in determining the impact tolerance of the facility in terms of a force rather than an impact speed, if necessary.

An isotropic hardening model was used for this benchmark and it was found that the experimental radial, hoop and thickness strains produced by Mamalis et al. (1997) had good agreement with the numerical radial, hoop and thickness strains obtained. See Figure 64. This

was not surprising since the ability for the AUTODYN solver to model isotropic hardening had already been validated in Section 3.4.4. The detailed description of this benchmark can be found in Appendix B.6.

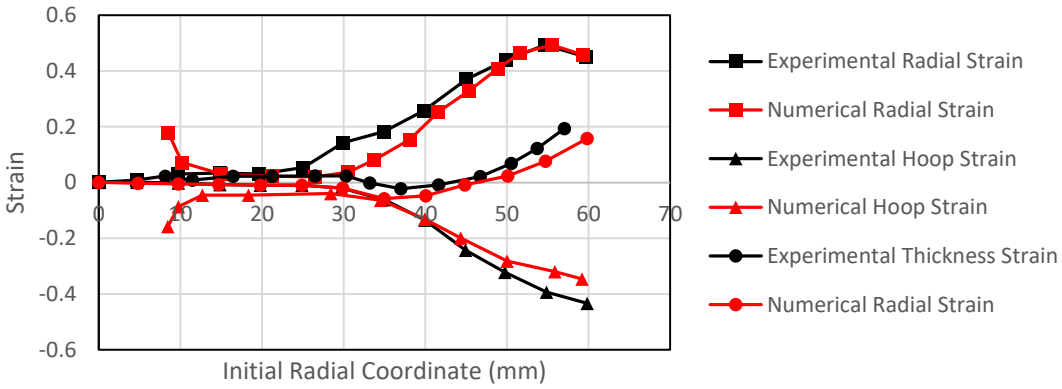

Figure 64 - Strain Distribution on 45 mm Cup Height

3.4.7 Taylor Bar Impact Test

The objective of this benchmark was to evaluate the use of the Linear Shock EOS and the Johnson-Cook strength model for shape predictions of a cylindrical projectile specimen impacting a rigid wall. In doing so, the validity of the parameter values for the following equation of state and strength model was evaluated. The material of the cylindrical projectile specimen that was investigated was steel 4340 and the parameter values were sourced from Banerjee (2007). The impact velocity of the projectile was 208 m/s. See Figure 65 for a picture of the problem being solved.

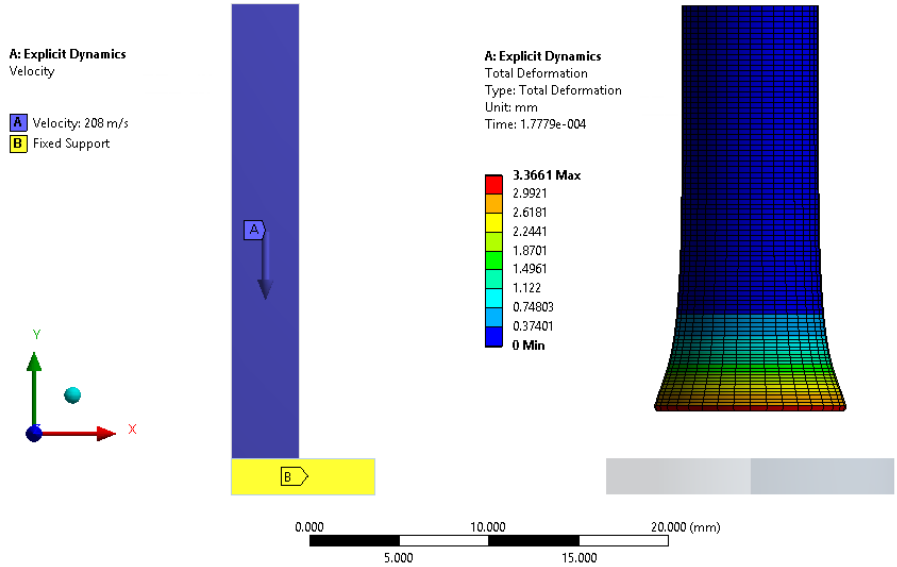

Figure 65 - Axisymmetric Model of Taylor Bar Impact Test (Left) and Deformed Projectile After Impact at a Speed of 208 m/s (Right)

This benchmark provided a quantitative assessment of AUTODYN's ability to replicate the mushrooming deformation of a cylindrical projectile. This deformation mode was of interest to replicating the T4 impact problem since the T4 piston showed this type of deformation during shot 10509.

It was found that the AUTODYN solution for the total deformation of the projectile came within good agreement with the experimental solution for the deformation of the projectile (see Figure 66). The experimental solution was obtained from Banerjee (2007). The mesh body size of the projectile specimen was decreased from 0.3 mm to 0.1 mm in order to determine whether mesh independence was reached in the numerical solution of the deformed projectile specimen. It was found that the numerical solution of the deformed projectile specimen was near identical when 4560 nodes were used or 13395 nodes. The detailed description of this benchmark can be found in Appendix B.7.

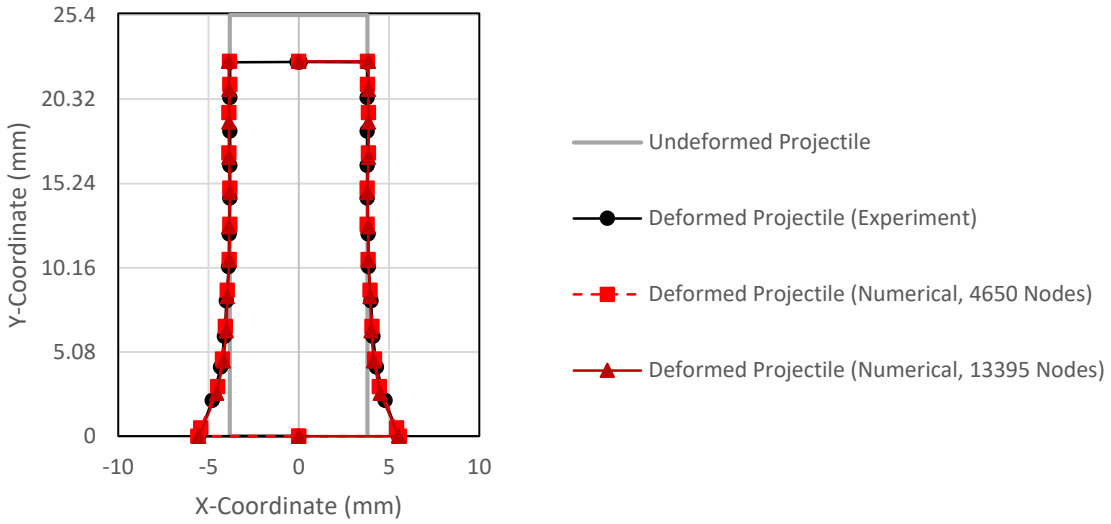

Figure 66 - Comparison between Steel 4340 Projectile Specien Before and After Impact with Rigid-Wall

It is important to note that the axisymmetric model of the Taylor bar impact test only applied when there was symmetric deformation. In the event that 3D deformation modes (such as buckling and fracture), an axisymmetric model would not capture the physical process correctly.

3.5 Conclusion

This chapter has detailed the selection and suitability of the AUTODYN solver in addressing the piston impact problems being investigated. It was found that the output from the AUTODYN solver was able to show close agreement with the reference solutions provided for the free vibration in a bar, stress wave propagation through a bar, the perfect plasticity and isotropic hardening model, friction between two surfaces, sheet metal forming and the Taylor bar impact test. Aside from serving as a benchmark to test AUTODYN's ability to capture the physical mechanisms involved in a high speed piston impact, the numerical simulation of the Taylor bar impact test provided an additional purpose in that it validated the high strain rate material data for 4340 steel which has significance to the explicit FEA of the T4 facility (see Chapter 4).

4 Explicit FEA of T4 Facility

4.1 Chapter Overview

This chapter details the reconstruction of the 2009 T4 high speed piston impact using AUTODYN as the explicit numerical solver. The chapter begins with the technican's comments on T4 shot 10509 such as the apparent minimal yield on the tube and observations made at the time of repair. This chapter then focuses on estimating the impact speed for T4 shot 10509, determining high strain rate material data for the components of the facility involved during the impact and the modelling techniques implemented to minimise the simulation run time as much as possible without sacrificing the accuracy of the numerical results. A discussion on the effective stress in the piston body and compression tube, the radial deformation of the compression tube and the contact pressure along the inner surface of the compression tube after T4 shot 10509 was presented. Furthermore, a look into higher T4 piston impact speeds was presented as well as the sensivity of results to changes in friction and material data used.

4.2 Technician Comments on T4 Shot 10509

The technician of the T4 RST facility made the following comments regarding the repair job which followed T4 shot 10509:

"After we undid the capstan and separated the shock tube from the compression tube, thus exposing the front face of the piston, the only visible part of any of the piston accessory components was the front face of the aluminium bronze nut." See Figure 67.

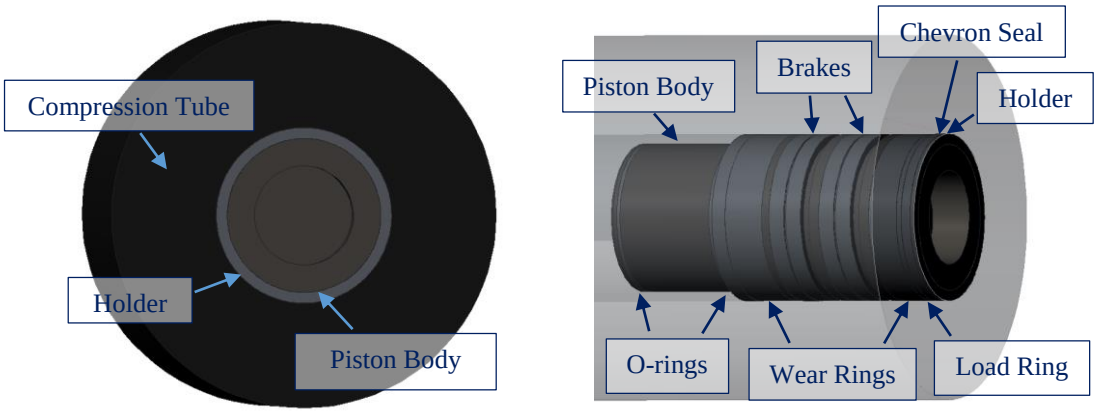

Figure 67 - Depiction of Compression Tube with Capstan Undone (Left) and Side View with Compression Tube made 75% Transparent (Right)

"I do not recall it as being fractured in any way. During the impact, it was supported by the rapidly expanding piston on its inside diameter (thread, 8 threads per inch, 60-degree thread form), while it's outside diameter was supported (after a small amount of deformation) by the inside diameter of the compression tube. The nut's rear face at 90 degrees to the piston axis was supported by the aluminium bronze backing ring, and the rest of the rear profile of the nut was supported by the chevron seal, which, in turn, would have been subjected to heavy compression on all sides from its contact with the nut, the backing ring, and the inside diameter of the compression tube. The front face of the nut was supported (or suffered impact, if you like), by whatever was left of the rubber buffer and its supporting backing rings. I am of the opinion that the nut did not fracture because it had nowhere to go.

We removed the nut by means of drilling it out while the piston was still seized within the compression tube. The chevron seal was also drilled out. Also, the backing ring was also drilled, and I doubt that it was fractured before we mutilated it in order to get it out.

The front wear ring was drilled out also, the evidence of which can still be seen on the piston, so the only part of it that would have been visible was its front face after the removal of the backing ring, and as the backing ring had to be removed by drilling it out, the front face would have appeared far from perfect after the removal of the backing ring.

The rear wear ring is still on the piston, and appears to be in quite reasonable condition. It is quite possible that others took photographs of the damage, but unfortunately I do not know of their existence."

These comments are of use to the numerical replication of shot 10509 as it provides a means of validating the numerical results. An important comment made was that no yielding was observed in the compression tube. This meant that the numerical solution should also lead to this result. Furthermore, it was stated that no fracturing occurred. This implied that a fracturing equation did not need to be defined for each material since no fracturing appeared to take place on the piston or the piston's accessories. Including a fracture equation, without conducting experiments to accurately determine the material properties for fracture, would not likely yield reliable results due to the uncertainty in the accuracy of the material data obtained.

4.3 Estimating Piston Impact Speed during Shot 10509

The 1-D Lagrangian CFD code, L1d3, can be used to model the internal operation of free-piston drive shock tunnels, including the velocity of the piston, V_p, as a function of position, X_p, for a given set of initial conditions. This means that it will be able to determine an indicative impact speed for shot 10509, which will be necessary for recreating the T4 piston impact problem in FEA.

In the L1d3 formulation, the piston is modelled as having a fixed mass, length and frontal area. There is a back pressure, P_B, acting on the piston which is used to model the effects of the reservoir air gas acting on the piston and the front pressure, P_F, comes from the driver gas ahead of the piston. The frictional force, F_f, comes from the "chevron" seal near the front face of the piston. The coefficient of friction between the contacting surfaces is set to 0.2 (Jacobs, 1998).

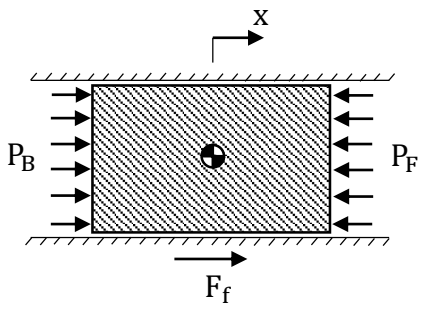

Figure 68 - Free Body Diagram of Piston in Compression Tube (Adapted from Jacobs, 1998)

From Figure 68, the following equations of motion can be derived:

$$\frac{d}{dt}V_p = \frac{1}{m_p}[A_p(P_B - P_f) + F_f] \tag{30}$$

In L1d3, a Lagrangian discretisation approach to modelling the gas slugs is undertaken and the explicit formulation is used where the CFL condition allows for convergence while solving for the partial differential equations present in the code. These partial differential equations describe the local fluid velocity to interface velocity; average density within the control-mass; rate of change of momentum and the rate of change of energy in the control-mass. The assumption of the gas slugs acting as calorically perfect gas are made to solve for the gas properties, including the pressures P_B and P_F, and the assumption of steady state heat flow is also made. The boundary layer along the tube walls are ignored in the formulation of the

dynamics equations but some of its effects are seen in the momentum equation due to the addition of wall shear stress if included in the model (Jacobs, 1998).

Validation with this type of calculation was required since the code relies on empircal correction factors to account for 2D and 3D flow processes which cannot be captured directly by the 1D formulation. Hence, a comparison between the simulated compression tube pressure results to shots with existing experimental data was conducted. Shot 7048 was used as the experimental data reference since its fill pressure values were close to that of shot 10509. The reservoir (air) pressure for shot 7048 was 1.40 MPa, the (helium) driver pressure was 34 kPa, the shock tunnel pressure was 220 kPa and the air test-section pressure was 400 Pa. In this investigation, the piston breaks were disengaged and a blank-off scenario was utilised. A blank-off scenario in L1d3 involves setting the rupturing threshold pressure of the primary diaphragm to be greater than the peak driver pressure so that the primary diaphragm does not rupture. This is done to measure the piston's performance.In the blank-off scenario, the pressure is measured at end of the compression tube just in front of the primary diaphragm (see Figure 69).

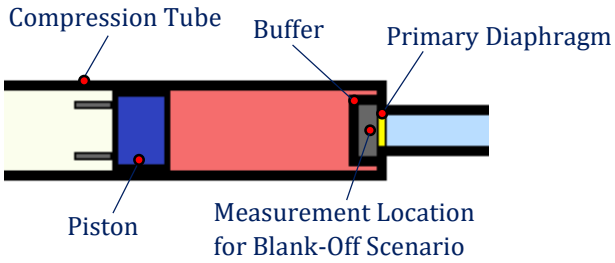

Figure 69 - Measurement Location for Blank-Off Scenario

The L1d3 solution for the driver pressure during shot 7048 was plotted against the known experimental solution. This is shown in Figure 70.

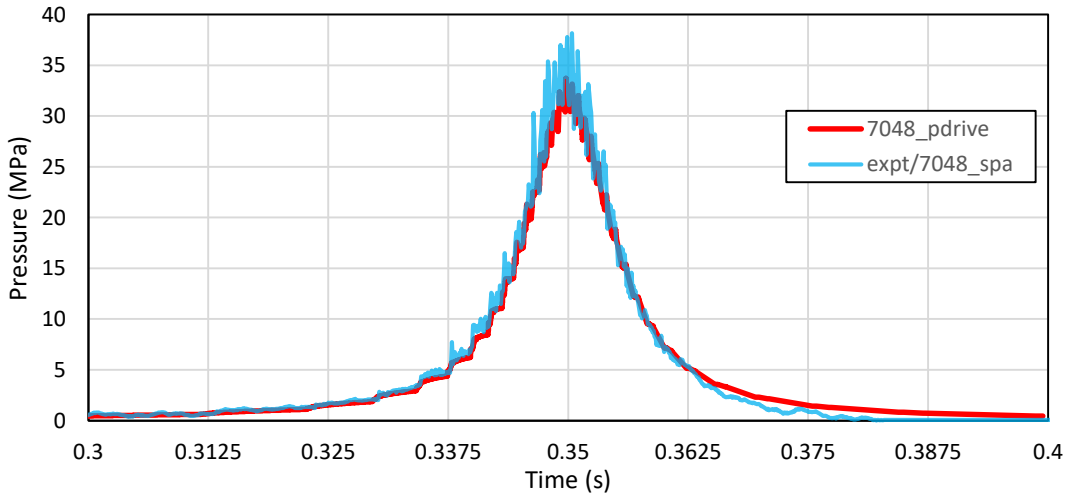

Figure 70 - T4 7048 Simulation and Experiment, Driver Pressure

A time shift for the experimental curve was required to match the curves. Figure 70 reveals a near-identical match between the simulated driver pressure (7048_pdrive) and the experimental curve (expt/7048_spa). Thus, the L1d3 had been validated for further studies.

The shot conditions for shot 10509, as listed in Table 1, was then used to determine the speed of the T4 piston as a function of its position along the compression tube (with x = 0 m being the starting point along the compression tube and x = 25.7 m being where the buffer is meant to catch the piston at the end of the compression tube). For this analysis, the piston brakes were engaged. The response of the T4 piston during shot 7048 was also included to be used as a comparison.

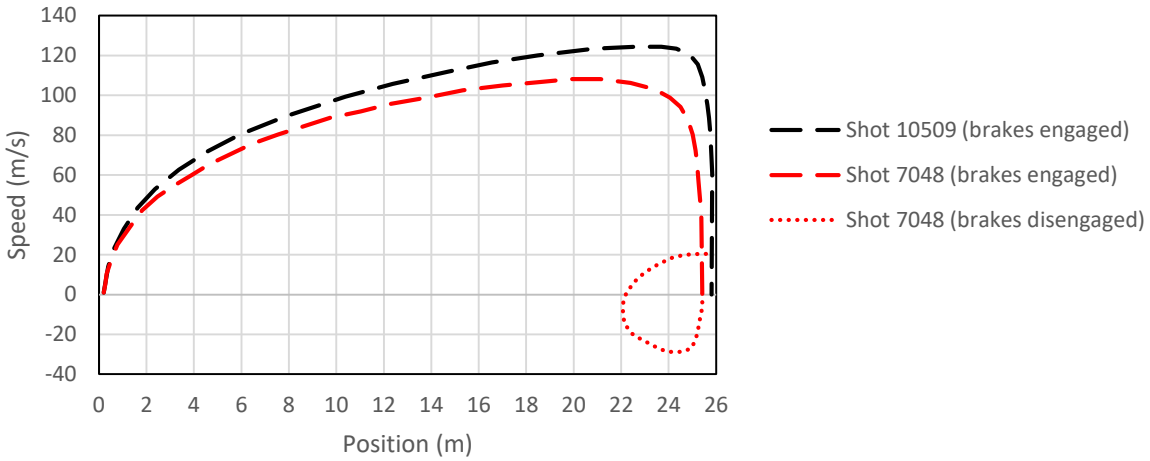

Figure 71 - L1d3 Plot of T4 Piston Speed against Position in Compression Tube

It can be seen in Figure 71 that the piston initially accelerated and as it approached the end of the tube, at approximately 24 m, the driver gas attempted to bring the piston to rest.

Figure 72 displays that for the case of shot 7048 where the brakes were engaged, the piston was able to come to rest where the buffer was meant to catch it. However, for shot 10509, the piston makes a direct impact into the buffer at an estimated impact speed of 61 m/s.

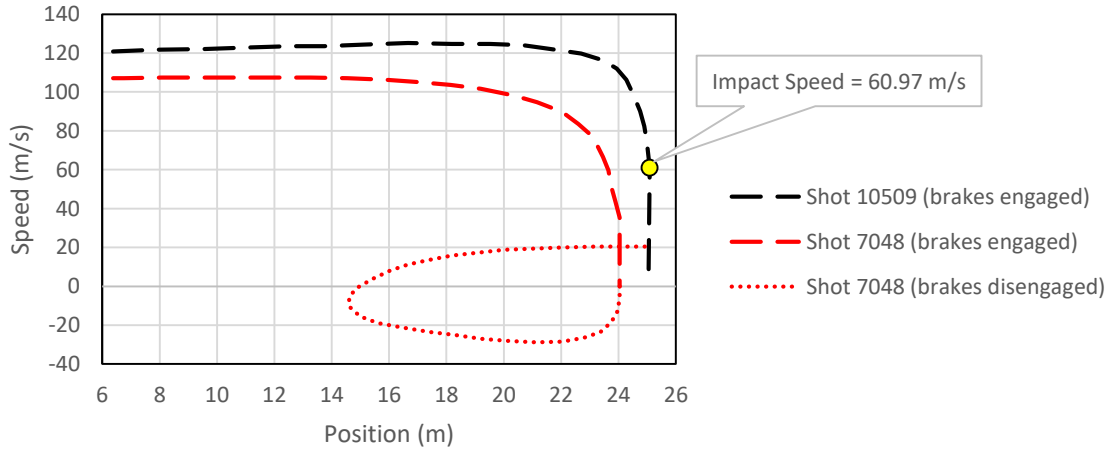

Figure 72 - L1d3 Estimate of T4 Shot 10509 Impact Speed

Therefore, the estimated impact speed of the T4 piston during shot 10509 was found to be 61 m/s.

4.4 Material Description for T4 Facility

The metal components of the facility involved in the impact problem included the compression tube, piston body, brake shoes, load ring, holder and backing plates of the buffer. These components experienced high strains and high strain rates during the high speed piston impact and the material properties used in the numerical model needed to reflect this. Thus, the Mie- Grünsien equation of state and Johnson-Cook strength models were used to capture this behaviour of these metals. Conducting the Split-Hopkinson pressure bar test or the Taylor bar impact test to determine the material parameters was deemed to be outside of the scope. Instead, the Johnson-Cook parameters used for these metals were obtained from existing literature.

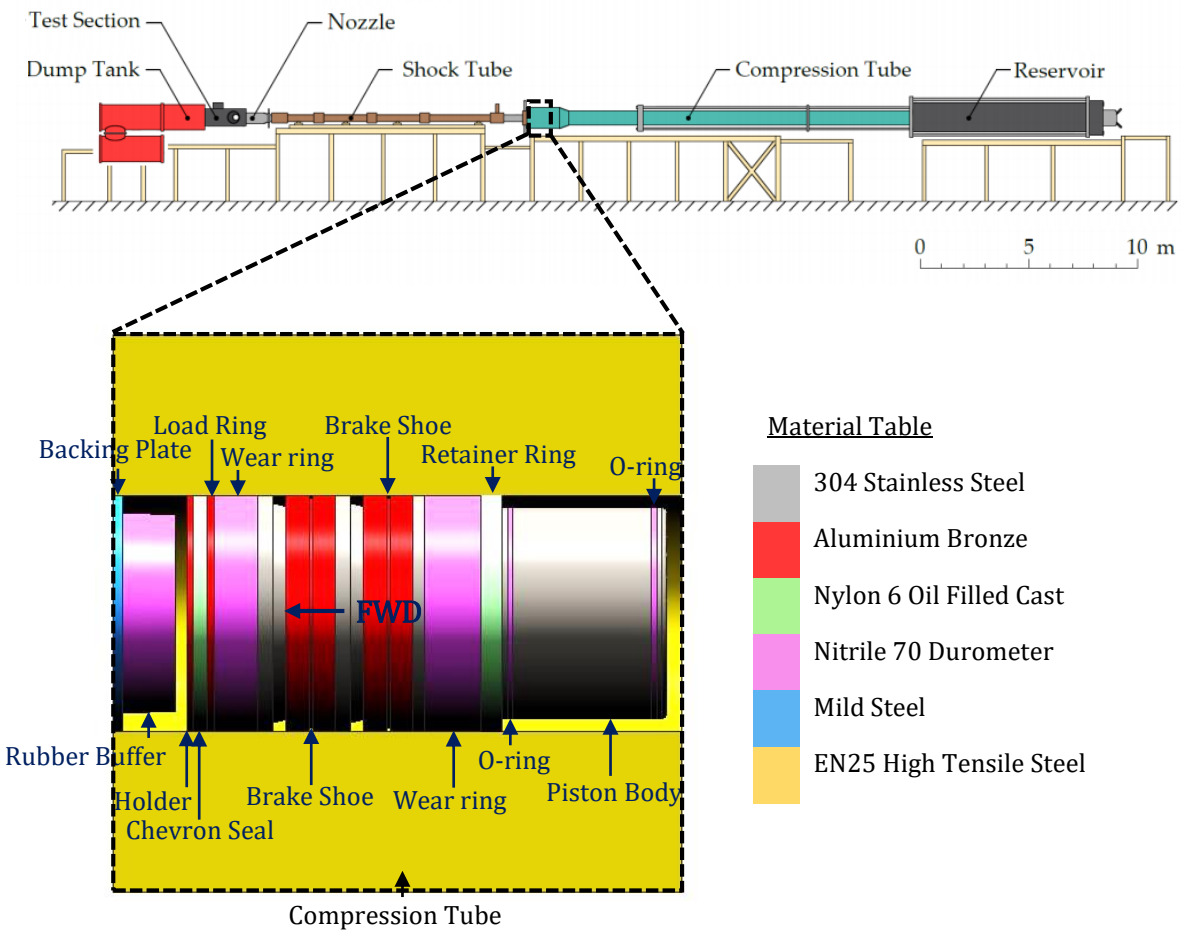

Figure 73 - Illustration of T4 Shock Tunnel Components with Material Annotations (Adapted from Robinson et al., 2015)

In order to acquire meaningful numerical results for the T4 piston impact analysis, the material description for the components of the facility needed to be thorough and its validity justified. Hence, high strain rate material data from multiple literature sources for each of the metals shown in Figure 73 were analysed and from this analysis a selection on the material parameters for each of the metals was made. Table 4 displays the sources analysed for the Johnson-Cook and Linear Shock EOS parameters of the four metals as well as the selected source. See Appendix C for further details on these sources and the decision for selecting the sources listed in Table 4.

Table 4 - Sources Analysed for Johnson-Cook and Linear Shock EOS Material Data

Material	Property	Sources Analysed	Source Selected
304 Stainless Steel	Johnson-Cook	Frontán et al. (2012), Mori et al. (2007), Krasauskas et al. (2015) and Olleak et al. (2015)	Frontán et al. (2012)
	Linear Shock EOS	Steinberg (1996), Duffy (1997), Los Alamos Scientific Laboratory (1969) and Winter et al. (2014)	Steinberg (1996)
Aluminium Bronze	Johnson-Cook	Li et al. (2015), Kay (2003), Dassault Systèmes (2012) and Fu et al. (2016)	Li et al. (2015)
	Linear Shock EOS	Cook et al. (1969) and Duffy (1997)	Johnson et al. (1969)
Mild Steel	Johnson-Cook	Seidt et al. (2007), Vedantam et al. (2006), Schwer (2007) and Cook et al. (1969)	Seidt et al. (2007)
	Linear Shock EOS	Roy (2015), O'Toole (2015) and Cook et al. (1969)	Roy (2015)
EN25 High Tensile Steel	Johnson-Cook	Banerjee (2007), Cook et al. (1985), Schreiber et al. (2013), Agmell et al. (2013) and Arrazola et al. (2002)	Banerjee (2007)
	Linear Shock EOS	Banerjee (2007), Steinberg (1996), Shivpuri et al. (2009) and Agmell et al. (2013)	Banerjee (2007)

The material data (for each of the metal components of the facility) from the source selected is listed in Table 5.

Table 5 - Material Data for Metals involved in T4 Piston Impact Analysis

Property	**Material**			
	304 Stainless Steel	**Aluminium Bronze**	**Mild Steel**	**EN25 High Tensile Steel**
Density (kg/m^3)	7900	7450	7850	7850
Specific Heat (J(/kg. °C))	440	410	510	475
Fitting Parameter A (MPa)	280	430	286	792
Fitting Parameter B (MPa)	802.5	904	500	510
Fitting Parameter n	0.622	0.66	0.228	0.26
Fitting Parameter C	0.0799	0.016	0.017	0.014
Fitting Parameter m	1	2.4	0.917	1.03
Melting Temperature (K)	1673	1038	1427	1793
Reference Strain Rate (/sec)	1	1	1	1
Shear Modulus (MPa)	77000	27000	81800	81800
Gruneisen Coefficient	1.93	2	2.17	1.69
Parameter C1 (m/s)	4570	5328	4569	3935
Parameter S1	1.49	1.338	1.49	1.578
Parameter Quadratic S2 (s/m)	0	0	0	0

Compared to the metal components involved in the impact analysis, the nylon chevron seal and retainer ring was not considered to contribute signifcantly to the deformation of the pistion body or the compression tube during impact. Thus, high strain rate data was not sought out for this material. Instead, the nylon material data in ANSYS Workbench Engineering Library was utilised to model nylon 6 oil filled cast (these material properties were refined in Chapter 6 when analysing the surviable impact of the nylon studs for the X3). The material properties used for nylon is shown in Table 6.

Table 6 - Material Properties of Nylon in ANSYS Workbench Engineering Library (Matuska, 1984)

Property	Value	Unit
Density	1140	kg/m^3
Bilinear Isotropic Hardening		
Yield Strength	5E+07	Pa
Tangent Modulus	0	Pa
Shear Modulus	3.68E+09	Pa
Shock EOS Linear		
Gruneisen Coefficient	0.87	
Parameter C1	2290	m/s
Parameter S1	1.63	
Parameter Quadratic S2	0	s/m

The material data for the rubber buffer and wear rings was obtained from ANSYS Workbench Engineering Library for the same reason as why the material data for nylon was obtained from ANSYS Workbench Engineering Library. The material properties used for rubber can be found in Table 7.

Table 7 - Material Properties of Rubber in ANSYS Workbench Engineering Library (Treloar, 1944)

Property	Value	Unit
Density	1000	kg/m^3
Mooney-Rivlin 2 Parameter		
Yield Strength	1.5E+05	Pa
Tangent Modulus	15000	Pa
Incompressibility Parameter D1	1.212E-9	1/Pa

4.5 T4 Numerical Model

A 2D axisymmetric analysis was chosen to model the 2009 T4 high speed piston impact problem. This was because a 2D axisymmetric analysis signifcantly reduced the simulation run times compared to a 3D model equivalent. An analysis was therefore conducted to ensure that no 3D deformation modes were present at the impact speeds investigated (up to 100 m/s). See Appendix D for evidence that no 3D deformation modes were present up to an impact speed of even 200 m/s.

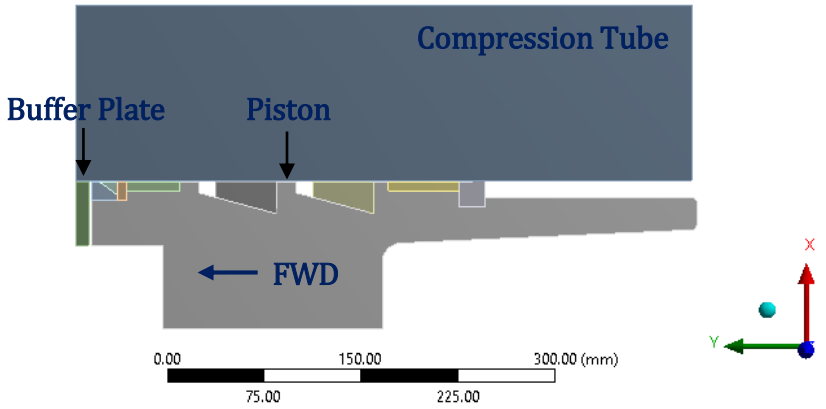

Figure 74 - Axisymmetric View of T4 Piston, Compression Tube and Buffer Plate

Some modifications were made to the geometry of the piston and buffer of the T4 facility in order to minimise simulation times. These are displayed in Figure 75 and Figure 76.

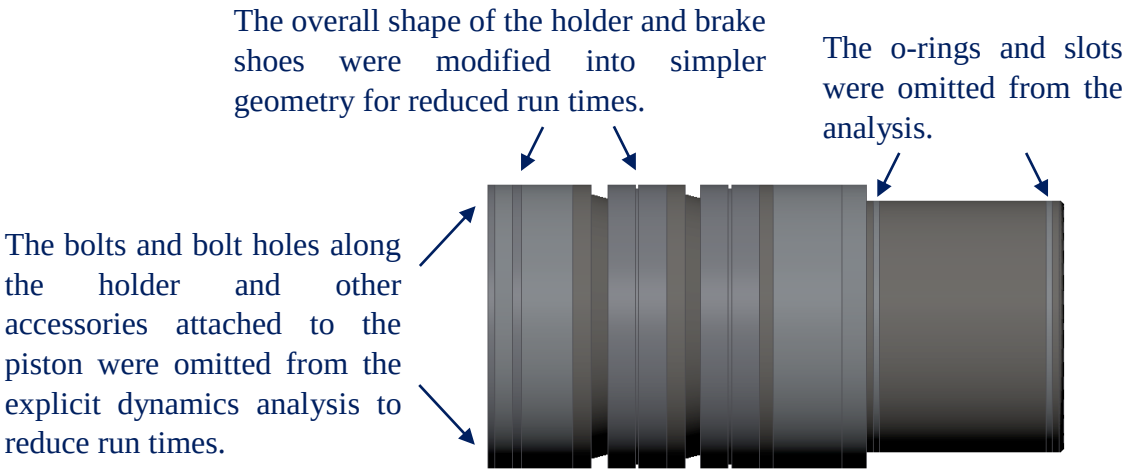

Figure 75 - Geometry Simplifications to T4 Piston

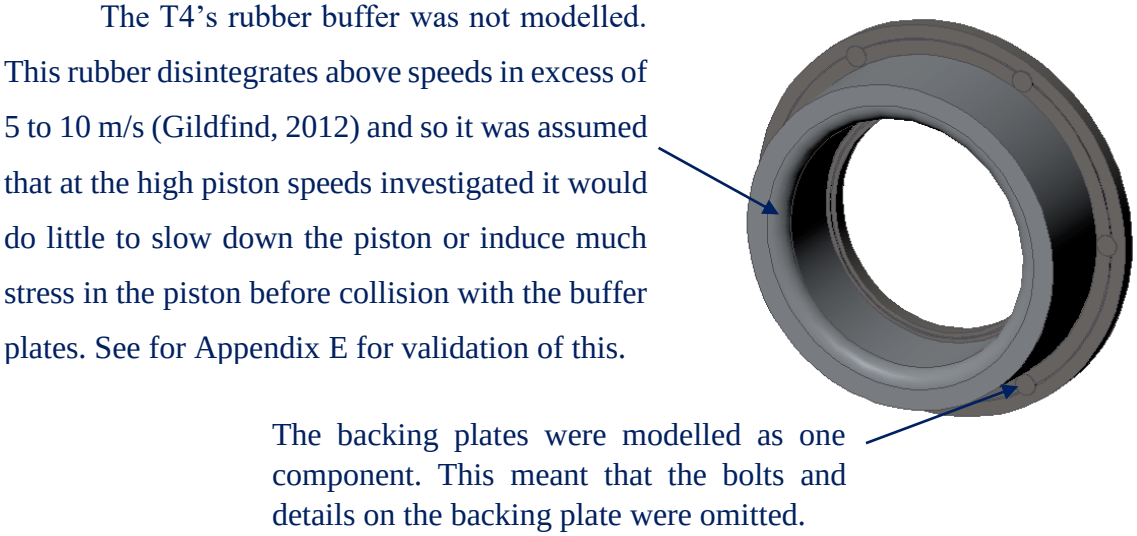

Figure 76 - Geometry Simplifications to T4 Buffer

As discussed in Section 2.7, using mesh connections to connect the joined parts in the model in a 2D explicit dynamics analysis would be more advantaegous compared to bonded contacts and constraint equations as it allows parts of different material assignments to be joined and leads to reduced run times compared to the use of constraint equations. Hence, this was used to connect the piston accessories to the piston with the exception of the piston brakes which had frictional contact with the piston. See Appendix F for validation that the mesh connections did work in connecting joined parts in a 2D explicit dynamics analysis.

A mesh independence study (seen in Appendix G) found that the piston body and piston accessories needed to have a minimum body size mesh of 1 mm applied to them. To save simulation run times the body size mesh applied to the compression tube was 3 mm at the front end (where most of the piston deformation would occur) and became progressively coarser further away from the front end up to a body size mesh of 5 mm (as seen in Appendix G). A 10 layer inflation was applied at the front end up the compression tube on the contacting surface between the piston, piston accessories and the compression tube to further refine the mesh of the compression tube.

The driver pressure and its contribution to the structural response of the compression tube, T4 piston and the piston's accessories during impact was not be considered. This was because it was assumed that the pressures from impact would likely far exceed the driver pressure. See Figure 77 for a picture of the problem being solved.

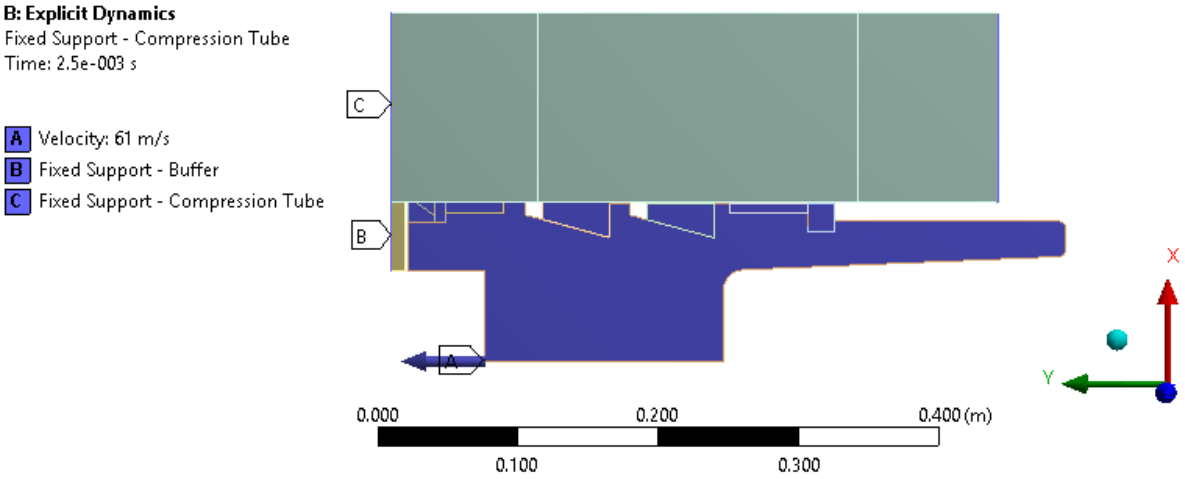

Figure 77 - Axisymmetric Model of T4 Shot 10509

As shown in Figure 77, a fixed support was applied to the two ends of the compression tube and also to the back surface of the buffer plate.

4.6 Yield Failure Analysis of Shot 10509

Table 8 displays the von-Mises stress in the piston body and the compression tube before and after the piston's collision with the end of the tube during T4 shot 10509. The compressive yield strength for the piston body and compression tube was outlined in a red box in Table 8.

Table 8 - Effective Stress in Piston Body and Compression Tube Before and After Impact

Piston Body	Compression Tube
Reconstruction of Shot 10509, Time Elapsed = 0 seconds	
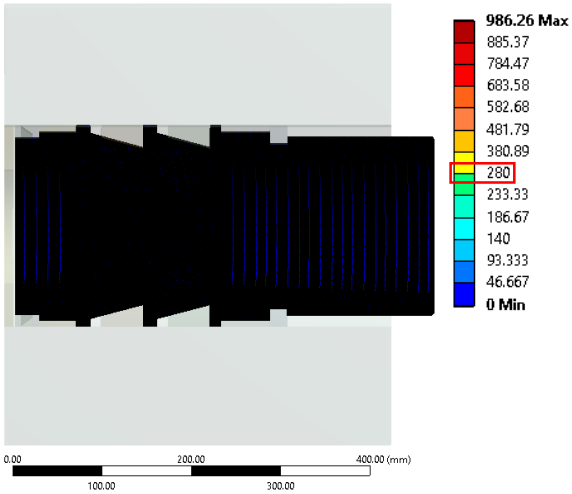	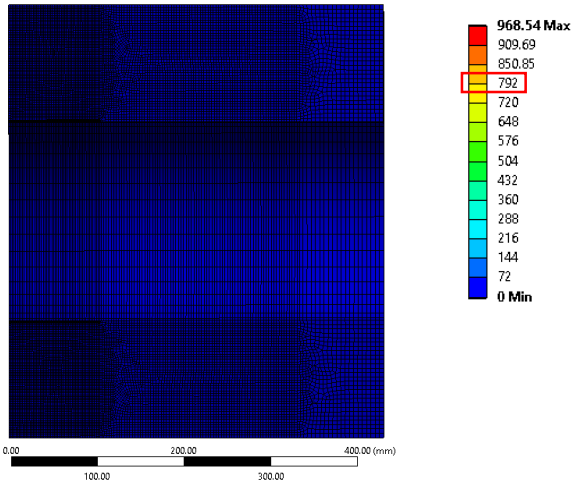
Figure 78 - View of Mesh Density of T4 Piston	Figure 79 - View of Mesh Density of Compression Tube
Reconstruction of Shot 10509, Time Elapsed = 2.5e-003 seconds	
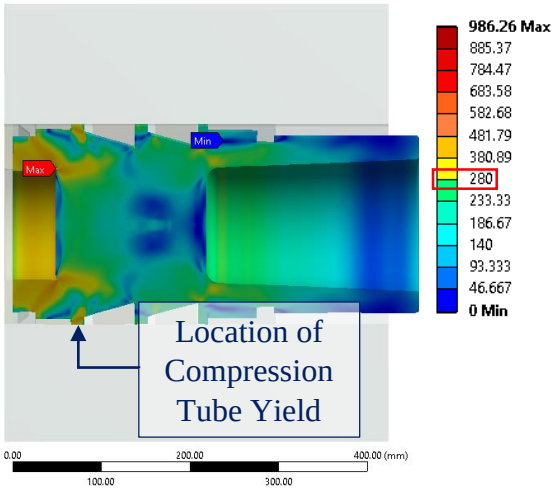	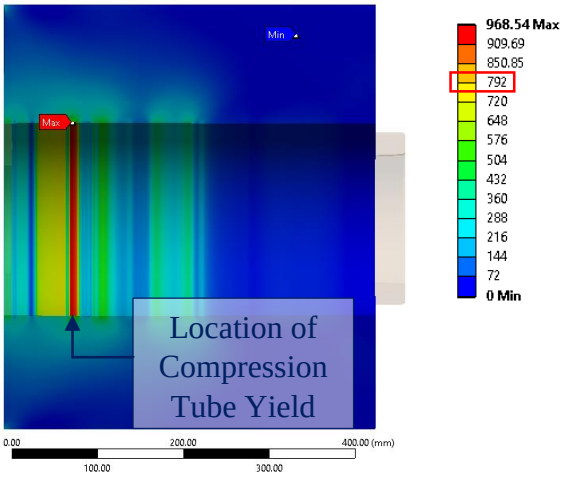
Figure 80 - von Mises stress (MPa) in Piston Body after Impact with the Buffer Plate	Figure 81 - von Mises stress (MPa) in Compression Tube after Piston Impact

As can be seen in Table 8, the numerical solver predicted yielding to have occurred in both the piston body and the compression tube following T4 shot 10509. The maximum von Mises stress in the piston reached 986.26 MPa and its initial compressive yield strength was 280 MPa. Furthermore, the maximum von Mises stress in the compression tube reached 968.54 MPa and its initial compressive yield strength was 792 MPa.

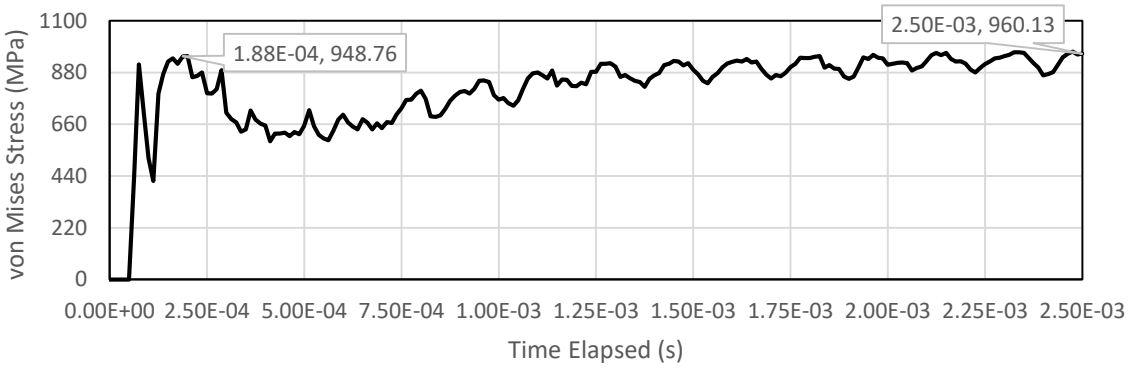

Figure 82 - Maximum von Mises Stress in Compression Tube

Figure 82 was used to determine whether the von Mises stress of the compression tube at an elapsed time of 2.5 milliseconds would be representative of the long-term response or whether the end time of the simulation needed to be extended. The curve in Figure 82 appeared to plateau after 1.5 milliseconds so the von Mises stress at 2.5 milliseconds could indeed be thought of as the long-term response.

Additionally, Figure 83 revealed that the von Mises stress in the piston body plateaud after 1 millisecond and so the elapsed time of 2.5 milliseconds was representative of the long term response.

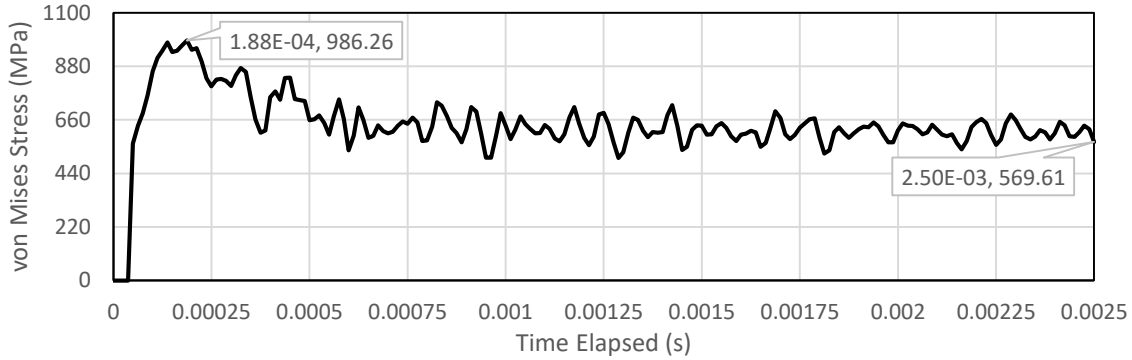

Figure 83 - Maximum von Mises Stress in T4 Piston Body

The yielding of the compression tube seemingly contradicted the technician comments, listed in Section 4.2. While an incorrect selection of material properties could have been the cause of this discrepancy, another likely reason could have been that yielding did occur in the compression tube following T4 shot 10509, however it was not detected during visual inspection. Figure 84 and Figure 85 are used as supporting evidence of this hypothesis.

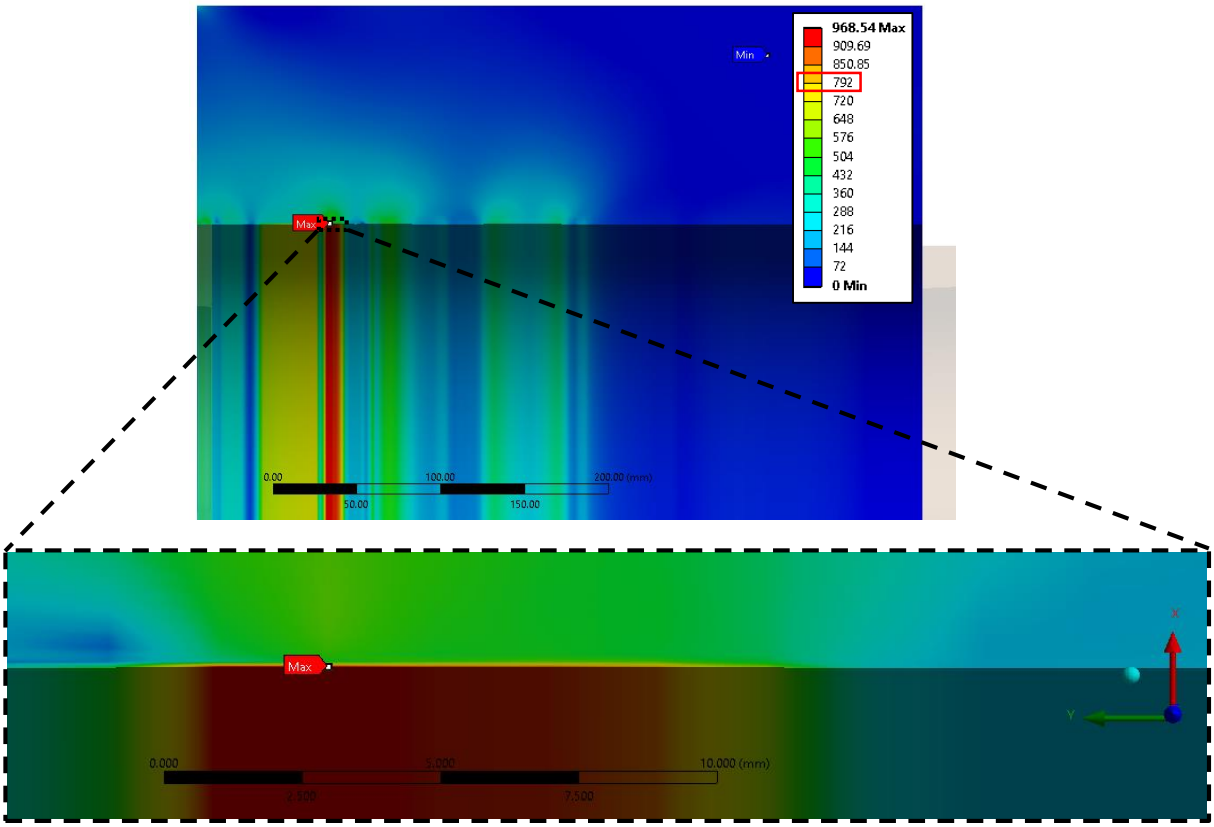

Figure 84 - Width of Yielded Inner Compression Tube Surface

As can be seen in Figure 84, the width of the compression tube in which yielding occured was less than 1 cm.

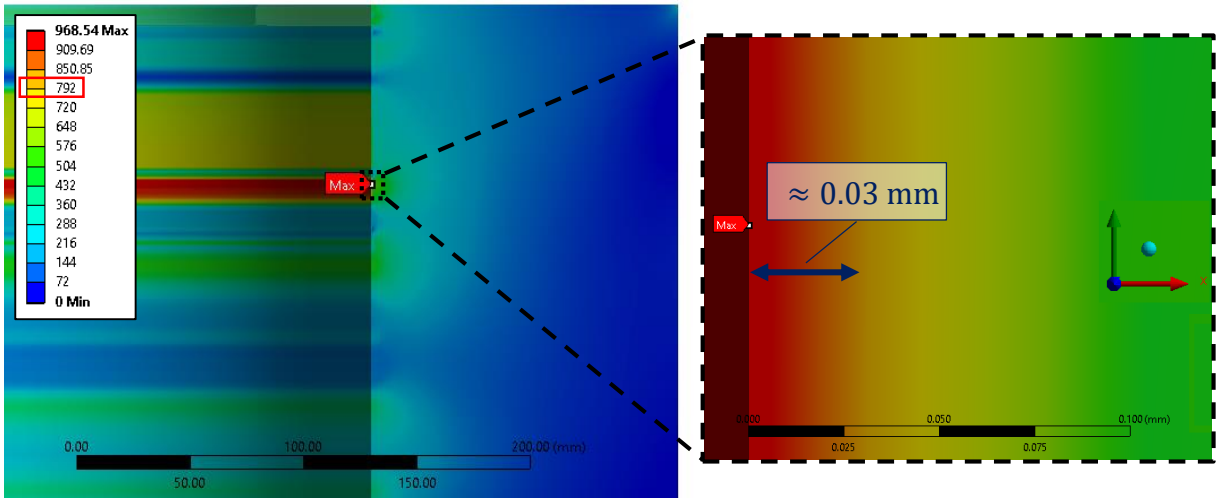

Figure 85 - Depth of Yielded Inner Compression Tube Surface

Furthermore, Figure 85 revealed that the depth of the yielded section of the compression tube was between 0.025 mm and 0.05 mm. The small portion of the compression tube in which yielding occurred would have made it difficult to be determined base off an eye inspection.

4.7 Radial Deformation of Compression Tube for Shot 10509

Figure 86 displays an exaggerated scale view of the radial deformation of the compression tube at a piston impact speed of 61 m/s. The maximum radial deformation of the tube was 0.1562 mm and this occured at 81 mm from the front end of the compression tube. Note that this deformation of 0.1562 mm would have become reduced when the piston was removed from the compression tube as only a depth of 0.025 mm to 0.050 mm was yielded.

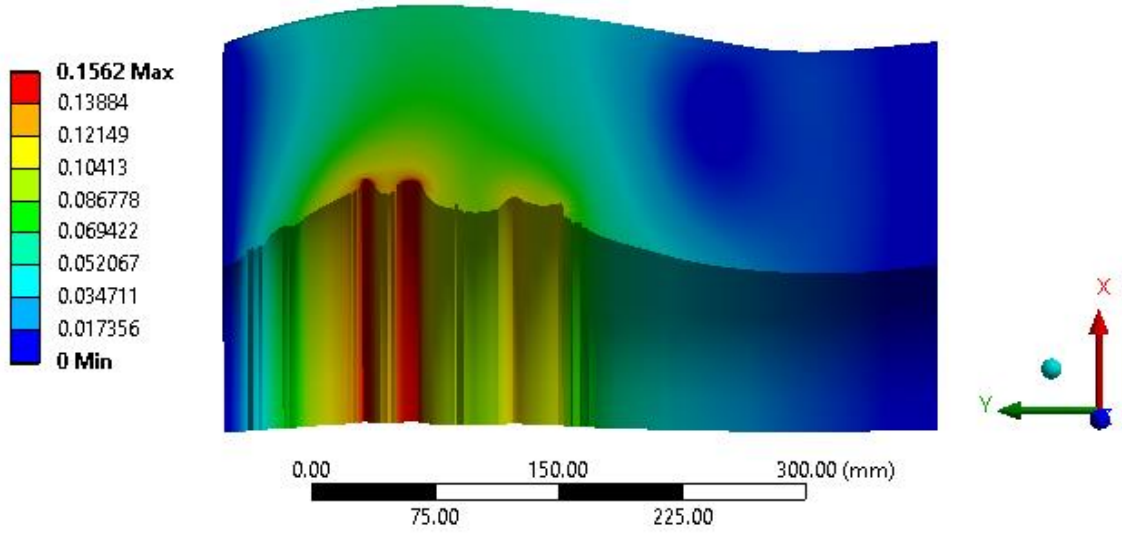

Figure 86 - Radial Deformation of Compression Tube (mm), Piston Impact Speed of 61 m/s, Exaggerated Scale View

The radial deformation of the inner surface of the compression tube can be seen in Figure 87 together with the deformed piston. As shown in Figure 87, the location that results in the maximum radial deformation of the compression tube results from a portion of the piston immediately right of the front wear ring. The second highest radial deformation comes from the front brake shoe.

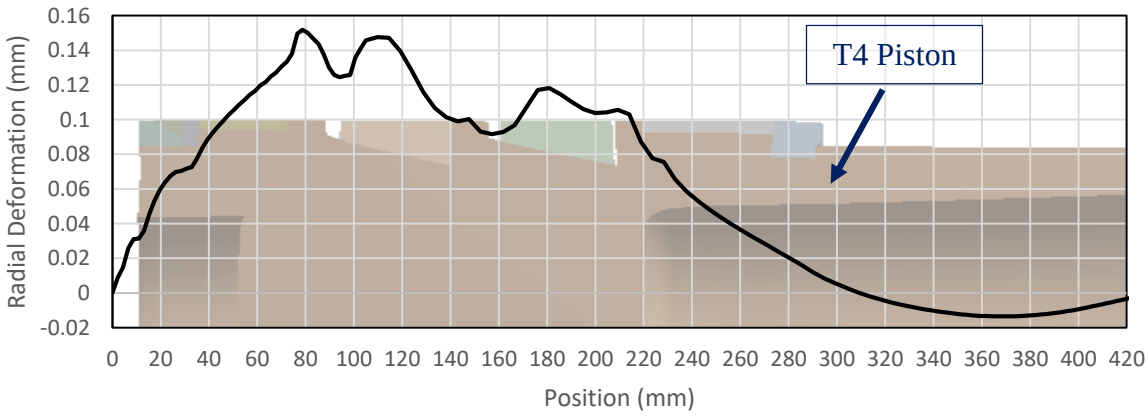

Figure 87 - Radial Deformation of Inner Surface of Compression Tube

4.8 Interference Pressure Analysis of Shot 10509

Figure 88 displays the maximum pressure acting on the inner surface of the compression tube plotted against time for the case where the impact velocity of the piston was 61 m/s.

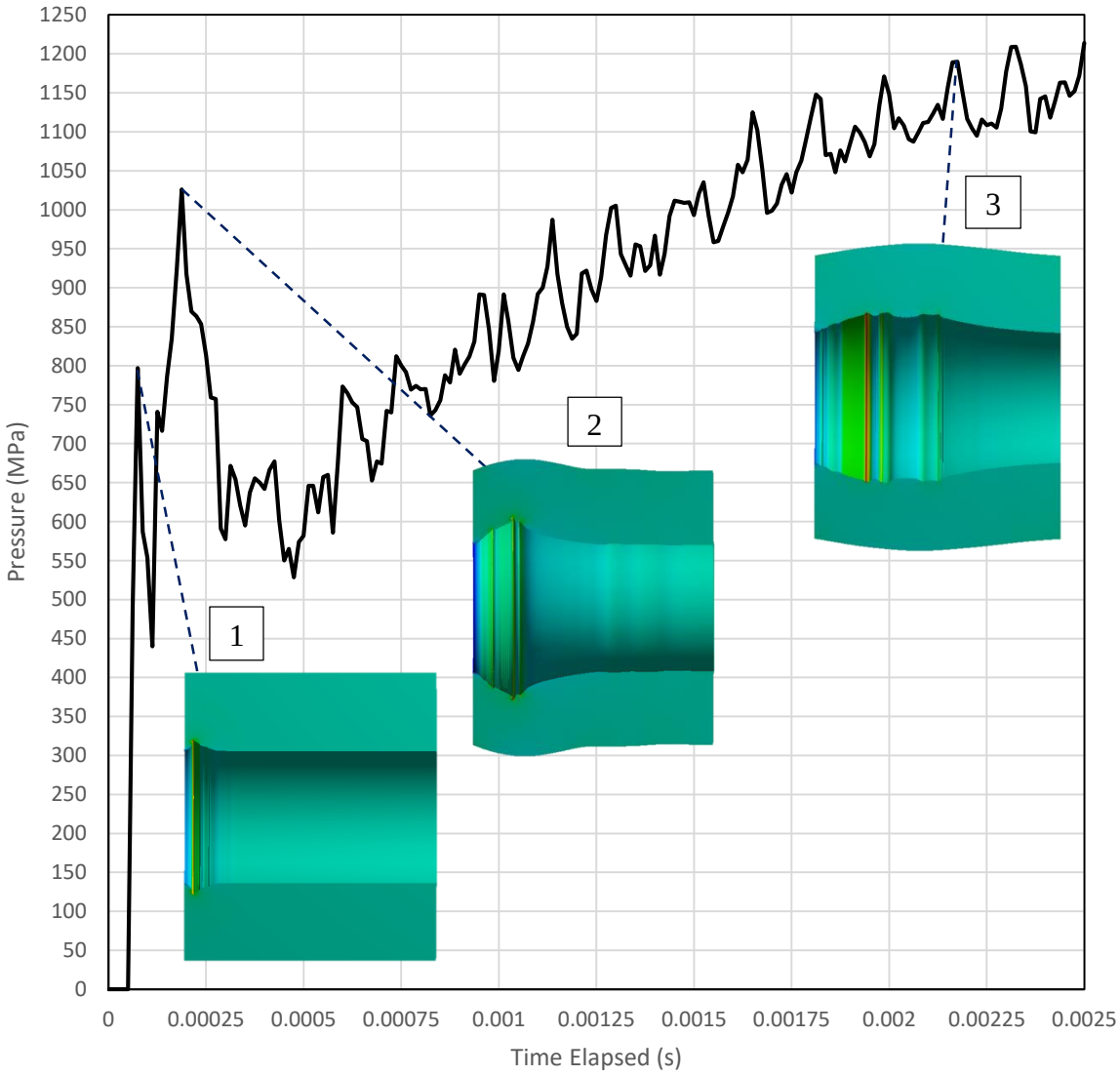

Figure 88 - Maximum Pressure acting on Inner Surface of Compression Tube at a Piston Impact Speed of 61 m/s

The pressure exerted onto the inner surface of the inner surface of the compression tube was proportional to its radial deformation. The maximum radial deformation of the compression tube, just as the piston collided into the buffer plate, was located between the piston holder and the compression tube. This was marked as point 1 in Figure 88. This impact produced a stress wave which travelled through the piston thus causing further radial deformation along the length of the piston. This was shown as point 2 and point 3 in Figure 88. The maximum

interference pressure acting on the inner surface of the compression tube came out to be 1214 MPa at an impact speed of 61 m/s.

4.9 Impact of Friction on Radial Deformation of Tube

The static and kinetic friction coefficients for the piston, piston accessories and compression tube are displayed in Table 9.

Table 9 - Defining Frictional Contact for the T4 (UCF Physics, 2016)

Contacts	Contacting Materials	Coefficients of Static Friction	Coefficients of Kinetic Friction
Rear Brake Shoe and Piston Body	Lubricated Aluminium on Steel	0.1	0.1
Front Brake Shoe and Piston Body	Lubricated Aluminium on Steel	0.1	0.1
Holder and Compression Tube	Aluminium on Steel	0.61	0.47
Front Wear Ring and Compression Tube	Rubber on Steel	1	0.5
Load Ring and Compression Tube	Aluminium on Steel	0.61	0.47
Piston Body and Compression Tube	Steel on Steel	0.74	0.57
Rear Wear Ring and Compression Tube	Rubber on Steel	1	0.5
Retainer Ring and Compression Tube	Plastic on Steel	0.3	0.1
Front Brake Shoe and Compression Tube	Aluminium on Steel	0.61	0.47
Rear Brake Shoe and Compression Tube	Aluminium on Steel	0.61	0.47

As discussed in Section 2.9, setting the kinetic friction to zero was recommended for crash simulations where results would be susceptible to noise. In this case, only the static friction was used. For the purposes of determining the sensitivity of results to the friction

coefficients, an upper and lower limit was applied to the T4 simulation for a piston impact speed of 61 m/s. The resulting radial deformation of the inner surface of the compression tube with frictionless contacts, lower limit friction coefficients and upper limit friction coefficients can be seen in Figure 89.

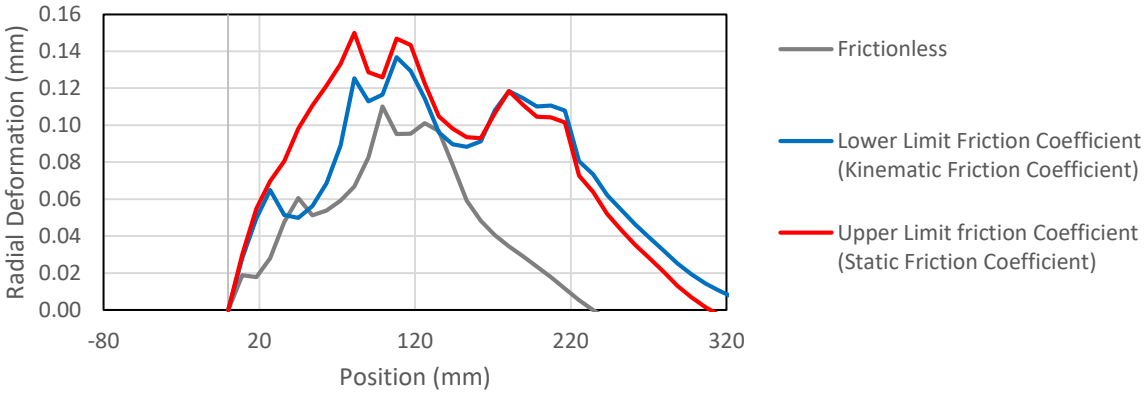

Figure 89 - Impact of Friction Coefficient on Radial Deformation of Inner Surface of Compression Tube

Using the upper limit (static) friction coefficient was a conservative selection for conducting the yield failure analysis of the compression tube as it resulting in the greatest deformation. Nonetheless, the lower limit friction coefficient response closely matched the upper limit friction coefficient except during position between 27 mm to 81 mm. This can be attributed to the fact that the friction coefficient for the holder, chevron seal and load ring changes significantly between the upper and lower friction coefficient limits. The energy error during the simulations was found to be below 10% thus removing the concerns that Section 3.4.5 introduced.

4.10 Varying Piston Impact Speeds

Figure 90 displays the maximum effective (von Mises) stress in the compression tube at impact speeds of 25 m/s, 50 m/s, 61 m/s, 85 m/s and 100 m/s. As can be seen in Figure 90, the impact speed of 25 m/s resulted in no yielding of the compression tube at all. However, at double this speed at 50 m/s, the effective stress response against time came close to the effective stress response against time at an impact speed of 100 m/s. The difference being an effective stress of approximately 150 MPa larger for the 100 m/s impact speed and an end response time that is approximately 0.5 milliseconds quicker. The maximum effective stress that was reached at an impact speed of 100 m/s was 1059 MPa.

These results demonstrated that the effective stress in the compression tube was not very sensitive to the impact speed (within limits) so confidence could be attained in using the estimated impact speed of 61 m/s to numerically replicate T4 shot 10509.

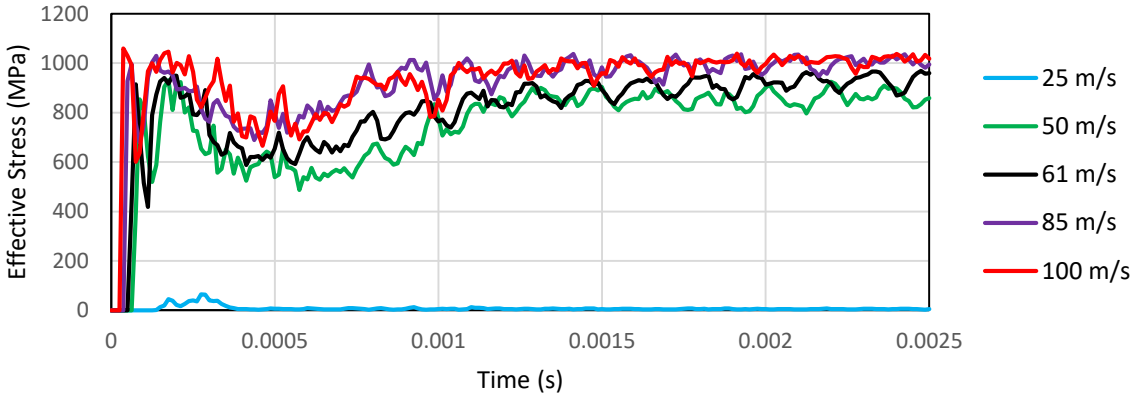

Figure 90 - Maximum Effective (von Mises) Stress in Compression Tube at Differing Piston Impact Speeds

Figure 91 revealed that the maximum effective (von Mises) stress in the piston body at impact speeds of 25 m/s, 50 m/s, 61 m/s, 85 m/s and 100 m/s. Again, the impact speed of 25 m/s results in no yielding of the piston but at double this speed at 50 m/s, the effective stress response against time comes close to the effective stress response against time at an impact speed of 100 m/s. That is, the range in the effective stress was between 800 to 1000 MPa at the end time. The same differences in the effective stress response against time for the piston was observed with the effective stress response against time for the compression tube.

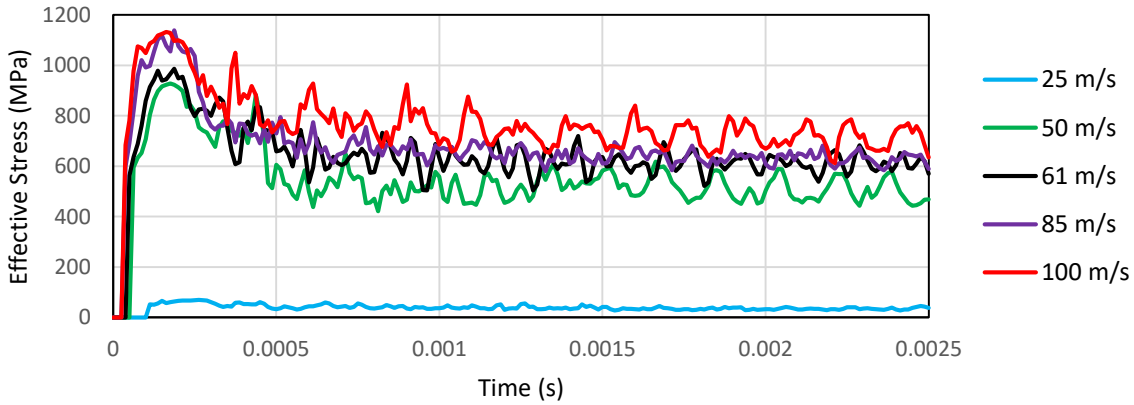

Figure 91 - Maximum Effective (von Mises) Stress in Piston Body at Differing Impact Speeds

Figure 92 shows the depth of yielding of the compression tube at higher impact speeds than 61 m/s. See Figure 85 for section location on the compression tube for the case where the piston impact speed was 61 m/s. As shown in Figure 92, the depth of yielding of the compression tube at impact speeds above 61 m/s revealed no evident change at impact speeds of 85 m/s and 100 m/s. While the depth did not change, the intensity of the effective stress did increase with an increase in the impact speed as would be expected.

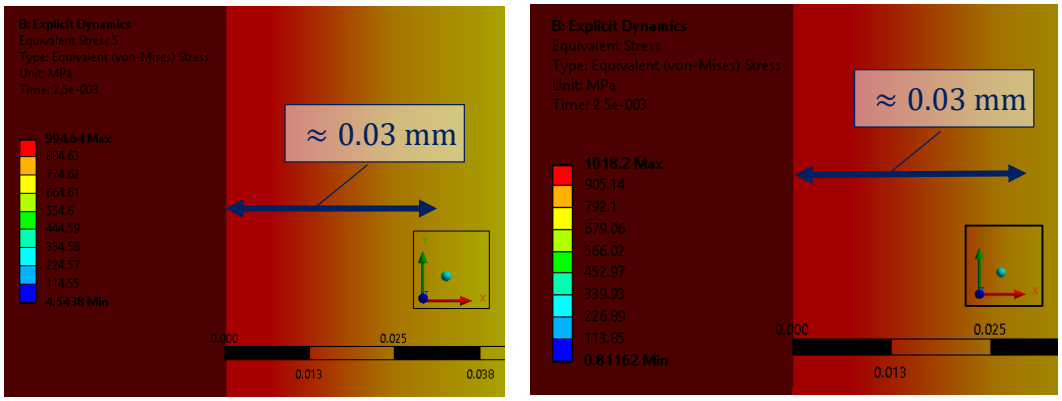

Figure 92 - Depth of Yield of Compression Tube at Piston Impact Speed of 85 m/s (Left) and 100 m/s (Right)

The increase in the effective stress of the compression tube can be explained by Figure 93. As the impact speed increased beyond 61 m/s, the radial deformation of the compression tube also increased thus resulting in a greater normal stress acting on the inner surface of the compression tube. An impact speed of 25 m/s resulted in no permanent radial deformation of the compression tube but at an impact speed of 100 m/s, the maximum radial deformation of the compression tube was 0.27 mm.

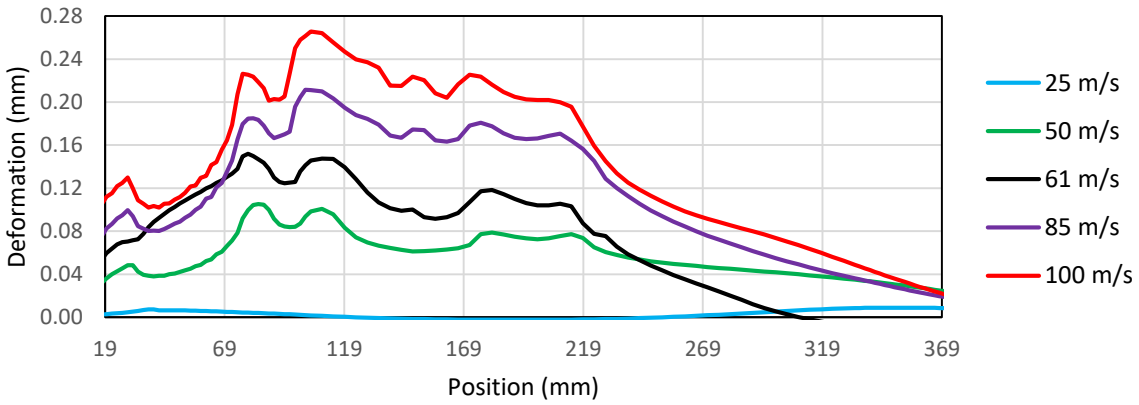

Figure 93 - Radial Deformation of Compression Tube at Varying Piston Impact Speeds

As shown in Figure 94, the pressure difference between the 50 m/s impact speed and 100 m/s impact speed was 636 MPa at the end response time of 2.5 milliseconds. Hence, while the change in impact speed between 50 m/s and 100 m/s did not result in significant changes to the von Mises stress acting on the compression tube, there was a large difference to the pressure acting on the inner surface of the compression tube as the impact speed was increased. This was because the necessity for radial expansion of the piston increased as the impact speeds increased but since the compression tube attempted to prevents this, it experienced larger contact pressures. The impact speed of 25 m/s resulted in no permanent deformation of the piston and so there was minimal pressure acting on the piston which would be caused due to vibrations that would eventually disappear with time.

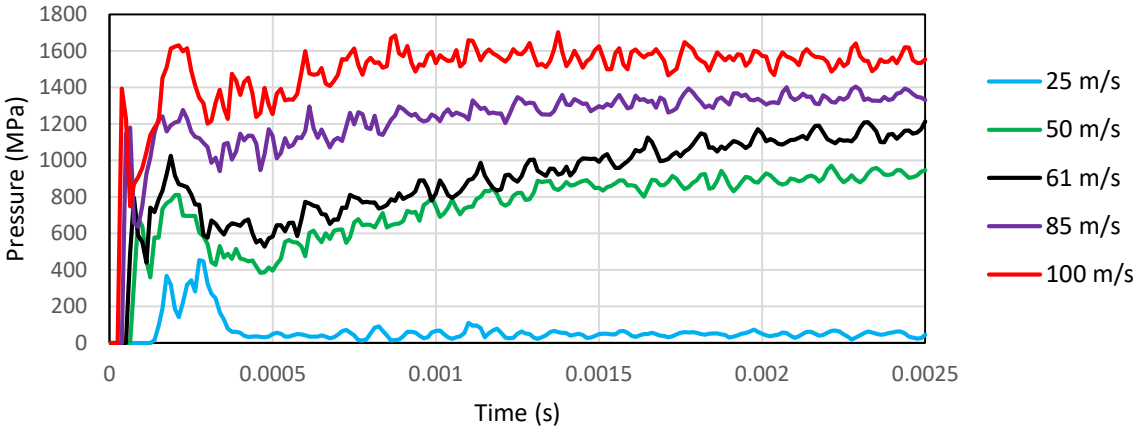

Figure 94 - Pressure Acting on Inner Surface of Compression Tube at Varying Piston Impact Speeds

4.11 Exploring Differing Material Properties

Figure 95 explores the effect that changes in material properties of the piston and the compression tube have on the radial deformation of the inner surface of the compression tube at an impact speed of 61 m/s.

Changing the material properties of the compression tube to that of 4140 high strength steel (softer compression tube) instead of 4340 high strength steel (nominal material properties) revealed no change in the radial deformation of the inner surface of the compression tube. This highlighted that the material properties of the compression tube had little sensitivity to the end results.

Figure 95 also revealed that changes in the material properties of the piston had a large effect on the end result. A piston body made from 4340 high strength steel (harder piston) compared to a piston body made from 304 stainless steel (nominal material properties) displayed less deformation to the compression tube as it did not expand radially as much.

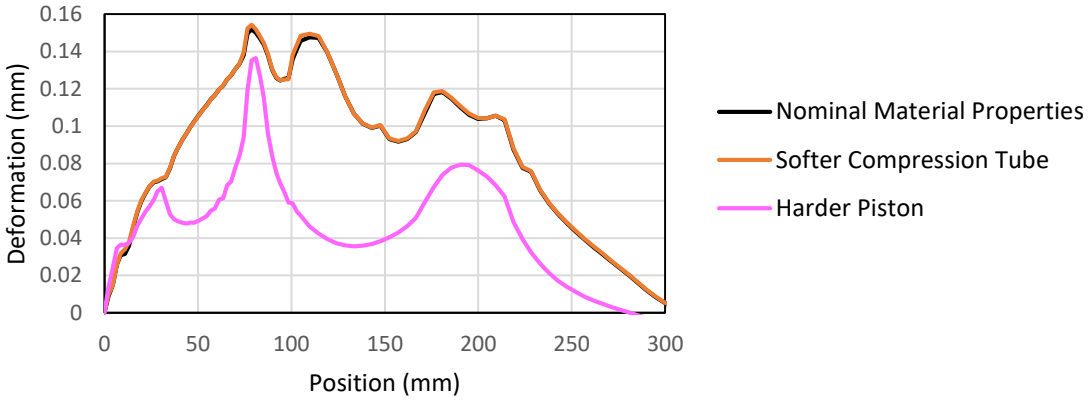

Figure 95 - Radial Deformation of Inner Surface of Compression Tube whilst Varying Material Properties (at Piston Impact Speed of 61 m/s)

The 4340 steel material (harder piston) sustained higher stresses for a given strain compared to 304 stainless steel which was why the effective stress for the harder piston was the highest in Figure 96. Figure 96 also showed that there was no change in the effecive stress response when the compression tube material changed from 4340 steel to 4140 steel.

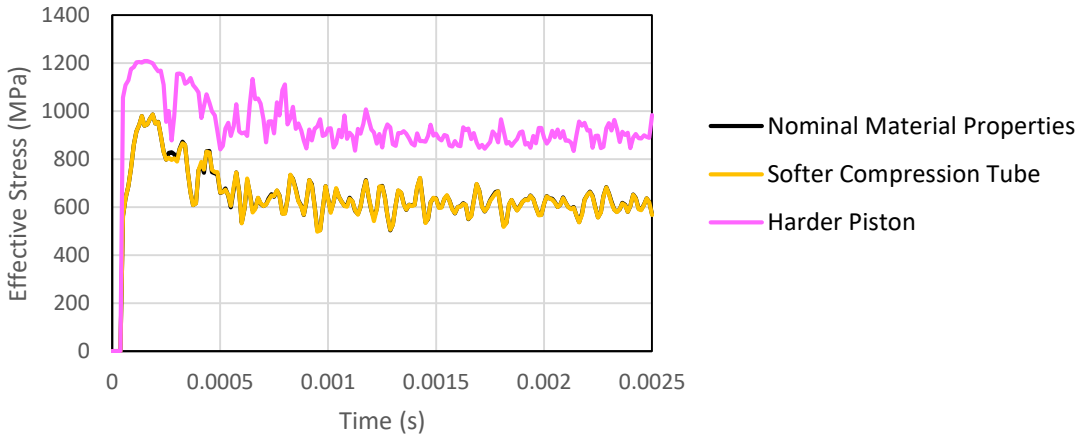

Figure 96 – Maximum Effective Stress in Piston Body whilst Varying Material Properties (at Piston Impact Speed of 61 m/s)

While the radial deformation of the inner surface of the compression tube was reduced when a harder material piston was used, the contact area between the piston and the compression tube was also reduced and so the effective stress increased in the compression

tube. The softer compression tube showed no change to the nominal material properties however.

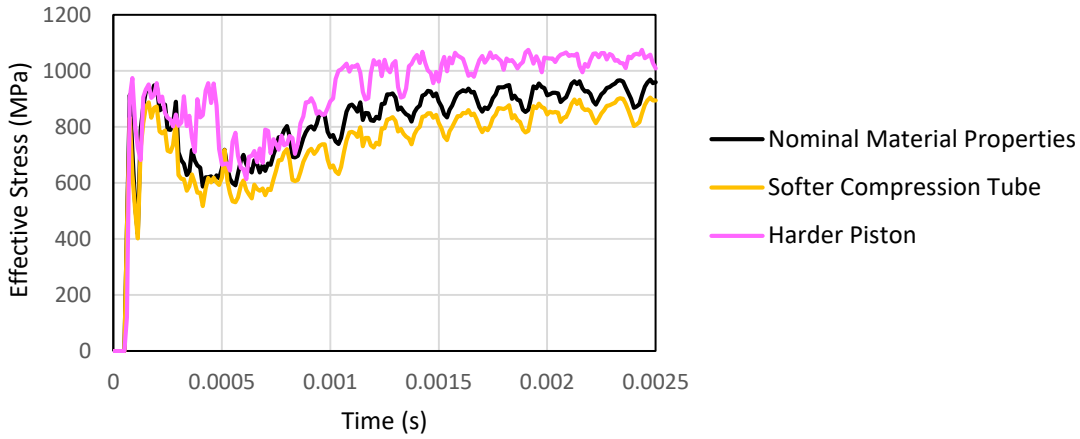

Figure 97 - Maximum Effective Stress (von Mises) Stress in Compression Tube at Impact Speed of 61 m/s

As expected, the pressure acting on the inner surface of the compression tube was also increased when a harder piston was used and the contact area between the piston and the compression tube was subsequently reduced as shown in Figure 98. Again, the softer compression tube displayed no changes to the nominal material properties.

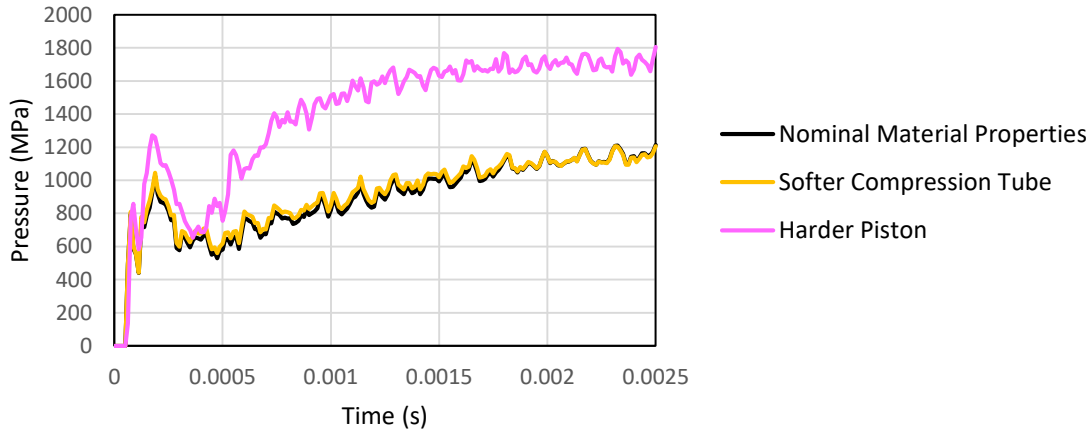

Figure 98 - Pressure along Inner Surface of Compression Tube at Varying Material Properties at Impact Speed of 61 m/s

Figure 99 displays the depth of yielding of the compression tube with varying material properties at an impact speed of 61 m/s. See Figure 85 for section location on the compression tube for the case where the piston impact speed was 61 m/s with nominal material properties. As shown in Figure 99, the depth of yielding of the compression tube with a harder piston or

softer compression tube revealed no evident changes compared to when the nominal material properties were used.

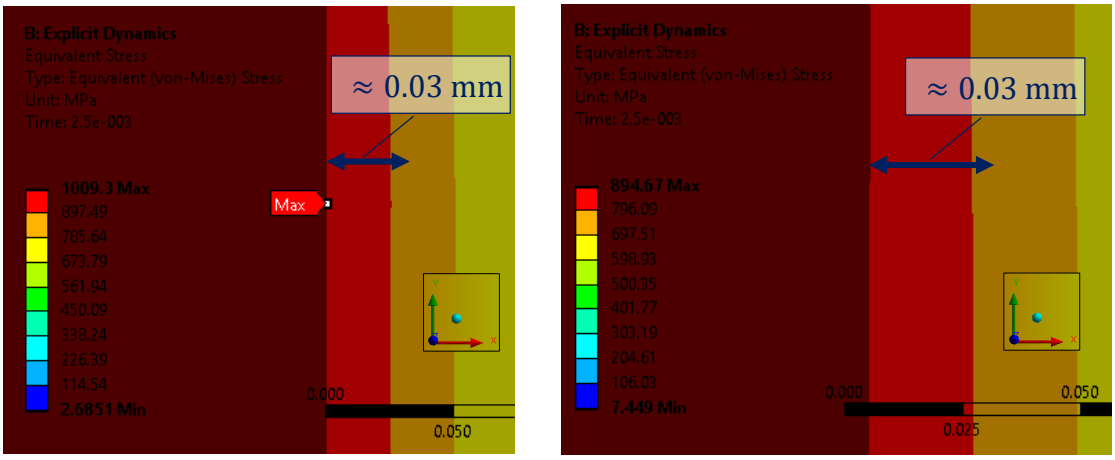

Figure 99 - Depth of Yield of Compression Tube with Harder Piston (Left) and with Softer Compression Tube (Right) at Piston Impact Speed of 61 m/s

4.12 Conclusion

A 2D axisymmetric analysis of the 2009 T4 high speed piston impact was conducted. The estimated impact speed for T4 shot 10509 was found to be 61 m/s. This estimate was obtained using the 1-D Lagrangian CFD code, L1d3. The Johnson-Cook and Linear Shock EOS parameters for 304 stainless steel, aluminium bronze, mild steel and EN25 high tensile steel was obtained through existing literature and was used to model the high strain rates involved in the metal parts of the facility during the piston impact.

The stress analysis of shot 10509 revealed that the piston body and the compression tube did experience yielding following T4 shot 10509. This seemingly contradicted the comments made by the technican that no yielding had occurred in the compression tube following the incident. While it was possible that the reason for this discrepency was because the material data used for the facility was incorrect, another explanation could have been that this yielding was not evident by eye inspection. This was supported by the fact that the width of the yielded portion of the inner compression tube surface was less than 1 cm and the depth of yielding was approximately 0.03 mm.

The maximum radial deformation of the compression tube following T4 shot 10509 was estimated by the solver to be 0.1562 mm. It was noted that this deformation of 0.1562 mm would have diminished signifcantly after the T4 piston was dislodged from the compression tube since the depth of yielding in the compression tube was only 0.03 mm.

It was also found that the pressure exerted onto the inner surface of the compression tube following the radial deformation of the piston (and consequently the compression tube) rose to approximately 1200 MPa following T4 shot 10509.

While the piston impact problem was found to be sensitive to the friction coefficients used to model the friction contact between the parts, the lower and upper limit friction coefficients provided a close enough match to be confident in the results with the friction coefficients that were selected.

At an impact velocity of 25 m/s, no yielding occurred in either the piston or the compression tube. However, when the impact velocity was increased to 50 m/s and above yielding was observed in the compression tube and the piston. It was also noticed that the effective stress in the compression tube and piston between an impact veloicty of 50 m/s and 100 m/s were similar, however the pressure acting on the inner surface of the compression tube continued to show obvious increases as the impact speed increased. This suggested that the effective stress in the compression tube and piston was not very sensitive to error in the estimated impact speed of T4 shot 10509 but that the contact pressure was.

It was found that slight changes to the material properties of the compression tube did not change the effective stress, radial deformation or pressure results. However, changes to the material properties of the piston did. A harder, stronger material used for the piston body resulted in increased von-Mises stress in the compression tube and increased contact pressure.

5 Explicit FEA of X2 Piston

5.1 Chapter Overview

This chapter details the validation of the static linear analysis of two separate load cases acting on X2's new lightweight piston using the AUTODYN solver and high strain rate material data to account for the transient effects involved in the problem. The chapter begins with the material description of X2's new lightweight piston. The discussion then focuses on whether X2's new lightweight piston can be treated as axisymmetric for the purposes of conducting an explicit dynamics analysis of the two load cases investigated. Finally, a dsicussion on the similiarity of results obtained from the static linear and explicit dynamics analysis and the implication of these results to the X3 lightweight piston is presented.

5.2 Material Description for X2 Piston

The X2 lightweight piston can be seen in Figure 100 and the material description for this piston is displayed in Figure 101. Refer to Gildfind (2012) for the X2 lightweight piston drawing set.

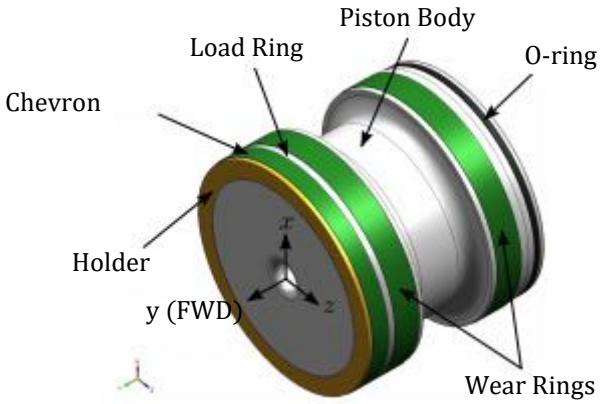

Figure 100 – X2 Lightweight Piston View (Gildfind, 2012)

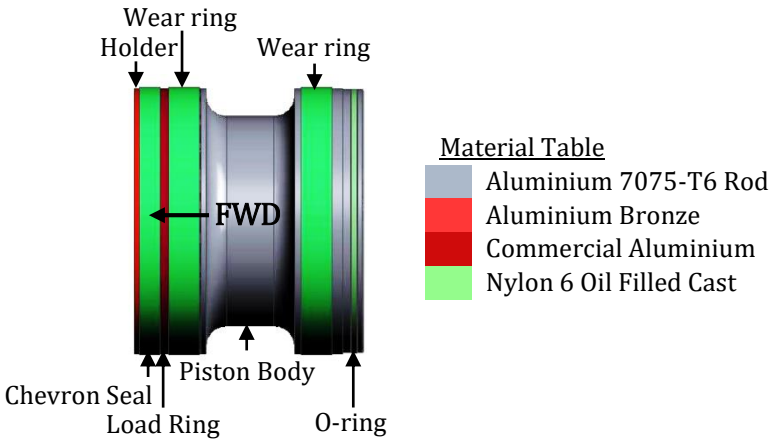

Figure 101 - X2 Lightweight Piston with Material Annotations

The material data for aluminium bronze that was listed in Table 5 in Section 4.4 was used for the holder and load ring on the X2 lightweight piston. The Johnson-Cook and Linear Shock EOS parameters of the aluminium 7076-T6 Rod was sourced from Brar (2009) and Cook et al. (1969). The material data for commercial aluminium was assumed to be the same as 7076-T6 Rod. See Table 10 for material data used for metal parts of the X2 lightweight piston.

Table 10 – Material Data for Metal Parts of X2 Lightweight Piston

Property	**Aluminium 7075-T6 Rod**	**Aluminium Bronze**	**Commercial Aluminium**
Density (kg/m^3)	2804	7450	2804
Specific Heat (J(/kg. °C))	848	410	848
Fitting Parameter A (MPa)	546	430	546
Fitting Parameter B (MPa)	678	904	678
Fitting Parameter n	0.71	0.66	0.71
Fitting Parameter C	0.024	0.016	0.024
Fitting Parameter m	1.56	2.4	1.56
Melting Temperature (K)	908.15	1038	908.15
Reference Strain Rate (/sec)	1	1	1
Shear Modulus (MPa)	26700	27000	26700
Gruneisen Coefficient	2.2	2	2.2
Parameter C1 (m/s)	5200	5328	5200
Parameter S1	1.36	1.338	1.36
Parameter Quadratic S2 (s/m)	0	0	0

The material data listed in Table 10 had signifiance not only to X2's new lightweight piston but also to X3's new lightweight piston since they were both constructed out of aluminium alloy materials. The material data for the nylon wear rings and chevron seal was taken from Table 6 in Section 4.4.

5.3 Axisymmetric Properties of X2's New Lightweight Piston

The axisymmetric geometry of the X2 piston changed since the introduction of the new lightweight piston for the X2 to achieve new free-piston driver conditions (see Figure 102 and Figure 103) (Gildfind, 2012).

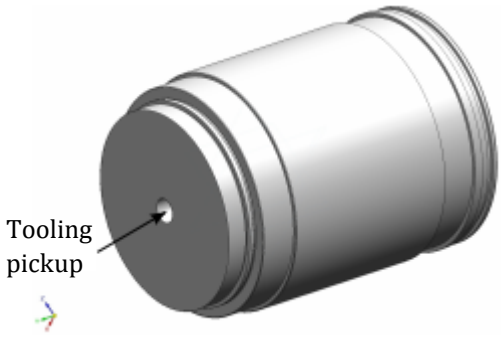

Figure 102 – Old 35 kg X2 Piston (Gildfind, 2012)

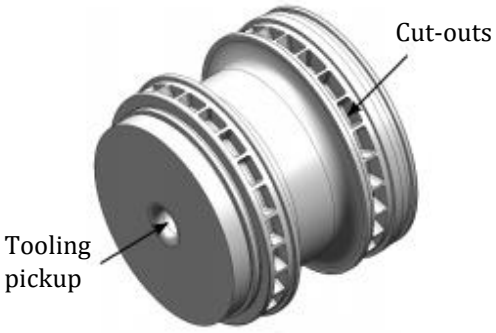

Figure 103 - New 10.68 kg X2 Piston (Gildfind, 2012)

Following this, an axisymmetric model of X2's new lightweight piston was developed and made to impact a rigid wall at 200 m/s to see whether this new piston could be treated as axisymmetric as well. The stress wave propagation through the axisymmetric model was compared to a quarter model of X2's new lighweight piston. A comparison was also made to the final deformation and stress state of the piston. These results can be found in Appendix H. The results shown in Appendix H revealed that X2's new lightweight piston could be treated as axisymmetric despite the cut-outs in the piston body (see Figure 103).

5.4 Numerical Model for Reservoir Pressure Load Case

Using the axisymmetric model of X2's new lightweight piston, the stress analysis from the reservour pressure load case conducted by Gildfind (2012) was reproduced using high strain rate (Johnson-Cook and Linear Shock EOS) material data instead of a linear material model. This was done not only to validate the high strain rate material data for the aluminium alloys involved but also to confirm that X2's new lightweight piston would not yield as a result of the peak reservoir pressure loadings.

As shown in Figure 104, the reservoir pressure load acts along the inside surface of the piston when it sits on the launcher. The maximum reservoir pressure loading for the X2 was stated to be 10 MPa and Gildfind (2012) applied a safety factor of 2 to give the ultimate load, thus making the reservoir pressure loading 20 MPa. This reservoir pressure was applied gradually over a time of 1 millisecond.

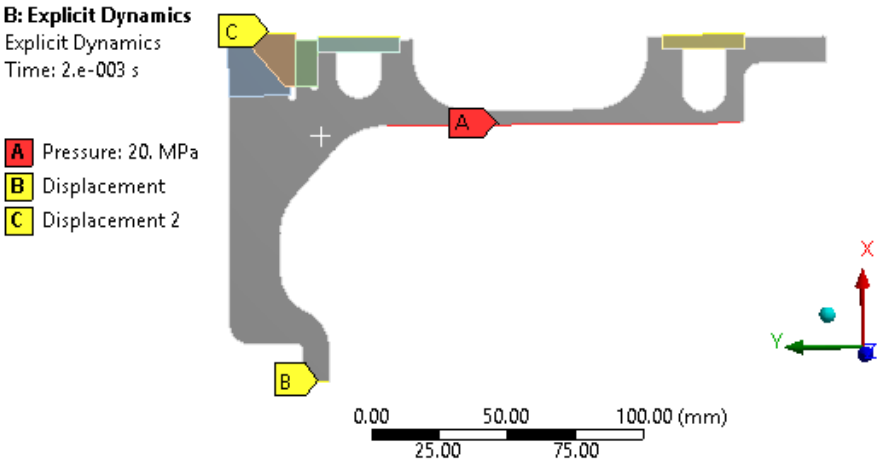

Figure 104 - Loads and Boundary Conditions, 20 MPa Reservoir Pressure Load Case, Exaggerated Scale View

5.5 Results for Reservoir Pressure Load Case

The total deformation of the X2 lightweight piston using a body size mesh of 0.5 mm can be seen in Figure 105. Comapring Figure 105 to Figure 107 it can be observed that a body size mesh of 1 mm was sufficient to achieve mesh independence. Thus, a body size mesh of 1 mm was used for subsequent analyses.

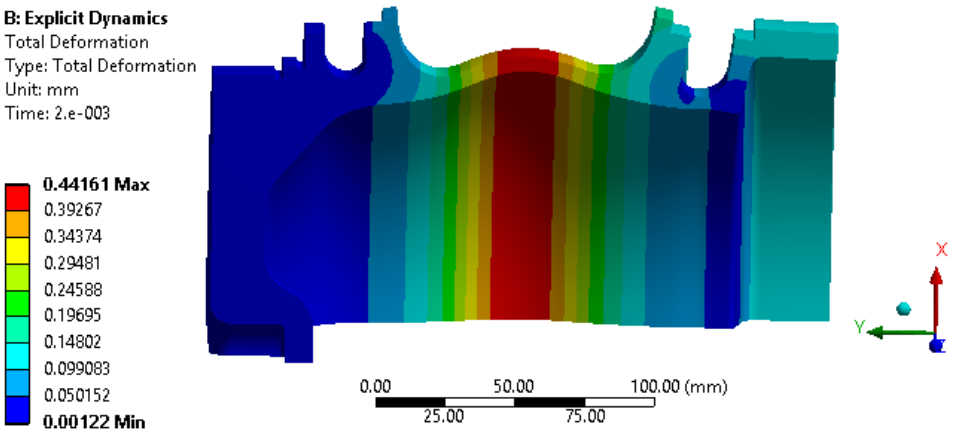

Figure 105 - Piston Deflection (mm), Johnson-Cook Material Model, 0.5 mm Body Size Mesh, 20 MPa Reservoir Pressure

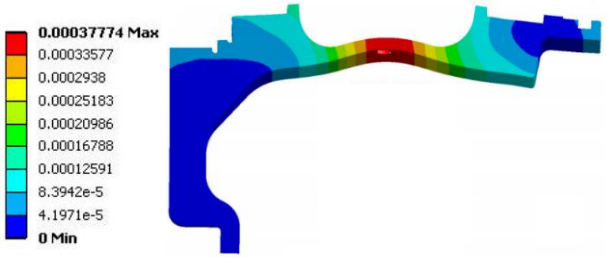

Figure 106 - Piston Deflection (m), Linear Material Model, 20 MPa Reservoir Pressure, Exaggerated Scale View

Figure 107 - Piston Deflection (mm), Johnson-Cook, 1 mm Body Size Mesh, 20 MPa Reservour Pressure, Exaggerated Scale View

Comparing Figure 106 and Figure 107, the piston deflection using the Johnson-Cook material model for the materials result in a difference of 14.83% compared to the linear piston material model. These values do represent the end time response of as shown in Figure 108. In Figure 108, the deformation reached its final end state as soon as the reservoir pressure reached its final value after 1 millisecond.

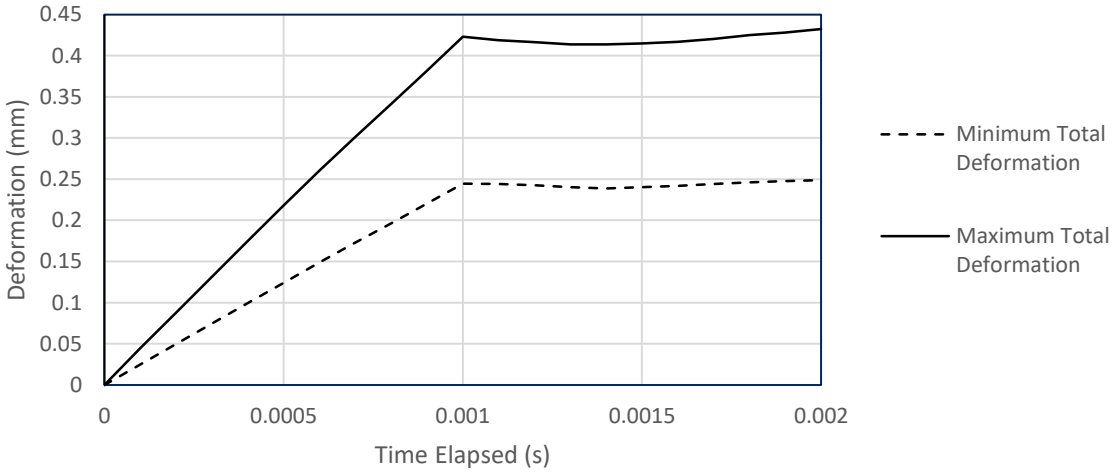

Figure 108 –Total Deformation of X2 Piston (at 20 MPa Reservoir Pressure)

A difference in the maximum von Mises stress distribution between the Johnson-Cook material model and the linear piston material model was also approximately 15% after comparing Figure 109 and Figure 110. Despite the higher maximum von Mises stress when using the Johnson-Cook model, this stress did not exceed the material yield stress of 441 MPa which was the yield stress provided by Gildfind (2012).

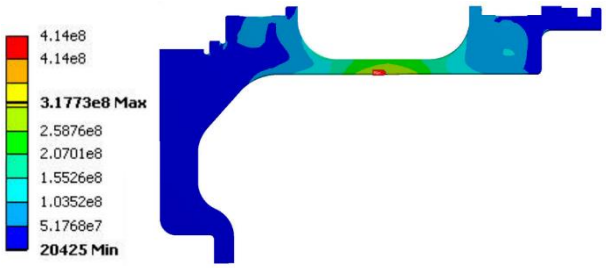

Figure 109 - von Mises Stress Distribution (MPa), Linear Material Model, 20 MPa Reservoir Pressure

Figure 110 - von Mises Stress Distribution (MPa), Johnson-Cook, 1 mm Body Size Mesh, 20 MPa Reservoir Pressure

5.6 Numerical Model for Driver Pressure Load Case

Using the axisymmetric model of X2's new lightweight piston, the stress analysis from the driver pressure load case conducted by Gildfind (2012) was reproduced using high strain rate (Johnson-Cook) material data instead of a linear material model.

As shown in Figure 104, the driver pressure acts on the front face of the piston. The maximum driver pressure loading for the X2 was stated to be 40 MPa and Gildfind (2012) applied a safety factor of 2 to give the ultimate load, thus making the driver pressure loading 80 MPa. This reservoir pressure was applied gradually over a time of 1 millisecond.

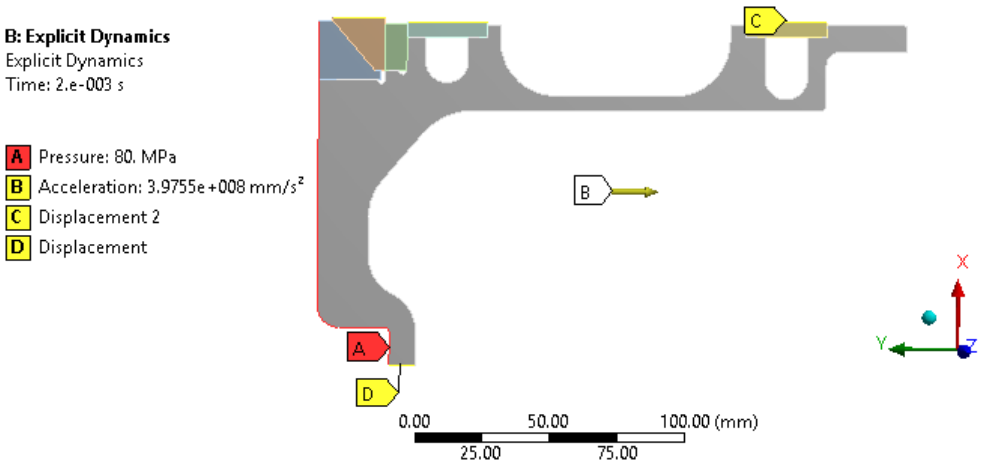

Figure 111 - Loads and Boundary Conditions, 80 MPa Driver Pressure Load Case

5.7 Results for Driver Pressure Load Case

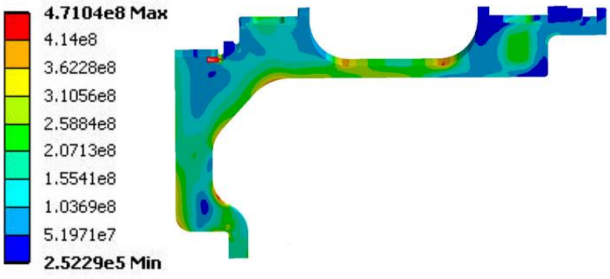

Figure 112 - von Mises Stress Distribution (Pa), Linear Material Model, 80 MPa Driver Pressure

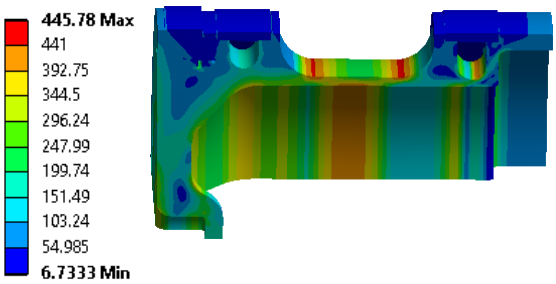

Figure 113 - von Mises Stress Distribution (MPa), Johnson-Cook, 1 mm Body Size Mesh, 80 MPa Driver Pressure

Comparing Figure 112 and Figure 113, the piston deflection using the Johnson-Cook material model for the materials result in a difference of 5.23% compared to the linear piston material model. These values do represent the end time response of as shown in Figure 114. In Figure 114, the deformation reached its final end state as soon as the reservoir pressure reached its final value at 1 millisecond.

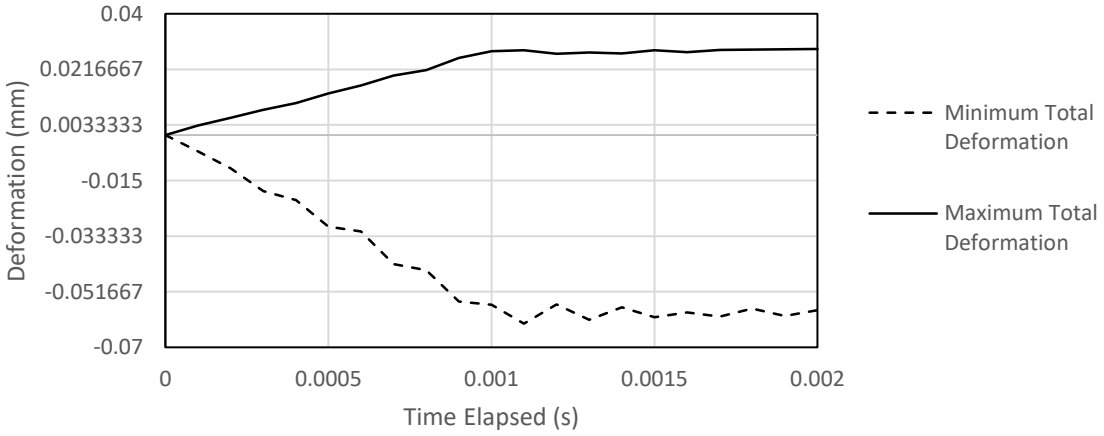

Figure 114 - Total Deformation of X2 Piston (80 MPa Driver Pressure)

As shown in Figure 112 and Figure 113 the driver pressure load case for both the linear material model and the Johnson-Cook material model proved to be critical. Part of the 2 × safety factor applied by Gildfind (2012) was to account for the transient effects that was not being modelled using the implicit method (as opposed to the explicit method) and for the fact that a linear material model was being used. To determine what the stress distribtion would be in the X2 lightweight piston (and whether it would still yield) with no safety factor, the driver pressure load was brought down from 80 MPa to 40 MPa. This is displayed in Figure 115.

Figure 115 shows the effective (von Mises) stress distribution in the X2 piston after a driver pressure of 40 MPa is applied to the piston instead of 80 MPa. In this case, yielding was not predicted to occur which indicated that the safety factor of 2 is unnecessarily high when attempting to account soley for the the transient effects of the system when using the Mechanical APDL solver.

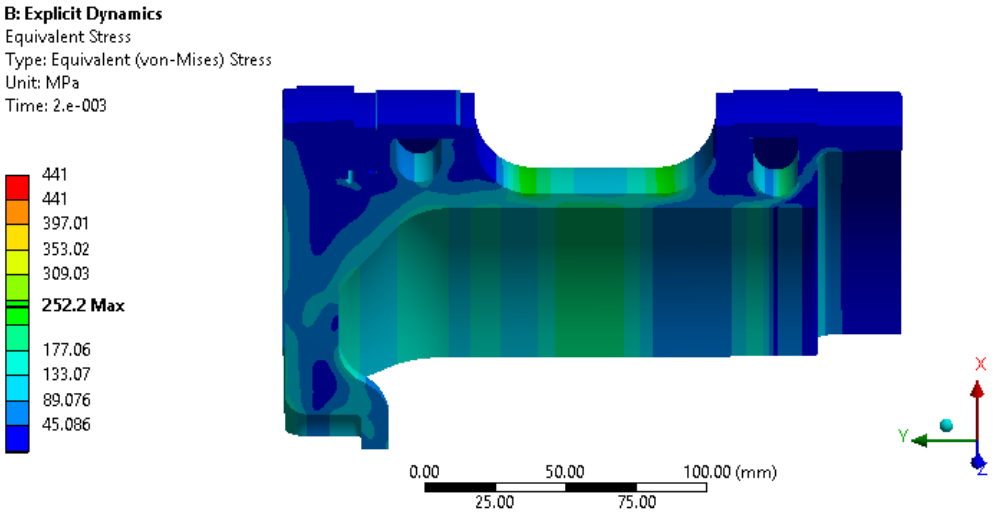

Figure 115 - von Mises Stress Distribution (MPa), Johnson-Cook, 1mm Body Size Mesh, 40 MPa Driver Pressure

5.8 Conclusion

The Johnson-Cook and Linear Shock EOS parameters for aluminium bronze, aluminium 7075-T6 rod and commercial aluminium was obtained through existing literature and was used to model the high strain rates involved in the metal parts of X2's new lightweight piston.

It was also discovered that X2's new lightweight piston could be treated as axisymmetric despite the cut-outs on the piston body. This had significance in that a 2D axisymmetric model could be used to validate the static linear analysis.

The static linear analysis of the peak pressure loadings acting on the X2 piston revealed close agreement with the analysis conducted using the AUTODYN solver and with high strain rate material data implemented. This meant that the high strain rate material data for the X2 piston was validated which could be used for future analysis of X2's new lightweight piston which accounted for transient effects and also X3's new lightweight piston since they shared similar materials.

6 Explicit FEA of Nylon Stud Buffer

6.1 Chapter Overview

The X2 facility and the X3 facility both use nylon studs as buffers as oppossed to the rubber buffer used by the T4. It is known that these nylon stud buffers can be configured to prevent damage to the aluminium piston better than the rubber buffer but a detailed assesment of piston impacts into these nylon studs has not yet been conducted (Gildfind, 2012). Like in the case of the X2 facility, a new lightweight piston for the X3 was developed in order to achieve new high performance tuned free-piston driver conditions. Consequently, instead of having a 200 kg aluminium piston, the mass would be reduced to 99.7 kg, which is much heavier than the 11 kg X2 lightweight piston (Gildfind, 2012). This chapter presents the analysis of the X3 lightweight piston impacting into the nylon studs in order to determine whether the nylon studs can tolerate an impact speed of 30 m/s from X3's lightweight piston. The chapter also presents a discussion on the effect that the length of the nylon studs and the strain rate in the studs (due to impact) have on the numerically predicted deformation and effective stress in these studs.

6.2 Material Description for Nylon Stud Buffer

As stated in Section 2.6.3, the Johnson-Cook material model does not capture the stress-strain curves of polymers accurately. Instead, a bilinear material model was used to model these nylon studs out of simplicity. This involved estimating the range of strain rates which the nylon studs would experience from a piston impact speed of up to 30 m/s. To do this the nylon material data in ANSYS Workbench Engineering Library was utilised and an axisymmetric model of the X3 piston impacting the nylon stud buffer was conducted.

To conduct this axisymmetric model, three key modelling techniques were implemented. This included dividing the mass of the piston by twelve given that there were twelve nylon studs in the X3 buffer. This assumed that the load from the piston was divided equally to each stud. Secondly, the geometry of the X3 piston was simplified down to a cylinder which had a sufficiently larger diameter than the stud to prevent the nylon stud from wrapping around the piston. See Appendix I for details of these two modelling techniques. Lastly, the piston and the floor were modelled as rigid as it was assumed the aluminium piston would not deform much relative to the stud. In this case, only the density was an important material property. A density of 2800 kg/m^3 was used for the aluminium piston. See Figure 116 for a picture of the problem being solved.

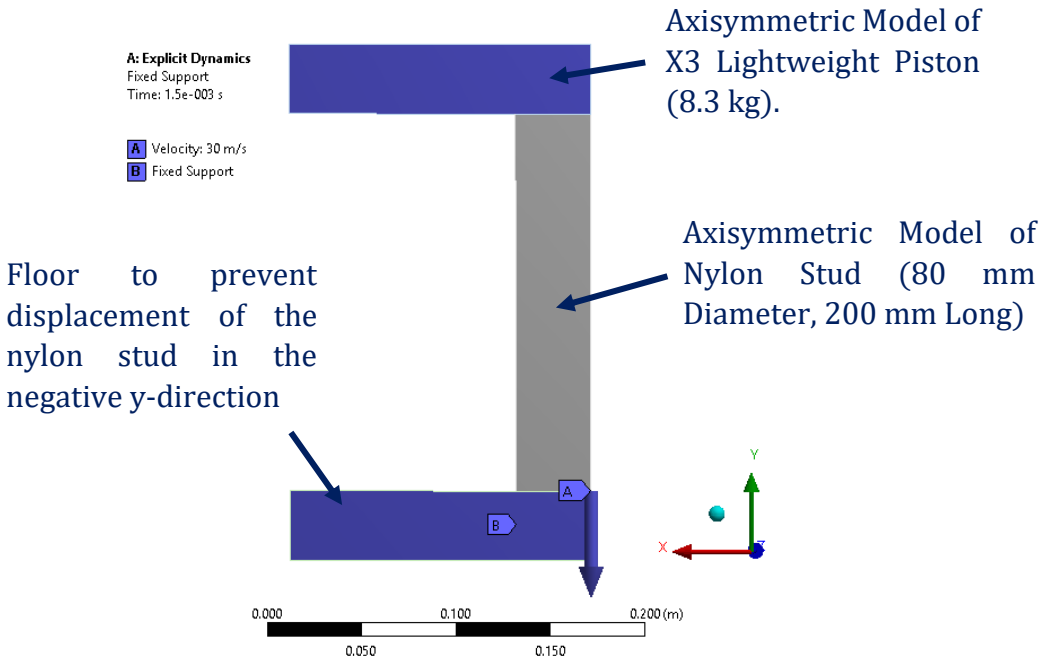

Figure 116 - Axisymmetric Model of X3 Lightweight Piston Impacting Nylon Stud at 30 m/s

A mesh size of 1 mm for the nylon stud was used, and as shown in Appendix I, this did achieve mesh independence of the nylon stud at an impact speed of 30 m/s.

The impact speed of the X3 lightweight piston varied from 15 m/s to 30 m/s in 5 m/s increments. The strain rate results obtained from this are displayed in Figure 117.

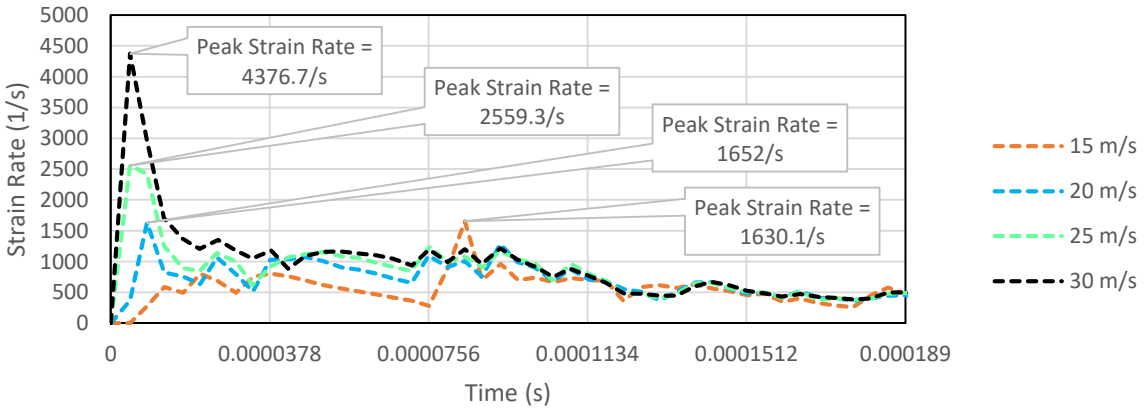

Figure 117 - Strain Rate in Nylon Stud at Varying Piston Impact Speeds

The peak strain rates experienced by the nylon studs from an impact speed of 15 m/s to 30 m/s varied between 1630.1/s to 4376.7/s. The strain rate then dropped to approximately 750/s at which point remained more or less steady and then after some time it died down to a strain rate of zero. A material model which can accounted for the strain rates in this range was needed to model the nylon studs for impact speeds between 15 m/s and 30 m/s.

The material data for nylon at this estimated strain rate range was sourced from Pouriayevali (2013). The response of nylon under dynamic compression was presented by Pouriayevali (2013) as true stress-engineering strain which was changed to true stress-true-strain as shown in Figure 118 before implementing the data into the numerical solver.

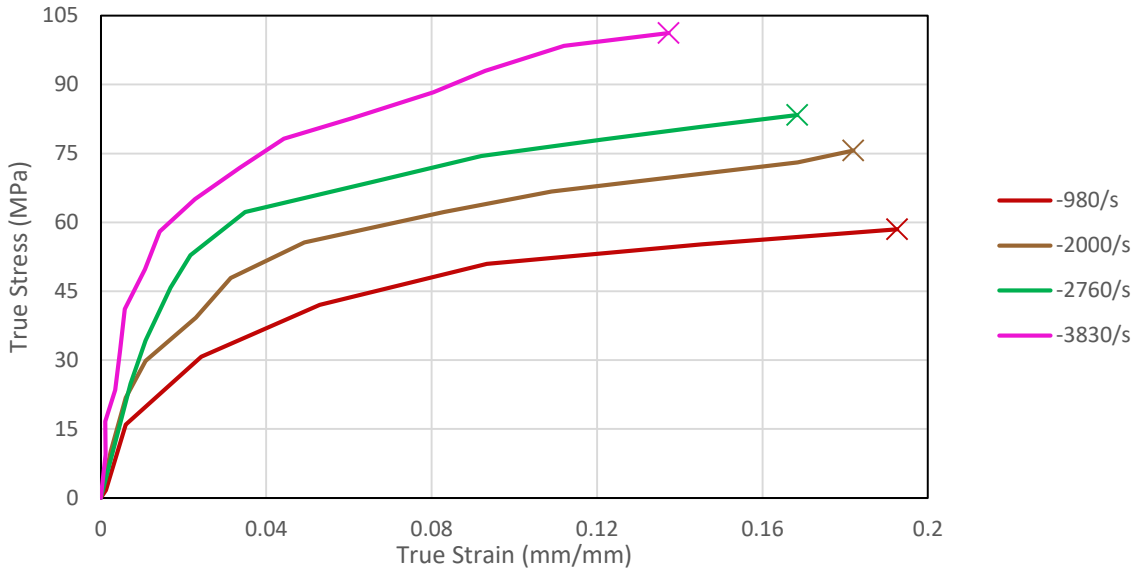

Figure 118 - Response of Nylon Under Dynamic Compression at Varying Strain Rates (Adapted from Pouriayevali, 2013)

The material properties for the bilinear material model was obtained from Figure 118. See Appendix J for the methodology adopted in determining these material properties.

Table 11 - Bilinear Material Model Data for Nylon at Different Strain Rates

Strain Rate	Yield Stress (MPa)	Young's Modulus (MPa)	Tangent Modulus (MPa)
-980/s	45	3000	78.26
-2000/s	48	4000	200.4
-2760/s	60	4286	205.4
-3830/s	68	6800	288.2

It can be seen from Table 11, that as the strain rate increased in magnitude, the yield stress, Young's modulus and Tangent modulus of the nylon material all increased with an increase in the strain rate magnitude. As such, the response of the nylon stud increasingly lied in the pre-yield region and the material could be thought of as behaving more brittle.

The density of 1140 kg/m^{-3} was kept from the material model of nylon that already existed in the Engineering Data library in ANSYS Workbench (Matuska, 1984). The poison's ratio for Nylon was taken to be 0.36 (Perepechko, 2013).

6.3 Compression Analysis of Studs at Varying Impact Speeds

Depending on the severity of compression of the nylon studs, there existed the potential for the nylon studs to come into contact with each other and also for contact to be made with the inner walls of the compression tube during deformation. In this case, the nylon studs would become constrained from deforming radially and the stiffness of the nylon studs would increase by orders of magnitude since further displacement would be required for actual volumetric reduction, as opposed to plastic redistribution (Gildfind, 2010).

The model displayed in Figure 119 was a similar model to that shown in Figure 116 in that the same fixed support was applied to the rigid floor surface and the same dimensions of the nylon studs were used. The difference was that Figure 119 was a quarter model of the X3 piston colliding into the nylon studs (instead of an axisymmetric model). Refer to Gildfind (2012) for the X3 lightweight piston drawing set. This quarter model was reflected about the Y-axis, the compression tube was made hidden and modelled as rigid as minimal deformation would be expected to result from the impact as shown in Chapter 4.

This figure revealed that the maximum compression of a 200 mm long nylon stud at an impact speed of 30 m/s was 16.14 mm. The radial distance between the centre point of the studs and the centre point of the backing plate was 195 mm. At this impact speed and nylon stud length, the studs were far from coming into contact with one another. This indicated that an axisymmetric analysis of the studs would be suitable.

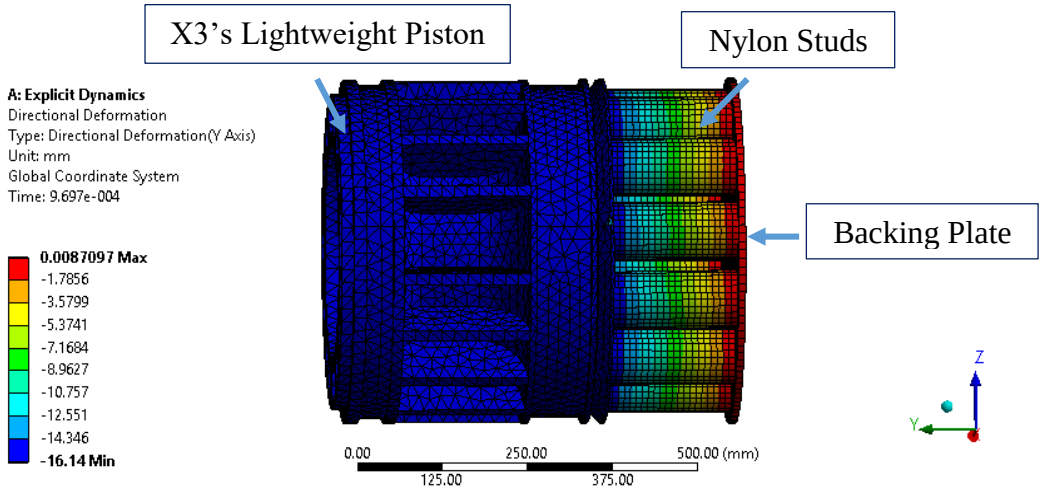

Figure 119 – Quarter Model of X3 Lightweight Piston Impacting Nylong Stud Buffer at 30 m/s

Figure 120 reveals the deformation of the 200 mm long nylon stud using the axisymmetric model shown in Figure 116 and a 3D model shown in Figure 120.

As shown in Figure 120, increase in the impact speed from 15 m/s to 30 m/s for the 200 mm nylon stud increased the compression of the nylon stud by at least 7.1 mm depending on what strain rate was being considered. When the impact speed was 30 m/s and a strain rate of -3830/s was considered, the maximum compression was 10.8 mm. However, at a lower strain rate of -980/s, this maximum compression increased to a little over 14.4 m/s which indicated that at lower strain rates, the maximum compressions of the nylon stud would be higher. At an impact speed of 15 m/s, compressions below 2 mm revealed little to no difference between the -980/s and -3830/s strain rates. When the impact speed was increased to 30 m/s, the compressions below 6 mm revealed little to no difference between the -980/s and -3830/s strain rates.

This same analysis was conducted for a stud length of 300 mm instead of 200 mm. The results for this is shown in Figure 121.

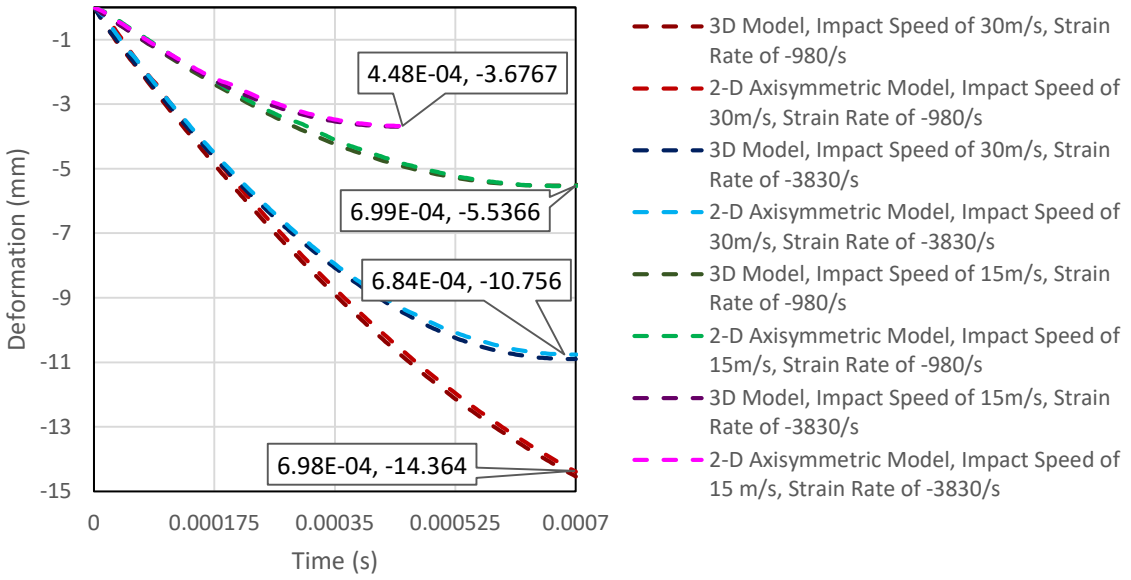

Figure 120 - Deformation of 200 mm Long Nylon Stud at Varying Impact Speeds and Strain Rates

The results for the 300 mm nylon stud (displayed in Figure 121) revealed similarity within 1 mm of compressive deformation between the 15 m/s and 30 m/s impact speeds. An increase in the impact speed from 15 m/s to 30 m/s increased the compression of the nylon stud by at least 7.2 mm depending on what strain rate was being considered. When the impact speed was 30 m/s and a strain rate of -3830/s was considered, the maximum compression was 11.5 mm. However, at a lower strain rate of -980/s, this maximum compression increased to a little

over 14.6 m/s. At an impact speed of 15 m/s, compressions below 2 mm revealed little to no difference between the -980/s and -3830/s strain rates. When the impact speed was increased to 30 m/s, the compressions below 6 mm revealed little to no difference between the -980/s and -3830/s strain rates.

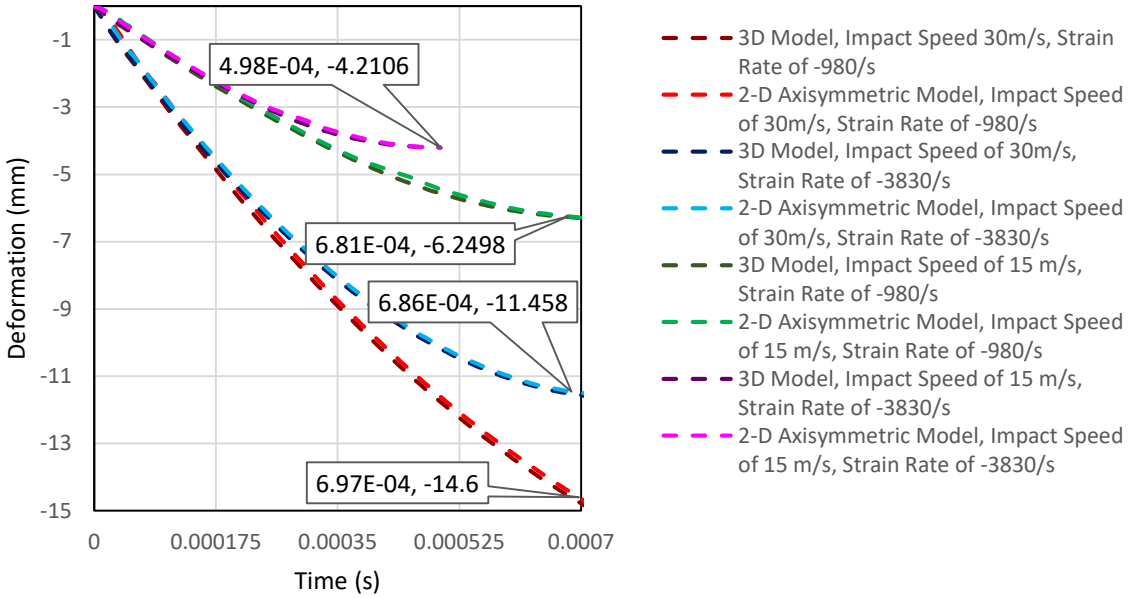

Figure 121 - Deformation of 300 mm Long Nylon Stud at Varying Impact Speeds and Strain Rates

The results displayed in Figure 120 and Figure 121 revealed near-identical matches between the 2D axisymmetric model and the 3D model. Furthermore, it was observed during the numerical simulations that there existed symmetric stress distributions throughout the nylon stud at the impact speeds investigated which further supported the validity of a 2D axisymmetric model over a 3D model (for use in future work in these simulations to reduce the run times).

Figure 122 revealed that the compressive deformation of the nylon studs was only slightly effected by a change in the nylon stud length between 200 mm and 300 mm. The sensitivity of the results between these two figures are however much higher to changes in strain rate. A larger strain rate meant a lower maximum longitudinal compression of the nylon studs.

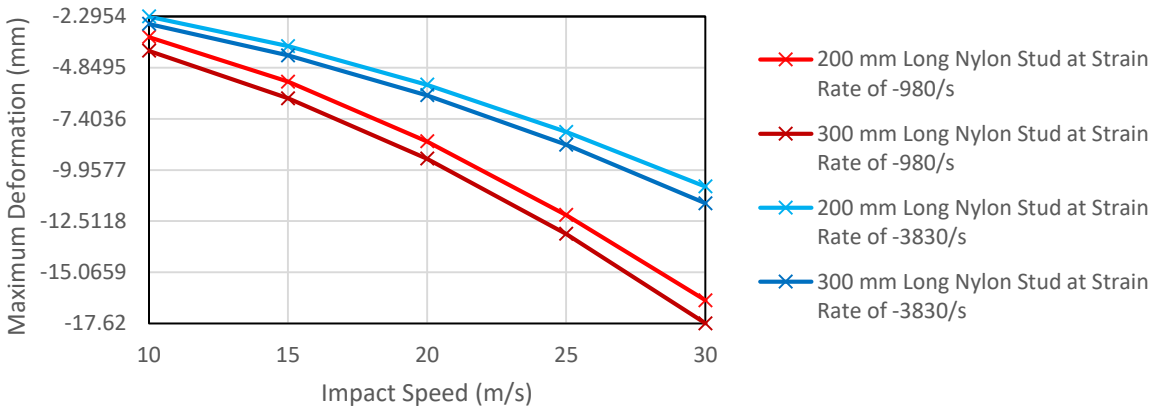

Figure 122 - Maximum Compression of Nylon Studs at Varying Impact Speeds, Strain Rates and Stud Lengths

6.4 Velocity Loss Analysis of X3 Piston Following Impact

As shown in Figure 123, the highest impact speed investigated of 30 m/s was sufficient to bring the piston to a velocity of zero after 1.3 milliseconds. Furthermore, when the impact speed was reduced, the piston was brought to a velocity of zero quicker which agreed with theory since the piston had less kinetic energy to dissipate. This was done using a 2D axisymmetric model. Figure 123 also revealed that the 3D model for an impact speed of 30 m/s and constant strain rate of -980/s, which was labelled as 'Actual' in Figure 123, displayed close agreement to the axisymmetric model equivalent. However, there was more "noise" present in the 3D model since the piston was not modelled as rigid in this case but rather using the material data for 'aluminium 7075-T6 rod' listed in Table 10 in Section 5.2. Mesh independence for the X3 piston was found to be achieved using a body size mesh of 3.5 mm. See Appendix for details of this mesh independence study.

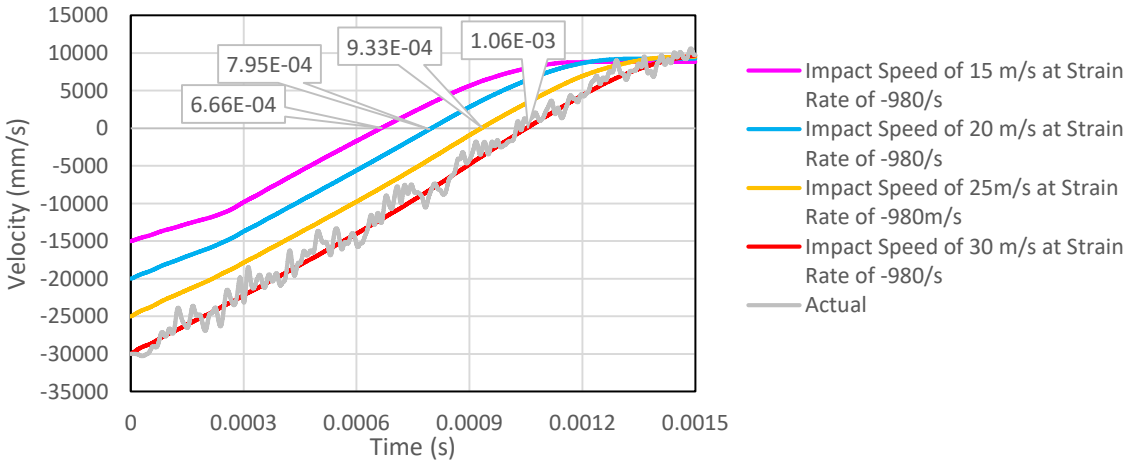

Figure 123 - Velocity plotted against Time of X3 Piston Impacting 200 mm Long Nylon Stud at a Strain Rate of -980/s

Figure 124 displays the loss in velocity of the X3 piston (as a percentage) against time. It can be observed that at approximately 2.5 milliseconds, the gradient of the curves changed. This was more prominent at the lower impact speeds.

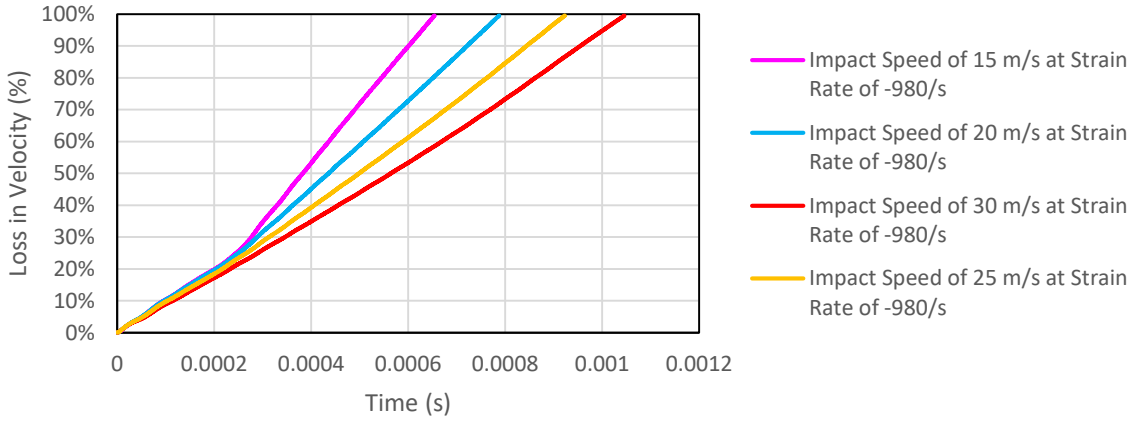

Figure 124 - Percent Loss in X3 Piston Velocity with Time after Impacting 200 mm Long Nylon Stud at Varying Impact Velocities

This phenomenon can be explained using Figure 125. As soon as the piston came into contact with the nylon stud, a stress wave was produced. This stress wave propagated through the stud until it reached the rigid floor (buffer plate). A reflected stress wave was produced which then travelled up the stud thereby increasing the effective stress in the stud. This reflected stress wave then reached the piston at approximately 2.5 milliseconds which corresponded to the change in the gradient of the curves shown in Figure 124.

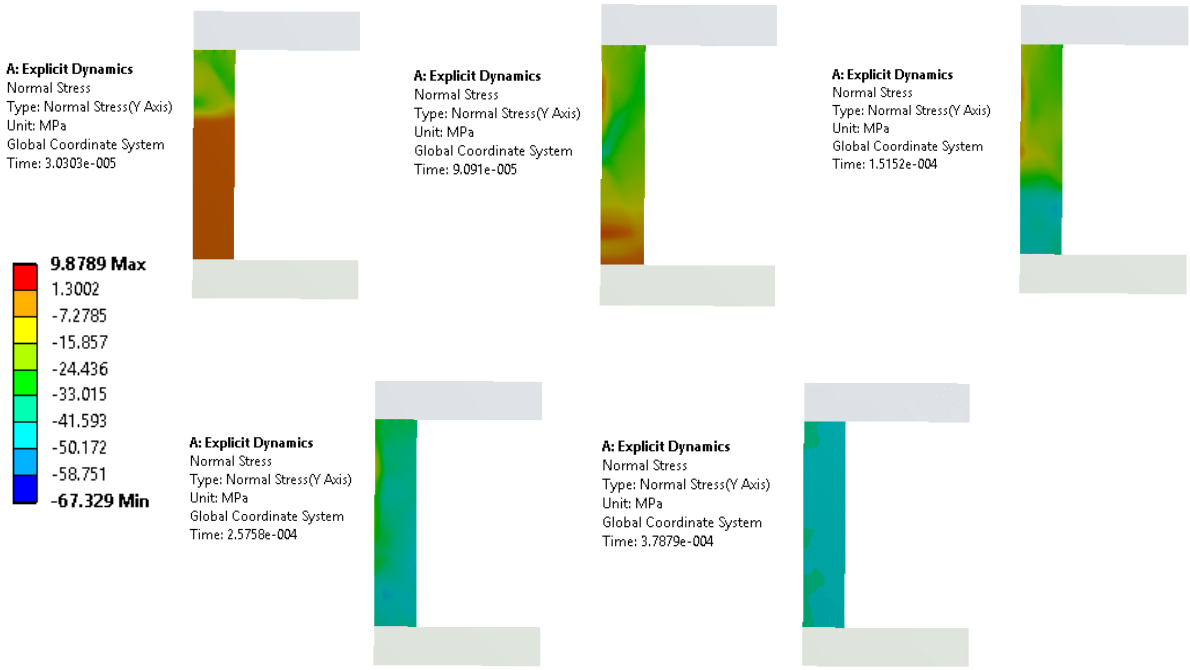

Figure 125 - Stress Wave Propagation through Nylon Stud at Impact an Impact Velocity of 15 m/s

6.5 Effective Stress Analysis of Studs at Varying Impact Speeds

Figure 118 revealed that the effective stress at which fracture of the nylon studs occured for when the strain rate was -980/s was 58 MP and when the strain rate was -3830/s it was 101 MPa.

As shown in Figure 126, the maximum von Mises stress experienced by the stud at a constant strain rate of -980/s was 52 MPa and at -3830/s was 86 MPa. These values were less than the effective stress at which failure occured and so these studs were not predicted to fail at strain rates between these bounds. Nonetheless, the impact speeds of 15 m/s to 30 m/s did result in yielding of the studs.

Once again, Figure 126 revealed that the compressive deformation of the nylon studs was only slightly effected by the change in the nylon stud length between 200 mm and 300 mm. The sensitivity of the results in Figure 126 are however much higher to changes in strain rate. A larger strain rate meant a higher effective stress experienced by the nylon studs.

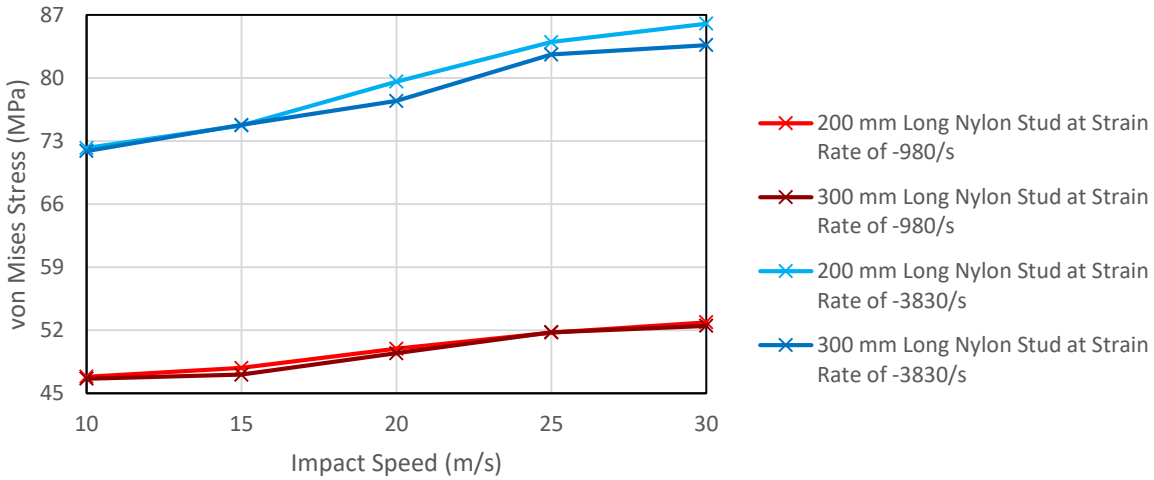

Figure 126 - Maximum von Mises Stress in Nylon Studs at Varying Impact Speeds, Strain Rates and Stud Lengths

6.6 Conclusion

The bilinear material model parameters for nylon under compression between a strain rate of -980/s and -3830/s was obtained from existing literature. This range of strain rates was found to correspond closely with the strain rates that the nylon studs would undergo following an impact velocity of between 15 m/s and 30 m/s with X3's lightweight piston.

It was found that the compresion of the nylon studs could be analysed using a 2D axisymmetric model at impact speeds of up to 30 m/s since the nylon studs did not come into

contact with one another or the inner tube walls of the compression tube during this loading condition.

The compressive deformation and the effective stress in the nylon stud buffer after impact with X3's lightweight piston displayed little sensitivty to the length of the stud but high sensitivty to the changes in material data due to changes in the strain rate being considered. Material data from a lower considered strain rate resulted in greater compressive deformation of the studs.

It was found that at an impact velocity of 30 m/s, the effective stress in the nylon studs was below that necessary to result in fracture of the nylon studs. However, it was high enough to plastically yield the studs. This was true for both the -980/s strain rate analysis and -3830/s strain rate analysis and also for both stud lengths of 200 mm and 300 mm that was considered.

7 Conclusions and Future Work

7.1 Conclusion

The aim of this thesis was to apply explicit FEA techniques to three main structural analysis problems including receating the 2009 T4 high speed piston impact, perfoming a transient analysis of the peak pressure loadings acting on the X2 piston using high strain rate material data and analysing the buffer for the X3 facility.

The AUTODYN solver was selected to conduct the explicit FEA for the three main structural analysis problems. To verify that this solver had the capability to capture the physical mechanisms involved during a high speed piston impact, a series of benchmarks was devised. The key areas that were focused on in these benchmarks included testing the solver's ability to be time accurate and to be able to correctly model materials under high strain rates. The numerical solutions from each of the benchmarks conducted revealed close agreement with the reference solutions obtained, which is detailed in Chapter 3.

After establishing confidence in the solver, a numerical reconstruction of the 2009 T4 high speed piston impact was conducted using AUTODYN. High strain rate material data for the T4 piston body, piston accessories and T4 compression tube was obtained from existing literature. It was found that the piston yielded at this impact speed thus resulting in inteference pressure between the piston and compression tube. Furthermore, the compression tube did yield following T4 shot 10509 which seemed to contradict the technician's comments that the tube did not in fact yield. This could have been the result of incorrect material data or that the yielding in the compression tube was not evident by eye inspection since the width and depth of yield along the inner wall of the compression tube was 1 cm and 0.03 mm, respectively. It was discovered that this problem was sensitive to the friction coefficients used in the analysis. Furthermore, it was discovered that the effective stress in the piston body and compression tube following the impact was not very sensitive to impact speeds above 50 m/s but was sensitive to changes in the material property of the piston body. This is detailed in Chapter 4.

A transient stress analysis of X2's lightweight piston was conducted and compared to a static problem conducted previously. High strain rate material data for X2's lightweight piston and piston accessories were obtained from literature which had implications for X3's lightweight piston as well since they were both made out of aluminium alloys. It was found that although cut-outs were made to X2's lightweight piston, it could still be treated as axisymmetric. The static linear analysis of the peak pressure loadings acting on the X2 piston

revealed close agreement with the analysis conducted using the AUTODYN solver and with high strain rate material data implemented. This is detailed in Chapter 5.

The potential damage caused by a piston impacting the end of the compression tube without a buffer was already analysed in Chapter 4. Hence, Chapter 6 focused on whether the nylon studs in the X3 facility could survive an impact speed of up to 30 m/s with X3's lightweight piston. Bilinear material model data at a range of strain rates were obtained from literature which corresponded to the strain rate that the nylon studs would undego following an impact with X3's lightweight piston at speeds of between 15 m/s to 30 m/s. It was found that the effective stress and compressive deformation results for the nylon studs were not sensitive to the length of the nylon studs but instead were highly sensitive to the changes in the material data (depending on what strain rate was being considered for the analysis). It was discovered however that while the nylon studs did yield between impact speeds of 15 m/s to 30 m/s for all strain rates and stud lengths investigated, none of the analyses suggested that fracture in these studs would occur. See Chapter 6 for further details.

7.2 Recommendations for Future Work

In regards to conducting explicit FEA of high speed piston impacts, recommendations for further work include the following:

- Experimentally acquire high strain rate material data for the materials used in the impulse facilities (possibly using the Split-Hopkinson pressure bar test as discussed in Section 2.6.2). It was found that the sensitivity of the results to changes in the material data used was the highest amongst all other factors. The high strain rate data for each material found in literature did vary and because of this the confidence in the material data used in the analyses was not as high as it could have been.
- Investigate the driver pressure's contribution to the structural response of the T4 facility during a high speed impact. In the reconstruction of T4 shot 10509 and subsequent T4 FEA analyses, the driver pressure's contribution was neglected due to the fact that the pressure from impact would likely far exceed the driver pressure. However, this could be included in future work to provide a more precise reconstruction of the incident.
- Conduct futher analysis of piston impacts. This investigation did not undetake a detailed analysis of X2 and X3's lightweight pistons impacting the end of the compression tubes at high speeds. Doing so would have allowed for the maximum survivable impacts of

these two facilities to be determined following an impact that destroys the nylon stud buffers.

- Compare the numerical solution of the compressive deformation of the X3 nylon stud buffer to experiments. This would be essential for validating that the numerical solutions obtained for the response of the nylon studs upon impact with X3's lightweight piston was accurate under the assumptions made.

References

Adams, B. (2003). Simulation of ballistic impacts on armored civil vehicles.Eindhoven University of Technology, Netherlands, MT, 6.

Agmell, M., Ahadi, A., & Ståhl, J. E. (2013). The link between plasticity parameters and process parameters in orthogonal cutting. Procedia CIRP, 8, 224-229.

Al-Maliky, N., & Parry, D. J. (1994). Measurements of high strain rate properties of polymers using an expanding ring method. *Le Journal de Physique IV*, *4*(C8), C8-71.

Al-Maliky, N. S. (1997). Strain rate behaviour of thermoplastic polymers (Doctoral dissertation, Noori Sabih Jarrih Al-Maliky).

Ames, R. G., & Boeka, R. D. (Eds.). (2014). BALLISTICS 2014: 28th International Symposium on Ballistics. DEStech Publications, Inc.

Andrew Ridings. (2012). UQ's T4 Shock Tunnel Data Acquisition System, slide 2/13. Retrieved from: http://australia.ni.com/sites/default/files/UQ%E2%80%99s%20T4%20Shock%20Tunnel%20Data%20Acquisition%20System%20by%20Guest%20Keynote%20Andrew%20Ridings.pdf.

ANSYS, Inc. (2009, February). ANSYS AUTODYN Chapter 9 Material Models. An ANSYS Web Resource. Retrieved from: < http://wenku.baidu.com/view/6dc41160ddccda38376bafe2.html>.

ANSYS, Inc. (2009, February). ANSYS Explicit Dynamics Chapter 9 Material Models. An ANSYS Web Resource. Retrieved from: < https://www.scribd.com/doc/80724591/ANSYS-AUTODYN-Chapter-9-Material-Models >.

ANSYS, Inc. (2010). ANSYS Mechanical Structural Nonlinearities. An ANSYS Web Resource. Retrieved from: < http://inside.mines.edu/~apetrell/ENME442/Labs/1301_ENME442_lab7.pdf>.

Arrazola, P. J., Meslin, F., Hamann, J. C., & Le Maitre, F. (2002). Numerical cutting modeling with Abaqus/Explicit 6.1. In 2002 ABAQUS User's Conference (pp. 29-31).

Atkinson, K. E. (2007). Numerical Analysis. Retrieved from: <http://www.scholarpedia.org/article/Numerical_analysis>.

Banerjee, B. (2007). Nonlinear finite elements/Lagrangian and Eulerian description. A Wikiversity Web Resource. Retrieved from: <https://en.wikiversity.org/wiki/Nonlinear_finite_elements/Lagrangian_and_Eulerian_descriptions>.

Banerjee, B. (2007). The mechanical threshold stress model for various tempers of AISI 4340 steel. *International Journal of Solids and Structures*,*44*(3), 834-859.

Banerjee, B. (2012). Johnson Cook Plasticity Model. An iMechanica Web Resource. Retrieved from: <http://imechanica.org/node/11802>.

Banerjee, A., Dhar, S., Acharyya, S., Datta, D., & Nayak, N. (2015). Determination of Johnson cook material and failure model constants and numerical modelling of Charpy impact test of armour steel. Materials Science and Engineering: A, 640, 200-209.

Barba, L and LeVeque, R. (2016). The Courant-Friedrichs-Lewy Condition. The Visual Room Web Resource. Retrieved from: <http://www.thevisualroom.com/courant_number.html>.

Becker, A. A. (2001). Understanding non-linear finite element analysis through illustrative benchmarks. NAFEMS 21-171.

Bhat, A. R. (2009). Finite element modeling and dynamic impact response evaluation for ballistic applications.

Bigoni, D., & Piccolroaz, A. (2004). Yield criteria for quasibrittle and frictional materials. International journal of solids and structures, 41(11), 2855-2878.

Blackman ME, Goldsmith W. The Mechanics of Penetration of Projectiles into Targets. J Eng Sci 1978;16:1-99

Bob McGinty. (2012). Von Mises Stress. A Continuum Mechanics Web Resource. Retrieved from: <http://www.continuummechanics.org/vonmisesstress.html>.

Broenink, F. J. (2000) Background Information on Simulation. Retrieved from:<https://www.ram.ewi.utwente.nl/aigaion/attachments/single/1255>.

Brar, N. S., Joshi, V. S., & Harris, B. W. (2009, December). Constitutive Model Constants for Al7075-t651 and Al7075-t6. In SHOCK COMPRESSION OF CONDENSED MATTER 2009: Proceedings of the American Physical Society Topical Group on Shock Compression of Condensed Matter (Vol. 1195, No. 1, pp. 945-948). AIP Publishing.

Buchely, M. F., Maranon, A., & Delvare, F. (2012). Engineering model for low-velocity impacts of multi-material cylinder on a rigid boundary. In EPJ Web of Conferences (Vol. 26, p. 04034). EDP Sciences.

Chen XW, Chen G, Zhang FJ. (2008). Deformation and Failure Modes of Soft Steel Projectiles Impacting Harder Steel Targets at Increasing Velocity. Exp Mech; 48:335-54.

Chung, W. J., Cho, J. W., & Belytschko, T. (1998). On the dynamic effects of explicit FEM in sheet metal forming analysis. Engineering Computations, 15(6), 750-776.

Crocombe, A. D. (2001). How to tackle non-linear finite element analysis. NAFEMS, 14-81.

Dassault Systèmes (2012) Simulation of the ballistic perforation of aluminum plates with Abaqus/Explicit. Retrieved from: http://www.3ds.com/fileadmin/PRODUCTS/SIMULIA/PDF/tech-briefs/aero-ballistic-perforation-alumnium-plates-12.pdf

Dorogoy, A., & Rittel, D. (2009). Technical note: Determination of the Johnson-Cook material parameters using the SCS specimen. Proceeding of the Society for Experimental Mechanics, 66, 881.

Duffy, T. S., & Ahrens, T. J. (1997). Dynamic compression of an Fe–Cr–Ni alloy to 80 GPa. Journal of applied physics, 82(9), 4259-4269.

Eureka.im. (2012). How to deal with Problem terminated – energy error too large. Eureka.im Web Resource. Retrieved from: <http://www.eureka.im/3132.html>.

Fiene, J. P. (2016). MEAM.Design: MEAM247-09a-UniaxialStrain. Retrieved from:<https://alliance.seas.upenn.edu/~medesign/wiki/index.php/Courses.MEAM247-09a-UniaxialStrain>.

Frontán, J., Zhang, Y., Dao, M., Lu, J., Gálvez, F., & Jérusalem, A. (2012). Ballistic performance of nanocrystalline and nanotwinned ultrafine crystal steel. *Acta Materialia*, *60*(3), 1353-1367.

Fu, Z. T., Yang, W. Y., Zeng, S. Q., Guo, B. P., & Hu, S. B. (2016). Identification of constitutive model parameters for nickel aluminum bronze in machining. Transactions of Nonferrous Metals Society of China, 26(4), 1105-1111.

Gildfind, D. E. (2012). Development of high total pressure scramjet flow conditions using the X2 expansion tube.

Gildfind, D. E. (2016). Part 1: Shock Wave Theory, Hypersonic Ground Testing, Local Surface Inclination Techniques, and Viscous Hypersonic Flow, slide 28/56 Retrieved from:https://learn.uq.edu.au/bbcswebdav/pid-1945461-dt-content-rid-9136674_1/courses/MECH4470S_6620_22245/mech4470-2016-dgildfind-notes-lecture-05.pdf

Gildfind, D. E. (2016). Part 1: Shock Wave Theory, Hypersonic Ground Testing, Local Surface Inclination Techniques, and Viscous Hypersonic Flow, slide 30/56 Retrieved from:https://learn.uq.edu.au/bbcswebdav/pid-1945461-dt-content-rid-9136674_1/courses/MECH4470S_6620_22245/mech4470-2016-dgildfind-notes-lecture-05.pdf

Gildfind, D. (2012). X3 lightweight piston, Drawing Number X3-LWP-000-0.

Gildfind, D. (2010). X2 Lightweight Piston Experimental Test Campaign, November 2009 to February 2010: Analysis and Observations (No. Technical Report 2010/04). The University of Queensland, School of Engineering, Division of Mechanical Engineering.

Gildfind, D. E., Morgan, R. G., & Sancho, J. (2015). Design and commissioning of a new lightweight piston for the X3 expansion tube. In 29th International Symposium on Shock Waves 1 (pp. 367-372). Springer International Publishing.

Gildfind, D. E., Morgan, R. G., & Jacobs, P. A. (2016). Expansion Tubes in Australia. In Experimental Methods of Shock Wave Research (pp. 399-431). Springer International Publishing.

Gildfind, D. E., Morgan, R. G., McGilvray, M., Jacobs, P. A., Eichmann, T., Stalker, R. J., & Teakle, P. (2010). Design of lightweight pistons for the X2 and X3 expansion tube free-piston drivers. In 17th Australasian Fluid Mechanics Conference 2010 (pp. 857-861). The University of Auckland.

Gildfind, D. E., James, C. M., & Morgan, R. G. (2015). Free-piston driver performance characterisation using experimental shock speeds through helium. Shock Waves, 25(2), 169-176.

Gildfind, D. E., Morgan, R. G., McGilvray, M., Jacobs, P. A., Stalker, R. J., & Eichmann, T. N. (2011). Free-piston driver optimisation for simulation of high Mach number scramjet flow conditions. Shock Waves, 21(6), 559-572.

Gildfind, D. E., Morgan, R. G., & Jacobs, P. A. (2012). Vibration isolation in a free-piston driven Expansion tube. In 18th Australasian Fluid Mechanics Conference. Australasian Fluid Mechanics Society.

Hassan, A. R. (2009). Contact stress analysis of spur gear teeth pair. World Academy of Science, Engineering and Technology, 58(1), 597-602.

He, A., Xie, G., Zhang, H., & Wang, X. (2014). A modified Zerilli–Armstrong constitutive model to predict hot deformation behavior of 20CrMo alloy steel.Materials & Design, 56, 122-127.

Heider, N., & Kenkmann, T. (2003). Numerical simulation of temperature effects at fissures due to shock loading. Meteoritics & Planetary Science,38(10), 1451-1460.

HBM. (2016). Split Hopkinson Bar in Materials Testing. A HBM Web Resource. Retrieved from: < https://www.hbm.com/en/2996/split-hopkinson-bar-material-tests/>.

Igra, O. (2015). Experimental Methods of Shock Wave Research, (Vol. 9). F. Seiler (Ed.) 183. Springer

Institut national des sciences appliquées de Toulouse (2014) Stress wave propagation in a bar. Retrieved from:<https://moodle.insa-toulouse.fr/pluginfile.php/13264/mod_resource/content/0/Exos-internet/Vibrations.pdf>.

Itoh, K., Ueda, S., Komuro, T., Sato, K., Takahashi, M., Miyajima, H., ... & Muramoto, H. (1998). Improvement of a free piston driver for a high-enthalpy shock tunnel. Shock Waves, 8(4), 215-233.

Jacobs, P. A. (1998). Shock tube modelling with L1d (No. Report 13/98).

Jacobs, P., Morgan, R., Brandis, A., Buttsworth, D., Dann, A., D'Souza, M., ... & McGilvray, M. (2013). Design, operation and testing in expansion tube facilities for super-orbital re-entry. In STO-AVT-VKI Lecture Series Radiation and Gas-Surface Interaction Phenomena in High Speed Re-Entry (2013-AVT-218) (pp. 5-1).

Jaiswal, A. (2011). ANSYS Explicit Dynamics and AUTODYN Applications. An ANSYS Web Resource. Retrieved from: https://support.ansys.com/staticassets/ANSYS/Conference/Palm%20Beach/downloads/ANSYS%20Explicit%20Dynamics%20-%20Ashish%20Jaiswal.pdf

Jha, N., & Kumar, B. K. (2014, December) Under Water Explosion Pressure Prediction and Validation Using ANSYS/AUTODYN.

J. K. Paik, J. Y. Chung, and M. S. Chun. (1996). “On quasi-static crushing of a stiffened square tube”, J. Ship Res., Vol. 40, No. 3, pp. 258–267.

Johnson & Cook. (1969). LA-4167-MS Selected Hugoniots EOS, 7th Int. Symp. Ballistics.

Johnson, G. R., & Cook, W. H. (1985). Fracture characteristics of three metals subjected to various strains, strain rates, temperatures and pressures. Engineering fracture mechanics, 21(1), 31-48.

Karaveer, V., Mogrekar, A., & Joseph, T. P. R. (2013). Modeling and finite element analysis of spur gear. International Journal of Current Engineering and Technology ISSN, 2277-4106.

Katukam, Ravi. (2014). Comprehensive Bird Strike Simulation Approach for Aircraft Structure Certification. Cyient white paper.

Kay, G. (2003). Failure modeling of titanium 6AI-4V and aluminum 2024-T3 with the Johnson-Cook material model. Office of Aviation Research, Federal Aviation Administration.

Kazanci, Z., & Bathe, K. J. (2012). Crushing and crashing of tubes with implicit time integration. International Journal of Impact Engineering, 42, 80-88.

Krasauskas, P., Kilikevičius, S., Česnavičius, R., & Pačenga, D. (2015). Experimental analysis and numerical simulation of the stainless AISI 304 steel friction drilling process. *Mechanics*, *20*(6), 590-595.

Lacey Jr, J. J. (1992). U.S. Patent No. 5,115,665. Washington, DC: U.S. Patent and Trademark Office.

Lee H. (2015) Finite Element Simulations with ANSYS Workbench 16, Section 15.1 Basics of Explicit Dynamics, 15.1-1 Implicit Integration Methods 563-564

Liu, Y. (2010). Thin-walled curved hexagonal beams in crashes–FEA and design. International Journal of Crashworthiness, 15(2), 151-159.

Liu, J., Li, Y., Gao, X., & Yu, X. (2014). A numerical model for bird strike on sidewall structure of an aircraft nose. Chinese Journal of Aeronautics, 27(3), 542-549.

Li, J., Guo, H., & Zhou, P. (2015). Experimental Study and Analysis of the Dynamic Mechanical Properties of Aluminium Bronze. Strojniški vestnik-Journal of Mechanical Engineering, 61(11), 680-686.

Lobo, H., & Hurtado, J. (2006). Characterization and modeling of nonlinear behavior of plastics. In ABAQUS User Conference.

Lodygowski, T., & Rusinek, A. (Eds.). (2013). Constitutive Relations Under Impact Loadings: Experiments, Theoretical and Numerical Aspects (Vol. 552). Springer Science & Business Media.

Los Alamos Scientific Laboratory. (May 1969). "Selected Hugoniots", LA-4167-MS.

LS-DYNA Support. (2016). Contact Modelling in LS-DYNA. Retrieved from:<http://www.dynasupport.com/tutorial/ls-dyna-users-guide/contact-modeling-in-ls-dyna>.

Mamalis, A. G., Manolakos, D. E., & Baldoukas, A. K. (1997). Simulation of sheet metal forming using explicit finite-element techniques: effect of material and forming characteristics: Part 1. Deep-drawing of cylindrical cups. Journal of materials processing technology, 72(1), 48-60.

Mashayekhi, Mohammad (2016) Comparison of Implicit and Explicit Procedures. Retrieved from: <http://mashayekhi.iut.ac.ir/sites/mashayekhi.iut.ac.ir/files//u32/presentation4.pdf>.

Matuska D.A. (1984, June) HULL Users Manual, AFATL-TR-84-59.

Mithun, N., & Mahesh, G. S. (2012). Finite element modelling for bird strike analysis and review of existing numerical methods. International Journal of Engineering Research and Technology (Vol. 1, No. 8 (October-2012)). ESRSA Publications.

Morgan, R. G. (2001). Free Piston-Driven Reflected Shock Tunnels. (pp. 587-601).

Morgan, R. G., Paull, A., Stalker, R. J., Jacobs, P., Morris, N., Stringer, I., & Brescianini, C. (1988). Shock tunnel studies of scramjet phenomena.

Mori, L., Lee, S., Xue, Z., Vaziri, A., Queheillalt, D., Dharmasena, K., & Espinosa, H. (2007). Deformation and fracture modes of sandwich structures subjected to underwater impulsive loads. *Journal of mechanics of materials and structures*, *2*(10), 1981-2006.

Olleak, A. A., Nasr, M. N., & El-Hofy, H. (2015). The Influence of Johnson-Cook Parameters on SPH Modelling of Orthogonal Cutting of AISI 316L.

O'Toole, B., Trabia, M., Hixson, R., Roy, S. K., Pena, M., Becker, S., & Matthes, M. (2015). Modeling Plastic Deformation of Steel Plates in Hypervelocity Impact Experiments. Procedia Engineering, 103, 458-465.

Page, N. W., & Stalker, R. J. (1983). Pressure losses in free piston driven shock tubes. In Shock tubes and waves, Proc. 14th International Symposium on Shock Tubes and Waves (p. 188). Sydney Shock Tube Symp. Publishers.

Perepechko, I. (2013). Low-temperature properties of polymers. Elsevier. 249.

Schreiber, Jeremy M. (2013) High-strain-rate Property Determination of High-strength Steel Using Finite Element Analysis and Experimental Data. Diss. The Pennsylvania State University, 2013.

Pointer, J. (2004). Understanding Accuracy and Discretization Error in an FEA Model. In ANSYS 7.1, 2004 Conference, Wooward Governor Company.

POURIAYEVALI, H. (2013). Describing Large Deformation of Polymers at Quasi-static and High Strain Rates (Doctoral dissertation).

Rakvåg, K. G., Børvik, T., Westermann, I., & Hopperstad, O. S. (2013). An experimental study on the deformation and fracture modes of steel projectiles during impact. Materials & Design, 51, 242-256.

Rakvåg, K. G., Børvik, T., & Hopperstad, O. S. (2014). A numerical study on the deformation and fracture modes of steel projectiles during Taylor bar impact tests. International Journal of Solids and Structures, 51(3), 808-821.

Rao, C. L., Narayanamurthy, V., & Simha, K. R. Y. (2016). Applied Impact Mechanics. John Wiley & Sons.

Rao, S. S. (2010) Mechanical Vibrations Fifth Edition, Pearson Education, 716-718.

Reid, J. D., & Hiser, N.R. (2004). Friction modelling between solid elements. International Journal of Crashworthiness, 9(1), 65-72.

Robinson, M. J., Rowan, S. A., Odam, J., Mee, D. J., Hitchcock, K. W., Malcolm, D. J. M., & Vanyai, T. (2015). T4 Free Piston Shock Tunnel Operator's Manual Version 2.0.

RockMechs. (2016). Principle stresses and stress invariants. A RochMechs Web Resource. Retrieved from: < Becker, A. A. (2001). Understanding non-linear finite element analysis through illustrative benchmarks. NAFEMS 21-171>.

Roy, S. K. (2015). An Approach to Model Plastic Deformation of Metallic Plates in Hypervelocity Impact Experiments.

Russ, B. H. (2012). Development of a CAD model simplification framework for finite element analysis. MARYLAND UNIV COLLEGE PARK DEPT OF MECHANICAL ENGINEERING.

RWTH Aechen University (2007) Hypersonic Shock Tunnel TH2. Retrieved from:http://www.swl.rwth-aachen.de/en/research/test-facilities/hypersonic-shock-tunnel-th2.php

Sabadin, G., Gaiotti, M., Rizzo, C. M., & Bassano, A. (2014). Optimization of the ballistic properties of an Advanced Composite Armor system: Analysis and validation of numerical models subject to high velocity impacts. Maritime Technology and Engineering, 463.

Schwer, L. (2007). Optional Strain-rate forms for the Johnson Cook Constitutive Model and the Role of the parameter Epsilon_0. LS-DYNA Anwenderforum, Frankenthal.

Seidt, J. D., Gilat, A., Klein, J. A., & Leach, J. R. (2007, June). High strain rate, high temperature constitutive and failure models for EOD impact scenarios. In Proceedings of the

SEM Annual Conference & Exposition on Experimental and Applied Mechanics (p. 15). Society for Experimental Mechanics.

Sharcnet. (2016). Erosion Controls. A Sharcnet Web Resource. Retrieved from:<https://www.sharcnet.ca/Software/Ansys/16.2.3/en-us/help/wb_sim/exp_dyn_theory_erosion_cont.html>.

Sharma, D.P. (2016). Gate Mechanical Engineering. Delhi: PHI Learning Private Limited.

Sharcnet. (2016). Define Connections. A Sharcnet Web Resource. Retrieved from: < https://www.sharcnet.ca/Software/Ansys/17.0/en-us/help/exd_ag/exd_ag_wf_connections.html>.

Shivpuri, R., Cheng, X., & Mao, Y. (2009). Elasto-plastic pseudo-dynamic numerical model for the design of shot peening process parameters. Materials & Design, 30(8), 3112-3120.

Shrot, A., & Bäker, M. (2012). Determination of Johnson–Cook parameters from machining simulations. Computational Materials Science, 52(1), 298-304.

Sierakowski, R. L. (2008). Strain rate behavior of metals and composites. In Convegno IGF XIII Cassino 1997.

Soares, C. G., & Santos, T. A. (Eds.). (2014). Maritime Technology and Engineering. CRC Press, 467.

Stalker, R. J. (1967). A study of the free-piston shock tunnel. AIAA Journal,5(12), 2160-2165.

Stalker, R. J. (1990, July). Recent developments with free piston drivers. In Current topics in shock waves 17th international symposium on shock waves and shock tubes (Vol. 208, No. 1, pp. 96-107). AIP Publishing.

Steinberg, D. (1996). Equation of state and strength properties of selected materials (pp. 3-6). Livermore, CA: Lawrence Livermore National Laboratory.

Steinberg, D. J., Cochran, S. G., & Guinan, M. W. (1980). A constitutive model for metals applicable at high-strain rate. Journal of Applied Physics,51(3), 1498-1504.

Straalen B. V. (2014) Implicit Time Stepping Methods used for Time-Dependent Hyperbolic PDE. Retrieved from:<https://www.researchgate.net/post/Why_are_implicit_time_stepping_methods_rarely_used_for_time-dependent_hyperbolic_PDE2>.

Taylor, G. (1948, September). The use of flat-ended projectiles for determining dynamic yield stress. I. Theoretical considerations. InProceedings of the Royal Society of London A: Mathematical, Physical and Engineering Sciences (Vol. 194, No. 1038, pp. 289-299). The Royal Society.

The Ohio State University. (2016). High Strain Rate Compression Tests. Retrieved from: <http://www.mecheng.osu.edu/lab/dmm/node/34>.

The University of Queensland. (2016). X2 Super-Orbital Expansion Tube. Retrieved from:http://hypersonics.mechmining.uq.edu.au/x2

Toniato, P., Gildfind, D. E., Jacobs, P. A., & Morgan, R. G. (2015). Development of a new Mach 12 scramjet operating capability in the X3 expansion tube. In 7th Asia-Pacific International Symposium on Aerospace Technology (APISAT).

Treloar, L. R. G. (1944). Stress-strain data for vulcanized rubber under various types of deformation. Rubber Chemistry and Technology, 17(4), 813-825.

Tsai, J. L., & Huang, J. C. (2006). Strain rate effect on mechanical behaviors of nylon 6–clay nanocomposites. Journal of composite materials, 40(10), 925-938.

UCF Physics (2016). Friction. Retrieved from: https://physics.ucf.edu/~saul/01-Spr_2048C/04-Forces/FrictionCoeffs.html.

Vedantam, K., Bajaj, D., Brar, N. S., & Hill, S. (2006, July). Johnson-cook strength models for mild and dp 590 steels. In AIP conference proceedings (Vol. 845, No. 1, p. 775). IOP Institute of Physics Publishing Ltd.

Weisstein, Eric W. (2016). "Courant-Friedrichs-Lewy Condition." MathWorld--A Wolfram Web Resource. Retrieved from: <http://mathworld.wolfram.com/Courant-Friedrichs-LewyCondition.html>.

Whiffin, A. C. (1948, September). The use of flat-ended projectiles for determining dynamic yield stress. II. Tests on various metallic materials. InProceedings of the Royal Society of London A: Mathematical, Physical and Engineering Sciences (Vol. 194, No. 1038, pp. 300-322). The Royal Society.

Winter, R. E., Cotton, M., Harris, E. J., Maw, J. R., Chapman, D. J., Eakins, D. E., & McShane, G. (2014). Plate-impact loading of cellular structures formed by selective laser melting. Modelling and Simulation in Materials Science and Engineering, 22(2), 025021.

Woodward RL, O'Donnell RG, Flockhart CJ. Failure Mechanisms in Impacting Penetrators. J Mater Sci 1992;27;6411-6

Yancey, R. (2011). Bird Strike Simulation Takes Flight. Retrieved from:<http://www.altair.com/ResLibDownload.aspx?file_id2=851&from_page=%2FResourceLibrary.aspx%3Fkeywords%3D%26industry%3DAll%26category%3DAll%26brand%3DAll%26page%3D14%23657>.

Yang, R., Zhang, H., Shen, L., Xu, Y., Bai, Y., & Dodd, B. (2014). A modified split Hopkinson torsional bar system for correlated study of τ–γ relations, shear localization and microstructural evolution. Philosophical Transactions of the Royal Society of London A: Mathematical, Physical and Engineering Sciences, 372(2015), 20130208.

Younes, M. M. (2009, May). Finite element modeling of crushing behavior of thin tubes with various cross sections. In 13th International Conference on Aerospace Sciences & Aviation Technology, ASAT-13, Paper: ASAT-13-ST-34.

Zhang, A., and Suzuki. K. (2007). “A study on the effect of stiffeners on quasi-static crushing of stiffened square tube with non-linear finite element method”, Int. J. of Imp. Eng., Vol. 34, pp. 544–555.

Zocher, M. A., Maudlin, P. J., Chen, S. R., & Flower-Maudlin, E. C. (2000, March). An evaluation of several hardening models using Taylor cylinder impact data. In Proceedings of European Congress on Computational Methods in Applied Sciences and Engineering.

Appendices

Appendix A
T4 Facility Drawing Set

A.1 T4 Piston Body

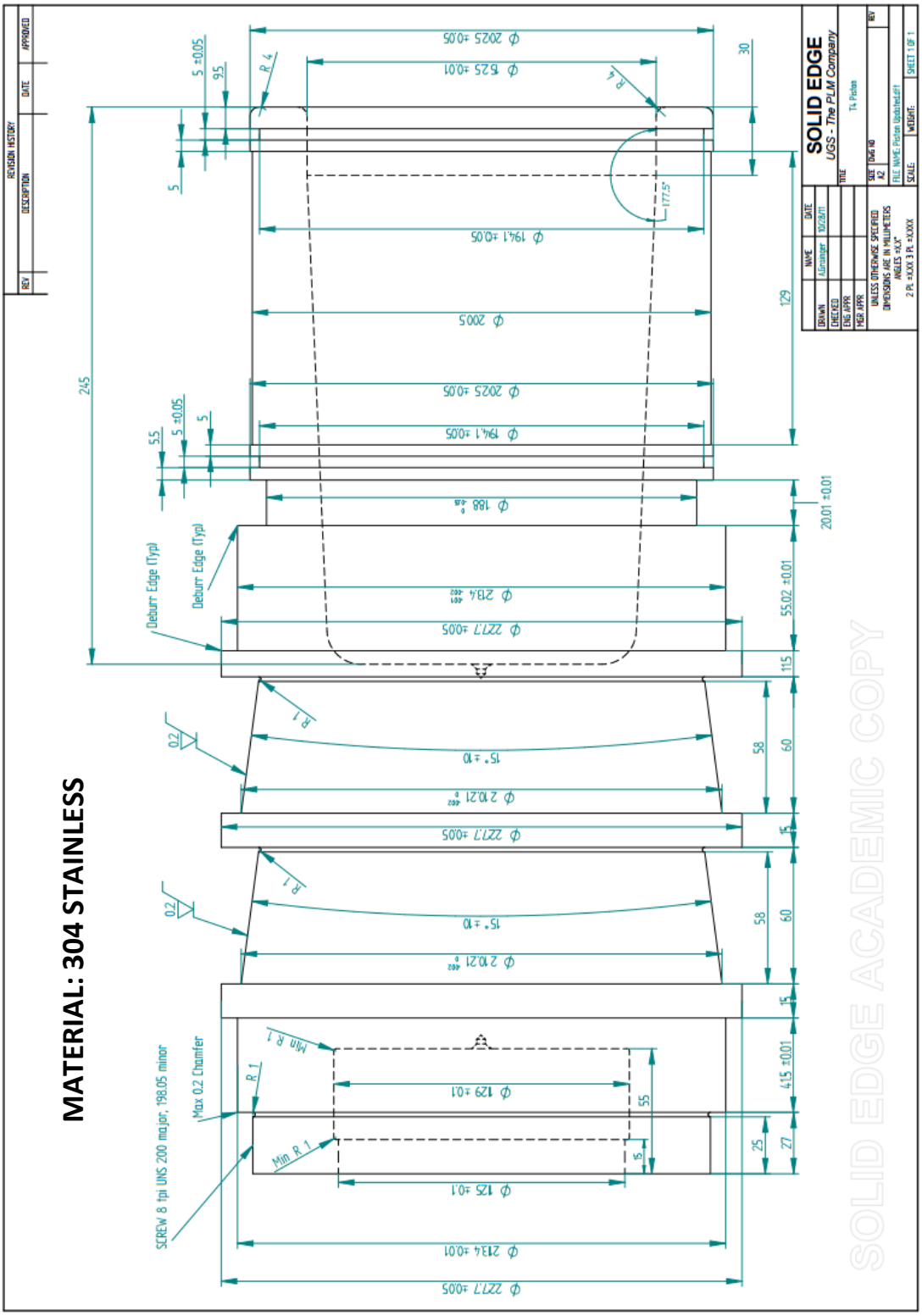

A.2 T4 Locking Ring (Piston Accessory)

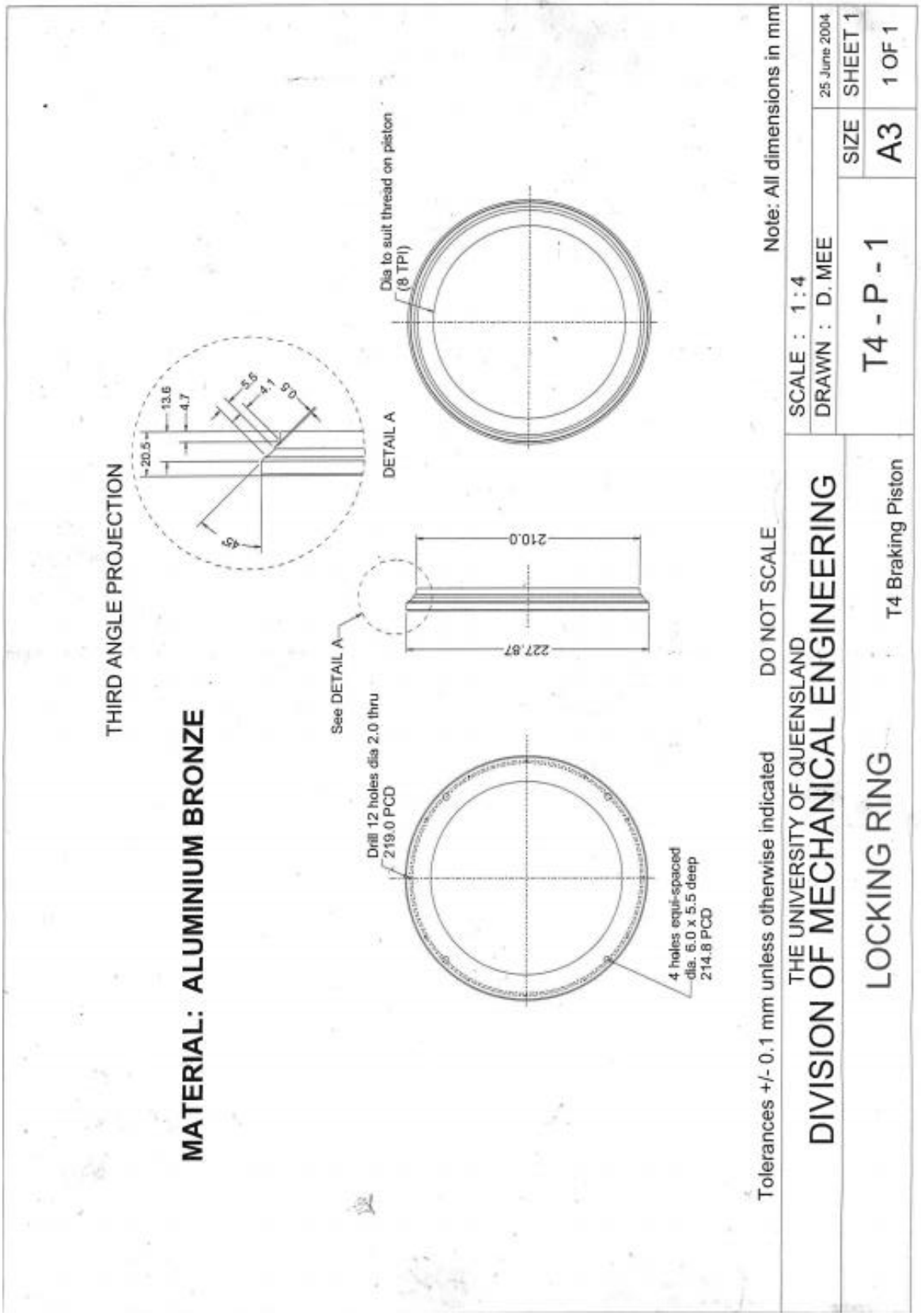

A.3 T4 Wear Ring (Piston Accessory)

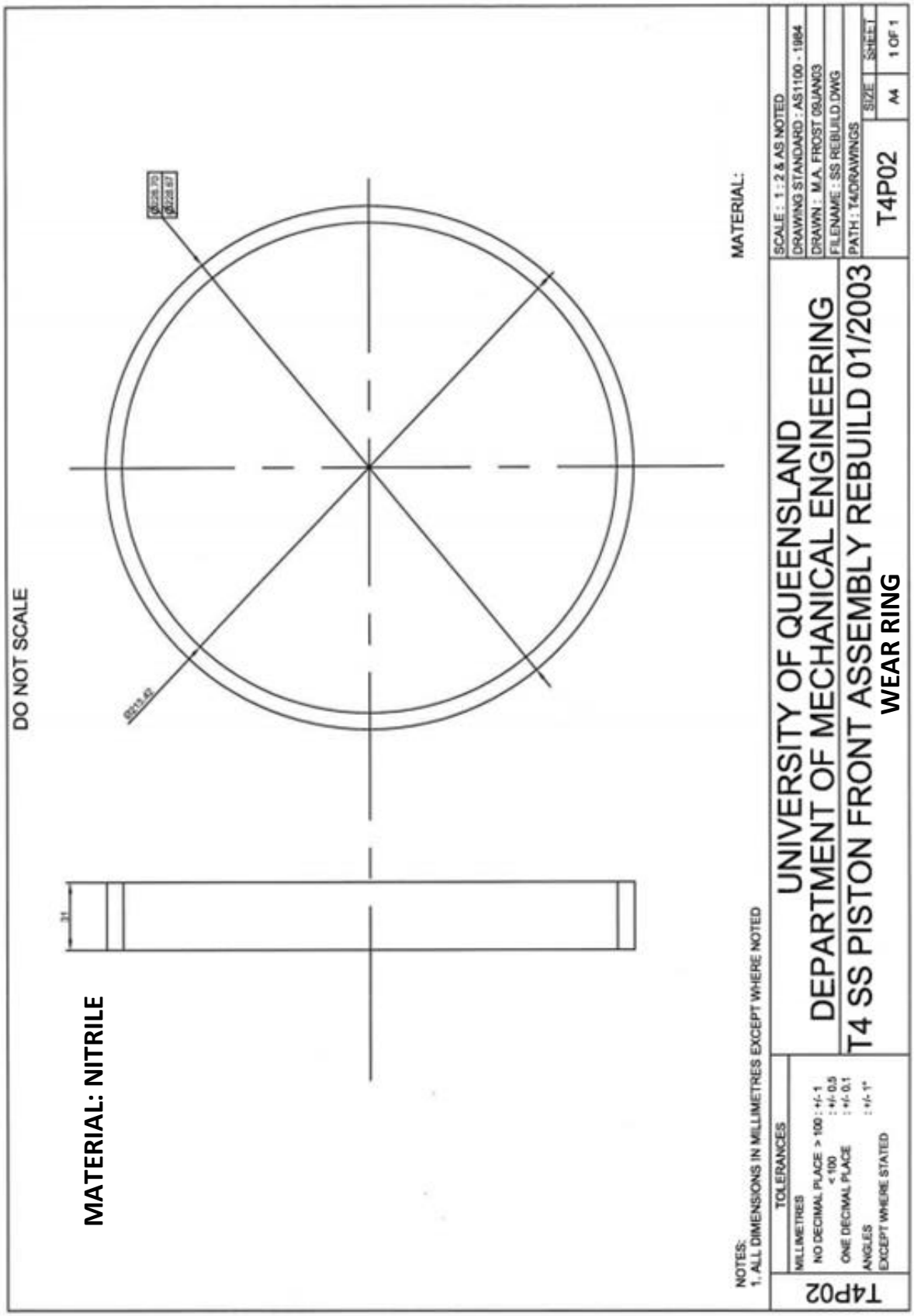

A.4 T4 Chevron Seal (Piston Accessory)

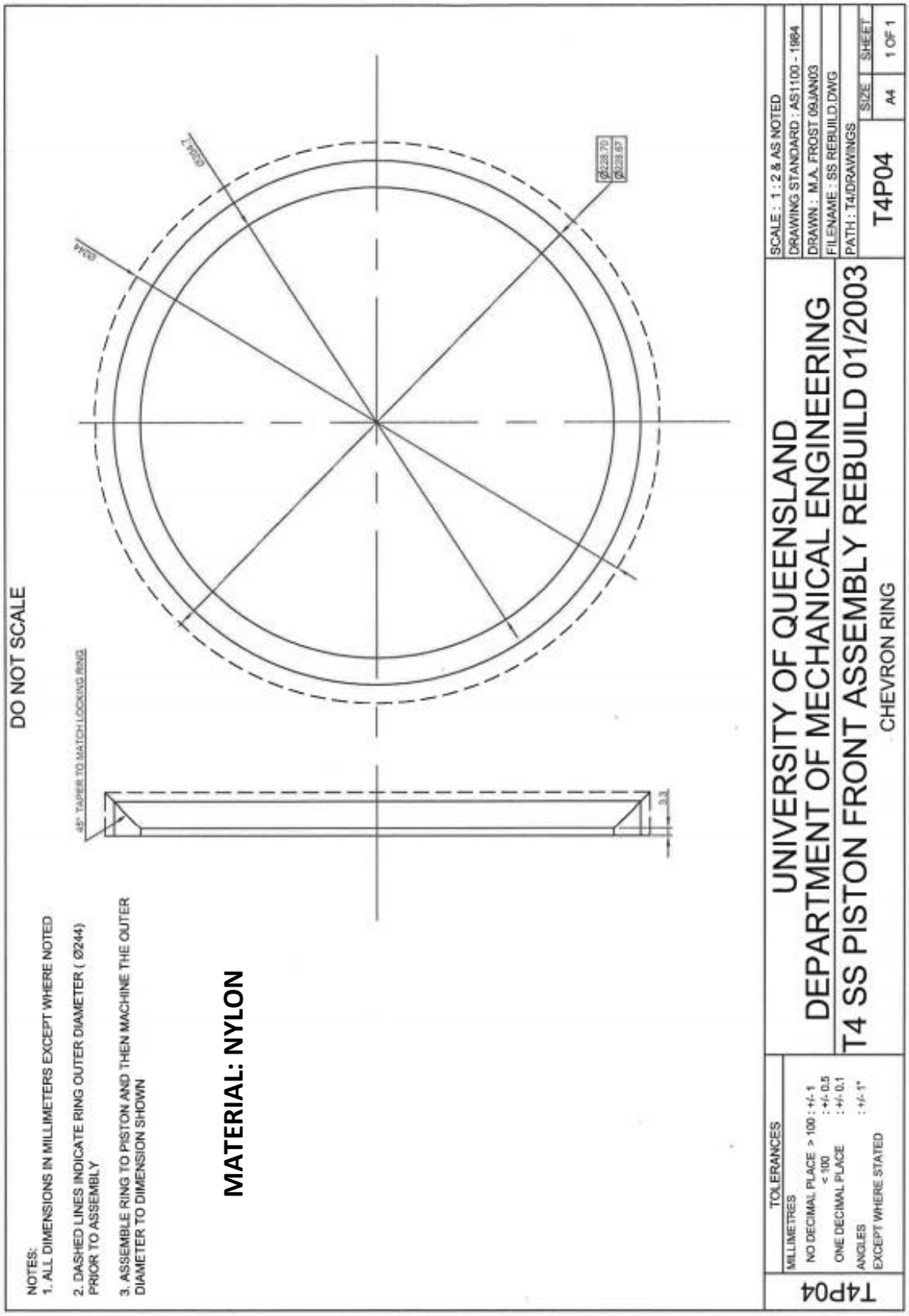

A.5 T4 Rubber Buffer

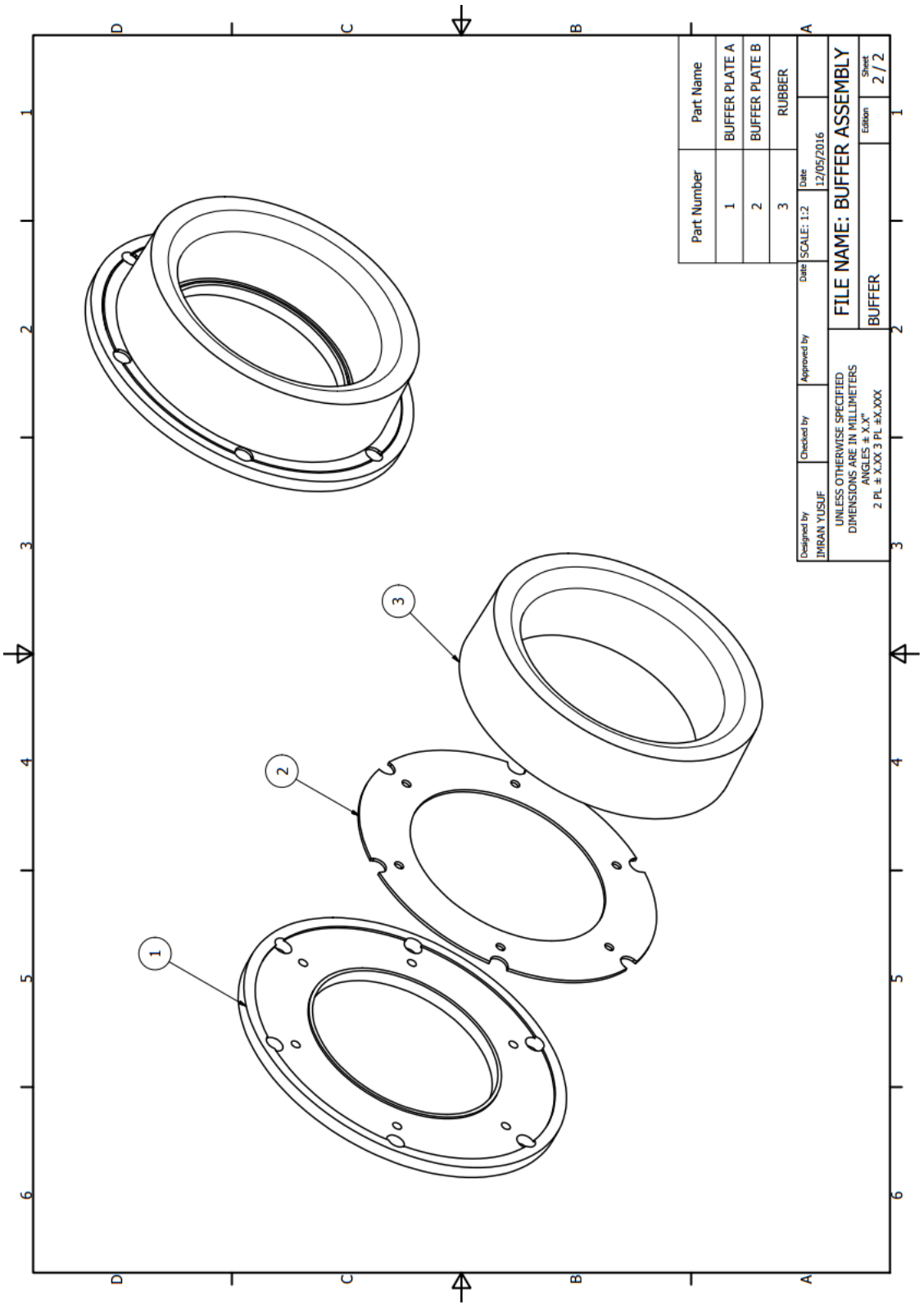

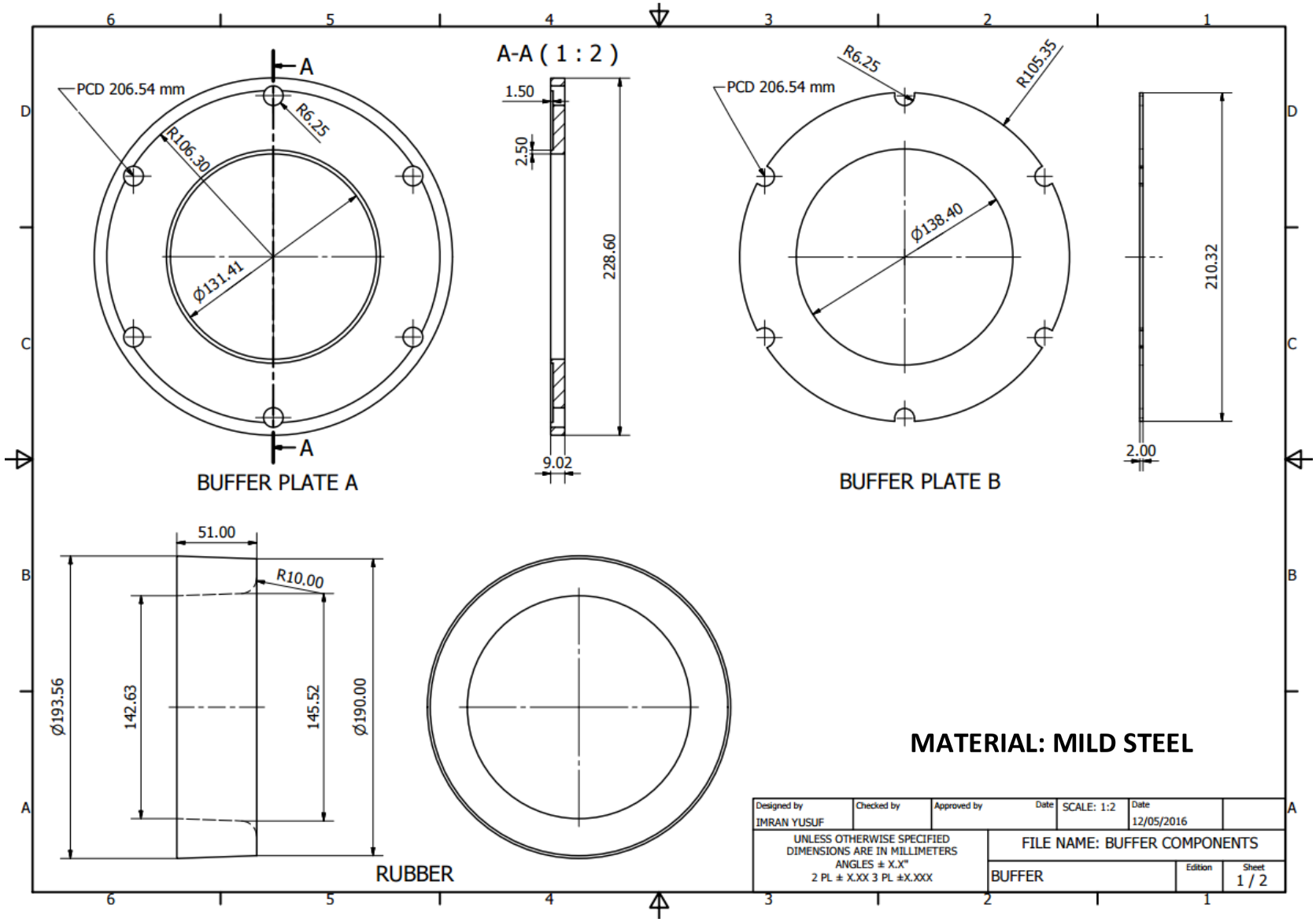
A-A (1 : 2)
PCD 206.54 mm
R6.25
R106.30
Ø131.41
A
A
BUFFER PLATE A
1.50
2.50
228.60
9.02
PCD 206.54 mm
R6.25
R105.35
Ø138.40
210.32
2.00
BUFFER PLATE B
51.00
R10.00
Ø193.56
142.63
145.52
Ø190.00
RUBBER
MATERIAL: MILD STEEL
Designed by
IMRAN YUSUF
Checked by
Approved by
Date
SCALE: 1:2
Date
12/05/2016
UNLESS OTHERWISE SPECIFIED
DIMENSIONS ARE IN MILLIMETERS
ANGLES ± X.X°
2 PL ± X.XX 3 PL ±X.XXX
FILE NAME: BUFFER COMPONENTS
BUFFER
Edition
Sheet
1 / 2

A.6 T4 Compression Tube

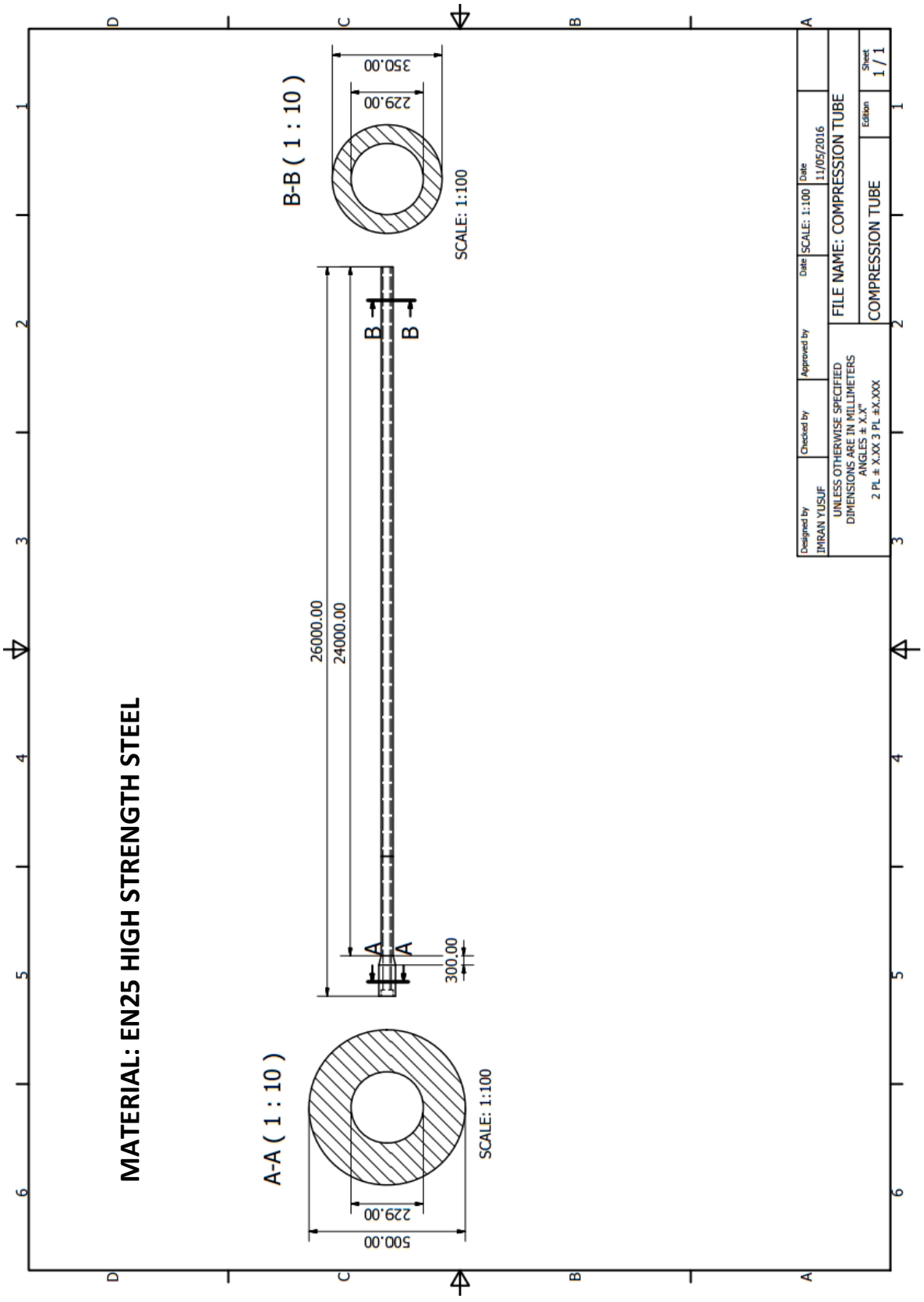

Appendix B
Benchmark Details

B.1 Hertzian Contact Stress

The maximum Hertzian contact stress, in the elliptic stress region formed between two contacting gear teeth, is given by (Hassan, 2009):

$$\sigma_0 = \sqrt{\frac{W\left(1+\frac{r_{p1}}{r_{p2}}\right)}{r_{p1}F\pi\left[\frac{1-\upsilon_1^2}{E_1}+\frac{1-\upsilon_2^2}{E_2}\right]\sin\phi}}$$

Where W is the load, r_{p1} and r_{p2} are the pitch radii of the pinion and gear, F is the face width of the pinion, υ_1 and υ_2 are the Poisson's ratios of pinion and gear respectively, E_1 and E_2 are the Modulus of Elasticity of the pinion and the gear respectively and ϕ is the pressure angle.

The spur gear geometry and loading and boundary conditions were taken from an existing worked solution FEA benchmark in the *Finite Element Simulations with ANSYS Workbench 16* textbook written by Huei-Hung Lee (2015). This was done in order to ensure the code was being used correctly. Hence, the values selected for the variables in the analytical solution for the maximum Hertzian contact stresses are found below.

Table B1 - Parameters for the Gear Analysis

Variable	Symbol	Value
Load (N)	W	53378.6614
Pinion Pitch Radii (mm)	r_{p1}	63.5
Gear Pitch Radii (mm)	r_{p2}	63.5
Face Width (mm)	F	25.4
Poisson's Ratio of Pinion	υ_1	0.3
Poisson's Ratio of Gear	υ_2	0.3
Modulus of Elasticity of the Pinion	E_1	2. e+005
Modulus of Elasticity of the Gear	E_2	2. e+005
Pressure Angle (°)	ϕ	20

This means that the maximum Hertzian contact stress is:

$$\sigma_0 = \sqrt{\frac{53378.6614\left(1+\frac{63.5}{63.5}\right)}{63.5 \times 25.4 \times \pi\left[\frac{1-(0.3)^2}{2\times10^5}+\frac{1-(0.3)^2}{2\times10^5}\right]\sin(20)}} = 2601.8\ \text{MPa}$$

The properties of the '*Geometry'* were set to '*2D Analysis'*. The geometry values for both spur gears are revealed below:

Table B2 - Geometry of Gears

Variable	Value
Number of Teeth	20
Pitch Circle Diameter (mm)	127
Addendum Radius (mm)	69.85
Dedendum Radius (mm)	55.88
Shaft Radius (mm)	31.75

The '*2D behaviour*' was set to '*Plane Stress*'. The thickness was set to 25.4 mm.

In the '*Sizing'*, the '*Size Function*' was set to '*Proximity and Curvature*'. '*Edge Sizing*', with an element size of 0.1mm, was applied to the contacting edges of the teeth.

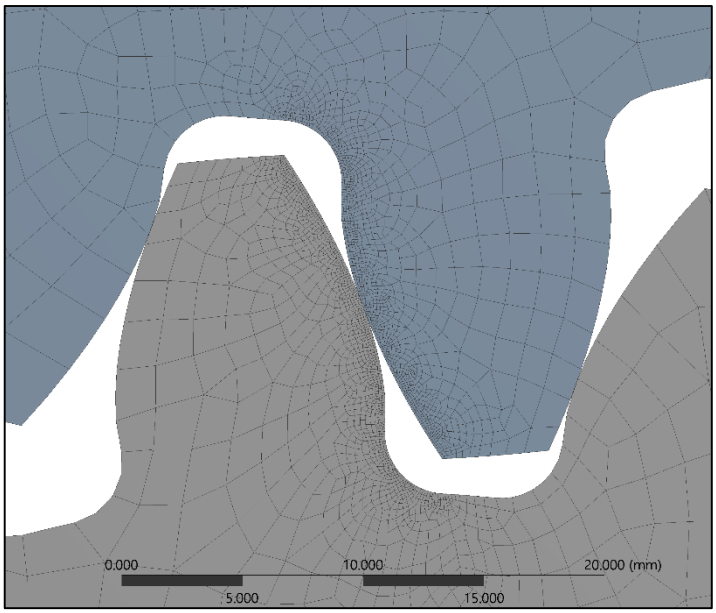

Figure B1 - Teeth Mating

Contact between the contacting edges of the teeth were set to '*Frictionless*'. The '*Formulation*' was set to '*Augmented Lagrange*'. The '*Interface Treatment*' was set to '*Adjust to Touch*'.

A fixed support was applied to the inner circle of the upper gear. A frictionless support was applied to the inner circle of the lower gear. A moment was then applied to the inner circle of the lower gear which would cause the lower gear to rotate in the clockwise direction.

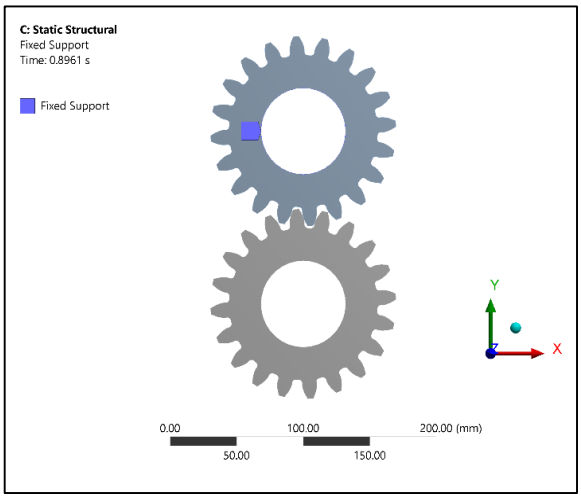

Figure B2 - Fixed Support Applied to Gears

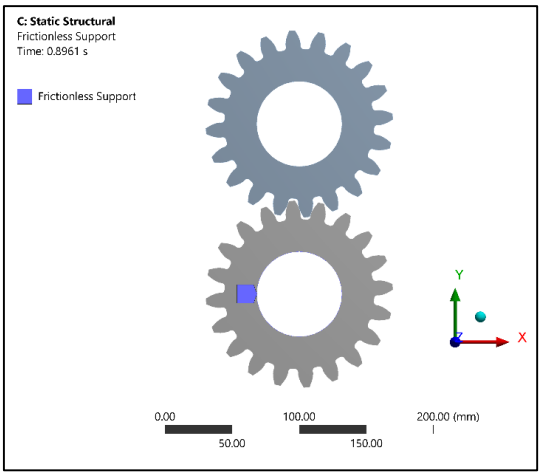

Figure B3 - Frictional Support Applied to Gears

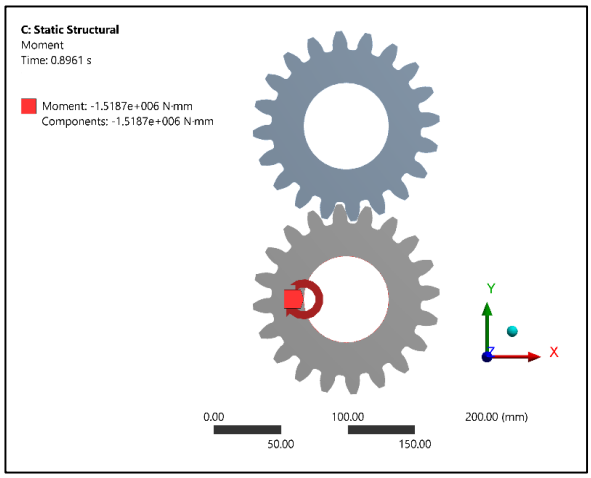

Figure B4 - Moment Applied to Gears

The '*Number Of Steps*' was set to 1, the '*Current Step Number*' was set to 1 and the '*Step End Time*' was set to 1. s.

The pressure from the *'Contact Tool'* states that the maximum contact stress between the two teeth is 1604.4 MPa.

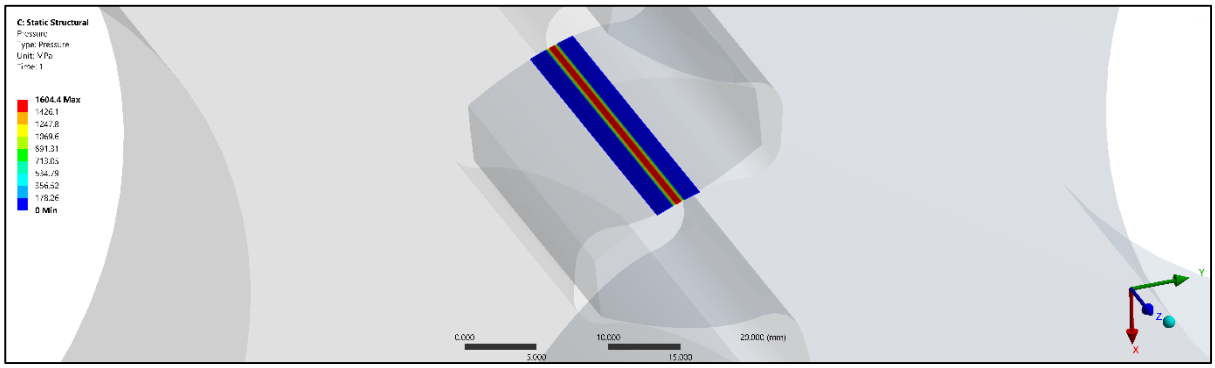

Figure B5 - Contact Stress between Two Mating Teeth

Qualitatively, the von Mises stress solution for the mating teeth indicates that the problem was carried out correctly as it shows that there is a contact between one point on both of the teeth which experiences plastic deformation.

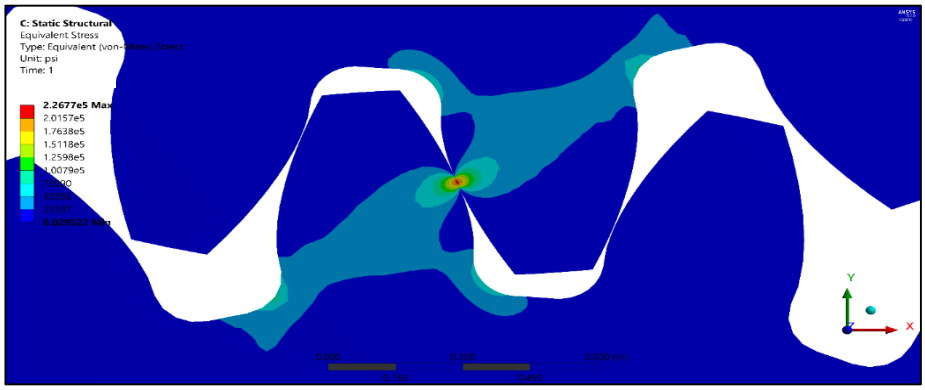

Figure B6 - von Mises Stress Distrubtion in Two Mating Teeth

The maximum von Mises stress comes out to be 2.2677e5 psi (1563.52 MPa) and the solution provided by Huei-Hung Lee in his textbook titled *Finite Element Simulations with ANSYS Workbench 16* comes out to 2.1923E+05 psi, shown below, which is nearly exact. This further validates that the problem was analysed correctly.

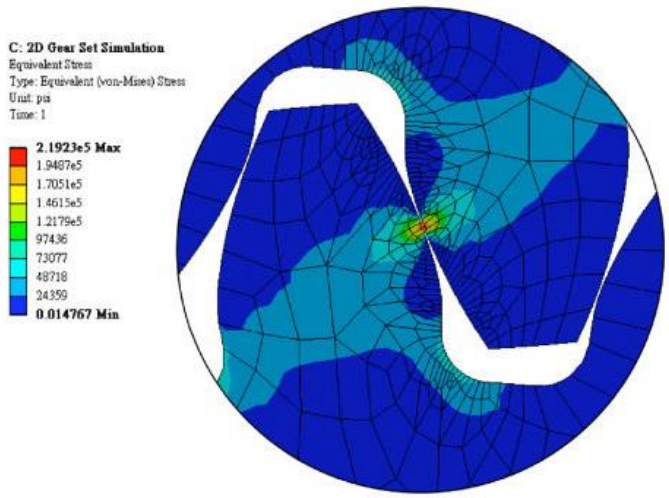

Figure B7 - Reference Solution to von Mises Stress Distribution in Two Mating Teeth (Lee, 2015)

This numerical result reveals an error of 39.9% from the analytical solution of 2601.8 MPa. It was found that a separate study conducted by Vivek Karaveer et al. (2013) arrived at a solution with 10.3% error from the analytical using the same geometry, loading and boundary conditions. It is believed that the reason for this is because a greater force than 53378.66 N.

B.2 Free Vibration

The equations for the following analytical solution was obtained from (Rao, 2010). The deflection of a bar, with respect to position and time, is given by:

$$u(x,t) = \sum_{n=0}^{\infty} u_n(x,t)$$

$$= \sum_{n=0}^{\infty} \sin\frac{(2n+1)\pi x}{2l}\left[C_n \cos\frac{(2n+1)\pi ct}{2l} + D_n \sin\frac{(2n+1)\pi ct}{2l}\right]$$

Where,

$$C_n = \frac{2}{l}\int_0^l u_0(x)\sin\frac{(2n+1)\pi x}{2l}\,dx$$

$$D_n = \frac{4}{(2n+1)\pi c}\int_0^l \dot{u}_0(x)\sin\frac{(2n+1)\pi x}{2l}\,dx$$

And,

$$c = \sqrt{\frac{E}{\rho}}$$

The compressive strain induced in the bar due to F_0 is:

$$\varepsilon = \frac{F_0}{EA}$$

Thus, the displacement of the bar just before the force F_0 is removed (initial displacement) is given by:

$$u_0 = u(x,0) = \varepsilon x = \frac{F_0 x}{EA}, \qquad 0 \le x \le l$$

$$C_n = \frac{2}{l}\int_0^l \frac{F_0 x}{EA}\sin\frac{(2n+1)\pi x}{2l}\,dx = \frac{8F_0 l}{EA\pi^2}\frac{(-1)^n}{(2n+1)^2}$$

Since the initial velocity is zero, we have:

$$\dot{u}_0 = \frac{\partial u}{\partial x}(x,0) = 0, \qquad 0 \le x \le l$$

Since $u_0 = 0, D_n = 0$

$$u(x,t) = \frac{8F_0 l}{EA\pi^2}\sum_{n=0}^{\infty}\frac{(-1)^n}{(2n+1)^2}\sin\frac{(2n+1)\pi x}{2l}\cos\frac{(2n+1)\pi ct}{2l}$$

The solution to $u(x,t)$ was solved iteratively using a Python code developed. The Python code used is shown below:

```
import math as mt
import matplotlib.pyplot as plt
import pylab as pl

F_0 = 1000
L = 1
E = 207*10**9
w=0.1
h=0.1
A = w*h
K = (8*F_0*L)/(E*A*mt.pi**2)

x=1
rho = 7850
c=(E/rho)**0.5

xlist=[]
x2list=[]
ylist=[]
y2list=[]
list1=[]

def solve(t):
    for n in range(0, 100, 1):
            t1=((-1)**n)/((2*(n))+1)**2
            t2=mt.sin(((2*(n)+1)*mt.pi)/2)
            t3=mt.cos(((2*(n)+1)*mt.pi*c*t)/2)
            e=t1*t2*t3
            list1.append(e)
    u=K*sum(list1) #mm
    print("at time, t", t, "u=", u)
    list1.clear()
    xlist.append(t)
    ylist.append(u)
```

```
35.
36. for t in pl.frange(0.0, 0.01, 0.00005):
37.     solve(t)
38. x2list=[] # the x-axis data from the AUTODYN solver output goes here
39. y2list=[] # the y-axis data from the AUTODYN solver output goes here
40. plt.ticklabel_format(style='sci', axis='y', scilimits=(1,4))
41. plt.hold()
42. plt.plot(xlist, ylist,'k--^', label='Analytical Solution')
43. plt.hold()
44. plt.plot(x2list, y2list, 'r-o', label='Numerical Solution')
45. plt.hold()
46. plt.title('Directional Deformation at Free End of Bar')
47. plt.xlabel('Time (s)')
48. plt.ylabel('Deflection (m)')
49. plt.legend(loc='upper right', numpoints=1)
50. pl.xlim([0,0.01])
51. plt.show()
52. plt.savefig('destination_path.eps', format='eps', dpi=1000)
```

The model begins by using the Mechanical APDL solver. This is done to create a 'Pre-Stress Environment' for the Explicit Dynamics (Autodyn Solver) program. The default '*Structural Steel*' material was kept for this bar. The '*Stiffness Behaviour'* was set to '*Flexible*'. The '*Reference Frame'* used was '*Lagrangian'*. Since the loading conditions were loading the bar in the linear-regime, the nonlinear effects could have been set to '*No*' but was left on as '*Yes*' as the same results would have been generated.

The vibrating element consisted of a simple bar with length 1m, width 0.1m and height 0.1m.

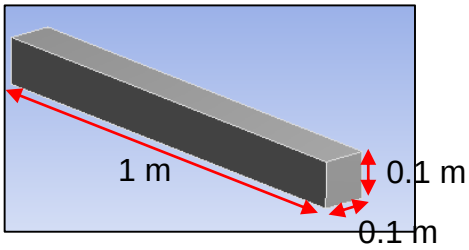

Figure B8 - 3D Model of Bar

'*Body Sizing*' with an '*Element Size*' of 1 mm was used. The '*Physics Preference*' was set to *'Explicit'* so that the mid-side nodes could be dropped. This was necessary for the solution to transfer to Explicit Dynamics (Autodyn Solver). The node and element count is given below.

Table B3 - Mesh Density of Bar

Variable	Value
Nodes	1303101
Elements	1250000

A ‘Fixed Support’ was applied to one end of the bar. A ‘Pressure’, with ‘Magnitude’ set to ‘Tabular Data’, was applied at the other end of the bar. The direction of the pressure was acting from the free-end of the bar towards the fixed-support. The tabular data for the applied pressure is illustrated below.

Table B4 - Tabular Data for the Applied Pressure on the Bar

Steps	Time (s)	Pressure (Pa)
1	0.	0.
	1.	1.e+005
2	1.0001	= 1.e+005
N/A	2.	1.e+005

Since the yield stress of Structural Steel is higher than 1.e+005, the bar was not being loaded in the non-linear regime which is required since the analytical solution will be in the linear regime.

The ‘*Number Of Steps*’ was set to 2, the ‘*Current Step Number*’ was set to 1 and the ‘*Step End Time*’ was set to 1. s.

The solution from Static Structural was transferred to the Setup for Explicit Dynamics (Autodyn Solver).

To pre-stress the bar, Static Structural, which utilised the implicit method, was used first and the solution was then transferred into Explicit Dynamics (Autodyn Solver), which utilised the explicit method.

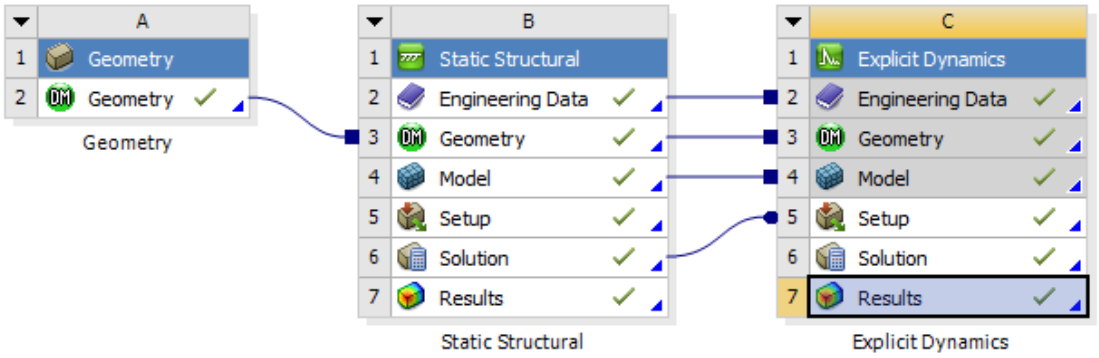

Figure B9 - Creating Pre-Stress Environment for Explicit Dynamics

The fixed support was re-applied to the bar at the same face as in the Static Structural setup as the boundary and loading conditions do not transfer over. No further loading conditions

needed to be added however as the bar was prescribed to be de-compressed at the time that the explicit dynamics analysis started.

The value for '*Resume From Cycle*' was set to 0. The '*End Time*' was set to 1.e-002s and the '*Maximum Energy Error*' was left a '0.1'. The '*Result Number of Points*' was set to 200' so that a clear image of the expected oscillatory motion of the bar could be captured.

The numerical solution in the form of tabular data was placed into a list in Python to be compared to the analytical solution calculated using an iterative process using Python. The Python code for this can be seen below.

B.3 Stress Wave Propagation

The equations for the analytical solution below was obtained from Institut national des sciences appliquées de Toulouse (2014). The speed of the elastic stress wave, c, propagating through the bar is given by:

$$c = \sqrt{\frac{E}{\rho}}$$

For the steel being investigated, this comes out to be:

$$c = \sqrt{\frac{207 \times 10^9}{7800}} = 5.15 \times 10^3 \text{ m/s}$$

The width of the elastic stress wave, z, propagating through the bar is given by:

$$z = ct$$

For this scenario, c is equal to 5.15×10^3 m/s and the time the load acts on the bar, t, is equal to 3.88×10^{-5} s.

$$\text{So, } z = 5.15 \times 10^3 \times 3.88 \times 10^{-5} = 0.2 \text{ m}$$

Therefore, in order to validate the numerical solution for the stress wave propagation through the bar being investigated, the speed of the wave will have to be 5.15×10^3 m/s and the width of the wave will have to be 3.88×10^{-5} m.

The elastic properties of the material used consist of:

- $E = 207 \times 10^3 \text{ N/mm}^2$
- $\upsilon = 0.3$
- $\rho = 7800 \text{ kg/m}^3$

The bar used for this benchmark was similar to the one used for the bar in Benchmark B.2, however, the following dimension changes were made:

- Width = 0.2m (instead of 0.1m);
- H = 0.2m (instead of 0.1m);
- L = 1.0m (remained the same at 1.0m).

A fixed support was applied at the front face of the bar. Displacement set to constant value of zero in z-direction along the top, left, right and bottom surfaces of the bar (with the face at which the fixed support is applied to be the front face as a reference). Displacement set to free in x-direction. It was found that these displacement boundaries were necessary to yield accurate results. A pressure of 0.1MPa was applied to the front face of the bar over a duration of 3.88E-5s. This pressure did load the system into the non-linear regime, which was important since the analytical solution is for the case of the linear regime.

The mesh that was applied to the bar was a body size mesh of 2.5 mm. This corresponded to 2630961 nodes and 2560000 elements.

The stress wave propagation through the bar as a function of position was analysed using the Path tool.

The speed of the wave, calculated by:

$$\left(\frac{\Delta\text{position}}{\Delta\text{time}} = \frac{0.212\text{ m} - 0.0833}{7.5\times10^{-5}\text{s} - 5.0\times10^{-5}\text{s}}\right) = 5.148 \times 10^3\text{ m/s}$$

$$\left(\frac{\Delta\text{position}}{\Delta\text{time}} = \frac{0.342\text{ m} - 0.212}{1.0\times10^{-4}\text{s} - 7.5\times10^{-5}\text{s}}\right) = 5.20 \times 10^3\text{ m/s}$$

$$\text{Average } = \frac{5.20 + 5.148}{2} = 5.174$$

The percent error for the average obtained from these two calculations compared to the analytical solution of 5.15×10^3 m/s is given by:

$$\left|\frac{5.15\times10^3 - 5.174\times10^3}{5.15\times10^3}\right| = 0.47\%.$$

The width of the wave, calculated by (0.3 m - 0.06 m=0.195 m) for the first wave and (0.78 m - 0.54 m = 0.196 m) for the second wave was found to be 0.196 m. The average of 0.1955 m analytical solution of 0.2 m. The percent error for this is $\left|\frac{0.2 - 0.1955}{0.2}\right| = 2.25\%$.

This analysis was replicated in the LS-DYNA solver as a further validation case for the numerical solution obtained using the Autodyn solver. As shown from the figures below, the maximum normal stress in the longitudinal direction was 100,000 Pa as well and the speed of the wave and the width is the same as in the case for the AUTODYN solver output.

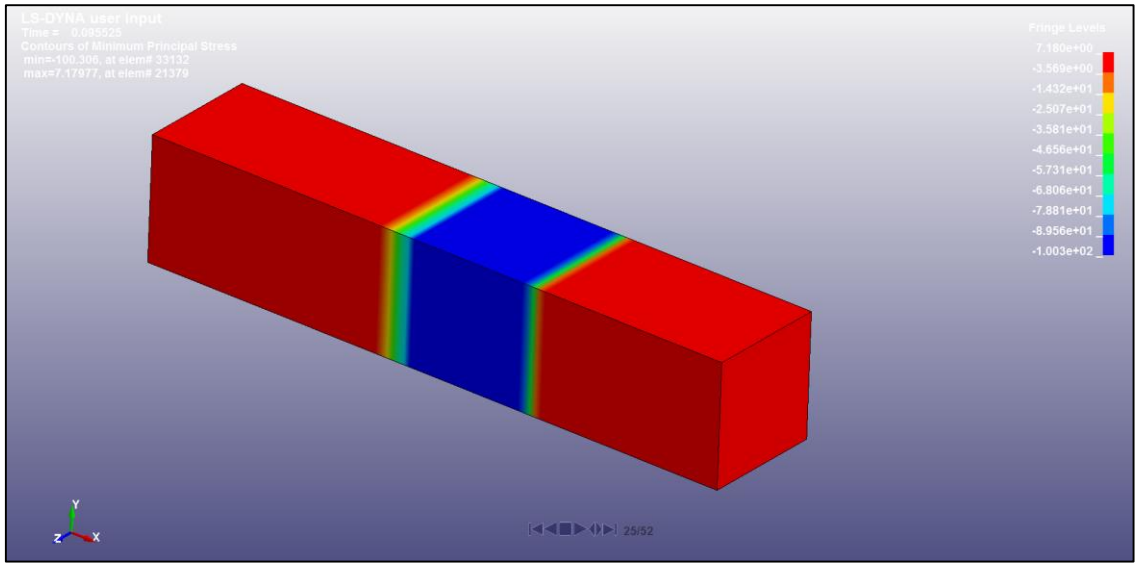

Figure B10 - Stress Wave Propagation in a Bar (using the LS-DYNA solver) at Time 1

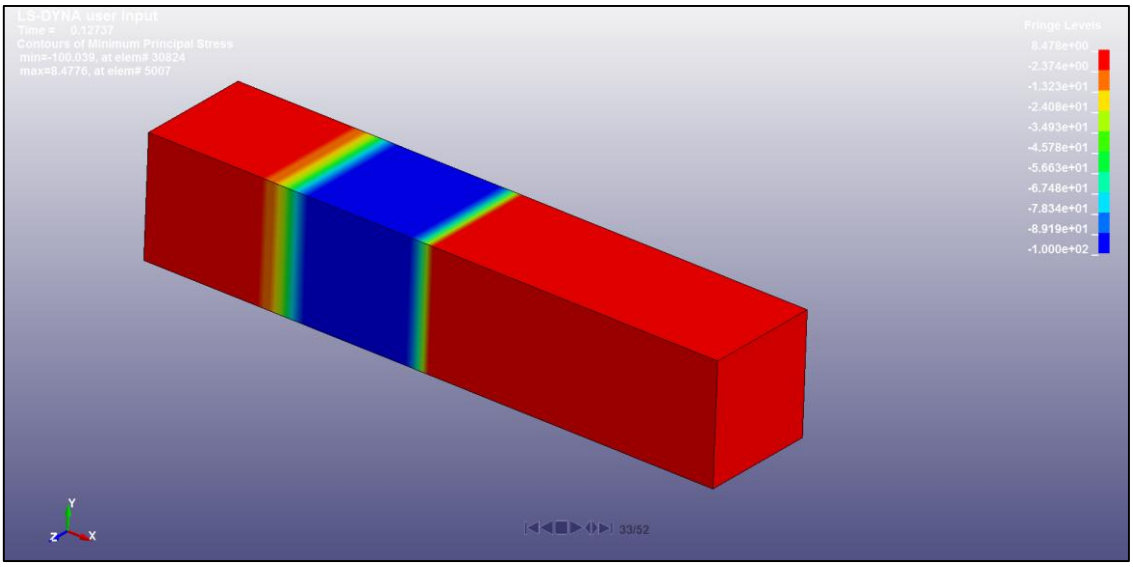

Figure B11 - Stress Wave Propagation in a Bar (using the LS-DYNA solver) at Time 2

B.4 The Perfect Plasticity Model and Isoptropic Hardening Model

The following procedure was used to conduct a study on the perfect plasticity problem.

The elastic properties used for this benchmark are:

- $E = 207 \times 10^3\ N/mm^2$
- $\upsilon = 0.3$

The plastic properties are:

- $\sigma_{ys} = 208\ N/mm^2$

The behaviour for this 2D analysis was set to axisymmetric.

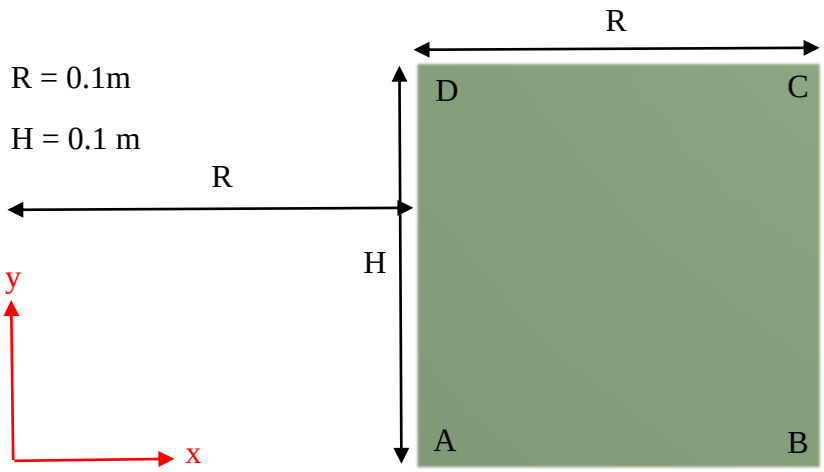

Figure B12 - Geometry used for Pressurised Cylinder Problem

64 eight-node elements were used to model this problem. This does not achieve mesh independency but for the reference solution provided by *NAFEMS* this is the mesh density that was used.

A displacement was set to constant value of zero in the y-direction along line AB and line DC. Displacement set to free in x-direction. The internal pressure at time equal to zero is always zero. Then, an internal pressure, P, at line AD is applied in five steps, as follows: P = 80, 100, 120, 140 and 160 MPa. The pressure is meant to ramp up from zero to these five steps.

The end time for this analysis was set to 1s. This was necessary for the numerical solution to match the reference solution provided by NAFEMS.

The same geometry, mesh and boundary conditions was used to conduct a study on the isotropic hardening model. However, to incorporate the isotropic hardening model into the material for the pressurised cylinder, a bilinear stress-strain relationship was used. For this, the tangent modulus, E_T was set to 4.2×10^3 MPa. Then, an internal pressure, P, at line AD is

applied in five steps, as follows: P = 10, 14, 24, 34 MPa. The pressure is meant to ramp up from zero to these five steps. Once again, the pressure ramped up from zero to these four steps.

B.5 Friction between Two Surfaces

The analytical solution for the final position, x_f, a cube reaches after a force, F, is applied to it to make it slide across a floor surface with a constant friction coefficient, μ, is given by:

$$x_f = \frac{1}{2}at^2 \text{ where } a = \frac{F - N\mu}{m}$$

For the case being studied, the cube has dimensions 0.16 m by 0.16 m by 0.16 m. Also, the force acting on the cube causing it to slide across the floor surface will be applied in seven steps: F = 14000 N, 12000 N, 10000 N, 8000 N, 6000 N, 4000 N and 3500 N. The coefficient of friction between the cube and the floor surface will be a constant friction coefficient of 0.5, which means when the cube is static or dynamic the friction coefficient will remain the same. The normal force acting on the top face of the cube was set to a constant value of 7000 N. The analytical solution will be shown in the format of a graph, together with the numerical solution, later in this section.

The cube, as previously dimensioned, was set to '*Rigid*' and the floor surface was set to '*Flexible*' since only one body can be set to rigid at a time in the Autodyn solver. Ideally, the cube and the surface should have been rigid.

The contact between the cube's bottom surface and the floor surface was set to '*Frictional*' and since the '*Target Surface*' always has to be the rigid surface, the cube's bottom surface was set as the target surface and the floor surface was set as the '*Contact Surface*'.

Since the cube was set to rigid and the deformation of the surface was not of concern, the default mesh density was used.

A fixed boundary condition was applied to the bottom face of the floor surface. The loads applied to the cube were applied in steps as discussed earlier.

B.6 Sheet Metal Forming

The reference solution for this benchmark comes from the work conducted by Mamalis et al. In his paper '*Simulation of Sheet Metal Forming using Explicit Finite-Element Techniques: effect of material and forming characteristics Part 1. Deep-Drawing of Cylindrical Cups*', Mamalis et al. produces experimental data for the punch load-punch travel for a metal forming process as well as experimental data for the radial, hoop and thickness strain endured by the blank. This benchmark is aimed at replicating the numerical and experimental results conducted by Mamalis et al.

The dimensions of the blank, punch and die used for the geometry can be found below. Refer to Figure 33 for a schematic of the sheet metal forming problem being discussed.

Table B5 - Geometry for Sheet Metal Forming Simulation (Mamlis et al.,1997)

Blank		**Punch**		**Die**		**Cup Height**
D_0 (mm)	**T_0 (mm)**	**D_1 (mm)**	**R_1 (mm)**	**D_2 (mm)**	**R_2 (mm)**	**h_{max} (mm)**
121	0.84	66.5	4	70	8	45

The wall thickness of the punch did not appear to be specified in the paper produced by Mamalis et al. and getting this wall thickness correct was necessary as the inertial forces involved will be effected by the mass of the punch. To solve this problem, an energy balance was conducted with the experimental data for the punch load-punch travel curve provided. This allowed for the mass of the punch to be estimated and from there assuming a height of 45 mm, the wall thickness could be calculated.

Energy balance:

KE = Work Done

$$\frac{1}{2}m_p v^2 = A$$

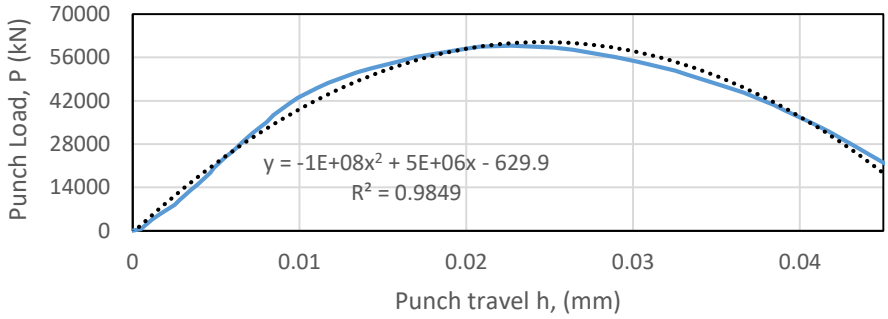

Figure B13 – Experimental-Simulated Curve for Galvanised Steel (Mamalis et al., 1997)

$$y = -1 \times 10^8 x^2 + 5 \times 10^6 x - 629.9$$

$$\int_0^{0.045} (-(1 \times 10^8)x^2 + 5 \times 10^6 x - 629.9)dx = 1996.65$$

So, A = 1996.65 J

$$m_p = \frac{2A}{v^2} = \frac{2(1996.65)}{(200)^2} = 0.0998325 \text{ kg}$$

Therefore, the mass of the piston, m_p, was 0.0998325. This corresponded to a wall thickness of approximately 1.1 mm.

The chosen material for the blank was 'Galvo 1' (Mamalis, 1997). The mechanical properties for this material can be found in the table below.

Table B6 - Material Properties for Blank made from 'Galvo 1' (Mamalis et al., 1997)

E (MPa)	Y (MPa)	E_t (MPa)	$\rho \left(\frac{kg}{m^3}\right)$
2.1E+04	286	482	7.8

Note that the density of the blank is an order of 10^3 smaller than the actual value in order to reduce the dynamic effects of the system by increasing the punch velocity.

The analysis was conducted as a 2D axisymmetric model. Furthermore, the punch and die were modelled as rigid to reduce CPU time required. The table below summarises the mesh density of the blank.

Table B7 - Mesh Density of the Blank

Nodes	824
Elements	589

A constraint was applied to the punch so that it was free to move only in the y-axis (but have a constant zero displacement in the x and z-axes). Furthermore, a fixed support was applied on the solid geometry of the die. The boundary interaction between the punch and the blank was made to be frictional with a frictional coefficient of 0.03. Also, a pressure of 9.1385 MPa was applied to the top surface of the blank through the blankholder positioned on top of the blank (this was equivalent to if a force of 26kN was applied). Finally, the simulated punch velocity was set to a constant value of 200 m/s.

In order to visualise the 2D model in 3D, '*Beta Options*' were turned on and *Symmetry* was introduced into the model. The Symmetry options were set to *2D Axisymmetric*.

A force reaction probe was added to the solution in order to validate that the simulated punch load-punch travel curve was achieved for this simulation. The options chosen for the probe can be seen below.

Details of "Force Reaction"	
Definition	
Type	Force Reaction
Location Method	Boundary Condition
Boundary Condition	Velocity
Orientation	Y Axis
Suppressed	No
Results	
Minimum	-3.3796e+005 N
Maximum	0. N
Filter	
Type	None

Figure B14 - View of Force Reaction Probe Settings

B.7 Taylor Bar Impact Test

The projectile was a perfectly cylindrical specimen with a radius of 3.81 mm and a length of 25.4 mm. The rigid wall it impacted was 8 mm in radius and 2 mm in depth.

The mesh of the projectile specimen was varied between a body sizing of 0.3 mm and 0.1 mm. The mesh of the wall did not matter since it was being modelled as rigid.

A fixed support was applied to the rigid wall that the piston impacted. Furthermore, the impact velocity of the cylindrical specimen into the rigid wall was set to 208 m/s to match the expriment conducted by Banerjee (2007) and the impacting face of the piston was drawn touching the reacting face of the rigid wall (thus, there was no gap between the piston and the wall at the initial time). Also, the contact between the projectile specimen and the wall was set to frictionless.

The end time of the analysis was set to 2E-04 as this was found to be a sufficient time for the projectile specimen to reach its final deformed state after impacting the rigid wall.

The high strain rate material data used for the 4340 steel projectile can be found in the table below.

Table B8- Material Data for Projectile Specimen (Banerjee, 2007)

Property	**4340 Steel**
Density (kg/m^3)	7850
Specific Heat (J(/kg. °C))	475
Fitting Parameter A (MPa)	792
Fitting Parameter B (MPa)	510
Fitting Parameter n	0.26
Fitting Parameter C	0.014
Fitting Parameter m	1.03
Melting Temperature (K)	1793
Reference Strain Rate (/sec)	1
Shear Modulus (MPa)	81800
Gruneisen Coefficient	1.69
Parameter C1 (m/s)	3935
Parameter S1	1.578
Parameter Quadratic S2 (s/m)	0

Appendix C
Material Details for Metal Parts in T4

C.1 Stainless Steel

The piston body is made from 304 stainless steel. The following section looks into the material description for stainless steel. The Johnson-Cook model fitting parameters obtained by Frontán, J. et al. (2012), at a reference strain rate of 1 s^{-1}, are illustrated in the table below.

Table C1 - Johnson-Cook Model Fitting Parameters for 304 Stainless Steel

Material	A (MPa)	B (MPa)	C	n	m	$\dot{\varepsilon}_0$ (s^{-1})
304 Stainless Steel	280	802.5	0.0799	0.622	1	1

According to A. Dorogoy et al. (2009), the material behaviour of most metals differ within the "quasi-static loading" regime compared to the "dynamic loading" regime. For the best representation of the material behaviour during dynamic loading, the reference strain rate ($\dot{\varepsilon}_0$) typically must be of the same order of magnitude as the transition strain rate. However, for the purposes of extending the range of validity of the Johnson-Cook material model from the dynamic loading regime into the quasi-static regime as well, the reference strain rate is typically set to 1 s^{-1}, as discovered in previous work.

The figure below compares the stress-strain curve acquired from a quasi-static and Hopkinson bar high-strain rate test to that predicted by the Johnson-Cook material model. The reference strain rate used for this study was 1 s^{-1}. Nevertheless, the results reveal that only an approximate match could be achieved for the quasi-static loading conditions, despite the fact that a reference strain rate of 1 s^{-1} was used in the calibration process, whereas an accurate match was achieved for the dynamic loading condition at a strain rate of 510 s^{-1}.

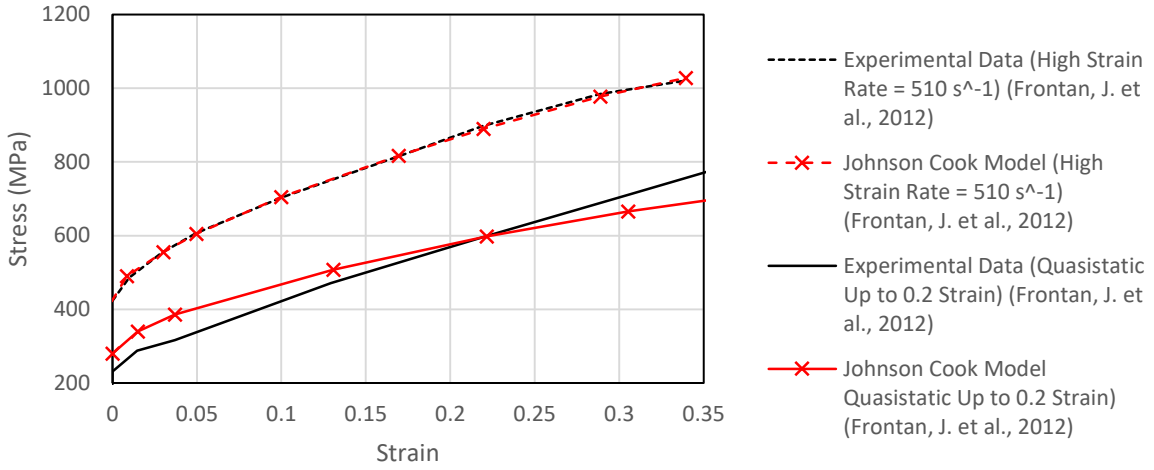

Figure C1 - Stress-Strain Plot for 304 Stainless Steel (T=298K)

In order to evaluate the influence that the fitting parameters from the Johnson-Cook material model had on the stress-strain curve for 304 stainless steel, the fitting parameters obtained by Frontán, J. et al. (2012) was compared to that obtained by Mori, L. et al. (2007) and Krasauskas, P. et al. (2015). These fitting parameters can be found in the table below. The fitting parameters for 316L, obtained by Olleak, A. et al. (2015), was also included in the table below so that a comparison between the material properties of these two different grades of stainless steel could be made.

Table C2 - Johnson-Cook Model Parameters for 304 Stainless Steel and 316L Stainless Steel.

Material	**A (MPa)**	**B (MPa)**	**C**	**n**	**m**	$\dot{\varepsilon}_0$ (s^{-1})	**Source**
304 Stainless Steel I	280	802.5	0.0799	0.622	1	1	Frontán, J. et al., 2012
304 Stainless Steel II	320	1000	0.07	0.65	1	1	Mori, L. et al., 2007
304 Stainless Steel III	280	802.5	0.0799	0.0622	1	1	Krasauskas, P. et al., 2015
316L Stainless Steel I	305	1161	0.01	0.61	0.517	1	Olleak, A. et al., 2015

The fitting parameters obtained by Frontán, J. et al. (2012) matched those obtained by Krasauskas, P. et al. (2015). Thus, 304 Stainless Steel III could be ignored from the analysis since it was already represented by 304 Stainless Steel I. However, Mori, L. et al. (2007)

obtained different fitting parameters which were still similar in values. The yield stress (A) hardening modulus (B) and hardening exponent (n) for 316L stainless steel are also similar in values to those of 304 stainless steel. This meant that the yield strength of the materials, as well as the flow stress and the strain hardening effect are similar. But, the strain rate coefficient (C) and thermal softening exponent (m) differ drastically. Since C was far lower for 316L stainless steel compared to 304 stainless steel, this indicated that the flow stress-to-strain rate for 316L was far less sensitive. Additionally, the lower m value indicated that the thermal softening phenomena in 316L was less compared to that observed by 304 stainless steel.

The effect that strain had on the stress-strain curve is displayed in the figure below.

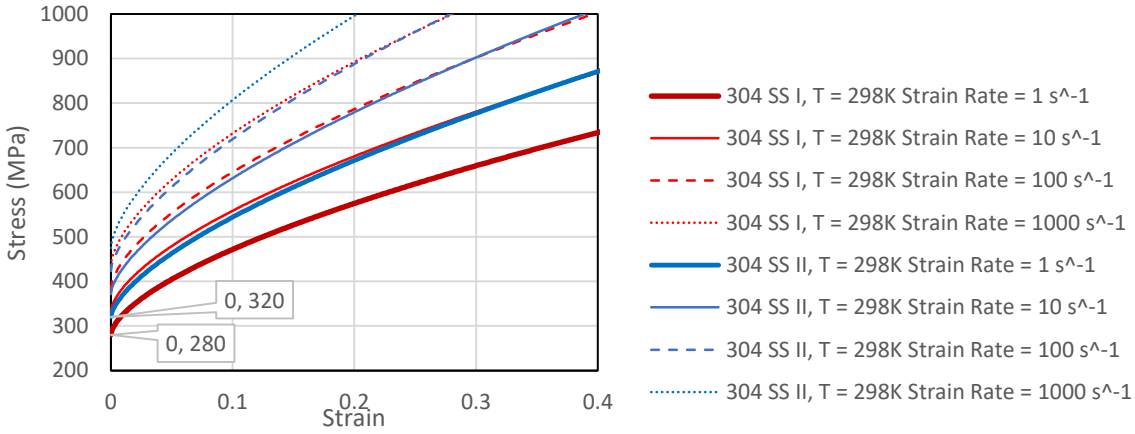

Figure C2 - Strain Rate Effect on Stress-Strain Plot for 304 Stainless Steel (Generated using Johnson-Cook Material Model)

The effect that temperature had on the stress-strain curve is displayed in the figure below.

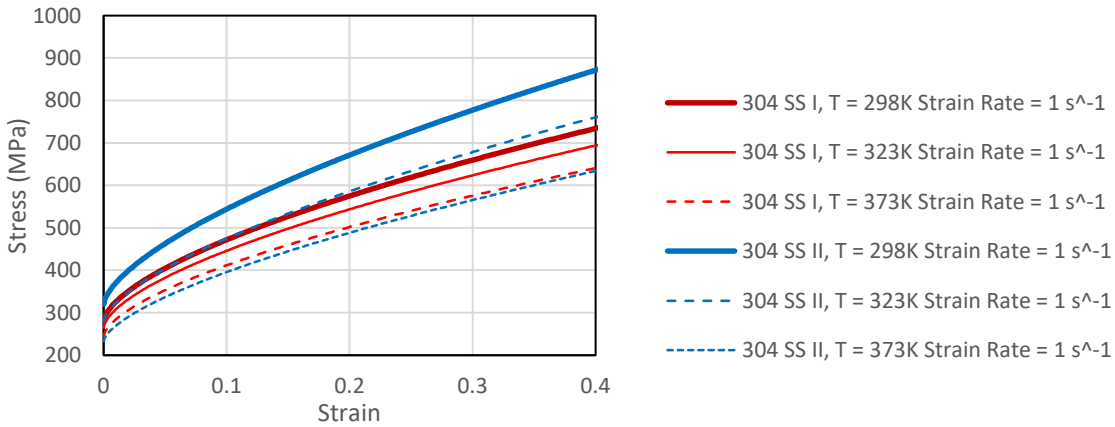

Figure C3 - Temperature Change Effect on Stress-Strain Plot for 304 Stainless Steel (Generated using Johnson-Cook Material Model)

As the strain rate increases, so too does the stress level predicted by the Johnson-Cook material model. As the temperature increases, the stress level decreases to that predicted by the Johnson-Cook material model. Furthermore, it can be seen from Figure that when the strain rate is equal to 1, the y-intercept equates to the fitting parameter (A) in the Johnson-Cook model. As the strain rate increases, so too does the value of the y-intercept and the overall stress levels. It is clear from Graph 2 that the fitting parameters used for 304 Stainless Steel I and 304 Stainless Steel II have a significant impact on the stress levels observed.

While Frontán, J. et al. (2012), Mori, L. et al. (2007) and Krasauskas, P. et al. (2015) all claimed to achieve accurate numerical results compared to their respective experimental investigations, it is apparent that there is no universally accepted fitting parameters for a material. For this thesis, the fitting parameters obtained by Frontán, J. et al. (2012) will be selected.

The parameters for the Mie- Grünsien equation of state for 304 stainless steel, and similar materials, were compiled from various sources which claimed to achieve accurate numerical results. These can be found in the table below.

Table C3 - Mie- Grunsien Equation of State Parameters for 304 Stainless Steel

Material	**Γ_0**	**C_0 (m/s)**	**S_α**	**Source**
304 Stainless Steel I	1.93	4570	1.49	Steinberg, D., 1996
304 Stainless Steel II	1.92	4581	1.49	Duffy, T. et al 1997
304 Stainless Steel III	2.17	4569	1.49	Los Alamos Scientific Laboratory, 1969
316L Stainless Steel	1.93	4569	1.49	Winter, R. et al., 2014

The results in the table above reveal that there is close agreement between the Grünsien coefficient, bulk speed of sound and linear Hugoniot slope coefficient for 304 stainless steel and also that the parameters for the 316L stainless steel are similar to that of 304 stainless steel. The equation of state parameters that will be chosen for 304 stainless steel in the explicit dynamics analysis will be that of 304 Stainless Steel I since its values lie approximately in the centre of the other listed 304 stainless steel material parameters.

C.2 Aluminium Alloys

The parameters for the Johnson-Cook strength model for Aluminium bronze, and similar materials, were obtained from various sources which claimed to achieve accurate numerical results. These can be found in the table below.

Table C4 - Johnson-Cook Model Parameters for Aluminium and Aluminium Bronze

Material	A (MPa)	B (MPa)	C	n	m	$\dot{\varepsilon}_0$ (s^{-1})	Source
Aluminium 2024-T3	370	684	0.0083	0.73	1.7	1	Kay, G., 2003
Aluminium 6061-T6	324	114	0.002	0.42	1.34	1	Dassault Systèmes, 2012
Aluminium Bronze (QAL9-4)	430	904	0.016	0.66	2.4	1	Li, J. Guo, 2015
Nickel Aluminium Bronze	295	759.5	0.023	0.4757	1.24	1	Fu, Z. et al., 2016

The effect that strain had on the stress-strain curve is displayed in the figure below.

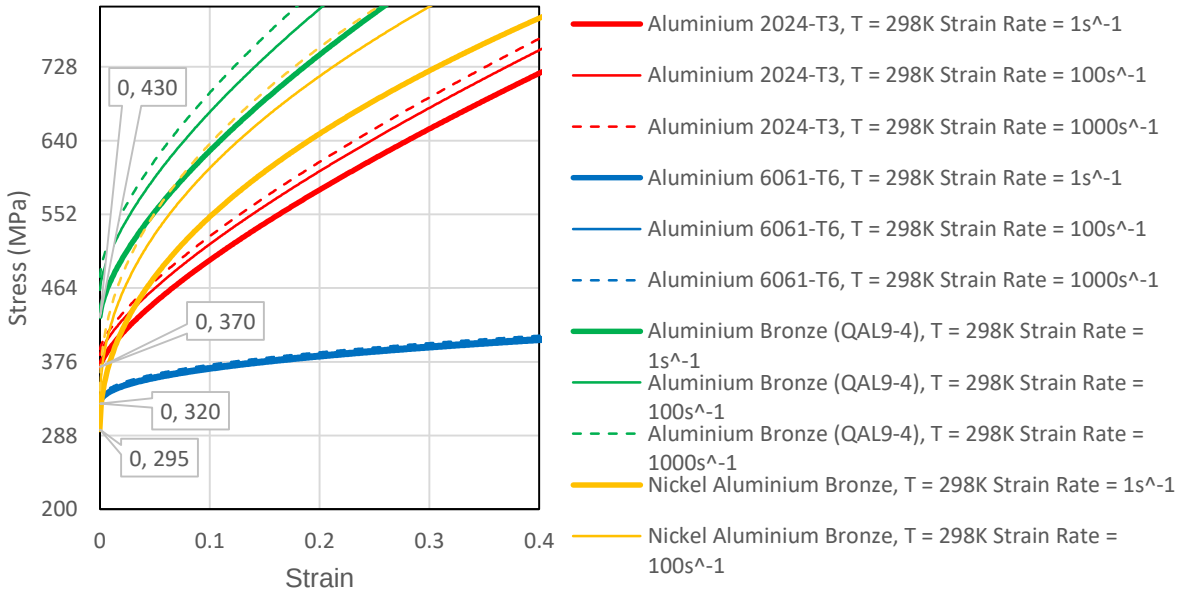

Figure C4 - Strain Rate Effect on Stress-Strain Plot for Aluminium and Aluminium Bronze (Predicted by the Johnson-Cook Material Model)

The effect that temperature had on the stress-strain curve is displayed in the figure below.

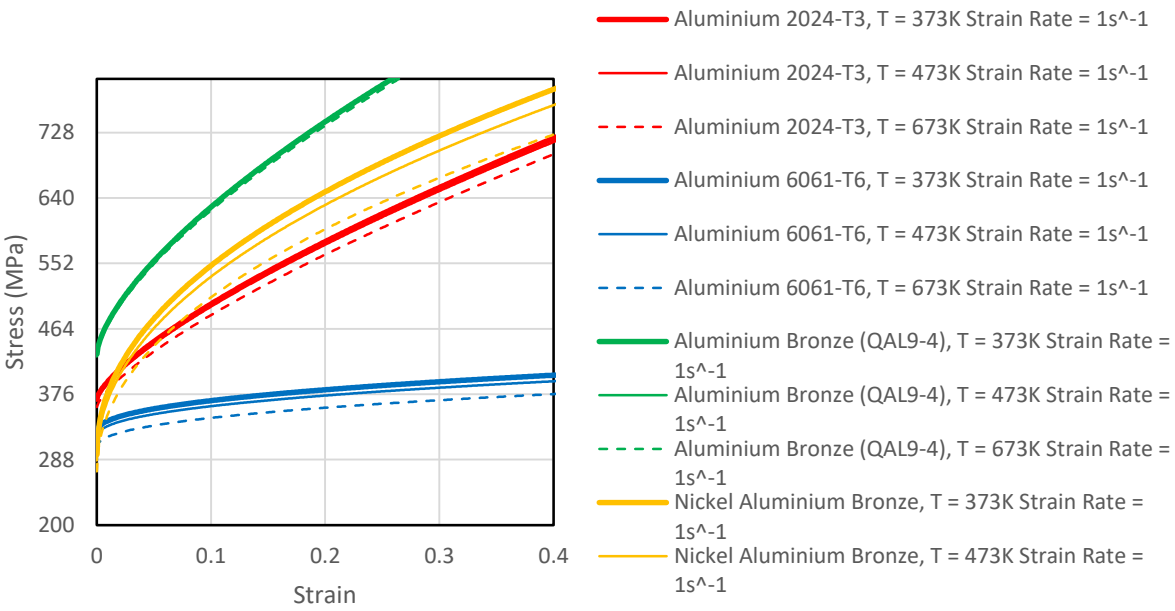

Figure C5 - Temperature Change Effect on Stress-Strain Plot for 304 Stainless Steel (Predicted by the Johnson-Cook Material Model)

Aluminium Bronze (QAL9-4) material data for the Johnson-Cook matrial model was selected to model the aluminium bronze components in the T4 piston impact analysis.

The parameters for the Mie- Grünsien equation of state for aluminium bronze, and similar materials, were also compiled from various sources which claimed to achieve accurate numerical results. These can be found in the table below.

Table C5 - Mie- Grunsien Equation of State Parameters for Aluminium Bronze

Material	Γ_0	C_0 (m/s)	S_α	Source
Aluminium Bronze	2.0	5328	1.338	Johnson & Cook, 1969
Aluminium 6061 -T6	2.0	5350	1.338	Duffy, T. et al 1997
Aluminium 2024-T3	2.0	5335	1.34	Duffy, T. et al 1997

The Aluminium Bronze material data in the above table for the Linear Shock EOS was selected to be the material to model the aluminium bronze components in the T4 piston impact analysis.

C.3 Mild Steel

The parameters for the Johnson-Cook strength model for mild steel, and similar materials, were also from various sources which claimed to achieve accurate numerical results. These can be found in Table 4.

Table C6- Johnson-Cook Strength Model Parameters for Mild Steel

Material	A (MPa)	B (MPa)	C	n	m	$\dot{\varepsilon}_0$ (s^{-1})	Source
Mild Steel	217	234	0.076	0.51	1	1	Vedantam, K. et al., 2006
A36 Mild Steel I	286	500	0.017	0.228	0.917	1	Schwer, L., 2007
A36 Mild Steel II	282	500	0.023	0.228	0.917	1	Seidt, J. et al, 2007
Steel 1006	350	275	0.022	0.36	1	1	Cook, W. et al., 1969

The effect that strain had on the stress-strain curve is displayed in the figure below.

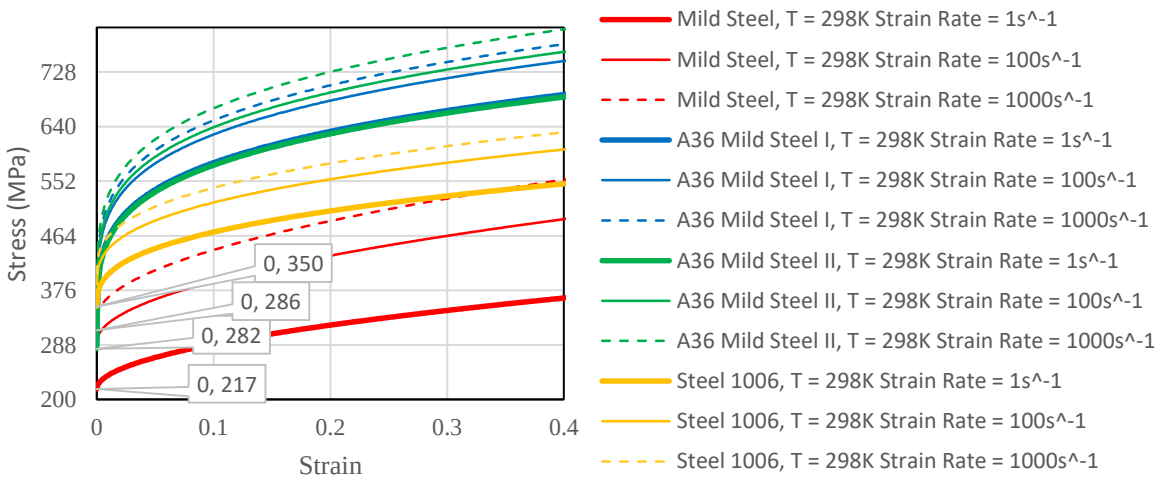

Figure C6 - Strain Rate Effect on Stress-Strain Plot for Mild Steel (Predicted by the Johnson-Cook Material Model)

The effect that temperature had on the stress-strain curve is displayed in the figure below.

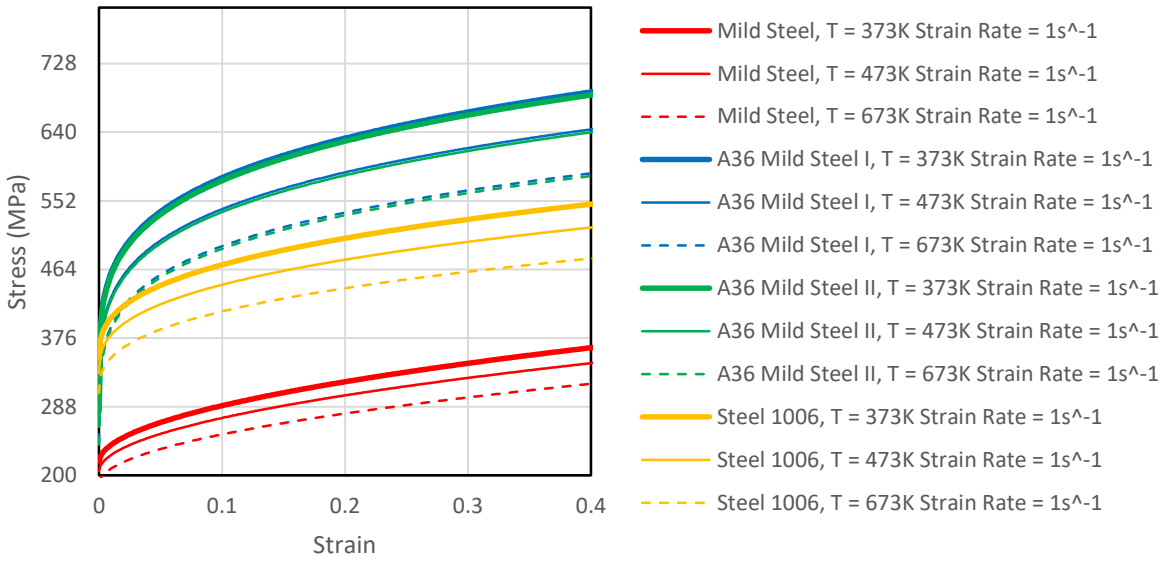

Figure C7- Temperature Change Effect on Stress-Strain Plot for Mild Steel (Predicted by the Johnson-Cook Material Model)

The A36 Mild Steel II material data for the Johnson-Cook matrial model was selected to be the material to model the buffer plate in the T4 piston impact analysis.

The parameters for the Mie- Grünsien equation of state for mild steel, and similar materials, were also compiled from various sources which claimed to achieve accurate numerical results. These can be found in the table below.

Table C7 - Mie- Grünsien Equation of State Parameters for Mild Steel

Material	Γ_0	C_0 (m/s)	S_α	Source
A36 Mild Steel I	2.17	4569	1.49	Roy, S., 2015
A36 Mild Steel II	2.17	4569	1.49	O'Toole, B. et al. 2015
Steel 1006	2.17	4569	1.49	Cook, W. et al., 1969

The A36 Mild Steel I material data in the above table for the Linear Shock EOS was selected to be the material to model the aluminium bronze components in the T4 piston impact analysis.

C.4 EN25 High Tensile Strength Steel

The parameters for the Johnson-Cook strength model for 4340 and 4140 high tensile steel were compiled from various sources which claimed to achieve accurate numerical results. These can be found in Table C8.

Table C8 - Johnson-Cook Strength Model Parameters for EN25 Steel

Material	A (MPa)	B (MPa)	C	n	m	Source
4340 High Tensile Steel I	792	510	0.014	0.26	1.03	Cook, W. et al., 1985
4340 High Tensile Steel II	792	510	0.014	0.26	1.03	Schreiber, Jeremy, 2013
4340 High Tensile Steel III	792	510	0.014	0.26	1.03	Banerjee, B., 2007
4140 High Tensile Steel I	595	580	0.023	0.133	1.03	Agmell, M. et al., 2013
4140 High Tensile Steel II	598	768	0.0137	0.2092	0.807	Arrazola, P.J. et al, 2002

The results in the above table reveals that there is close agreement between Johnson-Cook parameters for 4340 and 4140 steel. The nominal Johnson-Cook parameters that will be chosen for the EN25 steel material in the explicit dynamics analysis will be that of 4340 High Tensile Steel II these parameters were used in a benchmark and accurate results to experimental data were obtained whereas benchmarks were not conducted towards the validity of the other parameters (although the values for the parameters are similar).

The effect that strain had on the stress-strain curve is displayed in the figure below.

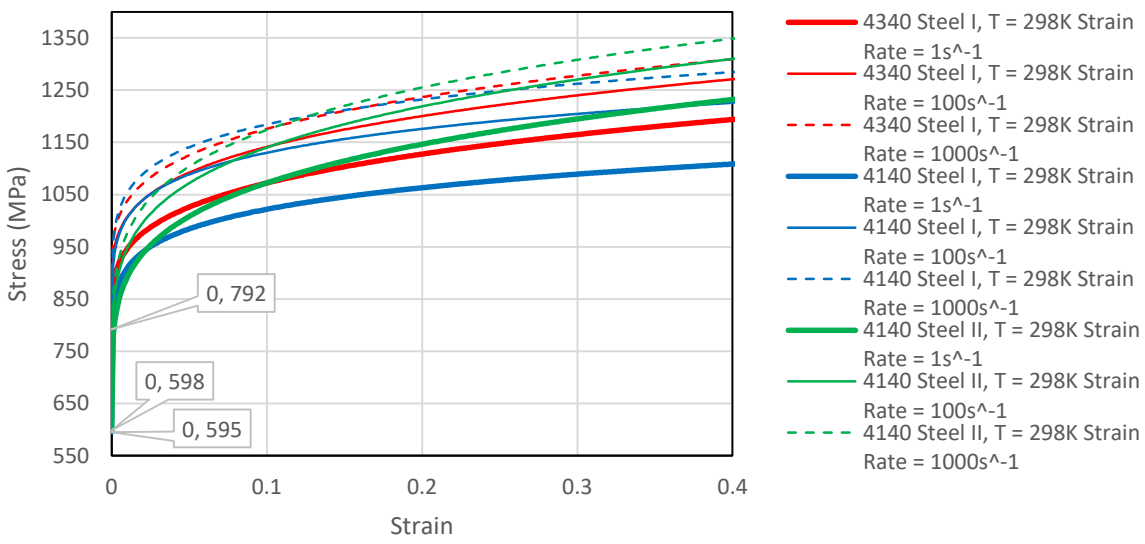

Figure C8 - Strain Rate Effect on Stress-Strain Plot for 4340 and 4140 Steel (Predicted by the Johnson-Cook Material Model)

The parameters for the Mie- Grünsien equation of state for 4340 and 4140 high tensile steels were also compiled from various sources which claimed to achieve accurate numerical results. These can be found in the table below.

Table C9 - Mie- Grunsien Equation of State Parameters for EN25 Steel

Material	Γ_0	C_0 (m/s)	S_α	Source
4340 High Tensile Steel I	1.69	3935	1.578	Steinberg, D., 1996
4340 High Tensile Steel II	1.69	3935	1.578	Banerjee, B., 2007
4340 High Tensile Steel III	1.69	3935	1.578	Shivpuri, R. et al, 2009
4140 High Tensile Steel I	1.69	3935	1.578	Agmell, M. et al., 2014

The results in the above table reveal that the Grünsien coefficient, bulk speed of sound and linear Hugoniot slope coefficient used in literature for 4340 and 4140 high tensile strength steel are the same. In this case it does not matter which material data is seleced to model the EN25 as they are all the same.

Appendix D
Axisymmetric T4 Piston

D. Axisymmetric Validity of T4 Piston

The following study involved having both a full 3D model and a 2D axisymmetric model of the T4 impact a rigid wall at a velocity of 200 m/s. This impact velocity was selected as it was higher than the impact velocities investigated in the explicit FEA of the T4 facility and thus if any 3D deformations would occur they would occur at the higher loadings involved in having the piston impact a rigid wall at higher velocities.

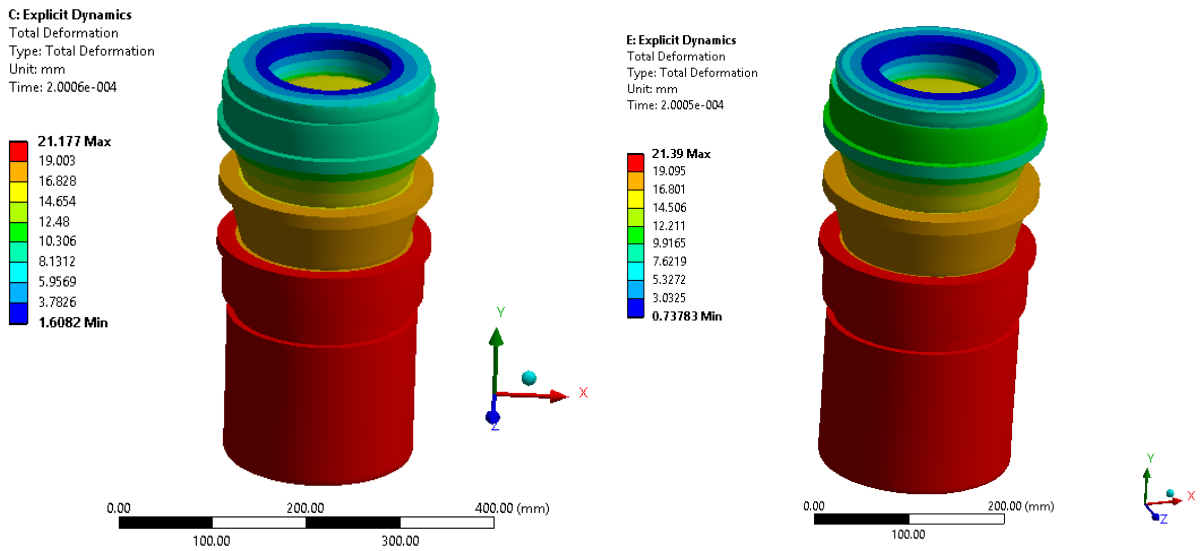

Figure 127 - Comparison of Total Deformation between 3D Model of T4 Piston (Left) and 2D Axisymmetric Model of T4 Piston (Right)

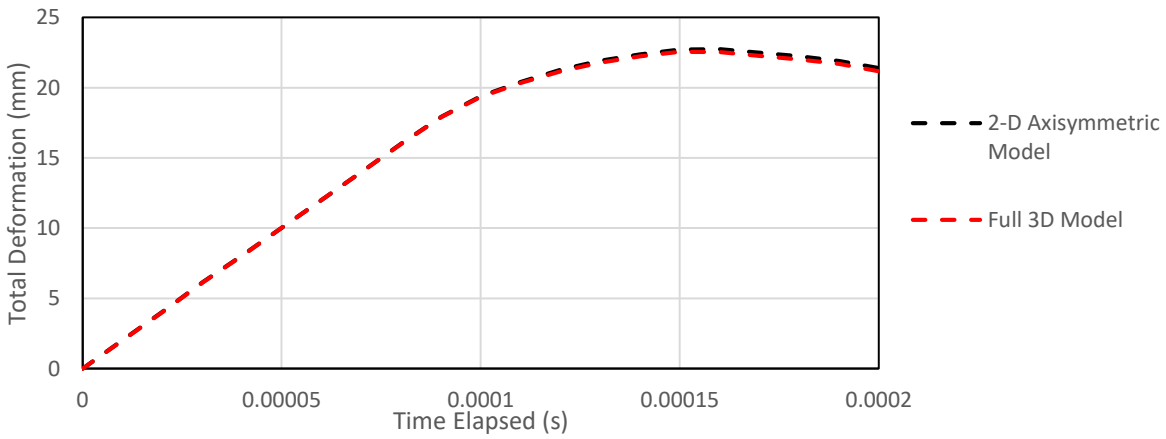

Figure D2 - Maximum Total Deformation of T4 Piston at Impact Speed of 200 m/s

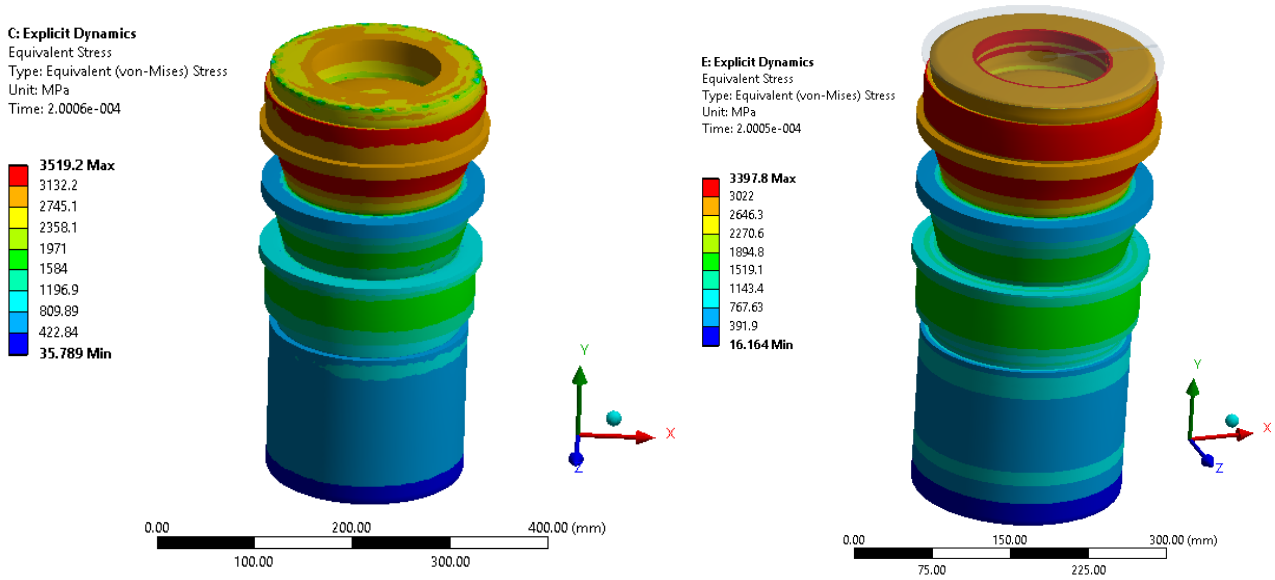

Figure D3 - Comparison of Equivalent (von-Mises) Stress between 3D Model of T4 Piston (Left) and 2D Axisymmetric Model of T4 Piston (Right)

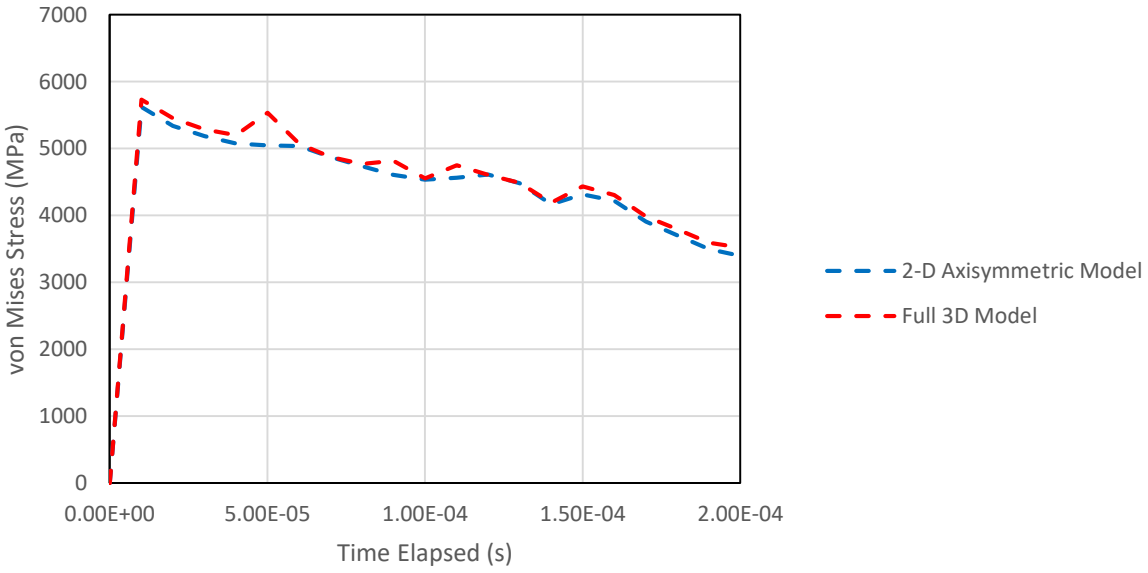

Figure D4 - Maximum Effective Stress of T4 Piston at Impact Speed of 200 m/s

It can be seen that the T4 piston can be treated as a 2D axisymmetric model rather than a 3D full model since the two separate models arrive at the same total deformation and von mises stress distributions in the T4 piston.

Appendix E
T4 Buffer

E. Buffer Analysis

The following study involved validating the fact that the rubber buffer would be completely obliterated at the impact velocity of 61 m/s. The figure below shows the T4 piston disintegrating the rubber buffer at an impact speed of 61 m/s. This realised by the red dots indicating that the erosion algorithm is deleting elements of the rubber buffer that are deforming more than 150% of their original size.

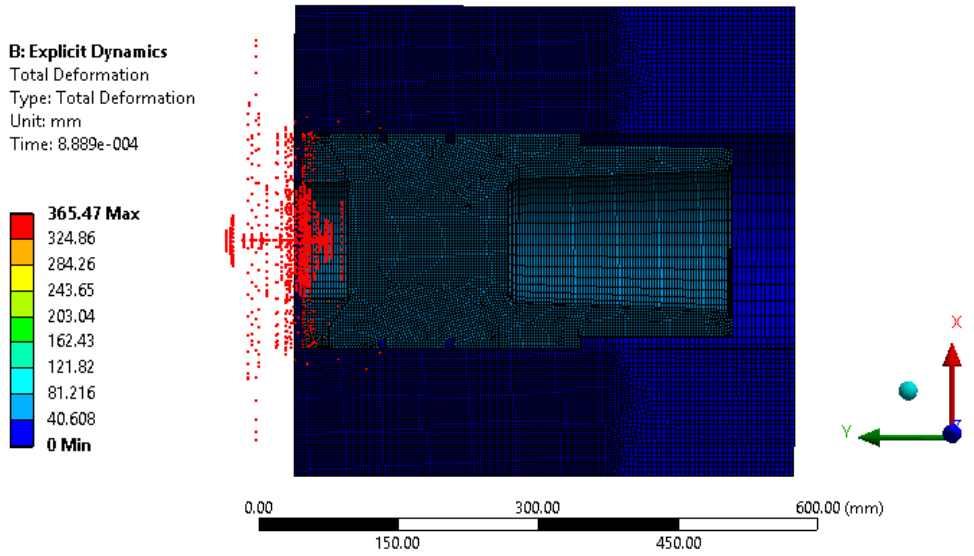

Figure E1- T4 Piston Disintegrating Rubber Buffer at an Impact Speed of 61 m/s

The figure below reveals that the rubber buffer slows down the piston before impacting the buffer plates from 61 m/s to 58 m/s. This was deemed to be a relatively small difference and thus the rubber buffer was omitted from the analysis.

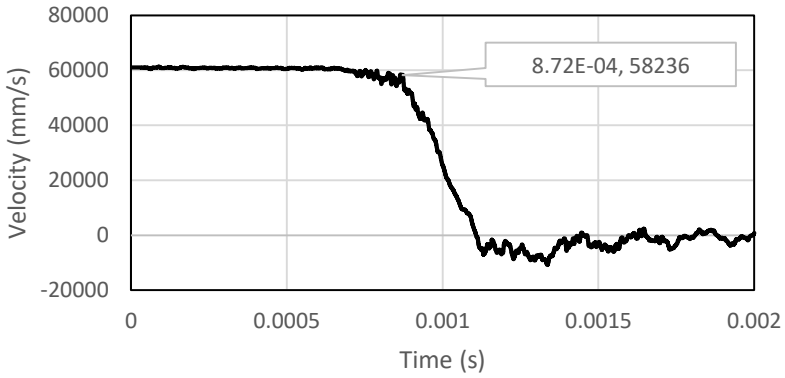

Figure E2 - T4 Piston Velocity plotted against Time after Initial Impact Speed of 61 m/s

Appendix F
Mesh Connections

F. Connecting Parts with Different Materials in a 2D Analysis

The following study involved confirming whether mesh connections would allow for parts with different material assignments to be connected in a 2D axisymmetric model. The figure below shows the assignment of different materials to the two parts needing to be connected together.

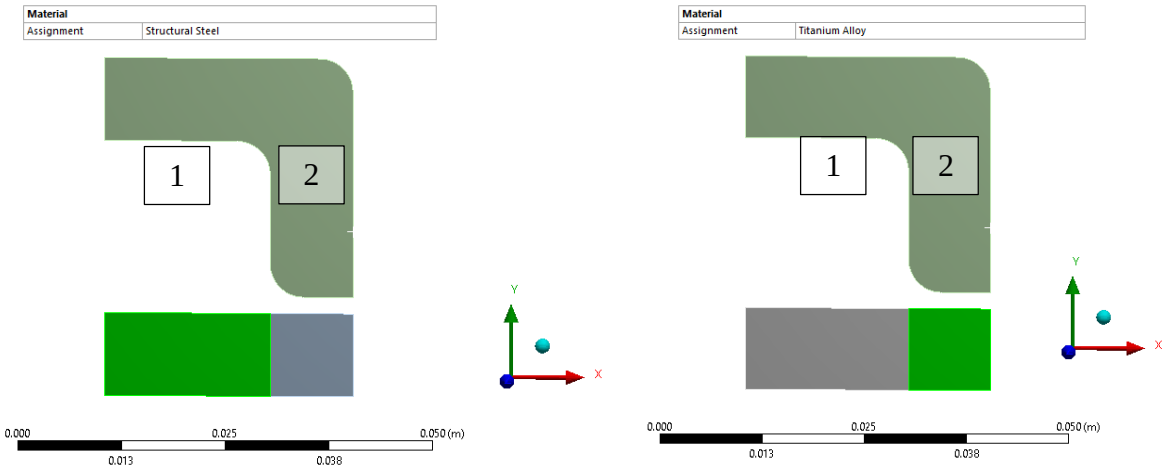

Figure F1 - Assigning Different Materials to Two Connected Bodies

Mesh connections were used to connect these two parts together. The figure below shows that without mesh connections the second part breaks off from the first upon impact with the colliding body. However, with mesh connections the two parts become connected.

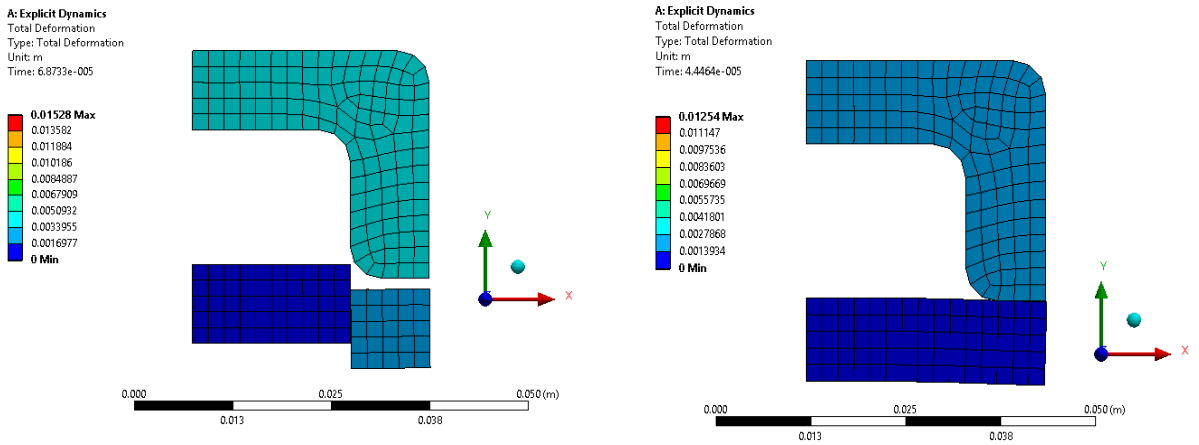

Figure F2 - Comparison between Applying No Mesh Connections (Left) and Applying Mesh Connections (Right)

Appendix G
T4 Mesh Independence

G. Mesh Independence of T4 Piston and Compression Tube

The following study involved coducting a mesh independence study for the piston and compression tube.

It was found that as the mesh density of the piston increased, the maximum von Mises stress continued to change even when the body size mesh for the piston was 0.1 mm. It was later realised that these stresses continued to increase due to the fact that they existed at corners and instead, the von Mises stress at locations outside of these corners should have been used to conduct the mesh independence study. The figure below reveals the path in which the von Mises stress was analysed in the T4 piston.

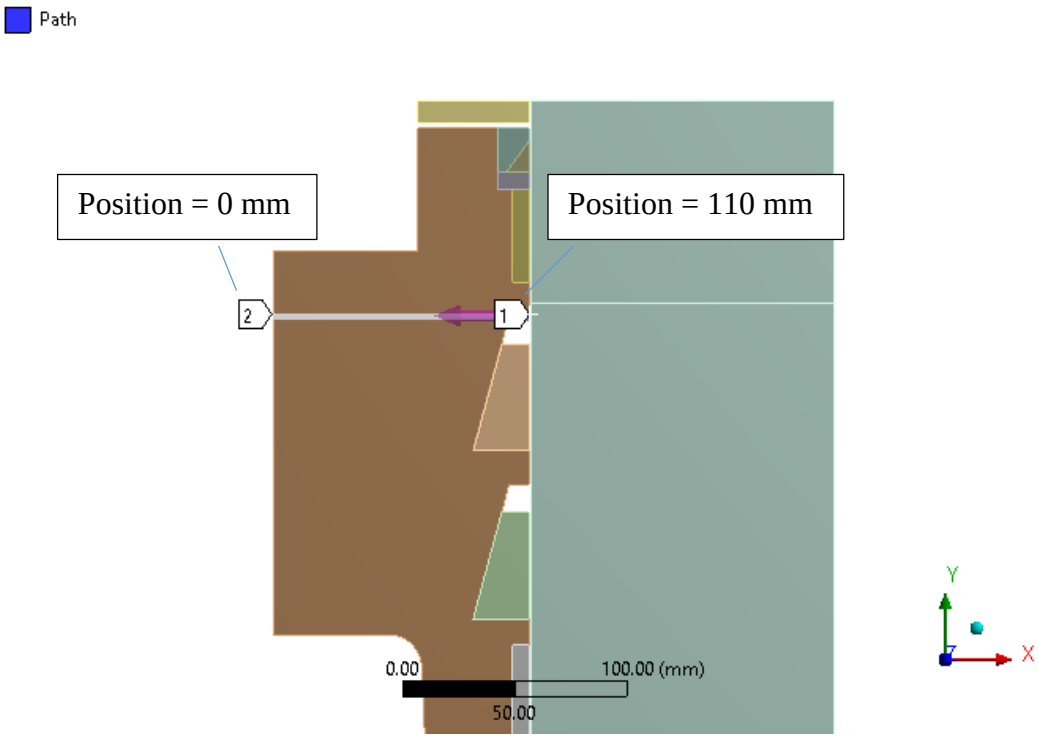

Figure G1 - Path on the T4 Piston Body in which the von Mises Stress was Analysed for the Mesh Independence Study

The von Mises stress along this path on the T4 piston body at differing mesh body sizes applied to the T4 piston body can be seen in the figure below.

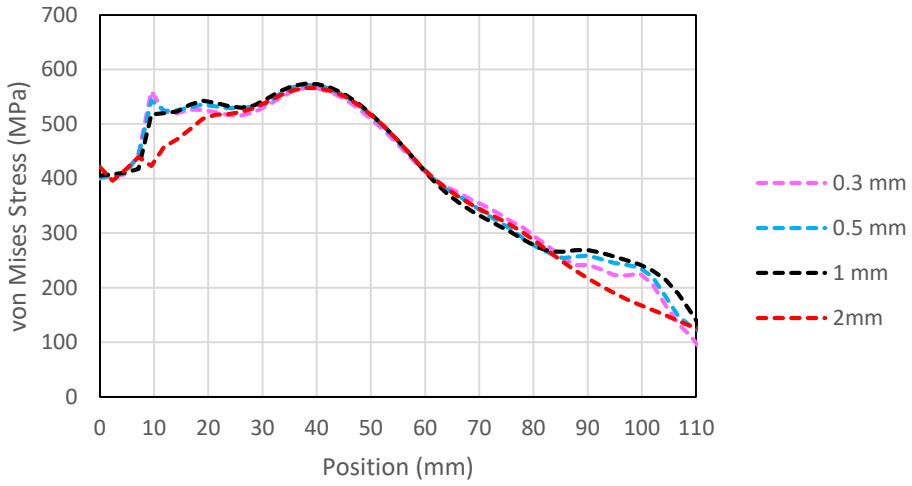

Figure G2 - von Mises Stress along Path on the T4 Piston Body at Differing Mesh Body Sizes

As shown in the above figure, a minimum mesh body size of 1 mm would need to be applied to the T4 piston in order to achieve mesh independence.

The subsequent analysis involved determining the mesh independence of the compression tube. The mesh shown below reveals a high mesh density in the piston (1 mm body size mesh) and in the compression tube towards the front end (3 mm body size mesh) where a majority of the deformation was expected to occur during a piston impact. The mesh density of the compression tube then progressively becomes coarser (to a 5 mm body size mesh) further away from the front end.

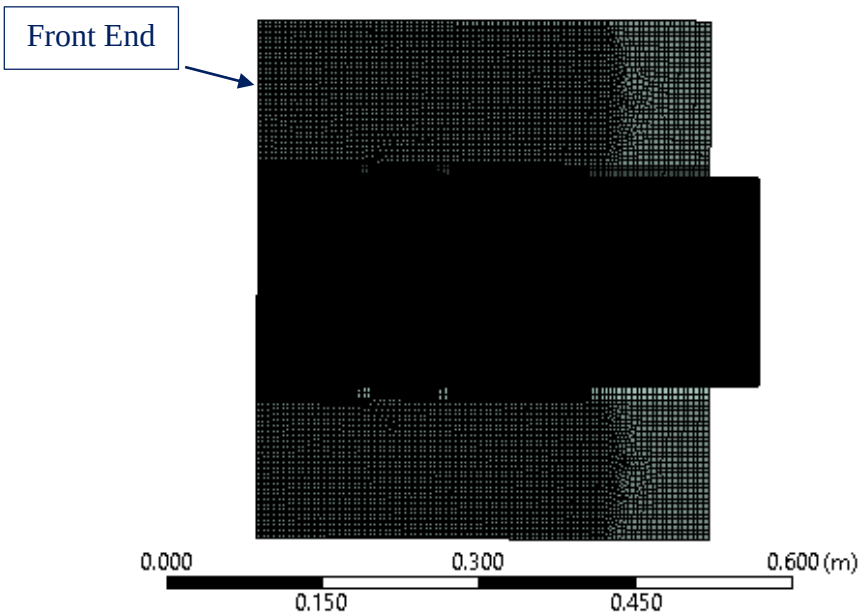

Figure G3 - View of Mesh Density Applied to T4 Piston and Compression Tube

Furthermore, inflation was added to the mesh in the compression tube at the front end of the piston which effectively increased the mesh density significantly at the contacting surface between the compression tube and the piston. A clearer view of the mesh applied to the compression tube can be shown below.

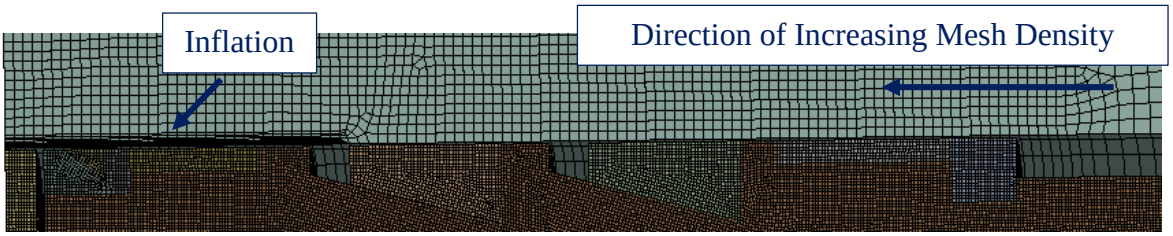

Figure G4 - Closer View of Mesh Density in Compression Tube

The figure below provides a view of inflation (with 10 layers) applied to the T4 compression tube.

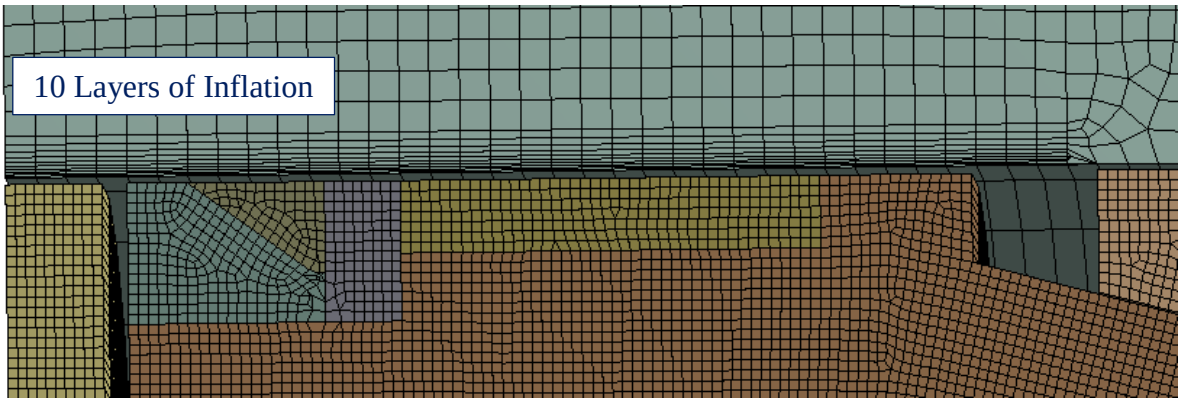

Figure G5 - View of Inflation (10 Layers) Applied to T4 Compression Tube

The figure below serves as a comparison to the figure above where no inflation is applied to the T4 compression tube.

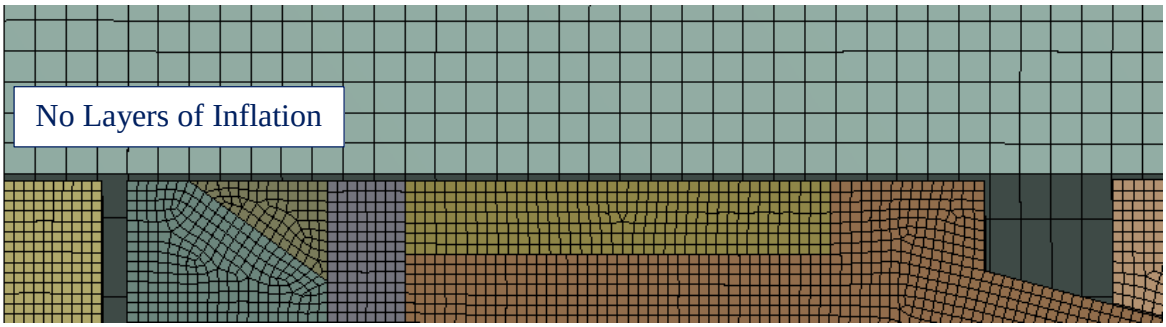

Figure G6 - View of T4 Compression Tube with no Inflation Applied

The maximum total deformation of the T4 compression tube and the pressure applied to the inner surface of the T4 compression tube at varying layers of inflation can be seen in the figures below.

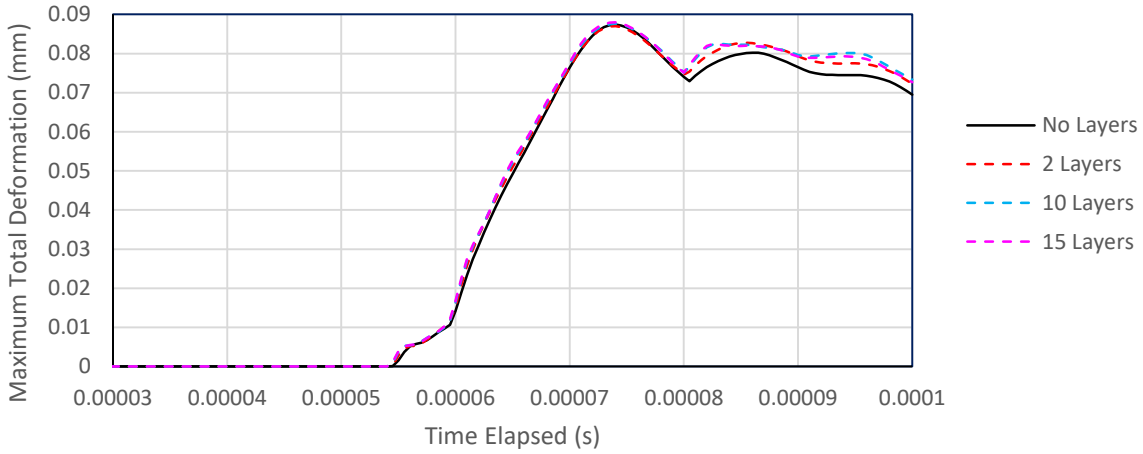

Figure G7 - Maximum Total Deformation along Inner Surface of T4 Compression Tube at Varying Inflation Layers

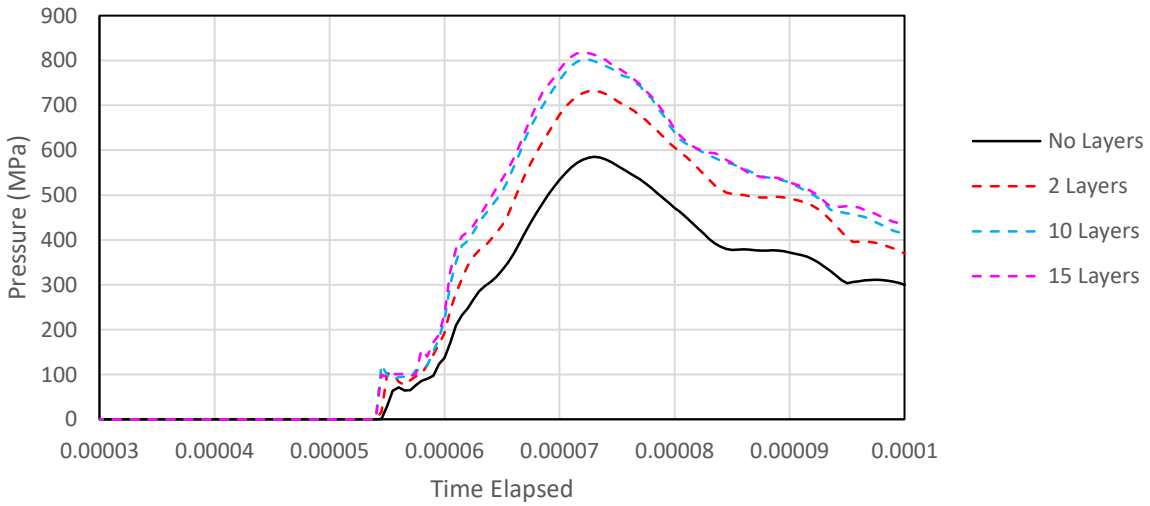

Figure G8 - Maximum Pressure along Inner Surface of T4 Compression Tube at Varying Inflation Layers

As shown in the above figure, a minimum number of inflation layers of 10 would need to be applied to the T4 compression tube in order to achieve mesh independence.

Appendix H
Axisymmetric X2 Piston

H. Axisymmetric Validity of X2 Piston

The following study involved analysing whether X2's new lightweight piston could be treated as axisymmetric despite the cut-outs on the piston body. This was achieved by producing a 2D axisymmetric model of the X2 lightweight piston and then setting up a model where this piston would impact a rigid wall at 200 m/s. The results obtained for this 2D axisymmetric model would then be compared to a full 3D model.

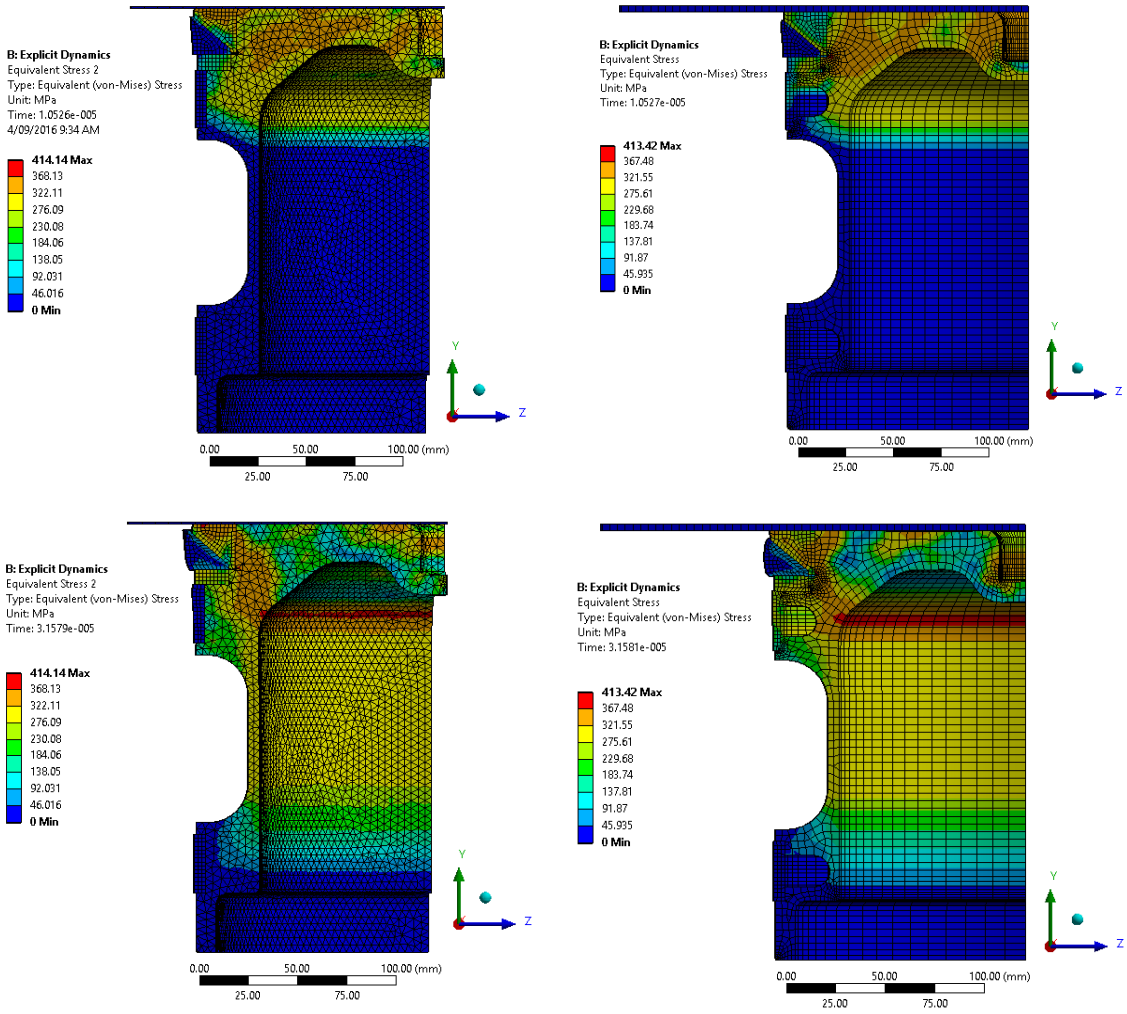

Figure H1 - Stress Wave Propagation through 3D Model (Left) and 2D Axisymmetric Model (Right) due to a Piston Impact Velocity of 200 m/s

As shown in the above figure, the stress wave propagation between the 2D and 3D models were near identicaly.

The maximum total deformation of the 2D and 3D model of X2's new lightweight piston over time following an impact at 200 m/s with a rigid wall can be seen in the figure below.

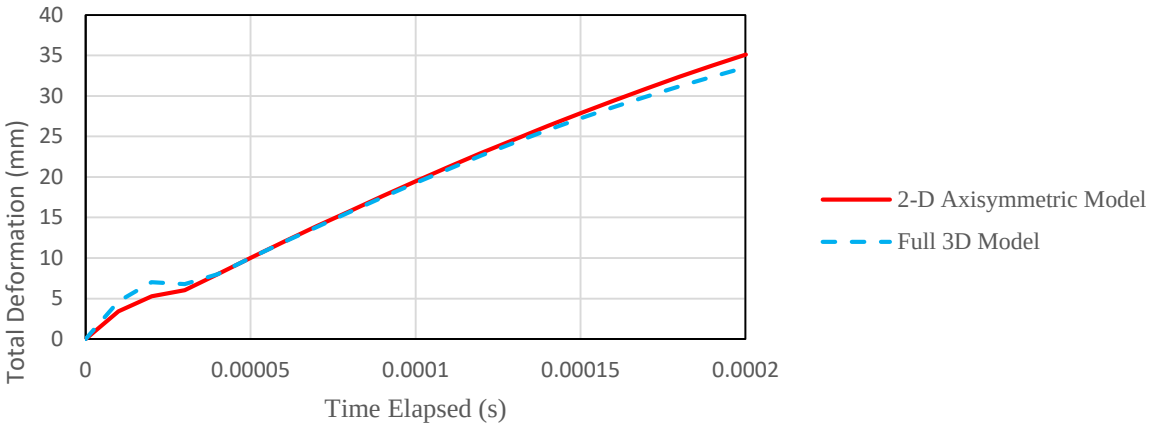

Figure H2 - Maximum Total Deformation of X2 Piston at Impact Speed of 200 m/s

A view of the final deformation of the 2D and 3D model of X2's new lightweight piston can be seen below.

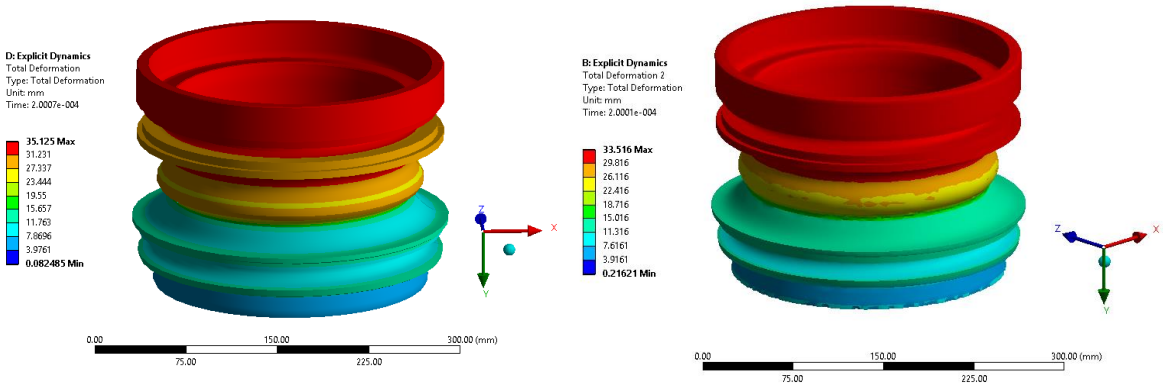

Figure H3 - View of Final Deformation of the 2D Piston Model (Left) and 3D Piston Model (Right) following an Impact at 200 m/s with a Rigid Wall

It is clear that X2's new lighweight piston can be treated as axisymmetric as it yields near identical results compared to the 3D model equivalent. Furthermore, it is clear that there exists no 3D deformation in the X2 piston at loadings following an impact speed of up to 200 m/s with a rigid wall.

Appendix I
Nylon Stud

I. Details on Axisymmetric Modelling Techniques

The X3 facility will be fitted with 12 studs which are 80mm in diameter. The lengths of these studs were estimated to be between 200 to 300 mm. The maximum impact velocity in which these studs were designed to withstand before damage to the other parts of the facility occurs was 30 m/s.

The mass, M, of the X3 piston, as per the simplified model used in the AUTODYN simulation, is given by:

$$\mathrm{M} = \rho \mathrm{V} = 2804 \frac{\mathrm{kg}}{\mathrm{m}^3} \times 0.035558\ \mathrm{m}^3 = 99.7\ \mathrm{kg}$$

With 12 studs installed, this means that $\frac{99.7}{12} = 8.3$ kg of the X3 piston will be acting on each stud if the load is assumed to be distributed evenly between the studs. Thus, the ratio between the diameter and the length of the X3 piston needs to be such that the mass is 8.3 kg for the axisymmetric model.

Having a sufficiently large diameter for the X3 piston in this model is required to prevent the nylon stud from wrapping around the piston (refer to the figure below).

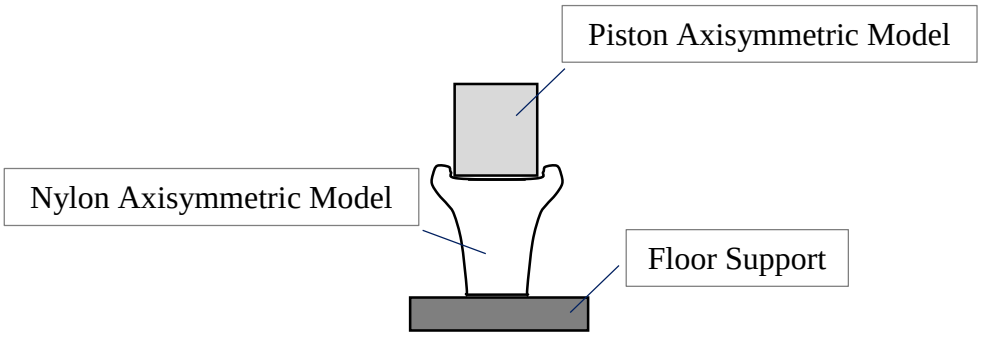

Figure I1 - Depiction of Nylon Wrapping around Piston during Impact with a Sufficiently Small Piston Diameter

For this same reason, a rigid plate with sufficient diameter needs to be placed underneath the nylon studs to prevent deformation in the negative longitudinal direction where the reference zero-point location is the bottom surface of the stud.

If the diameter of the nylon stud is 80 mm, then the diameter of the piston will be made to be 320 mm. If this is not a sufficient diameter it can be changed at a later time. With this diameter, the height of the piston that will yield a piston mass of 8.3 kg can be calculated as follows:

$$L = \frac{m}{\pi R^2 \rho} = \frac{8.3087\ \text{kg}}{\pi\left(\frac{320}{2} \times \frac{1}{1000}\right)^2\ \text{m}^2 \times 2804\ \frac{\text{kg}}{\text{m}^3}} = 0.0368\ \text{m or } 36.8\ \text{mm}$$

The dimensions for the bottom supporting rigid plate will be made the same as the piston for simplicity.

A mesh independence study for the nylon studs was conducted to determine how fine the mesh needed to be to yield reliable results from the solver. At impact speeds up to 30 m/s, a mesh of 10 mm will yield mesh independency. However, at higher impact speeds where the nylon stud deflections are larger, it is expected that a finer mesh is required to capture the larger deformations properly. A mesh of 10 mm would be sufficient for impact speeds up to 30 m/s. Nonetheless, a mesh size of 1mm will be used as a 2D axisymmetric model can produce runs within 15 minutes which was considered to be a reasonably short amount of time.

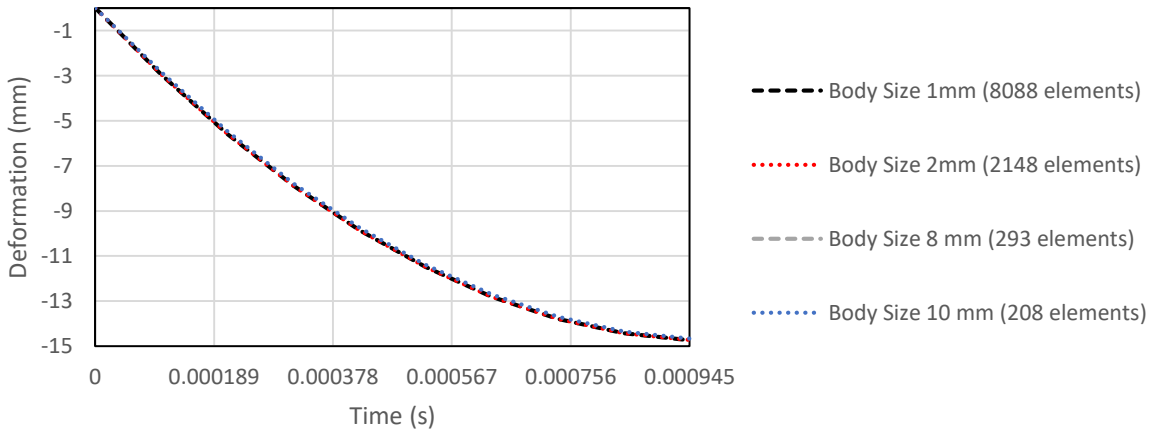

Figure I2 – Influence of Nylon Mesh Density on the Maximum Deformation of Nylon Stud following a Lightweight X3 Piston Impact Speed of 30 m/s

Appendix J
Nylon Material Details

J. Determinig Bilinear Material Model Data of Nylon

The method of estimating the onset of yielding of the nylon material was taken from Pouriayevali (2013).

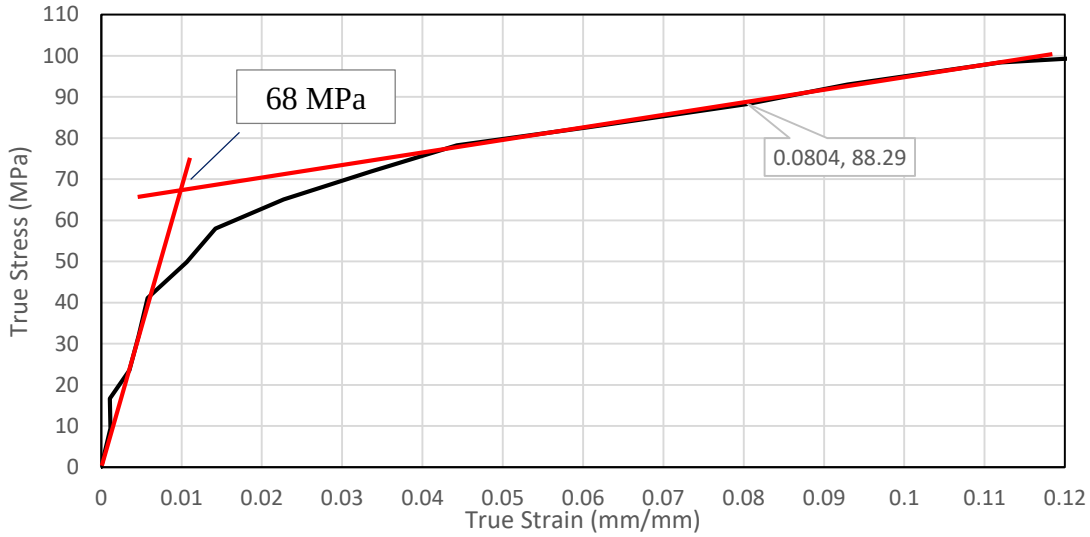

Figure J1 - True Stress-True Strain Curve for Nylon under Compression at a Strain Rate of -3830/s

Details extracted from above figure:

- Yield Stress = 68 MPa
- Young's Modulus $= \frac{68\ \text{MPa} - 0\ \text{MPa}}{0.01 - 0} = 6800\ \text{MPa}$
- Tangent Modulus $= \frac{88.29\ \text{MPa} - 68\ \text{MPa}}{0.0804 - 0.01} = 288.2\ \text{MPa}$

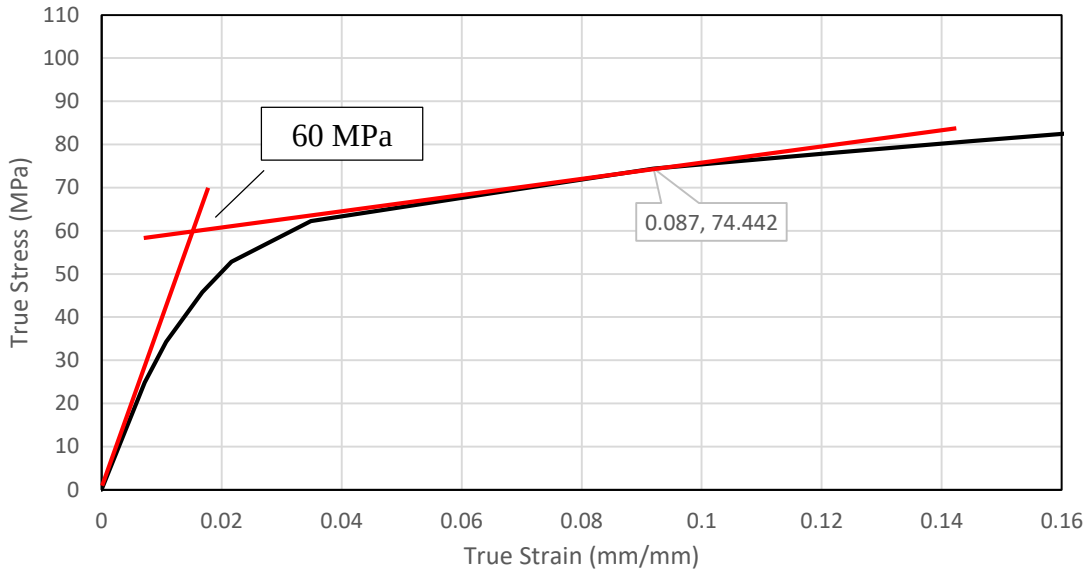

Figure J2 - True Stress-True Strain Curve for Nylon under Compression at a Strain Rate of -2760/s

Details extracted from above figure:

- Yield Stress = 60 MPa
- Young's Modulus $= \frac{60\ \text{MPa} - 0\ \text{MPa}}{0.014 - 0} = 4286\ \text{MPa}$
- Tangent Modulus $= \frac{74.44\ \text{MPa} - 60\ \text{MPa}}{0.087 - 0.0168} = 205.4\ \text{MPa}$

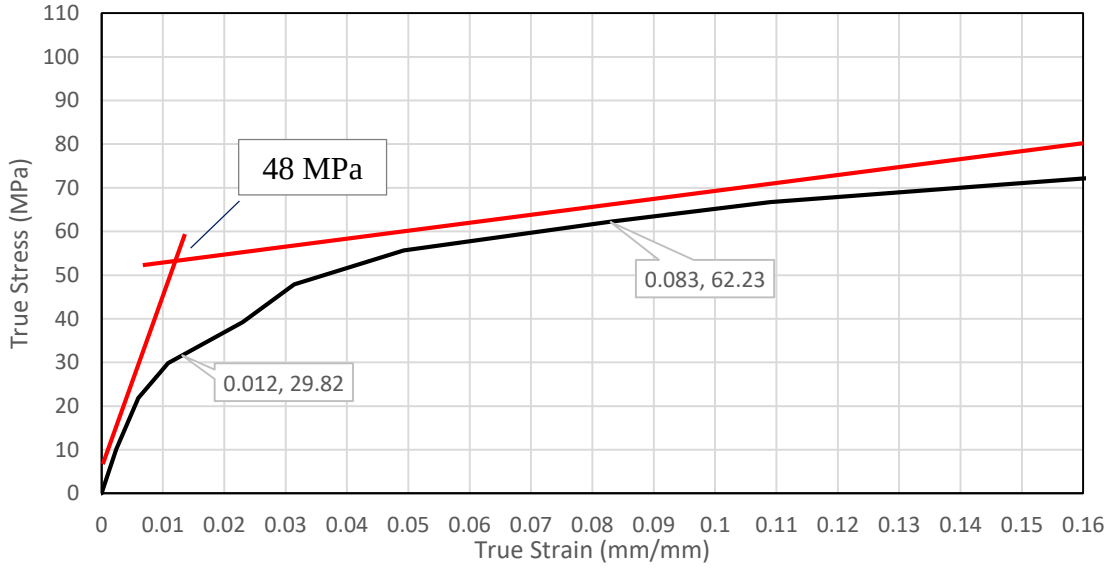

Figure J3 - True Stress-True Strain Curve for Nylon under Compression at a Strain Rate of -2000/s

Details extracted from above figure:

- Yield Stress = 48 MPa
- Young's Modulus $= \frac{48\ \text{MPa} - 0\ \text{MPa}}{0.012 - 0} = 4000\ \text{MPa}$
- Tangent Modulus $= \frac{62.23\ \text{MPa} - 48\ \text{MPa}}{0.083 - 0.012} = 200.4\ \text{MPa}$

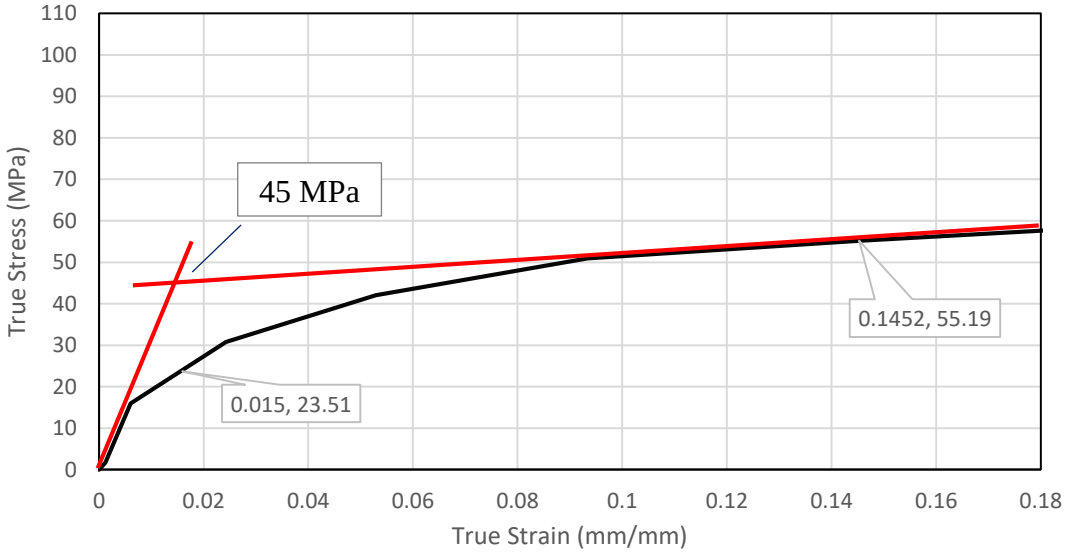

Figure J4 - True Stress-True Strain Curve for Nylon under Compression at a Strain Rate of -980/s

Details extracted from above figure:

- Yield Stress = 45 MPa
- Young's Modulus $= \frac{45\ \text{MPa} - 0\ \text{MPa}}{0.015 - 0} = 3000\ \text{MPa}$
- Tangent Modulus $= \frac{55.19\ \text{MPa} - 45\ \text{MPa}}{0.1452 - 0.015} = 78.26\ \text{MPa}$

Appendix K
X3 Mesh Independence

K. Mesh Independence of X3 Lightweight Piston

The following study involved determining the minimum body size mesh which achieved mesh independence for the X3 piston body following a 100 m/s impact into a rigid wall. In this analysis, a 1/36th solid model of the X3 piston was used.

The results for the equivalent stress after using a body size mesh of 1.75 mm and 5 mm can be seen below.

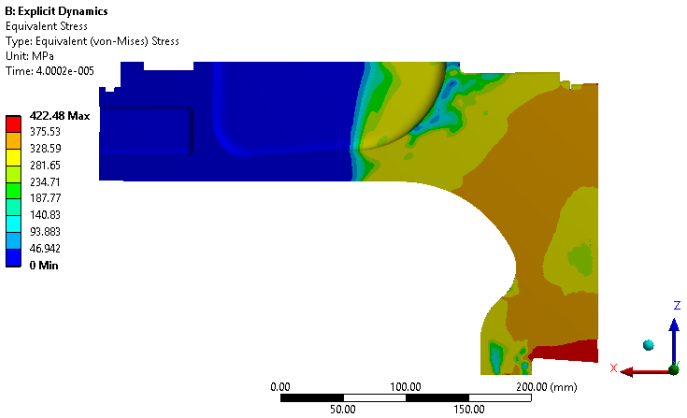

Figure K1 - Equivalent Stress in X3 Piston Body using a Body Size Mesh of 1.75 mm

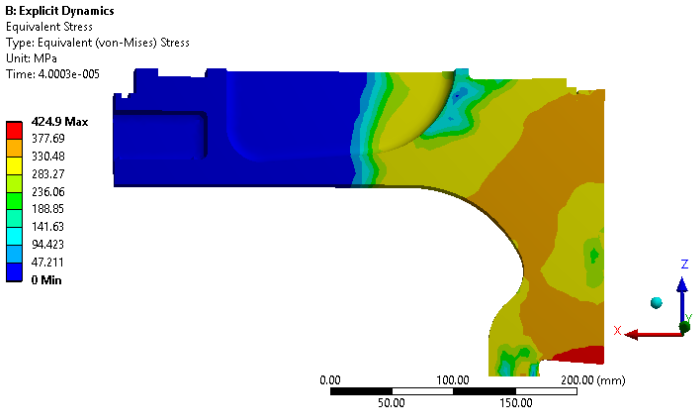

Figure K2 - Equivalent Stress in X3 Piston Body using a Body Size Mesh of 5 mm

The equivalent stress and total deformation results at various mesh densities from this analysis can be found in the table below.

Table K1 - Equivalent Stress and Total Deformation in X3 Piston at Varying Mesh Densities

Body Size	Nodes	Elements	Equivalent Stress (MPa)	Total Deformation (mm)
1.75	302084	1585617	422.48	5.7589
3.5mm	42410	202806	419.85	5.794
5mm	16433	72506	424.9	5.7286
6mm	10306	44283	430.5	5.9285
Automatic Mesh	3830	13770	432.03	6.1289
30mm	1265	5481	400.84	4.3898

The total deformation results against the mesh density in the X3 piston body can be seen in the figure below.

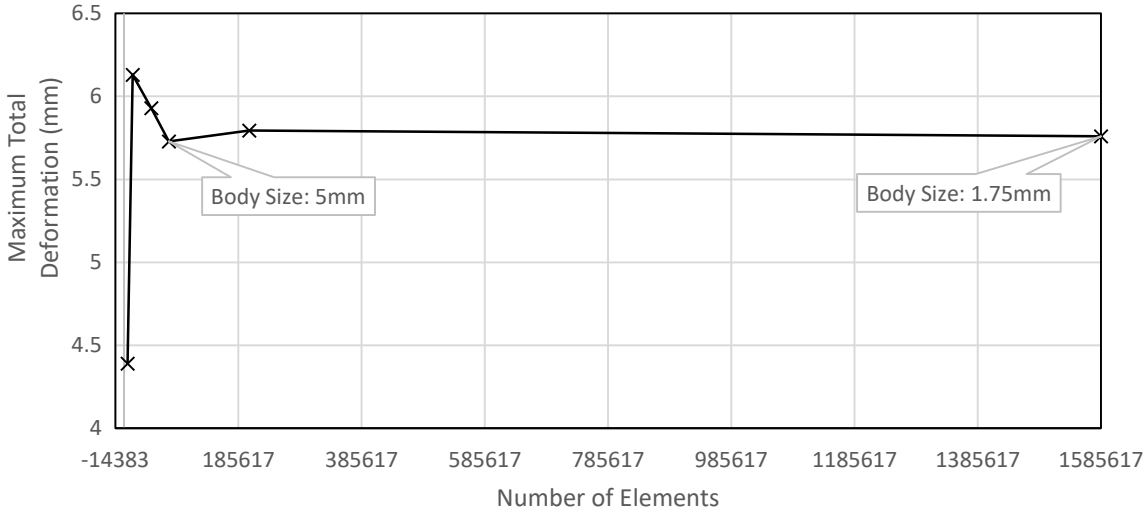

Figure K3 - Maximum Total Deformation plotted against the Number of Elements in the X3 Piston Mesh

This analysis reveals that a mesh body size of 5 mm applied to X3's lightweight piston would achieve mesh independence.